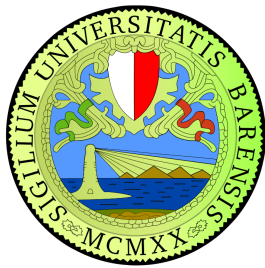


UNIVERSITÀ DEGLI STUDI DI BARI "ALDO MORO"



Dipartimento interateneo di fisica "M. Merlin"

DOTTORATO DI RICERCA IN FISICA

Ciclo XXVI

Settore scientifico disciplinare Fis/04

Study of multi-strange baryon production with ALICE at the LHC energies

Dottorando:
Domenico COLELLA

Coordinatore:
Ch.mo Prof. Gaetano SCAMARCIO

Supervisore:
Dott. Domenico ELIA

In conclusion, it appears to me that nothing can be more improving to a young naturalist, than a journey in distant countries. It both sharpens, and partly allays that want and craving, which, as Sir J. Herschel remarks, a man experiences although every corporeal sense be fully satisfied. The excitement from the novelty of objects, and the chance of success, stimulate him to increased activity. Moreover, as a number of isolated facts soon become uninteresting, the habit of comparison leads to generalization. On the other hand, as the traveller stays but a short time in each place, his descriptions must generally consist of mere sketches, instead of detailed observations. Hence arises, as I have found to my cost, a constant tendency to fill up the wide gaps of knowledge, by inaccurate and superficial hypotheses. But I have too deeply enjoyed the voyage, not to recommend any naturalist, although he must not expect to be so fortunate in his companions as I have been, to take all chances, and to start, on travels by land if possible, if otherwise, on a long voyage. He may feel assured, he will meet with no difficulties or dangers, excepting in rare cases, nearly so bad as he beforehand anticipates. In a moral point of view, the effect ought to be, to teach him good-humoured patience, freedom from selfishness, the habit of acting for himself, and of making the best of every occurrence. In short, he ought to partake of the characteristic qualities of most sailors. Travelling ought also to teach him distrust; but at the same time he will discover, how many truly kind-hearted people there are, with whom he never before had, or ever again will have any further communication, who yet are ready to offer him the most disinterested assistance.

The Voyage of the Beagle, Charles Darwin

CONTENTS

Introduction	1
1 Physics of the Quark-Gluon Plasma	5
1.1 Standard model	5
1.2 QCD and Quark-Gluon Plasma	8
1.3 Heavy-Ion collisions	16
2 Strangeness production in a Quark-Gluon Plasma	23
2.1 Strange quark and hyperons	23
2.2 Strangeness as a QGP signature	25
2.3 Theoretical models	30
2.3.1 Hydrodynamic models	30
2.3.2 Microscopic models	31
2.3.3 Statistical models	32
2.3.4 Event Generators	37
2.4 Production mechanisms	38
2.4.1 Nuclear modification factors	40
3 The ALICE experiment	45
3.1 The LHC project	45
3.2 The ALICE project	48
3.2.1 The ALICE detector	48
3.2.2 Data Acquisition (DAQ) and Trigger systems	57
3.2.3 Data flow: from the Online to the Offline	58
3.2.4 ALICE Offline software framework	60
3.2.5 Event reconstruction	62

3.2.6	Particle identification with the TPC	65
3.2.7	Centrality definition and determination	67
4	Cascade identification using topological reconstruction	71
4.1	Introduction to multi-strange baryons	71
4.2	Topological reconstruction	75
4.3	Reconstruction in pp and Pb–Pb environments	78
5	Multi-strange baryon analysis in Pb–Pb collisions	81
5.1	Data sample and event selection	81
5.2	Topological cuts and invariant mass distribution	83
5.3	Transverse momentum spectra	100
5.3.1	Signal extraction	100
5.3.2	Acceptance-efficiency correction	103
5.3.3	Normalization	111
5.3.4	Point-by-point systematic uncertainties	112
5.3.5	Corrected spectra	117
5.3.6	Analysis check: $c\tau$	118
5.4	Yield extraction	120
6	Multi-strange baryon analysis in pp collisions	125
6.1	Data sample and event selection	125
6.2	Topological cuts and invariant mass distribution	127
6.3	Transverse momentum spectra	130
6.3.1	Signal extraction	130
6.3.2	Acceptance-efficiency correction	130
6.3.3	Normalization to the inelastic collisions	138
6.3.4	Point-by-point systematic uncertainties	140
6.3.5	Corrected spectra	144
6.3.6	Analysis check: $c\tau$	144
6.4	Yield extraction	145
7	Further results and discussion	151
7.1	Spectra comparison with model predictions	151
7.2	Strangeness enhancements	154
7.3	Nuclear modification factors	160
Conclusions		169
Bibliography		171

LIST OF FIGURES

Figure 1	Standard Model: the fundamental constituents.	6
Figure 2	Standard Model: the forces.	7
Figure 3	QCD lagrangian in terms of Feynman diagrams.	10
Figure 4	α_S as a function of the energy scale Q.	11
Figure 5	Schematic view of two scenarios for hadronic matter.	13
Figure 6	Energy density as a function of T/T_c predicted by lattice QCD.	14
Figure 7	Phase diagram of nuclear matter.	15
Figure 8	Snapshots illustrating a collision of two nuclei.	19
Figure 9	Schematic representation of the participant/spectator model.	20
Figure 10	Time evolution of a heavy-ion collision in a Bjorken scenario.	21
Figure 11	The $J^\pi = 1/2^+$ ground state baryon octet.	24
Figure 12	The $J^\pi = 3/2^+$ baryon decuplet.	24
Figure 13	Feynman diagrams for the $s\bar{s}$ production in QGP.	26
Figure 14	Time evolution of strangeness to baryon density in a plasma.	27
Figure 15	Strangeness enhancement as a function of $\langle N_{\text{part}} \rangle$.	29
Figure 16	Λ/K_S^0 ratios as a function of p_T .	32
Figure 17	Equilibrium SHM fit to experimental data from NA49 and STAR.	34
Figure 18	Equilibrium SHM fit to experimental data from ALICE.	34
Figure 19	Non-equilibrium SHM fit to experimental data from ALICE.	35
Figure 20	Centrality dependence of the enhancement predicted by a canonical approach statistical model.	36
Figure 21	Competition between fragmentation and coalescence.	39
Figure 22	Prediction for p_T spectrum of charged hadrons from fragmentation and recombination models.	40

Figure 23	R_{AA} for charged particles measured in different colliding systems by ALICE and STAR.	42
Figure 24	R_{AA} as a function of p_T for identified particles measured by ALICE.	43
Figure 25	R_{AA} and R_{CP} as a function of p_T measured by STAR.	44
Figure 26	The CERN accelerator complex.	46
Figure 27	The ALICE detector.	50
Figure 28	Schematic view of the ITS.	52
Figure 29	Track impact parameter to primary vertex resolution in the transverse plane.	53
Figure 30	The X and Z coordinate vertex resolutions.	54
Figure 31	Schematic view of the TPC.	55
Figure 32	Momentum resolution in Pb–Pb collisions.	56
Figure 33	Global view of ALICE’s data flow.	59
Figure 34	ALICE Grid sites.	61
Figure 35	Schema of the AliRoot framework.	62
Figure 36	Principle of track reconstruction in an ALICE event.	64
Figure 37	Specific energy loss in the TPC as a function of momentum.	67
Figure 38	Distribution of the summed amplitudes in the VZERO.	69
Figure 39	Geometric properties obtained from a Glauber Monte Carlo.	70
Figure 40	Sketch of the cascade decay for charged multi-strange baryons.	73
Figure 41	ALICE Event Displays for Pb–Pb and pp collisions.	74
Figure 42	Definition of V^0 and cascade cut variables.	76
Figure 43	Physical track-finding efficiency in Pb–Pb and pp.	79
Figure 44	Ω invariant mass value against Ξ invariant mass values.	85
Figure 45	Invariant mass distributions for Ξ and Ω	87
Figure 46	Quality Assurance check procedure on the topological cuts value.	89
Figure 47	QA plots, STEP A: cosine of pointing angle for the Ξ^-	91
Figure 48	QA plots, STEP A: fiducial radius in the transverse plane for the Ξ^-	92
Figure 49	QA plots, STEP A: DCA between the V^0 daughters for the Ξ^-	93
Figure 50	QA plots, STEP A: decay length distribution for the Ξ^-	94
Figure 51	QA plots, STEP C: cosine of pointing angle for the Ξ^-	95
Figure 52	QA plots, STEP C: fiducial radius in the transverse plane for the Ξ^-	96
Figure 53	QA plots, STEP C: DCA between the V^0 daughters for the Ξ^-	97
Figure 54	QA plots, STEP C: decay length distribution for the Ξ^-	98
Figure 55	Invariant mass distributions for Ξ and Ω in two different sets of cuts.	99

Figure 56	Invariant mass distributions for Ξ^- and Ω^- for different centrality bins.	99
Figure 57	Example of signal extraction on the Ω^- invariant mass distribution.	101
Figure 58	Cascades uncorrected p_T spectra in five centrality bins.	102
Figure 59	Distribution in rapidity of the Ξ^- acceptance-efficiency.	104
Figure 60	Distribution in rapidity of the Ω^- acceptance-efficiency.	105
Figure 61	Ratios of efficiencies computed using “good” and “bad” runs.	106
Figure 62	Ratios of efficiencies computed using “injected” and standard HIJING.	107
Figure 63	Rapidity distributions for MC generated particles with and without the $dy/d\theta$ weighting.	108
Figure 64	Ratios of efficiency computed using or not the $dy/d\theta$ weighting.	109
Figure 65	Cascade and daughter momentum correlation.	110
Figure 66	GEANT3/FLUKA correction factors for the primary proton and antiproton.	111
Figure 67	Fit on the efficiency factors as a function of p_T for the Ξ^- and for the Ω^-	111
Figure 68	Efficiencies as a function of p_T and centrality for Ξ^- and Ω^-	112
Figure 69	Systematic as a function of p_T for the Ξ mass hypothesis in Ω reconstruction.	114
Figure 70	Systematic as a function of p_T for topological cut variation.	115
Figure 71	Systematic as a function of p_T for signal extraction technique.	116
Figure 72	Corrected p_T spectra in the five centrality classes for each particle.	118
Figure 73	Fitted distributions of mcL/p for generated (injected) particles.	119
Figure 74	Corrected mcL/p distributions for the four cascades.	120
Figure 75	Corrected spectra for Ξ^- (left) and Ω^- fitted with different functions.	122
Figure 76	Invariant mass distributions for the cascades in pp collisions.	129
Figure 77	Examples of signal extraction in pp collisions analysis.	131
Figure 78	Uncorrected p_T spectra for cascades in pp collisions analysis.	132
Figure 79	Distributions in rapidity of acceptance-efficiency in pp collisions.	133
Figure 80	GEANT3-FLUKA correction factors.	134
Figure 81	Efficiency as a function of p_T in pp collision analysis.	135
Figure 82	Distribution of the Z coordinate of Primary Vertex in Data and MC.	135
Figure 83	Dependence of the efficiency on the Z vertex selection.	137

Figure 84	Efficiency factors re-weighted to the experimental data Z_{PV} distribution.	138
Figure 85	Comparison of the standard and re-weighted efficiency.	139
Figure 86	Systematic as a function of p_T for rapidity cut.	141
Figure 87	Systematic as a function of p_T for Ξ mass hypothesis in Ω reconstruction.	141
Figure 88	Systematic as a function of p_T for signal extraction.	142
Figure 89	Systematic as a function of p_T for the number of TPC clusters .	142
Figure 90	Systematic as a function of p_T for selection cuts.	143
Figure 91	Corrected p_T spectra for the cascades in pp collision analysis.	145
Figure 92	Decay length check in pp collision analysis.	146
Figure 93	Lévy-Tsallis fit on the corrected p_T spectra.	147
Figure 94	Check the yield uncertainty due to the extrapolation procedure.	148
Figure 95	Corrected spectra with Ω particle and antiparticle separated. .	149
Figure 96	Signal extraction in critical bins.	150
Figure 97	Spectra in Pb–Pb collisions compare with hydro model predictions.	152
Figure 98	Spectra in pp at collisions $\sqrt{s} = 2.76$ TeV compared with PYTHIA predictions.	154
Figure 99	Spectra in pp at $\sqrt{s} = 7$ TeV collisions compared with PYTHIA predictions.	155
Figure 100	Ratio of spectra in pp collisions at $\sqrt{s} = 2.76$ TeV and the prediction by PYTHIA Perugia 2012 tune.	155
Figure 101	Cascade yields in pp collisions at $\sqrt{s} = 2.76$ TeV extrapolated. .	156
Figure 102	Enhancements as a function of the mean number of participants.	158
Figure 103	Hyperon-to-pion ratios as a function of $\langle N_{\text{part}} \rangle$	159
Figure 104	Ratio of the spectra and the fit functions.	161
Figure 105	Spectra in pp collisions with extrapolated points.	162
Figure 106	Fitting on the spectra in pp collisions comparison.	164
Figure 107	Ratio between fitting using Lévy-Tsallis function and the modified Hagedorn function.	164
Figure 108	R_{AA} as a function of p_T in five centrality classes.	166

LIST OF TABLES

Table 1	Degeneracy factors as a function of the number of flavours.	14
Table 2	Parameters of past and present heavy-ion beam facilities.	17
Table 3	Quark quantum numbers and masses.	23
Table 4	Summary of the ALICE detector sub-systems characteristics.	51
Table 5	Properties of Λ , Ξ and Ω baryons.	72
Table 6	Decay length in the laboratory frame for three different values of the total momentum for Ξ and Ω	73
Table 7	Values of the set of topological cuts in Pb–Pb collision analysis.	85
Table 8	Effect of $c\tau$ cut on signal extraction in Pb–Pb collisions.	86
Table 9	Transverse momentum binning chosen for the cascade spectra.	102
Table 10	Overview of the variation of the measured yields for systematic study.	114
Table 11	Yields from the fitting of corrected spectra using different functions.	122
Table 12	Total yields for cascades in Pb–Pb collisions for different centrality intervals.	123
Table 13	Event selections effects in pp collision analysis.	127
Table 14	Values of the set of topological cuts in pp collision analysis.	128
Table 15	Binning for the cascade transverse momentum spectra.	130
Table 16	Summary of systematic uncertainties study.	140
Table 17	Integrated yields in pp collisions at different energies.	148
Table 18	Yields from the fitting of corrected spectra using different functions.	148
Table 19	Integrated mid-rapidity ($ y < 0.5$) yields for Ω^- and $\bar{\Omega}^+$ separated. The errors contain both statistical and systematic uncertainties added in quadrature.	149

Table 20	Measured cascade yields compared with the interpolated yields.	156
Table 21	Summary of the estimated geometric properties of Pb–Pb collisions.	157
Table 22	Fit parameters for the Lévy-Tsallis function.	163
Table 23	Statistical errors for the last experimental point and the two extrapolated points in the pp spectra.	163
Table 24	Values of the systematic uncertainty on the extrapolated points.	165

INTRODUCTION

The present thesis is the result of my Ph.D. research programme as member of the ALICE Collaboration at the CERN (European Organization for Nuclear Research) laboratories. The main interest of this high energy physics experiment is connected to the study of one of the four fundamental interaction forces. On the nuclear dimension scale (1-3 fm) this is the force that binds protons and neutrons (nucleons) together to form the nucleus of an atom, and in this form, it is often referred to as the nuclear force; on a smaller scale (less than about 0.8 fm, the radius of a nucleon), it is the force that holds quarks together to form protons, neutrons and other particles, all called hadrons.

More in detail, the goal of the experiment is to understand the characteristics of the nuclear matter phase diagram. The theoretical model of the strong interaction, the quantum chromodynamics (QCD), predicts the existence of a state of matter, the so called *Quark-Gluon Plasma* (QGP), in certain thermodynamic conditions. This is the state of matter that is believed to have existed in the early stages of the evolution of our universe. In this state protons, neutrons and the other hadrons are dissolved into their elementary constituents, that become free to move within the whole volume of the system.

Experimentally the study of the QGP is conducted by means of high energy collisions involving ions and protons. The ion-ion collision is believed to pass through the phase transition, producing the QGP. In this context, the ion-proton and the proton-proton collisions can be used as references. The behaviour of the system created in the collisions, in both ion-ion and proton-proton collisions, strongly depends on the energy, and with the recent data collected at LHC a new energy domain has become accessible.

In the analysis reported in this document the production rates of charged multi-strange baryons, Ξ and Ω and their antiparticles have been measured in

Pb–Pb and pp collisions at the same energy in order to study the behaviour of one of the first proposed signatures for the QGP formation, the *strangeness enhancement*. The original prediction that the strange quark would be produced with a higher probability in a QGP scenario with respect to that expected in a pure hadron gas scenario (as the one thought to be created in pp collisions) was confirmed in measurements at lower energies. These studies can now be revisited at the much higher LHC energy, where results on strangeness enhancement and their comparisons with lower energy measurements can help to clarify the full picture.

In addition, the study of the so called nuclear modification factor as a function of transverse momentum (p_T) and the study of multi-strange baryon production in pp collisions can give insight into their production mechanism. In particular, the large transverse momentum range covered by the identification techniques adopted in the ALICE experiment provides the possibility of studying the competition between the hard mechanism (fragmentation) and soft mechanism (coalescence) in the different p_T regions.

This thesis is divided in seven chapters.

CHAPTER 1 The general physics context, with an introduction to QCD and the connection with the idea of the QGP, obtained at high density and temperature, is given in this first chapter. In addition a general description of the fundamental characteristics of heavy-ion collision and the time evolution of the created system are presented.

CHAPTER 2 This chapter is focused on the theoretical description of the strangeness production mechanisms (within the thermodynamical description) and the original idea of strangeness enhancement. Furthermore, results on the nuclear modification factor and the strangeness enhancement obtained in lower energy experiments are shown.

CHAPTER 3 In this chapter the detection capabilities of the ALICE apparatus are given. Moreover, the details on the different steps necessary to convert the electronic signals from the detectors into data suitable for analysis are presented.

CHAPTER 4 Here, the identification technique, based on the topological reconstruction of the weak decay of the multi-strange baryons, is described. Details on the difference between the two systems produced during the collision in Pb–Pb and pp are discussed.

CHAPTERS 5 AND 6 In these two chapters all the needed steps to measure the production rates of multi-strange baryons, in Pb–Pb and pp collisions respectively, are detailed.

CHAPTER 7 In this last chapter the physical results are presented. Transverse momentum spectra are first compared to model predictions. Then, results on the strangeness enhancement and the nuclear modification factors for the multi-strange baryons at the LHC energy are presented and discussed.

1

PHYSICS OF THE QUARK–GLUON PLASMA

1.1 STANDARD MODEL

Our current understanding concerning the question what the world is made of is collected in the *Standard Model* of particle physics (SM) [1], that describes our universe in terms of matter and forces.

In this picture matter is composed of 12 point-like particles, which have a spin of 1/2 (fermions) and can be classified according to how they interact or equivalently to what charges they carry. There are six quarks (up, down, charm, strange, top and bottom) and six leptons (electron, electron neutrino, muon, muon neutrino, tau, tau neutrino) as reported in Figure 1.

The interactions between elementary particles are described by the exchange of gauge bosons (usually as virtual particles¹) or equivalently by mean of a field. Mathematically, the SM is a quantized Yang-Mills theory² based on the non-abelian symmetry group $U(1) \times SU(2) \times SU(3)$ and has a total of twelve gauge bosons: the photon, three weak bosons and eight gluons. The interactions included in such a model are the electromagnetic force, the weak force and the strong one (Figure 2). Quarks have a property called *colour*, playing the role of charge in the strong force. Both quarks and leptons are affected by the weak force and all the charged particles interact electromagnetically.

The models that describe these interactions are listed as follows:

QUANTUM ELECTRODYNAMICS (QED) describes how light and matter interact.
This is the first theory where full agreement between quantum mechanics

¹ This is a transient fluctuation of an interaction field that, accordingly to the Heisenberg uncertainty principle, can violate the conservation law of the energy for a very short time, acquiring a mass and exhibiting many of the characteristics of an ordinary particle.

² Yang-Mills theory is a gauge theory based on the $SU(N)$ group.

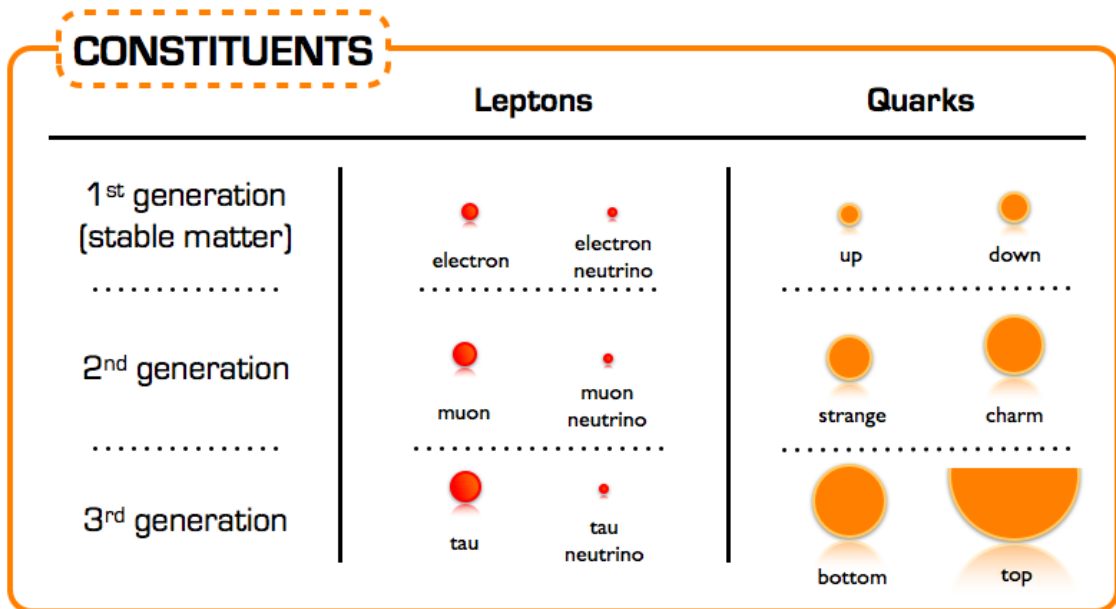


Figure 1: Fundamental constituents of the matter in the Standard Model description.

and special relativity is achieved. It was developed between 1946 and 1950 by Tomonaga Shinichiro, Julian S. Schwinger and Richard P. Feynmann. They were awarded the Nobel prize in 1965.

ELECTROWEAK THEORY (EW) is the unified description of two of the four known fundamental interactions of nature: electromagnetism and the weak interaction. It first appeared in 1961, driven by Sheldon Lee Glashow, and was completed in 1967 by Abdus Salam and Steven Weinberg. They were awarded the Nobel prize in 1979. The first measurement of the existence of the weak bosons W^+ , W^- and Z^0 was performed in 1983, when they were produced and directly observed in $S\bar{p}\bar{p}S$ collisions at CERN; during the next year the Nobel prize for this experimental result was assigned to Carlo Rubbia and Simon van der Meer. In 1999 Gerardus 't Hooft and Martinus Veltman were awarded the Nobel prize for showing that the electroweak theory is renormalizable.

QUANTUM CROMODYNAMICS (QCD) is the theory of the strong interaction (colour force), describing the interactions between quarks and gluons which make up the hadrons. Starting from the classification of the large amount of particles discovered during the fifties, the original idea of the quark model by Gell-Mann (Nobel Prize in 1969) has been developed during the sixties until 1973, when David J. Gross, H. David Politzer and Frank Wilczek discov-

INTERACTIONS				
Interactions	Charge	Quark	Leptons	Lifetime Range α_i
Strong	Color		--	10^{-23} sec 1fm 1
Electromagnetic	Electric charge [e]			$10^{-20}-10^{-16}$ sec ∞ 10^2
Weak	Weak charge [g]			10^{-12} sec 10^2-10^1 fm 10^6

Figure 2: Fundamental interactions between particles and their characteristics in the Standard Model description.

ered the “asymptotic freedom” property of the strong nuclear interaction (Nobel Prize in 2004).

Moreover, the SM provides for the existence of an antiparticle in correspondence of each particle. These, whose existence was predicted in the Dirac equation [2] and first proved by the Anderson experiment in 1932 [3], are characterized by same mass, spin and decay time but opposite charges (either electrical, weak or colour).

Pairs of quarks and leptons are grouped into three different generations exhibiting similar behaviour. Each member of a generation has greater mass than the corresponding particles of lower generations. The first generation particles do not decay; hence all ordinary (baryonic) matter is made of such bricks. Specifically, all atoms consist of electrons orbiting around an atomic nuclei, ultimately made of up and down quarks. Second and third generation charged particles, on the other hand, decay with very short half lives, and are observed only in very high energy environments.

The SM has been shown to agree very well with a large amount of experimental evidence and has been able to predict the existence of a lot of particles. Examples are the already cited bosons of the weak interaction, W and Z. To give an idea of the success of the SM, the measured masses of the W and Z bosons can be compared with the masses predicted by the SM: $M_W = 80.420 \pm 0.031$ GeV/c²

(Exp) [$M_W = 80.384 \pm 0.014 \text{ GeV}/c^2$ (SM)] and $M_Z = 91.1876 \pm 0.0021 \text{ GeV}/c^2$
 (Exp) [$M_Z = 91.1874 \pm 0.0021 \text{ GeV}/c^2$ (SM)] [4]. Over time and through many experiments, this model has become established as a well-tested physics theory.

1.2 QCD AND QUARK–GLUON PLASMA

When, starting in 1950s, the number of known particle species became large, the idea that these could be the elementary constituents of matter was replaced by the notion that these species could in fact be composite objects made up of fewer, more elementary particles, in a similar way to what had already happened to the elements of Mendeleev’s Periodic Table. The original idea by Gell-Mann (1964) was that the hadrons could be obtained as combination of the fundamental representation of an $SU_f(3)$ ³ group, where three different flavours of quark ($q = u, d, s$) combine to build mesons ($q\bar{q}$) and hadrons (qqq).

However, when cataloguing hadrons using the $SU_f(3)$ group, there are anomalous states, such as the Ω^- (sss) and the Δ^{++} (uuu), that are combinations of three quarks of the same flavour, in clear contrast with the Pauli exclusion principle for fermions. A solution was proposed in 1965 by Moo-Young Han with Yoichiro Nambu and Oscar W. Greenberg, who independently solved the problem by proposing that quarks possess an additional $SU(3)$ gauge quantum number, later called colour charge.

This new quantum number may assume three states, represented by the three primary colours: red, green and blue (denoted symbolically by R, G and B, respectively). The introduction of this new quantum number also provides an explanation to other empirical evidence, such as the fact that no qq , $\bar{q}\bar{q}$ or the single quark have never been observed directly. On the other hand, the existence of colour charge gives rise to the possible existence of differently coloured states for each particle; thus, we could have many states for the proton, such as $u_R u_G d_B$, $u_R u_G d_G$, $u_B u_R d_R$, and so on. The fundamental rule that solves such contradictions is that all the particle states observed in nature are “colourless” or “white” (or, to be more precise, unchanged under $SU_c(3)$ rotations).

The dynamics of the quarks and gluons are controlled by the gauge invariant QCD Lagrangian:

³ This is not a perfect symmetry group mainly because of the large mass difference between the two lighter flavour quarks and the strange quark. Nevertheless, it’s useful in the enumeration of the hadron states. Incidentally, flavour $SU_f(3)$ symmetry group is completely unrelated to the colour $SU_c(3)$ symmetry group, that will be introduced in the following.

$$\mathcal{L}_{\text{QCD}} = \underbrace{i\delta_{ij}\bar{\psi}_q^i \gamma^\mu \partial_\mu \psi_q^j}_{\mathcal{L}_1} + \underbrace{g_s \bar{\psi}_q^i \gamma^\mu t_{ij}^a A_\mu^a \psi_q^j}_{\mathcal{L}_2} - \underbrace{m_q \bar{\psi}_q^i \psi_{q,i}}_{\mathcal{L}_3} - \underbrace{\frac{1}{4} F_{\mu\nu}^a F^{a\mu\nu}}_{\mathcal{L}_4},$$

where the coloured gluon field tensor, $F_{\mu\nu}^a$ (with colour index a) and the squared gauge coupling parameter, g_s^2 (associated to the strong coupling constant α_s) are defined as:

$$F_{\mu\nu}^a = \partial_\mu A_\nu^a - \partial_\nu A_\mu^a + g_s f^{abc} A_\mu^b A_\nu^c \quad \text{and} \quad g_s^2 = 4\pi\alpha_s,$$

and:

- ψ_q^i is the quark field with flavour q and colour index $i \in [1;3]$, such as $\psi_q = (\psi_{qR}, \psi_{qG}, \psi_{qB})^T$ and A_μ^a is the gluon field with colour index a (adjoint representation);
- γ^μ are the Dirac matrices that express the vector nature of the strong interaction, with μ being the Lorentz vector associated index;
- m_q is the quark mass, a priori not equal to zero (resulting from the Higgs mechanism or equivalent);
- t_{ij}^a are the generator matrices of the group $SU_c(3)$, proportional to the Gell-Mann matrices, that perform revolutions in colour space, representing interactions of quarks and gluons;
- f^{abc} is the structure constant of QCD.

Each of the four terms of the QCD Lagrangian expresses an aspect of the interaction, specifically:

\mathcal{L}_1 : gives the kinetic energy of the quark field ψ_q^i ;

\mathcal{L}_2 : gives the interaction between quarks (fermions) and gluons (the bosons of the interaction);

\mathcal{L}_3 : gives the mass of the quarks;

\mathcal{L}_4 : gives the kinetic energy of the gluons.

The terms of this equation, together with the fundamental parameters α_s and m_q , summarize in just one expression all the features of the strong interaction. Looking at the expression of the gluon field tensor, the QCD lagrangian could be symbolically interpreted as in Figure 3.

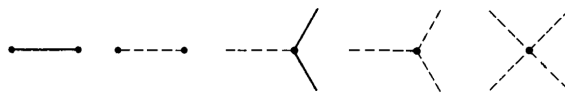


Figure 3: Symbolic representation of the QCD lagrangian in terms of Feynman diagrams.

The first three terms describe the free propagation of quarks and gluons and the quark-gluon interaction. The remaining two terms show the presence of three and four gluon vertices in QCD and reflect the fact that gluons themselves carry colour charge. This is a consequence of the non-abelian⁴ character of the gauge group.

This peculiarity of the QCD interaction imposes the evolution of the strong coupling constant, α_s . The corresponding trend has been measured experimentally, and compared in Figure 4 with predictions. A practical consequence of this behaviour is that the corresponding potential has a completely different shape than the other fundamental interactions and can be expressed by the following equation:

$$V_{\text{QCD}} = -\frac{4}{3} \frac{\alpha_s(r) \hbar c}{r} + kr, \quad (1.1)$$

where r is the distance between the two quarks and $k \approx 1 \text{ GeV/fm}$.

Three are the main properties of the QCD interaction:

CONFINEMENT At large distances between quarks and gluons (i.e. small values of transferred momentum Q in Figure 4) the coupling constant is large and the associated force is strong enough to keep these elementary constituents (usually called *partons*) confined in bounded states. As expressed in the Equation 1.1, the attractive potential increases with the increasing of the relative distance between the two partons preventing the separation of an individual quark or gluon. This explains the meaning of the term “confinement” adopted to describe this energy regime. From the theoretical point of view, the large value of α_s make impossible any perturbative approach in the solution of the Hamilton equation of the system. A successful solution is to perform the study of the system on a discrete space. Such techniques are known as lattice QCD and are based on numerical Monte Carlo simulations. The challenge for the calculations is to reduce the lattice spacing in order to approach the continuum.

⁴ The non-abelian term is used to distinguish from the idea of an abelian group, where all of the elements of the group commute.

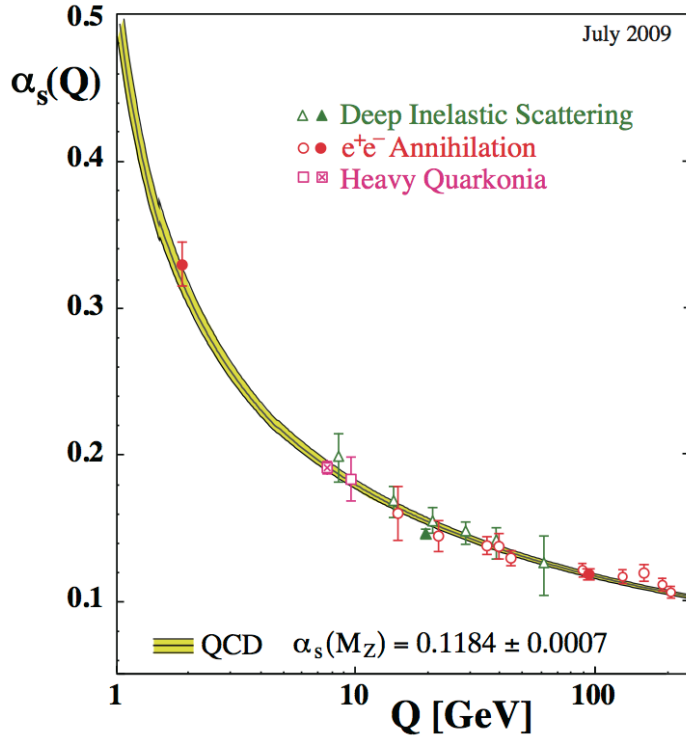


Figure 4: Summary of measurements of α_s as a function of the respective energy scale Q . The curves are QCD predictions. The points come from different α_s determination techniques based on the study of different physics processes (e.g. radiative decays of the $\Upsilon(1s)$, non-singlet structure functions from deep inelastic scattering, inclusive jet cross section measurements in neutral current, deep inelastic scattering at high Q^2 , hadronic event shapes and jet rates in e^+e^- annihilation final states). [5]

ASYMPTOTIC FREEDOM Reducing the distance between quarks and gluons (i.e. increasing Q in Figure 4) the coupling constant α_s becomes smaller. As anticipated, this is a unique feature among the forces and comes from the non-abelian nature of the QCD gauge symmetry. Such a phenomenon is also depicted by the weakening of the anti-screening effect of the surrounding virtual gluons with decreasing distance. In this way two quarks closer and closer in space show each other a smaller and smaller color charge.

CHIRAL SYMMETRY One further property of interest is connected to the chirality of the quark⁵. It can be verified that the QCD lagrangian for massless quarks is invariant under a chiral rotation ($SU_L(N_f) \times SU_R(N_f)$), while the

⁵ A chiral phenomenon is one that is not identical to its mirror image. The spin of a particle may be used to define a handedness (helicity), that could be Right (spin and momentum has the same

operator $\bar{q}q = \bar{q}_L q_R + \bar{q}_R q_L$ is not invariant (in the axial part), meaning that the mesons (state $\bar{q}q$) should have the same mass. Experimentally this is clearly not true, and it could be shown that the axial current is conserved (PCAC and the Goldberger-Treiman relation). The solution to this puzzle is that the chiral (axial-vector) symmetry is spontaneously broken; this means that the symmetry of the Hamiltonian is not a symmetry of the corresponding ground state [6]. It has also been shown, by G. t’Hooft, that the confinement implies a dynamical breaking of the chiral symmetry [7]; this means that the breaking comes from the interaction between the objects in the system. From this follows that the masses of the quarks are strongly increased because of the interaction with the constituents of the system. This mechanism, known as dynamical chiral symmetry breaking (DCSB, [8]) justifies the mass of the hadrons, reducing the role of the Higgs mechanism in the mass explanation at least for the light hadrons.

The asymptotic freedom property suggests the existence of a state of matter, called *Quark-Gluon Plasma* (QGP), in which the constituents of the hadrons are deconfined. This idea was first proposed in the seventies [9, 10]. A pictorial representation of what happens to quarks according to the separation between them is shown in Figure 5. When the density of hadrons increases to the point where the relative distance becomes of the order of the nucleon radius one may expect that nucleon boundaries are no longer a constraint for quark dynamics. This requires a density that is approximately 8 times greater than the standard nuclear density. In this condition the quarks become deconfined, in the sense that they continue to interact with each other but can now potentially access the entire volume occupied by the system, losing the identity of the hadrons they come from. Another way to achieve such transition is creating thermally excited states (that can be only colour-white particles) from the vacuum. At a certain critical temperature the hadrons start to overlap, dissolving into a system of quarks and gluons that are not bound to any specific hadron. In the chiral limit ($m_q = 0$), such transition could be described using a bag model⁶ and assuming a free pion

versus) or Left (spin and momentum has opposite versus). A symmetry transformation between the two states is called parity. Invariance under parity for a massless fermion is called chiral symmetry.

⁶ In such a model [11], hadrons may be considered as bags embedded in a non-perturbative QCD vacuum. A special boundary condition is introduced for quarks and gluons to incorporate the confinement so that colour charge does not leak out from the bag. Inside the bag quarks and gluons are treated perturbatively. The model can describe the mass spectra of light hadrons composed of u, d and s quarks reasonably well, with a suitable choice of the a parameter, called bag constant, which represents the energy necessary to create a perturbative region in the non-perturbative vacuum ($B \sim (220 \text{ MeV})^4$).

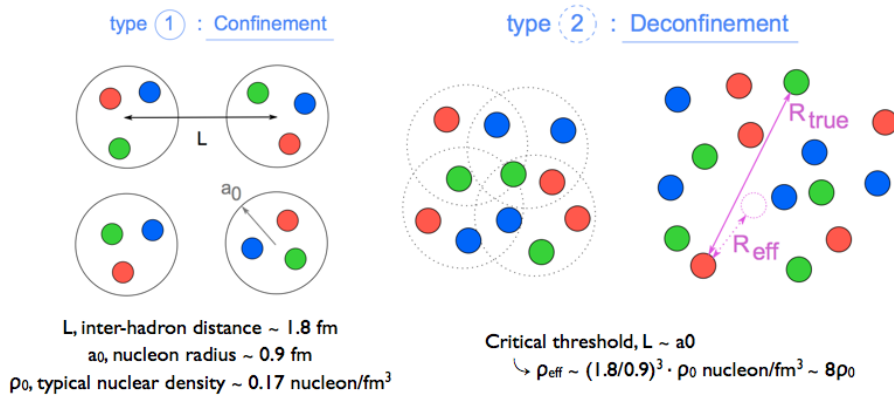


Figure 5: Schematic view of the two possible scenarios for hadronic matter: 1) ordinary matter condition and 2) high density matter in a deconfined state. [12]

gas at low T and a free quark-gluon gas at high T (as a first approximation). The energy density of the massless pion gas and of the QGP should be respectively:

$$\epsilon_\pi = 3 d_\pi \left(\frac{\pi^2}{90} \right) \cdot T^4, \quad (1.2)$$

$$\epsilon_{\text{QGP}} = 3 d_{\text{QGP}} \left(\frac{\pi^2}{90} \right) \cdot T^4 + B, \quad (1.3)$$

where B is the bag constant and the coefficient $\pi^2/90$ comes from the definition of the grand potential⁷. The two coefficients d_π e d_{QGP} are respectively the number of Nambu-Goldstone bosons and the effective degeneracy factor of the quarks and gluons in the QGP phase. These can be expressed as a function of the number of flavours (N_f) in the following way:

$$d_\pi = N_f^2 - 1, \quad (1.4)$$

$$d_{\text{QGP}} = d_g + \frac{7}{8} d_q = [2_{\text{spin}} \cdot (N_c^2 - 1)] + \frac{7}{8} \cdot [2_{\text{spin}} \cdot 2_{q\bar{q}} \cdot N_f \cdot N_c], \quad (1.5)$$

where d_g and d_q are the degeneracy for gluons and quarks, the coefficient 7/8 accounts for the different statistics and N_c is the number of colours.

Fixing the number of flavours, it can be noticed that the degeneracy factor increases by an order of magnitude from the hadronic phase to the QGP phase due

⁷ In statistical mechanics the grand potential is an important quantity for calculations when the number of particles of the system under study cannot be fixed. Such a potential is related to the grand partition function \mathcal{Z} that describes the statistics of a constant volume system that can exchange both heat and particles with a reservoir. Such an ensemble is often considered in the description of the system generated during a nucleus-nucleus collision, as explained in Section 2.3.3.

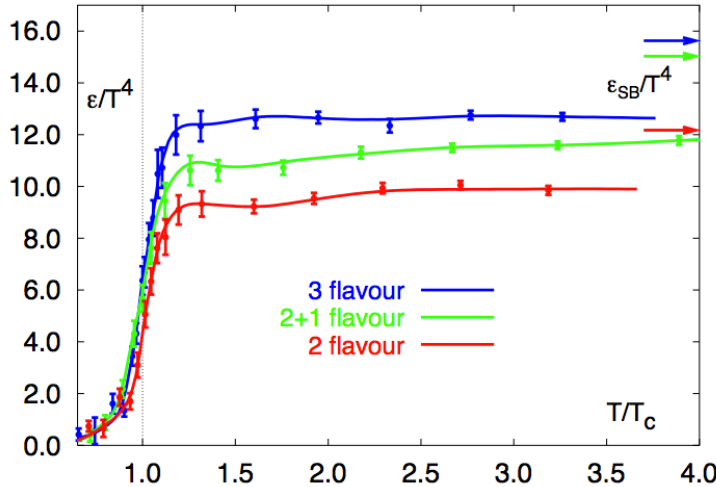


Figure 6: Energy density as a function of T/T_c predictions in lattice QCD. [13]

Table 1: Degeneracy factors of the pion d_π , the quark d_q , the gluon d_g and the QGP d_{QGP} for $N_c = 3$ and with massless N_f flavour. [14]

N_f	0	2	3	4
d_π	0	3	8	15
d_g	16	16	16	16
d_q	0	24	36	48
d_{QGP}	16	37	47.5	58

to the activation of colour degrees of freedom. The values for the degeneracies of pion gas and QGP are reported in Table 1 for $N_f = 0, 2, 3, 4$.

The behaviour of the energy density as a function of the temperature T in this simplified model shows a clear phase transition in correspondence of a critical value of the temperature, T_c .

A more quantitative and precise estimate comes from lattice QCD, that again predicts a phase transition at a critical temperature $T_c(N_f = 3) \simeq 155$ MeV. This is evident in the sudden jumps for the ϵ/T^4 plotted as a function of T/T_c curves, for three different number of flavour hypotheses (Figure 6).

Lattice QCD also predicts that, at high temperature and/or density, the quark condensate should dissolve, adding to the confinement/deconfinement transition another transition that concerns the chiral symmetry of the quarks [15]. As mentioned before, when these are confined inside hadrons they have large dynamical masses, called constituent or QCD masses. Here the chiral symmetry is said to be “broken” (or hidden). In the small α_s limit some quarks will have

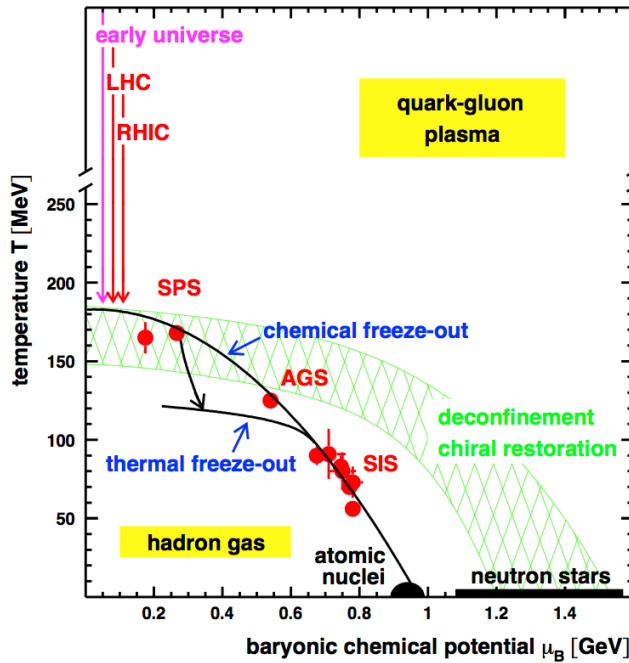


Figure 7: Phase diagram of hadronic and partonic matter. The chemical freeze-out points are determined from thermal model fits to heavy-ion data at SIS, AGS, and SPS energies. [17]

small mass, called current mass. In this limit, chiral symmetry is said to be (partially) restored.

There are two main reasons to study the properties of the QGP. The first reason concerns the study of the Standard Model: the strong interaction can be studied in an unexplored energy regime with respect to the usual Yukawa model⁸, but in a partonic environment. New light can be shed on many open questions of the Standard Model such as the chiral symmetry restoration and the connection with the mass of the quarks, the collective behaviour of the quarks and the process of hadronization. On the other hand, as can be seen in Figure 7, there is a connection with another field of physics, cosmology [16]. Indeed a QGP is expected to have existed shortly after the Big Bang and currently it may exist in the very dense cores of neutron stars [18]. In this Figure two relevant thermodynamical observables of the system are plotted: the temperature T and the baryonic chemical potential μ_B ⁹. The red points have been obtained from thermal models

⁸ Used to describe the interaction of the nucleon within nuclei.

⁹ The chemical potential is defined as the partial derivative of the free energy (Gibbs energy) of a system with respect to the amount of particles at constant temperature and pressure: $\mu = (\partial G / \partial N)_{T,P}$. Usually many chemical potentials are defined to take into account the varia-

fit on data from different experiment [17] and lie along a line that represent the limit between the two phases. Here it becomes clearly visible that the transition can be achieved in different ways: changing the temperature and/or the net baryonic density (by changing μ_B). In the last twenty years the existence and the properties of the QGP have been studied in the laboratory with collisions of heavy-nuclei at ultra-relativistic energies. In the next Section the fundamental ideas behind the techniques used for these studies will be discussed.

1.3 HEAVY-ION COLLISIONS

A practical way to reach a critical condition in which a nuclear system should undergo a phase transition to the QGP, at high temperature and/or matter density, is to collide two nuclei at sufficiently high energy. Therefore, relativistic and ultra-relativistic heavy-ion collisions are a unique tool to study nuclear matter under extreme conditions. A summary of the characteristics of the heavy-ion colliding systems studied in the past and present with the different accelerator facilities at ultra-relativistic energy is shown in Table 2.

Since the early seventies interest in heavy-ion collision experiments at relativistic energies has been growing within the nuclear-physics community. The initial experimental programme was launched at the Lawrence Berkeley Laboratory (LBL) at Berkley in 1971 [19] and at the Joint Institute for Nuclear Research (JINR) at Dubna in 1979 [20]. The Bevalac facility enabled the acceleration of nuclear projectiles to about $1A\text{ GeV}^{10}$. At the JINR in Dubna, a similar programme of research with an accelerator capability restricted to lighter ions has been developed. In 1984, a collaboration of researchers from LBL and from GSI Helmholtz Centre for Heavy Ion Research (Germany), working at the Bevalac, found the first direct evidence that nuclear matter can be compressed to high temperature and density in an accelerator [21]. This marked the first major milestone in the search for the QGP. The success of these pioneers convinced GSI to build a ring accelerator, the heavy-ion synchrotron SIS-18, in Darmstadt [22]. When in 1993 the Bevalac relativistic heavy-ion programme was shut down, SIS became the main accelerator complex for heavy-ion collisions. All these facilities are able to compress the matter to only few times the ordinary density of the nucleus and reach a temperature of the system below 100 MeV, conditions that

tion of different observables (e.g. baryon number, strangeness, isospin). At chemical equilibrium or in phase equilibrium the total sum of chemical potentials is zero, as the free energy is at a minimum.

¹⁰ The capital A stands for number of nucleons in the accelerated ion. So this is a “per nucleon” energy.

Table 2: Parameters of past and present ultra-relativistic heavy-ion beam facilities.

A_{\max} stands for the mass number (nucleon number) of heavier ions accelerated by the machine. The rapidity (y) is a relativistic variable proportional to the velocity of the particle and invariant under a Lorentz boost in the beam direction. It can be expressed as a function of the colliding energy per nucleon by the following relation: $y = \text{arcosh}(E/m) = \ln[(E/m) + \sqrt{(E/m)^2 - 1}]$, where m is the mass of the particle. In the calculation of the half rapidity window, Δy , a mass of the nucleon of $m = 0.938 \text{ GeV}/c^2$ has been used.

	AGS	AGS	SPS	SPS	SPS	RHIC	RHIC	RHIC	LHC
Starting year	1986	1992	1986	1994	1999	2000	2001	2012	2010
A_{\max}	^{28}Si	^{197}Au	^{32}S	^{208}Pb	^{208}Pb	^{197}Au	^{197}Au	^{238}U	^{208}Pb
$\sqrt{s_{\text{NN}}} [\text{GeV}]$	5.4	4.7	19.2	17.2	8.75	130	200	190	2760
$\Delta y/2$	1.72	1.57	3.02	2.91	2.22	4.93	5.36	5.31	7.99

are generally considered inadequate to produce a QGP. But these first attempts clarified the possibility of studying the properties of compressed and excited nuclear matter, giving start to the research programme at the BNL (Brookhaven National Laboratory) and CERN.

The first oxygen beam at 60 A GeV was extracted from the Super Proton Synchrotron (SPS) accelerator at CERN and met a target in the late autumn of 1986, about the same time as the BNL started its experimental programme at the Alternate Gradient Synchrotron (AGS) accelerator with a 15 A GeV silicon-ion beam. Very soon thereafter, the energy of the SPS beam was increased to 200 A GeV and sulphur-ion source was added. In order to study the relatively large volumes and longer lifetimes expected in dense matter formed in the collisions of the heavier nuclei, an upgrade of the SPS injector system was approved, which, as of 1994, made it possible to accelerate lead (^{208}Pb) ions to 158 A GeV. At the BNL, a gold (^{197}Au)-ion beam with energy up to 11 A GeV became available at that time.

At a special seminar held at CERN on 10 February 2000, spokespersons from the experiments on CERN's Heavy Ion programme presented compelling evidence for the existence of a new state of matter in which quarks, instead of being bound, are liberated to roam freely [23]. Professor Luciano Maiani, CERN Director General, said:

The combined data coming from the seven experiments on CERN's Heavy Ion programme have given a clear picture of a new state of matter. This result verifies an important prediction of the present theory of fundamental forces between quarks. It is also an important step forward in the understanding of the early evolution of the universe. We now have evidence of a

new state of matter where quarks and gluons are not confined. There is still an entirely new territory to be explored concerning the physical properties of quark-gluon matter. The challenge now passes to the Relativistic Heavy Ion Collider at the Brookhaven National Laboratory and later to CERN's Large Hadron Collider.

Within five years from this announcement, changes in the experimental data (start of the Relativistic Heavy Ion Collider (RHIC) at BNL programme few months later, with colliding nuclear beams at up to 100 A GeV) and theoretical understanding have tempered some of conclusions contained in that communicate. The new results obtained with the four dedicated experiments at RHIC led to an official announcement at the end of the first three years of data taking (18 April 2005) [24, 25]:

[...] they've created a new state of hot, dense matter out of the quarks and gluons that are the basic particles of atomic nuclei, but it is a state quite different and even more remarkable than had been predicted. In peer-reviewed papers summarizing the first three years of RHIC findings, the scientists say that instead of behaving like a gas of free quarks and gluons, as was expected, the matter created in RHIC's heavy ion collisions appears to be more like a liquid.

not only giving a final word on the existence of this new state of matter, but also opening the way to the next step in this research, the characterization of the QGP.

Today, two are the facilities that perform relativistic heavy-ion collision at ultra-relativistic energies. At BNL, the RHIC, completed in 1999, has dominated the last ten year experimental landscape in this field, with a long list of energies and colliding systems explored until today [26]. At CERN, the first heavy-ion collision performed by the Large Hadron Collider (LHC) has been realized on November 2010, with lead-ion at the greatest energy ever reached. The ALICE experiment is contributing to the goal of the characterization of the QGP studying the heavy-ion collisions produced at the LHC energy.

In the following a collision between ions at high energy is described; a pictorial representation of it in three main steps is given in Figure 8. The colliding ions, traveling at 99.995% the speed of light, which causes them to be Lorentz contracted, can be thought of as thin disks.

A simple and successful description of the geometric aspects of an high energy heavy ion collision is given by the “participant-spectator model”. Here the nucleons in the colliding nuclei are classified into two groups: the *participants*, shown by the dotted area and the *spectators* shown by the cross-hatched areas in

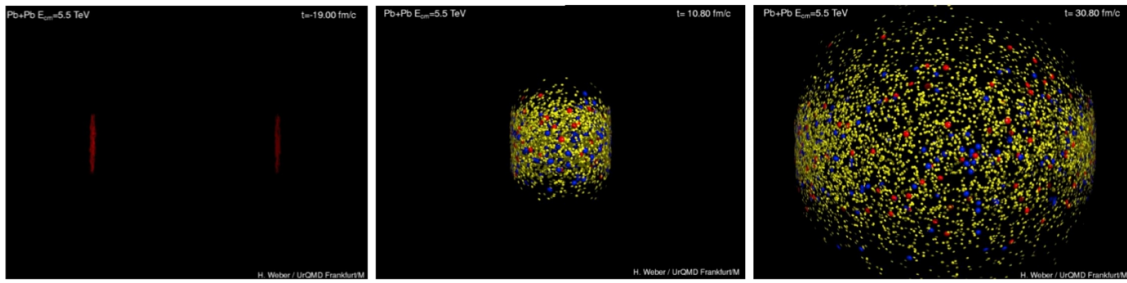


Figure 8: Three snapshots illustrating a nuclear collision of two nuclei. (Left frame) The two incident nuclei are Lorentz contracted as the incident velocities are already close to the speed of light. (Middle frame) The moment of highest compression. (Right frame) The expansion stage, when most of the particles already no longer interact strongly. These pictures, resulting from a simulation, are extracted from a movie available on [27].

Figure 9 (panel b). The number of participants N_{part} (sometimes called wounded nucleons) is then defined as the number of nucleons in the two ions which underwent at least one inelastic collision. An anti-correlation between the number of participants and that of spectators is implicit in the model. The numbers of the participants and spectators are connected to the *impact parameter*, b , that is defined as the distance between the centres of the two nuclei in the transverse direction to the beam line (Figure 9, panel a). Different classes of collisions can be defined looking at the impact parameter of the collision. In particular, a distant collision (panel c), a peripheral collision (panel d) and a central collision (panel e) are sketched in Figure 9. In most heavy ion experiments, information about the “centrality” of the collision, i.e. the impact parameter between the two colliding ions, is obtained by measuring observables proportional to the number of the spectators and/or the participants and comparing the experimental distributions with some model predictions, as explained in Section 3.2.7. The most popular model, that allow to estimate parameters such as the number of participant nucleons, the number of binary collisions or the impact parameter is the semi-classical Glauber model [28, 29].

The reference description that helps in understanding what should happen during an heavy-ion collision was proposed by J.D. Bjorken in 1983 [30]. Although the present description of the system evolution is more complex, this simplified view already contains the most important aspects that need to be considered. Figure 10 help to imagine how the system evolves, giving a schematic representation. Three dynamically distinct stages can be identified.

QGP PHASE ($\tau < 10 \text{ fm/c}$) After the head-on collision of the two beam partons a lot of exited states are created. During a period that takes fraction of

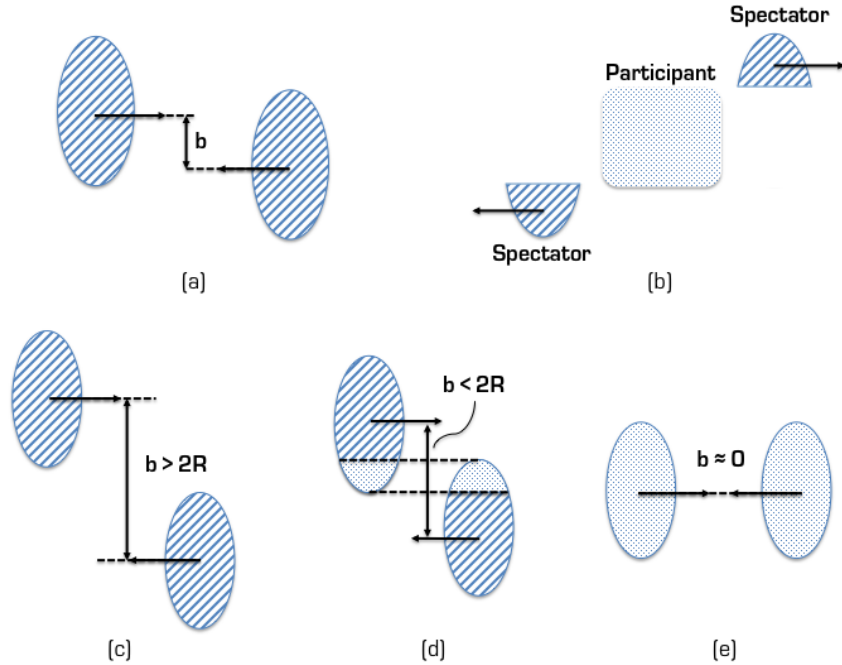


Figure 9: Schematic representation of the participant/spectator model. In pad (a) is defined the impact parameter of the collision. In pad (b) the meaning of participant and spectator nucleons is clarified. Three different collision geometries are reported in pads (c), (d) and (e).

1 fm/c (pre-equilibrium stage) quarks and gluons are produced by de-excitation and an equilibrium is reached. In this span of time partons with $p_T \gg 1$ GeV/c are also created. At the time τ_0 (Figure 10) an equilibrated system composed by real quarks and gluons is created, the so-called, quark-gluon plasma. From this point onward it may be possible to define a system temperature and the thermodynamical description of the QGP is thought to become applicable. The system expands and gradually cools down by elastic and inelastic collisions. The notion of relativistic hydrodynamics may be used to describe the expansion of the system. The temperature of the QGP decreases with the system expansion reaching the critical temperature T_C : the coupling constant α_s becomes large enough to confine partons into hadrons (confinement).

HADRON GAS ($10 \lesssim \tau \lesssim 15$ fm/c) The relative abundance of hadron species can change as long as the hadron gas is able to interact inelastically. When the collisions have an energy that is too small to be inelastic, the abundances are fixed and chemical freeze-out is reached (T_{ch}). As a consequence, the

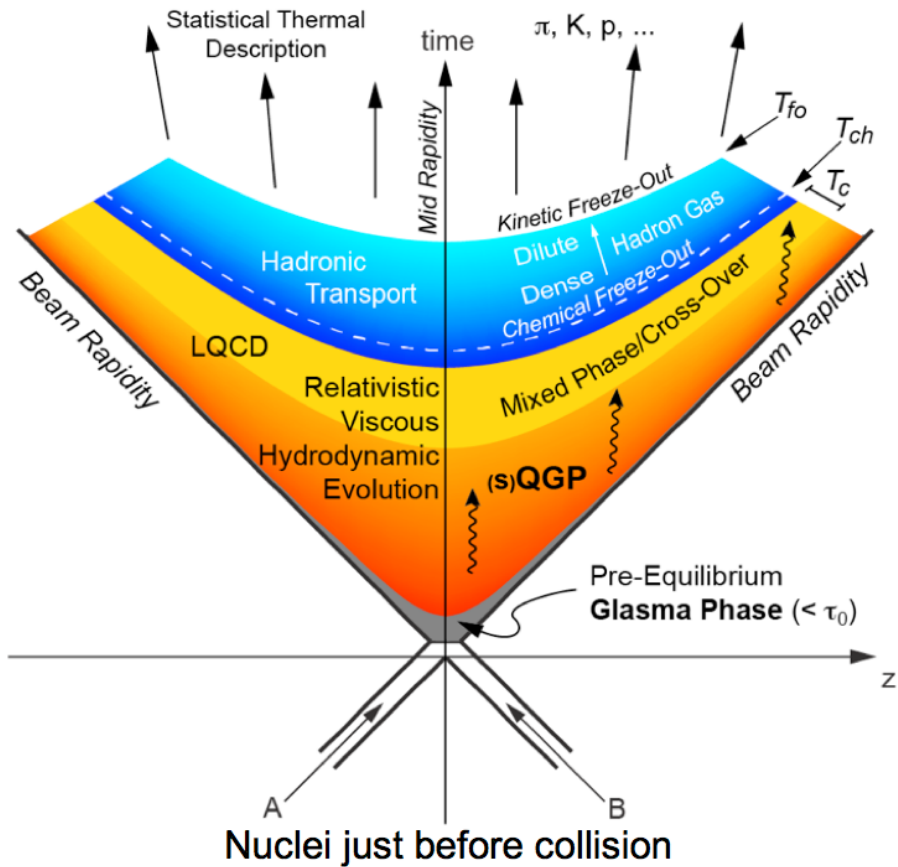


Figure 10: Time evolution of a heavy-ion collision in a Bjorken scenario. [31]

ratios between production rates of different particle species (e.g. K/π and p/π) can provide information on the system at this stage of the evolution. Elastic interactions are still present and continue to modify the kinetic properties of the hadrons. When the distances between hadrons are larger than the range of the interaction, also elastic collisions stop and the kinematical freeze-out is reached (T_{fo}). Now, also the kinematical distribution of the hadrons are fixed. Hence, information on the kinetic freeze-out temperature can be obtained from the hadron momentum spectra.

FREE HADRON STREAM ($\tau \gtrsim 15 \text{ fm}/c$) Hadrons freely stream to the experiment where they are detected. Along the way they continue to suffer interaction that can modify their momentum distribution: the short-lived unstable particles decay and interactions with the detector structure material can happen. In both cases new particles (more abundant light particles as π or K) are produced and must be distinguished.

Usually the spatial distribution of the produced particles in the polar direction (emission angle of a particle with respect to the beam direction) is expressed as a function of the pseudo-rapidity η . This variable is defined such that at very high relativistic energy can be approximated with the rapidity y (defined in the caption of Table 2), and is directly computable from the measurement of the polar angle θ :

$$\eta = -\ln\left(\tan\frac{\theta}{2}\right). \quad (1.6)$$

By looking at the net proton rapidity distribution in experiments at different energies [32], it has been shown that two different scenarios can be qualitatively distinguished, related to the behaviour of the colliding nuclei. For a collision at an energy of a few GeV per nucleon in the centre-of-mass system (like AGS or SPS), the nuclear stopping power determines whether the colliding baryons will be stopped in the centre-of-mass system and pile up to form a state with large net baryon density, which is the stopping regime (Landau picture). In the transparent regime at higher energies (like RHIC or LHC), the nuclear stopping power determines whether the projectile baryons and target baryons will recede away from the centre-of-mass without being completely stopped, leaving behind a state with very little or even no net baryon contents (Bjorken picture).

At the LHC energies, in the study of QGP formation in heavy ion collisions, it is important to measure the particle production at mid-rapidity ($y \sim 0$), namely at $\theta \sim 90^\circ$, i.e. on the region of minimum baryon density and maximum energy deposit.

2

STRANGENESS PRODUCTION IN A QUARK-GLUON PLASMA

2.1 STRANGE QUARK AND HYPERONS

The Quark Model, proposed independently by Murray Gell-Mann and Yuval Ne'eman in 1964 [33], enables the classification of hadrons in terms of their constituent quarks. In this model, the lighter mesons and baryons are representations of an $SU_f(3)$ group, whose fundamental representation is the three dimensional vector (u , d , s). These are the three lighter quarks whose characteristics are reported in Table 3; here, the masses of the heavier quarks are also reported for comparison.

Table 3: Quantum numbers and masses associated to the three lighter quarks: u , d and s . Also reported the masses for the heavier quarks.

Light flavour	d	u	s
Baryon number (B)	+1/3	+1/3	+1/3
Electric charge (Q)	-1/3	+2/3	-1/3
Isospin (I)	-1/2	+1/2	0
Strangeness (S)	0	0	-1
mass (GeV/c^2)	$0.0023^{+0.0007}_{-0.0005}$	$0.0048^{+0.0005}_{-0.0003}$	0.095 ± 0.005
Heavy flavour	c	b	t
mass (GeV/c^2)	1.275 ± 0.025	4.18 ± 0.03	$173.07 \pm 0.52 \pm 0.72$

The hadronic states are obtained from the decomposition of the following scalar products of the fundamental representations of the group:

$$\text{MESONS } (q\bar{q}) \ 3 \otimes \bar{3} = \mathbf{1} \oplus \mathbf{8};$$

$$\text{BARYONS } (qqq) \ 3 \otimes 3 \otimes 3 = \mathbf{10}_S \oplus \mathbf{8}_M \oplus \mathbf{8}_M \oplus \mathbf{1}_A.$$

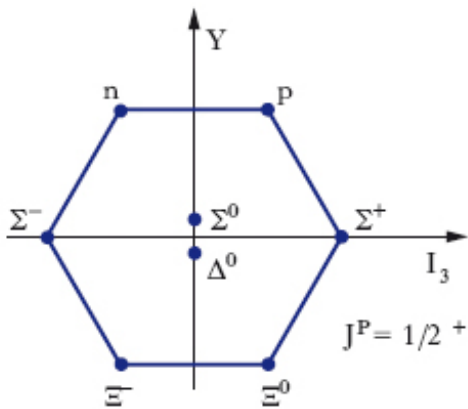


Figure 11: The $J^\pi = 1/2^+$ ground state baryon octet.

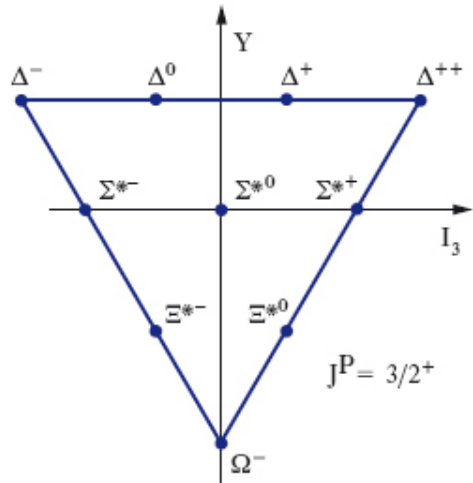


Figure 12: The $J^\pi = 3/2^+$ baryon decuplet.

Adding the spin to the baryons, one gets a 56 representation¹, that can be decomposed in an octet ($J^\pi = 1/2^+$) and a decuplet ($J^\pi = 3/2^+$), as can be seen in Figures 11 and 12. On the axes of the plots there are the third component of the isospin, I_3 , and the hypercharge², defined as $Y = B + S$, where B is the baryon quantum number and S is the strangeness quantum number.

¹ Taking as fundamental representation a six dimensional vector composed by the three lighter quarks in the two spin states, one get for the baryon states the following decomposition of the scalar product: $6 \otimes 6 \otimes 6 = 56_S \oplus 70_M \oplus 70_M \oplus 20_A$. The symmetric 56 representation decomposes into: $56 = 10^{\frac{3}{2}} \otimes 8^{\frac{1}{2}}$.

² The hypercharge is connected to the electric charge by the following relation: $Q = I_3 + \frac{1}{2}Y$.

Among the hadrons, the special family of particles that contain at least one strange quark but not heavier quarks (like charm or bottom), are called hyperons. These are: the $\Lambda(uds)$, the triplet $\Sigma^+(uus)$, $\Sigma^0(u\bar{d}s)$, $\Sigma^-(d\bar{d}s)$, the doublet $\Xi^-(dss)$, $\Xi^0(uss)$ and the $\Omega(sss)$ and the corresponding antiparticles. Ξ and Ω are the only hyperons containing more than one strange quark, hence they are called multi-strange baryons.

In the following, a general overview of the role of the strange quark within the QGP studies with heavy-ion collisions is given.

First of all, no net strangeness is present in the colliding objects before collision. Indeed, both the nucleons, proton and neutron, contain only u and d quarks among their valence quarks. All the net strangeness present in the final states (particles) is then created during the collision, and therefore the s quark plays an interesting role in the study of particle production.

Other arguments can be made looking at the naked mass of the quarks, reported in Table 3. As can be seen, the s quark is the third lightest quark, with a mass value that is half-way between the two lighter and the three heavier quarks. This means a relatively low production energy cost, which ensures an abundant production of strange hadrons among the produced particles. Thus, a relatively small amount of events is needed for hyperon analyses if compared to the requirements of heavy flavour studies.

Additional considerations can be done for hyperons: their main characteristics and the identification techniques are described in Chapter 4.

2.2 STRANGENESS AS A QGP SIGNATURE

The original interest in the strangeness in the context of the QGP comes from an idea by Johann Rafelski and Berndt Müller. In 1982, they suggested a possible signature for the formation of a QGP in a heavy-ion collision [34]. The key argument, at a fixed collision energy, rests on the different production mechanism of the s quark within two different systems:

1. **Hadron Gas (HG)**, where the degrees of freedom are the hadronic ones, as quarks and gluons are confined;
2. **QGP**, where the degrees of freedom are the partonic ones, with quarks and gluons free with respect to each other.

The following two arguments have been adopted in the comparison between the production rates of the strange quark in the two systems.



Figure 13: Feynman diagrams for the $s\bar{s}$ production in QGP: the leftmost diagram represents a quark-antiquark annihilation, while the other three correspond to gluon fusion processes.

REACTION THRESHOLD The energy needed to produce strange mesons or baryons in a thermally equilibrated HG is significantly higher than in the case of a QGP. In the following we discuss the production mechanisms and the corresponding energy thresholds in the two systems.

HG The great abundance of pions in the HG suggests to consider the production of strange particles from the reaction between them. Direct production ($\pi + \pi \rightarrow \pi + \pi + \text{strange hadron} + \text{antiparticle}$) is penalized because of the baryon and strange number conservation. This means that it is necessary to produce strange particle and antiparticle jointly. The reaction threshold corresponds to two times the rest mass of the hadrons: 2230 MeV for the $\Lambda + \bar{\Lambda}$, 2642 MeV for the $\Xi^- + \bar{\Xi}^+$, 3344 MeV for the $\Omega^- + \bar{\Omega}^+$.

In the case of indirect production, the thresholds are lower. In this case, one would have two reactions in a sequence, starting with the production of lighter hadrons ($\pi + N \rightarrow K + \Lambda$) and followed by a reaction of these intermediate products to produce the heavier hadrons ($\pi + \Lambda \rightarrow K + \Xi$ and $\pi + \Xi \rightarrow K + \Omega$). In this case the combined thresholds for the production of a Ξ is $(535 + 565)$ MeV = 1100 MeV and for the production of an Ω is $(535 + 565 + 710)$ MeV = 1810 MeV.

QGP The high gluon density gives the possibility to have new production mechanisms abreast the usual quark-pair annihilation. These are the gluon fusion processes, whose corresponding Feynman diagrams are the three rightmost processes depicted in Figure 13; these become the dominant processes, producing 80% of the $s\bar{s}$ pairs. In these reactions the energy threshold, due also to the partial chiral symmetry restoration, is equal to the naked mass of the two strange quarks $\approx 2 \cdot 100$ MeV.

EQUILIBRATION TIME The second important point is that the equilibration times of partonic reactions, especially due to the gluon fusion processes, are much shorter than the ones of hadronic reactions. The difference is particularly large, due to the corresponding low hadronic cross-section, if rare

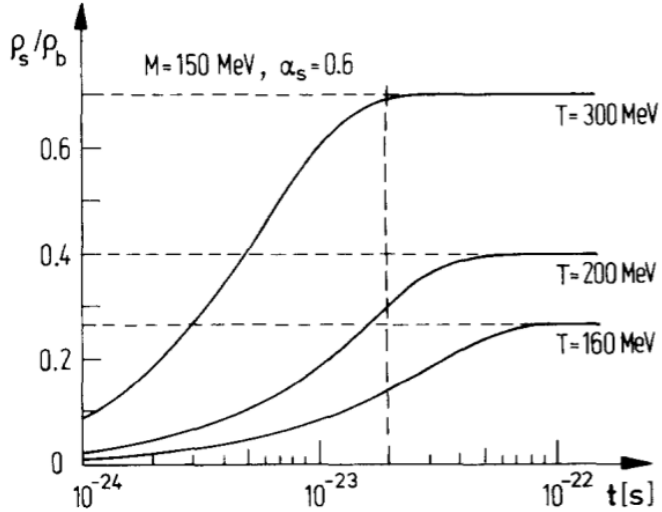


Figure 14: Time evolution of the relative strangeness to baryon density (ρ_s / ρ_b) produced in the plasma for various temperatures T , with $m_s = 150 \text{ MeV}$ and $\alpha_s = 0.6$. The vertical line corresponds to a time of $\approx 6 \text{ fm}/c$. [35]

multi-strange (anti)baryons are considered.

In a partonic scenario, with a typical temperature of $T = 200 \text{ MeV}$, equilibration times of $\tau_{\text{QGP}}^{\text{eq}} \approx 10 \text{ fm}/c$ are theoretically achievable in an ideal gas of quarks and gluons [34] (Figure 14). This is of the order of the expected total duration of a heavy-ion reaction, from the first parton collisions to the final freeze-out of the hadrons. Notice that in such description the hadronization time is negligible with respect to the equilibration time of the quark-gluon plasma, hence the hadrons have similar production times. It was found [35] that, in a gas of free hadrons, including resonances, the typical times to reach an equilibrium state depend strongly on the strange particle species. While for particles with strangeness $|S| = 1$, like kaon and Λ , chemical equilibrium might be reached after $\tau_{\text{HG}}^{\text{eq}}(K) \approx 30 \text{ fm}/c$, the timescales for rare (anti)hyperons should be an order of magnitude longer.

Thus, following these arguments, it would be much more difficult to produce multi-strange particles in a HG than in the QGP. In the latter case the production probability depends on the density of the strange quarks to the power of the number of strange quarks contained in the considered hadron. This consideration, together with the previous one on the production mechanism for the multi-strange baryons in a HG, gives the following relations:

$$\Omega/\Xi(\text{QGP}) \approx \Xi/\Lambda(\text{QGP}), \quad (2.1)$$

$$\Omega/\Xi(\text{HG}) < \Xi/\Lambda(\text{HG}), \quad (2.2)$$

$$\Omega/\Xi(\text{QGP}) > \Omega/\Xi(\text{HG}), \quad (2.3)$$

$$\Xi/\Lambda(\text{QGP}) > \Xi/\Lambda(\text{HG}). \quad (2.4)$$

Note that the second relation comes from the ratios of the production energy thresholds for Λ , Ξ and Ω in the HG system. Therefore, the signature of the QGP proposed by Rafelski and Müller, known as *strangeness enhancement*, lie on the overabundance of strangeness production in a QGP scenario (A–A collisions) with respect to a HG scenario (a priori, pp collisions).

From the experimental point of view, one should understand how to compare the production yields in the HG and in the QGP. The point is to define the correct normalization to highlight the previously cited hierarchies. Usually the yields are normalized to the average number of participant nucleons $\langle N_{\text{part}} \rangle$. This number is equal to two in the case of pp collisions and depends on the centrality³ in the A–A collisions. Therefore, the experimental observable, usually associated to strangeness enhancement in A–A to pp collisions, for a given hadron species h , is defined as:

$$E(h) = \frac{dN/dy(h)^{\text{AA}}}{N_{\text{evt}}^{\text{AA}} \langle N_{\text{part}} \rangle^{\text{AA}}} \frac{\langle N_{\text{part}} \rangle^{\text{pp}} N_{\text{evt}}^{\text{pp}}}{dN/dy(h)^{\text{pp}}}, \quad (2.5)$$

where dN/dy represents the production yield per rapidity unit and N_{evt} the number of events for each colliding system.

This observable has been studied at different energies and using different colliding ions, both at SPS (WA97/NA57 [36, 37]) and RHIC (STAR [38]), showing the predicted characteristics: for a given collision energy the enhancement grows with the centrality of the collision and with the strange content of the baryons. The measurements of the strangeness enhancement performed at SPS and RHIC energies for the multi-strange baryons and the Λ and the corresponding antiparticles are reported in Figure 15. A significant behaviour is that, for increasing colliding energy and for the most central event class, the $\bar{\Lambda}$, Ξ^- and $\Omega^- + \bar{\Omega}^+$ enhancements weaken, moving from the lower to the higher energy. This trend has been explained, within the thermodynamical description of the system, with the progressive removal of *canonical suppression* from the proton-proton system (see Section 2.3.3).

³ The meaning of participant nucleon and centrality in a heavy-ion collision has been clarified in Section 1.3.

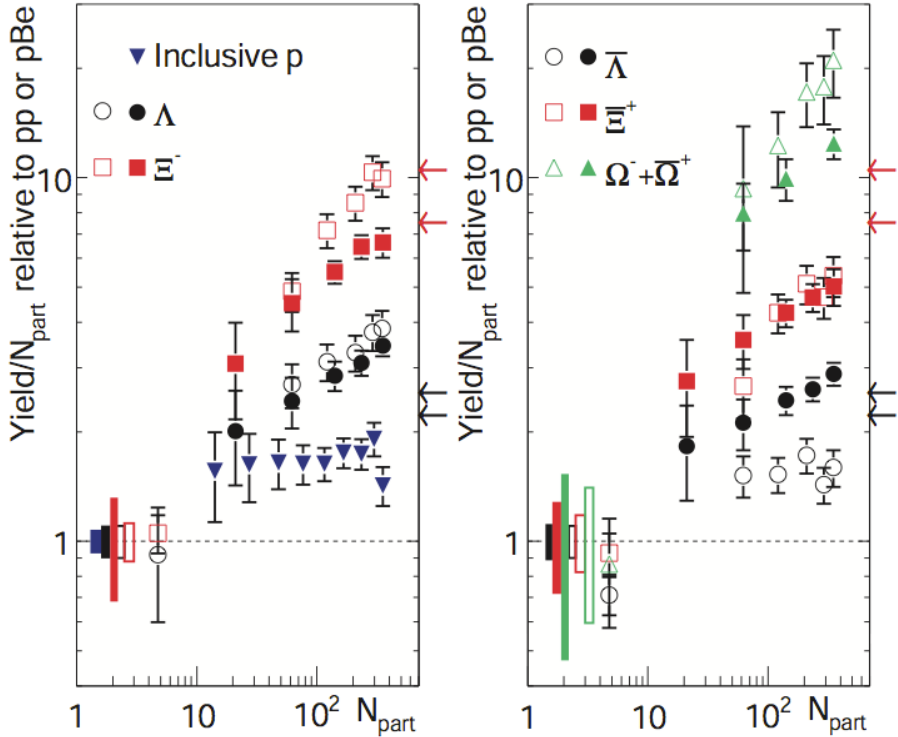


Figure 15: Mid-rapidity $E(h)$ as a function of $\langle N_{\text{part}} \rangle$ for Λ , $\bar{\Lambda}$ ($|y| < 1.0$), Ξ^- , Ξ^+ , $\Omega^- + \bar{\Omega}^+$ ($|y| < 0.75$) and inclusive p ($|y| < 0.5$) measured by STAR Collaboration in Au–Au collisions at $\sqrt{s_{\text{NN}}} = 200$ GeV (solid markers). Measurements by the WA97 and NA57 Collaborations in Pb–Pb at $\sqrt{s_{\text{NN}}} = 17.3$ GeV (open symbols) for Λ , Ξ and Ω ($|y| < 0.5$) are also reported. Boxes at unity show statistical and systematical uncertainties combined in the pp (p–Be) data. Error bars on the data points represent those from the heavy-ion measurements. The arrows on the right axes mark the predictions from a thermal model based on Grand-Canonical formalism (details will be give in the Section 2.3.3) when varying T from 165 MeV to 170 MeV. The red arrows indicate the predictions for Ξ and the black arrows those for Λ . [38]

2.3 THEORETICAL MODELS

At present, there is not a unique theoretical description of the underlying⁴ hadron-hadron and subsequent parton-parton interactions, with their vastly different characteristics at different incident energies and in different kinematic intervals. As we already observed, perturbative quantum chromodynamics (pQCD) can be applied to describe hard processes, i.e. processes with large four-momentum transfer, Q^2 . But pQCD is formally inappropriate for the description of the soft interactions because of the absence of the large Q^2 -scale. Therefore, low p_T particle production is best described in terms of phenomenological models.

A large variety of models for hadronic and nuclear collisions have been developed. They may be subdivided into macroscopic (statistical and hydrodynamical) models and microscopic (string, transport, cascade, etc) models.

In the following a general introduction on these models will be given, and special attention will be placed on the models that will be used in Chapter 7, when the experimental results on multi-strange baryons will be shown and compared with theoretical predictions.

2.3.1 Hydrodynamic models

As anticipated in Section 1.3, after the pre-equilibrium phase, when thermodynamical equilibrium is quickly reached, the system expands and cools down (Figure 10). To describe the behaviour of the system a hydrodynamical approach can be used. This kind of description was proposed in 1953 by Landau [39]. This original suggestion was verified with the measurement on heavy-ion collisions at ultra-relativistic energies performed at the RHIC. Sizeable values of elliptic flow at larger energies (in particular STAR, PHOBOS and PHENIX results) indicate that produced matter in Au–Au collisions at RHIC does not behave as a weakly interacting gas (for which v_2 ⁵ would be negligible), but instead as a strongly coupled liquid [40]. The new data from the LHC confirm this picture and agree, at least qualitatively, with hydrodynamic predictions of elliptic flow for Pb–Pb collisions at the LHC energy [41].

Initial conditions provide the input for the hydrodynamic evolution of the system and the equation of state $P(\epsilon, n_B)$ (EoS, with energy density ϵ , pressure P

⁴ The underlying event in a hadron-hadron or heavy-ion collision is defined as the collection of processes except the hard parton-parton process of interest. It receives contributions from beam-remnants plus initial and final state gluon radiations.

⁵ The elliptic flow describes the azimuthal momentum space anisotropy of particle emission from non-central heavy-ion collisions in the plane transverse to the beam direction, and is defined as the second harmonic coefficient of the azimuthal Fourier decomposition of the momentum distribution, v_2 .

and baryon density n_B) is the missing piece in order to complete the system with the conservation equations of the relativistic hydrodynamic (such as quantum numbers, energy and momentum conservations). The success of hydrodynamical approach in the *ideal* limit ($\eta/s = 0$) in the explanation of the experimental data and the theoretical lower limit for the shear viscosity over entropy ratio ($\eta/s > 1/4\pi$) [42, 43, 44], leads to the interpretation of the state created during a relativistic heavy-ion collision as a nearly “perfect” fluid. However the agreement in the description of the data is not perfect (especially at high p_T), therefore the usage of dissipative hydrodynamics is stimulated. Also, in such condition the strict assumption of local thermal equilibrium (needed in the ideal limit) is relaxed to the assumption of near local thermal equilibrium, extending the range of validity of hydrodynamic description.

An example of a pure viscous hydrodynamic model is VISH₂₊₁ [45]. The Kraków model [46], on the other hand, introduces non-equilibrium corrections due to viscosity in the transition from a hydrodynamic description to one involving the final state particles. In both models the description of the transition from hydrodynamic fluid to free particles which reach the detector is done using the Cooper-Frye freeze-out picture [47]. In this picture it is assumed that the momentum distribution of the final state particles is essentially the momentum distribution within the fluid, towards the end of the hydrodynamical expansion, and parts of the fluid are instantaneously converted into free particles.

2.3.2 Microscopic models

Another way to describe the transition from the hydrodynamic to the free particle phase or from the pre-equilibrium to the QGP phase is using a microscopic description of the dynamics of the constituents of the system based on transport theory. Such models are known as *cascade models*. Here the trajectories and interactions of all particles (baryons and mesons in the case of hadronic transport models or quarks and gluons in the case of a parton cascade models) are followed individually and, as a transport model, the ultimate goal is to find solutions to the equations of motion. The main needed ingredients in this description are the interaction cross sections and the decay widths of the unstable particles. The important point is that the particles travel in a hot, dense and even not equilibrated medium, that might change significantly the previous quantities with the respect to the ones known in the vacuum. This is a very difficult target to obtain, and drastic model approximations are needed.

Examples of hadronic transport models used in heavy-ion physics for studying particle production are: Ultra-relativistic Quantum Molecular Dynamics

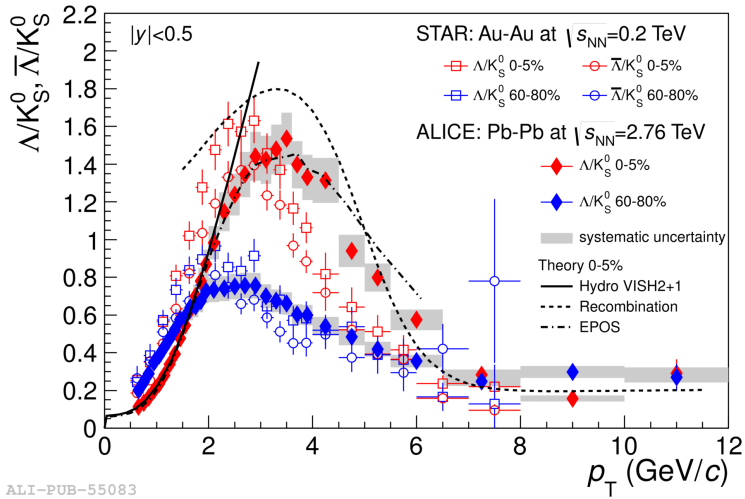


Figure 16: Λ/K_S^0 ratios as a function of p_T measured by the ALICE Collaboration in Pb-Pb collisions at $\sqrt{s_{NN}} = 2.76$ TeV, compared with Λ/K_S^0 and $\bar{\Lambda}/K_S^0$ ratios measured in Au–Au collisions at $\sqrt{s_{NN}} = 200$ GeV by STAR Collaboration. The dot-dashed line show the corresponding ratios from EPOS model. [57]

(UrQMD) [48, 49], Relativistic Quantum Molecular Dynamics (RQMD) [50], Hadron String Dynamics (HSD) [51].

HKM [52, 53] is an example of ideal hydrodynamic model, similar to VISH₂₊₁, which, in addition, introduces a hadronic cascade (UrQMD) following the partonic hydrodynamic phase. On the other hand, the EPOS model (Energy conserving quantum mechanical multiple scattering approach, based on Partons, Off-shell remnants, and Splitting of parton ladders) [54, 55, 56], follows a phenomenological approach that is based on an initial parton model. It aims to be a comprehensive model and event generator, describing all p_T domains with the same dynamical picture; in particular it incorporates hydrodynamics and models the interaction between high p_T hadrons and the expanding fluid. As can be seen in Figure 16, this model is able to describe the baryon-to-meson enhancement observed by the STAR and ALICE Collaborations in the intermediate p_T region ($2 < p_T < 6$ GeV/c).

2.3.3 Statistical models

The goal of statistical hadronic models (SHM) is to describe the system after the hadronization using a statistical formalism. The idea is to use a minimum number of thermodynamic variables to determine the ensemble of observables

that best describe the chemical composition in the hadronic phase. The basic ingredient of these models is the partition function. The particle production from the large volume system created in the A–A collisions can be described adopting a Grand-Canonical (GC) formalism. In this case, the mean hadron multiplicities $\langle N_i \rangle$ are defined as [58]:

$$\langle N_i \rangle = (2J_i + 1) \frac{V}{(2\pi)^3} \int d^3 p \frac{1}{\gamma_S^{-S_i} \exp[(E_i - \mu_i)/T_{ch}] \pm 1}, \quad (2.6)$$

where the involved parameters are the chemical freeze-out temperature T_{ch} , the chemical potentials $\mu_i = \mu_B B_i + \mu_S S_i + \mu_{I_3} I_{3i}$, the volume V , the strange quarks fugacity γ_S , the spin J_i and the number of strange quarks S_i of a given particle type i . The chemical potentials μ_S and μ_{I_3} are determined by the constraint of global strangeness and charge conservation, while the baryonic potential μ_B is a free parameter. To account for different statistical behaviour, the + sign in the denominator is valid for fermions, while the – sign is used for bosons.

Several implementations of this model are frequently applied in this context. Some models add an additional factor γ_q to account for a possible non-equilibrium of the non-strange particles. Depending on the assumption on the equilibration of the system, three main options can be distinguished [59]:

CHEMICAL EQUILIBRIUM ($\gamma_S = \gamma_q = 1$) A full equilibrium is assumed both for non-strange and strange particles. In some implementations, as it is done in [60], the particle ratios are fitted, the volume parameter drops out and only T_{ch} and μ_B remain as free parameters. These models are in good agreement with measurements done at SPS and RHIC, as shown in Figure 17. In Figure 18 similar fits have been performed with preliminary data by ALICE in Pb–Pb collisions at $\sqrt{s_{NN}} = 2.76$ TeV. Since the antibaryon over baryon ratios [61] suggest a vanishing baryon-chemical potential at the LHC μ_B is fixed to 1 MeV in the fits of Figure 18. Here, some tensions between model predictions and measured particle yields are present and a lower temperature ($T = 156$ MeV) of the system is estimated with respect to the one obtained from the data measured by STAR ($T = 164$ MeV). In particular the proton and antiproton yields are under the model (by a deviation of 2.7 and 2.9σ , respectively, with small experimental errors) and, on the other hand, the cascade yields are above the model (by about 2σ). In the same Figure are also reported results for a statistical model calculation using $T = 164$ MeV and $\mu_b = 1$ MeV, where the disagreement for the antiprotons is increased to about 50%. Note that leaving protons out of the fit, the temperature would increase by 2 MeV to $T = 158$ MeV with an otherwise perfect fit with a reduced χ^2 less than one. Consequently one could talk

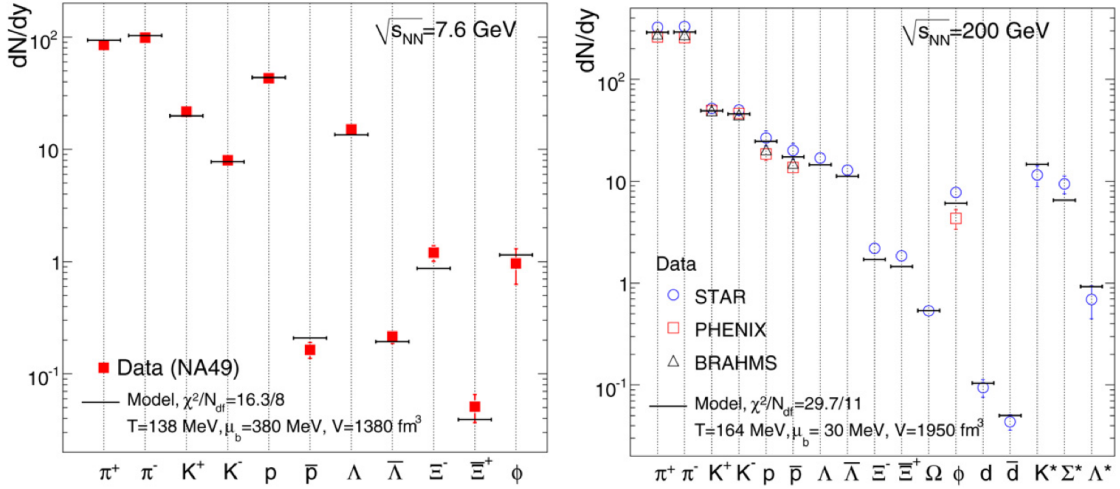


Figure 17: Experimental hadron yields and model calculations for the parameters of the best fit at the centre-of-mass energies of 7.6 GeV by the NA49 Collaboration (left panel) and 200 GeV by the STAR Collaboration (right panel). [62]

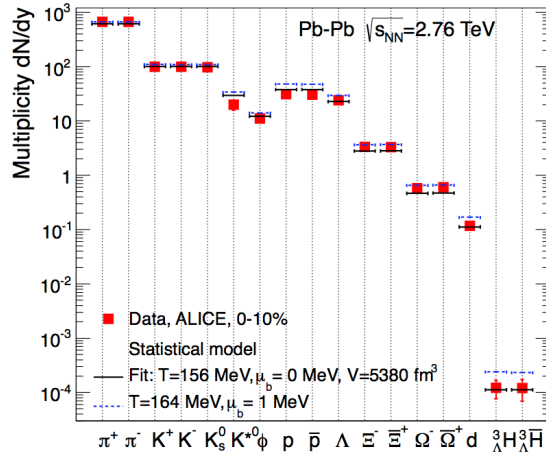


Figure 18: Integrated yields at mid-rapidity dN/dy in central (0 – 10%) Pb–Pb collisions at $\sqrt{s_{NN}} = 2.76 \text{ TeV}$ with results from a thermal fit. [63]

about a proton anomaly, that can also be expressed saying that the proton-to-pion ratio is overpredicted by about 50% [64, 65].

CHEMICAL SEMI-EQUILIBRIUM ($\gamma_q = 1$, $\gamma_s \neq 1$) The strange quark fugacity is used to allow the possibility that strangeness might not be fully equilibrated ($\gamma_s < 1$). Some implementations, as it is done in [66], directly calculate the multiplicities according to Equation 2.6.

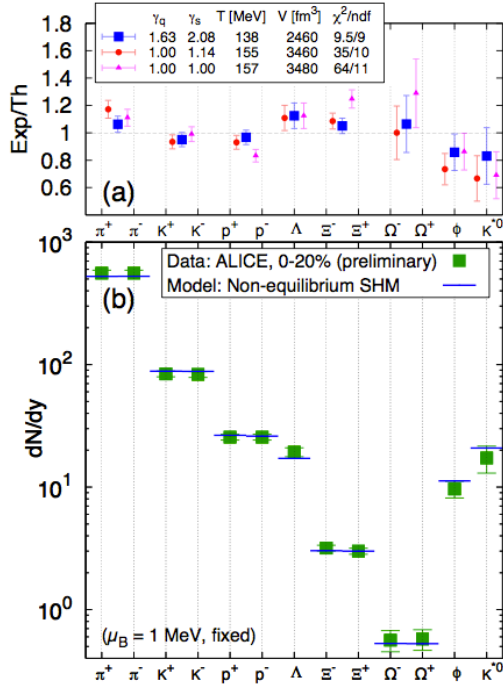


Figure 19: The lower panel shows the non-equilibrium SHM fit to experimental data measured by the ALICE experiment in Pb–Pb collisions at $\sqrt{s_{\text{NN}}} = 2.76$ TeV for 0 – 20% centrality. The upper panel shows the ratio of model values to experimental data for the three SHM variants and presents the key parameter values for: chemical non-equilibrium (solid squares), chemical semi-equilibrium (solid circles) and chemical equilibrium (solid triangles). [70]

CHEMICAL NON-EQUILIBRIUM ($\gamma_q \neq 1, \gamma_s \neq 1$) Further implementations allow the non-strange quarks to be out of equilibrium as well and therefore introduce an additional factor γ_q [67, 68]. An example is the SHARE code [69], which assumes a QGP in thermal equilibrium and an instantaneous hadronization process. Predictions from this model, shown in Figure 19, are in good agreement with the measurements at LHC energy, though more free parameters are needed in this case.

As already observed, in a large system with a large number of produced particles, the conservation law of a quantum number (e.g. strangeness) can be implemented on the average by using the corresponding chemical potential, within the GC formulation. In a small system, such as a pp collision, with small particle multiplicity, conservation laws must be implemented locally on an event-by-event basis, requiring a Canonical formulation (C). The C conservation of quantum numbers is known to severely reduce the phase space available for

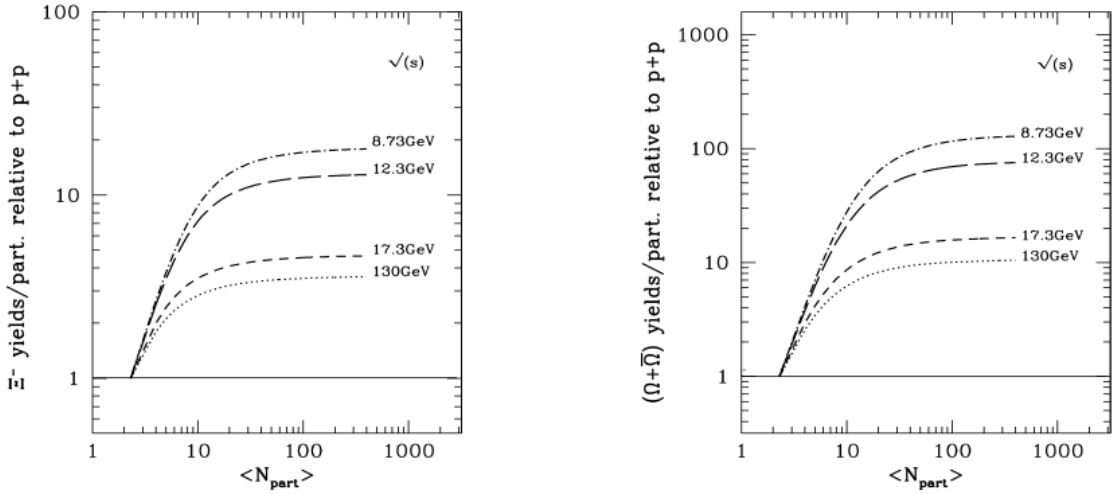


Figure 20: Centrality dependence of the relative enhancement normalized to $\langle N_{\text{part}} \rangle$, for Ξ^- (left) and $\Omega^- + \bar{\Omega}^+$ (right), at different collision energies, obtained in the statistical approach with canonical formalism. [72]

particle production. This is the canonical suppression (CS) mechanism [71, 72]. This means that, in Equation 2.5, if the denominator is reduced by CS then $E(h)$ is increased. In Figure 20 the predictions for the enhancement as a function of the centrality are shown for different colliding energies. These predictions show the same energy dependence seen for the data in Figure 15, thus indicating a decrease in the canonical suppression for increasing colliding energy.

The argument of the canonical suppression does not fully explain all the aspects of the problem. As can be seen in Figure 20, this model, at given energy, does not reproduce the centrality dependence of the strangeness enhancement experimentally observed (Figure 15). In particular, the model predicts a saturation of the enhancement for the most central collisions.

A possible solution to the $\langle N_{\text{part}} \rangle$ dependence of the enhancement was proposed within the *core-corona model* [73]; here, the system is thought to be composed of two parts: a core, composed by an hadron gas in chemical equilibrium and a corona where the production of strange particles happens via nucleon-nucleon collisions. The centrality dependence of the strangeness enhancement is accounted increasing the weight of the core with respect to corona going to most central collisions. Measurements of the strangeness enhancements by STAR at $\sqrt{s_{\text{NN}}} = 200$ GeV, with Au–Au and Cu–Cu [74], have been found in agreement with the prediction by this model.

Whether the strangeness enhancement in larger systems is due only to phase space suppression in the smaller systems (such as pp to p–A), or is indeed due

to an increased strangeness production from a deconfined partonic medium is still an ongoing discussion, and the results reported on this thesis (Chapter 7) may contribute to clarify this important point.

2.3.4 Event Generators

General-purpose Monte Carlo (GPMC) event generators provide fully exclusive modeling high energy collisions. They are built from several components, that describe the physics starting from very short distance scales, up to the typical scale of hadron formation and decay. An event generator can be used in many different ways. The main applications are the following [75]:

1. to give physicists a feeling for the kind of events one may expect/hope to find, and at what rates;
2. as a help in the planning of a new detector, so that detector performance is optimized, within other constraints, for the study of interesting physics scenarios;
3. as a tool for devising the analysis strategies that should be used on real data, so that signal-to-background conditions are optimized;
4. as a method for estimating detector acceptance corrections that have to be applied to raw data, in order to extract the true physics signal;
5. as a convenient framework within which the observed phenomena can be interpreted in terms of a more fundamental underlying theory (usually the Standard Model).

In this Section the physical hypothesis and the characteristics of the two event generator used in the analysis described in this thesis are briefly sketched.

PYTHIA [75] has been used extensively for e^+e^- , ep and pp/ $\bar{p}p$ physics, e.g. at LEP, HERA and the Tevatron, and during the last 20 years has probably been the most used generator for LHC physics studies. Its aim is to describe as accurate as possible the properties of the event, including in the model a lot of interactions, within and beyond the Standard Model. Due to the lack of an exact description of the phenomenon, the program is based on a combination of analytical results and QCD-based models. The current version of Pythia contains almost 300 different hard processes that, according to the number of final-state objects, can be divided in: $2 \rightarrow 1$, $2 \rightarrow 2$ and $2 \rightarrow 3$. Another classification is given according to the physics

scenario: hard and soft QCD, heavy-flavour production, prompt photon production, photon-induced processes, Deep Inelastic Scattering, W/Z production, Standard Model Higgs production and more. Other included effects are: the initial- and final-state corrections via parton showers, beam remnants and multiple interactions, hadronization via string fragmentation (Lund model) and decay of particles.

HJING (Heavy Ion Jet INteraction Generator) [76] was developed by M. Gyulassy and X.-N. Wang with special emphasis on the role of *minijets*⁶ in pp, p-A and A-A reactions at collider energies. In high energy heavy-ion collisions, minijets have been estimated [77, 78] to produce 50% (80%) of the transverse energy in central heavy ion collisions at RHIC (LHC) energies. HJING combines a QCD inspired model for jet production with the Lund model for jet fragmentation. The formulation of HJING was guided by the Lund FRITIOF and Dual Parton model for soft A-B reactions at intermediate energies ($\sqrt{s} \lesssim 20$ GeV/nucleon) and the successful implementation of pQCD processes in PYTHIA model for hadronic collisions. Also nuclear matter effects have been introduced and include nuclear shadowing of parton structure functions and a schematic model of final state interaction of high p_T jets in terms of an effective energy loss parameter (dE/dx).

2.4 PRODUCTION MECHANISMS

One of the known particle production mechanisms in elementary collisions is hard scattering, via parton fragmentation into hadrons. In this picture the single parton spectrum is convoluted with the probability for a parton to hadronize into a hadron, which carries a fraction of the momentum of the parent parton. The cross sections of these interactions are calculable using pQCD methods.

Experimental evidence such as the baryon-to-meson enhancement (Figure 16 for Λ/K_S^0 , also visible for non-strange particles) lack a consistent explanation in this standard picture of hadron production at high transverse momentum. Whereas the observed suppression of the meson yield is attributed to the energy loss of partons during their propagation through the hot and dense matter created in the nuclear collision, the absence of a similar effect in the proton spectrum is puzzling.

⁶ Jets with small transverse energy, $E_T < 5$ GeV, are usually referred to as minijet. In this case, it is increasingly difficult to resolve minijets from the underlying background, but an effort to model this contribution is still needed as theoretically we expect contributions from hard scatterings also for lower transverse momentum.

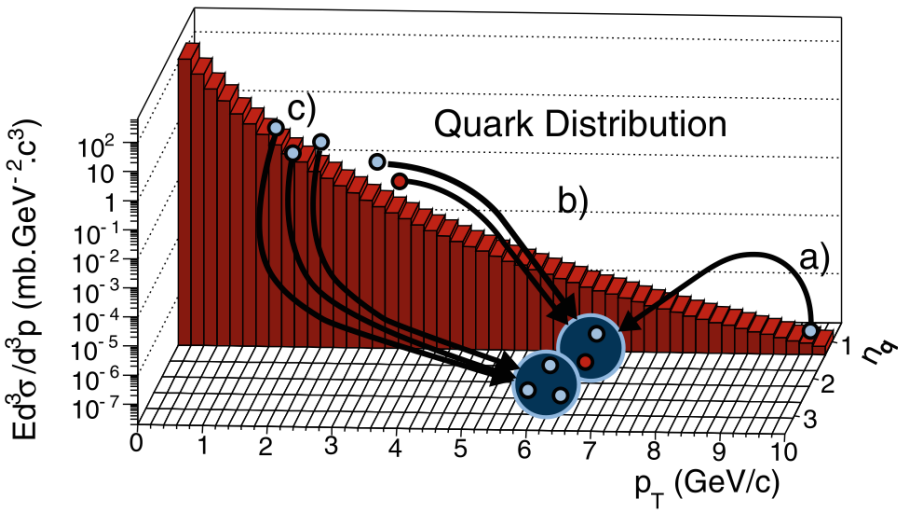


Figure 21: Illustration of the possible competition between fragmentation and coalescence at mid p_T . The depicted processes corresponds to: a) high p_T quark fragmentation into a meson, b) and c) creation respectively of a meson and baryon by recombination. [8o]

A possible proposed solution to this “baryon-meson puzzle” is that in high parton density environment hadron production at momenta of a few GeV/c may occur by recombination of partons, rather than fragmentation [79].

The underlying assumption in the recombination model is that the particles that populate the intermediate p_T region are composed of a mixture of partons coming from different transverse momentum regions. As is depicted in Figure 21, on one hand, a high p_T parton fragments to form lower p_T hadrons. On the other hand, partons produced softly coalesce into a hadron with a p_T that is sum of the p_T of the constituent partons. This can happen both for mesons and baryons, but for the latter, for a fixed p_T of the produced particle, lower p_T partons are needed. However, the thermal description of the system at low p_T tells us that from the exponential distribution it is (exponentially) easier to have partons with lower p_T and thus to produce a baryon instead of a meson for a given p_T via coalescence. This mechanism is not present in the absence of a QGP, in which case fragmentation will disfavor baryons over mesons, thus suggesting an increased baryon over meson ratio in the QGP scenario if compared to HG system. Then the puzzle can be qualitatively explained by simple consideration on the shape of the parton spectrum.

As can be seen in Figure 22 the two processes switch roles the dominant production mechanism in the region of intermediate transverse momentum.

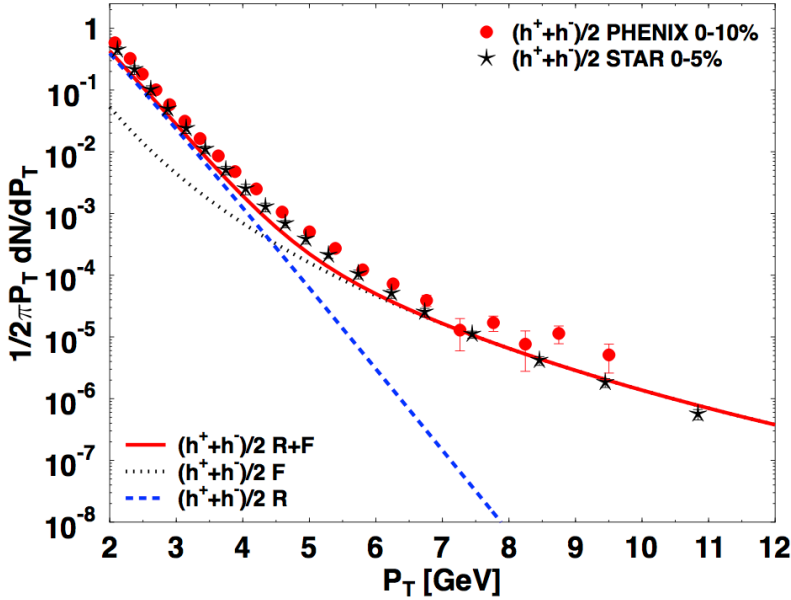


Figure 22: Transverse momentum spectrum of charged hadrons $(h^- + h^+)/2$ at mid-rapidity for central Au–Au collisions produced at RHIC, measured by PHENIX (in red, 0 – 10% central events) and by STAR (in black, 0 – 5% central events). Prediction from fragmentation model (dotted black line) and recombination model (dashed blue line) and the sum of both (solid red line) are showed. [81]

2.4.1 Nuclear modification factors

A way to learn about particle production mechanisms in nuclear matter is to compare particle spectra measured in A–A collisions to those obtained from the data where a QGP is not expected, such as pp collisions. In particular one would like to understand the role of the hot and dense medium in the particle production. In this context, one expects that, particularly for high p_T partons, there will be some energy loss via gluon radiation while traversing the medium [82].

This is usually performed measuring the *nuclear modification factors*, R_{AA} , defined as follows:

$$R_{AA} = \frac{1}{T_{AA}} \frac{(d^2N^{AA}/dp_T dy)}{(d^2\sigma^{NN}/dp_T dy)}. \quad (2.7)$$

This is the ratio between the yield in A–A collisions ($d^2N^{AA}/dp_T dy$) and the cross-section of particle production in pp collisions ($d^2\sigma^{NN}/dp_T dy$), normalized

by the geometric nuclear overlap function T_{AA} ⁷ estimated for the corresponding centrality class of the A–A collisions. At high p_T particle production is expected to be dominated by hard processes; this means that a A–A collision should scale with the number of binary nucleon-nucleon collisions N_{coll} (binary collision scaling). In case of absence of effects of the created medium, the R_{AA} at high p_T ($p_T \geq 2 - 3 \text{ GeV}/c$ for hadrons) should be unity.

As can be seen in Figure 23, the measurements in A–A collisions at RHIC, recently confirmed by the ALICE Collaboration, have shown that the production of high p_T charged hadrons is suppressed compared to the expectation from an independent superposition of nucleon-nucleon collisions. The left plot of Figure 23 shows that the suppression becomes higher for more energetic collisions [83].

Moreover, one can measure similar observables also in p–A collisions, thought to be a reference for the study of the initial and final-state effects⁸. In this right plot of Figure 23 the R_{AA} in Pb–Pb collisions at $\sqrt{s_{\text{NN}}} = 2.76 \text{ TeV}$ in the most central and most peripheral classes have been compared with the recent measurement in p–Pb collisions at $\sqrt{s_{\text{NN}}} = 5.02 \text{ TeV}$ by the ALICE Collaboration. This measurement indicates that the strong suppression of hadron production at high p_T observed in Pb–Pb collisions at the LHC is not due to an initial-state effects, present in both p–A and A–A collisions [84].

More hints could come studying the R_{AA} for the different species. This has been performed by the ALICE Collaboration (Figure 24) for the hadrons $\pi^- + \pi^+$, $K^- + K^+$, $p + \bar{p}$ and ϕ in the most central class collisions at $\sqrt{s_{\text{NN}}} = 2.76 \text{ TeV}$. Results for the R_{AA} of multi-strange baryons will be shown in Section 7.3. A first clear observation is the different behaviour for mesons and protons at low and intermediate p_T ($p_T < 6 \text{ GeV}/c$). This can be interpreted as new evidence of the baryon-to-meson anomaly. On the other hand, at high p_T ($p_T > 6 \text{ GeV}/c$), there is practically no difference in the amount of suppression for the different species. Such common behaviour suggests that any flavour dependent effects on the in-medium parton energy loss for the light flavours must be small.

⁷ The nuclear overlap function T_{AB} , is a function of the impact parameter b and is normalized so that $\int T_{AB}(b) d^2b = AB$, where A and B are the mass numbers of the two colliding nuclei. In the Glauber model the mean value $\langle T_{AB} \rangle$ for a certain centrality class (set of events with impact parameters in a defined range of values) is calculated as $\langle T_{AB} \rangle = \langle N_{\text{coll}} \rangle / \sigma_{\text{inel}}^{\text{NN}}$, where N_{coll} is the number of binary nucleon-nucleon collisions and $\sigma_{\text{inel}}^{\text{NN}}$ is the inelastic nucleon-nucleon cross section.

⁸ The effects that can determine the breakdown of the binary scaling are usually divided in two classes: “initial state effects” (such as the nuclear shadowing [85] and the Cronin effect [86]) and “final-state effects” (due to the interaction of the produced partons with the medium formed in the collision). The former can be studied by comparing pp and p–A collisions, where the formation of a high-density medium is not expected. The latter is investigated in A–A collisions.

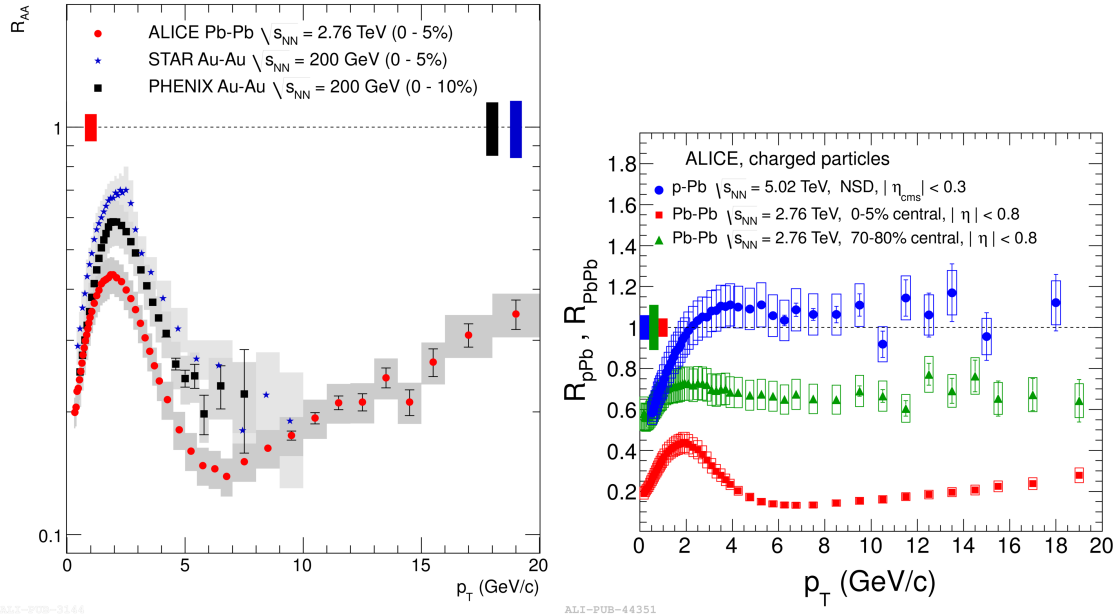


Figure 23: (Left) Comparison of R_{AA} for unidentified particles in central Pb–Pb collisions at LHC to measurements at $\sqrt{s_{NN}} = 200$ GeV by the PHENIX and STAR experiments at RHIC. For both ALICE and PHENIX, the statistical and systematic errors are separated and represented by the lines and the boxes, respectively. For STAR the two errors are combined and represented by boxes. The vertical bars around R_{AA} equal to unity indicate the p_T independent scaling errors on R_{AA} . [83] (Right) The nuclear modification factor of charged particles as a function of p_T in minimum bias (NSD) p–Pb collisions at $\sqrt{s_{NN}} = 5.02$ TeV, compared to measurements in collisions at $\sqrt{s_{NN}} = 2.76$ TeV by the ALICE Collaboration. The errors are represented as in left plot for ALICE measurements. [84]

Measurements of the nuclear modification factors for $p + \bar{p}$, Λ and $\Xi^- + \Xi^+$ performed by STAR in most central (a) and most peripheral (b) Au–Au collisions at $\sqrt{s_{NN}} = 200$ GeV are reported in the left plots of Figure 25. What is clear here is that in the most central collision $R_{AA}(\Lambda) \approx R_{AA}(\Xi) \neq R_{AA}(p)$, at least above $p_T \sim 1.5$ GeV/c [38]. In addition, in the most central collisions for $p_T > 1.5$ GeV/c and in the full measured p_T range for the most peripheral collisions the R_{AA} for Λ and Ξ is greater than one, possibly due to the phase space effects in the reference pp collisions. The limited p_T range does not allow the study of the behaviour of these particles at higher p_T .

Especially for the lower energies experiments where the production rate for the multi-strange baryons is lower and very large statistics are needed, an alter-

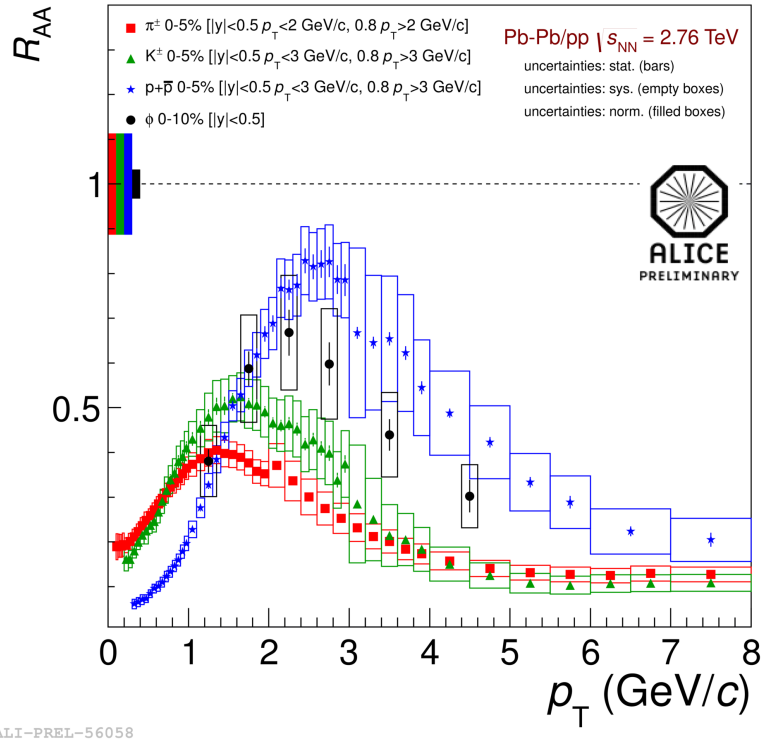


Figure 24: Nuclear modification factors as a function of the transverse momentum for π^\pm , K^\pm , p and ϕ in the most central class collisions preliminary measured by the ALICE Collaboration. [87]

native way to study the nuclear effect on the production of particles is provided by the R_{CP} observable. This is defined as:

$$R_{CP} = \frac{N_{coll}^{\text{peripheral}}}{N_{coll}^{\text{central}}} \frac{(d^2N^{\text{cent}}/dp_T dy)}{(d^2N^{\text{per}}/dp_T dy)}, \quad (2.8)$$

where $N_{coll}^{\text{peripheral}}$ and $N_{coll}^{\text{central}}$ are the numbers of binary nucleon-nucleon collision in peripheral and central A–A collisions.

The assumption is that the information provided by either ratios should be consistent, based on the idea that peripheral Pb–Pb and pp data are similar, in the sense that in none of these systems a dense medium is created which could cause many hadronic or partonic re-scatterings in the final state. This observable measured for the p , Λ and Ξ by the STAR Collaboration is reported in Figure 25 (right plots). It appears that $R_{CP}(\Lambda) \approx R_{CP}(\Xi) \approx R_{CP}(p)$ and this observed behaviour may be explained by the fact that the phase space effects limiting the strangeness production in pp collisions should disappear in the larger system

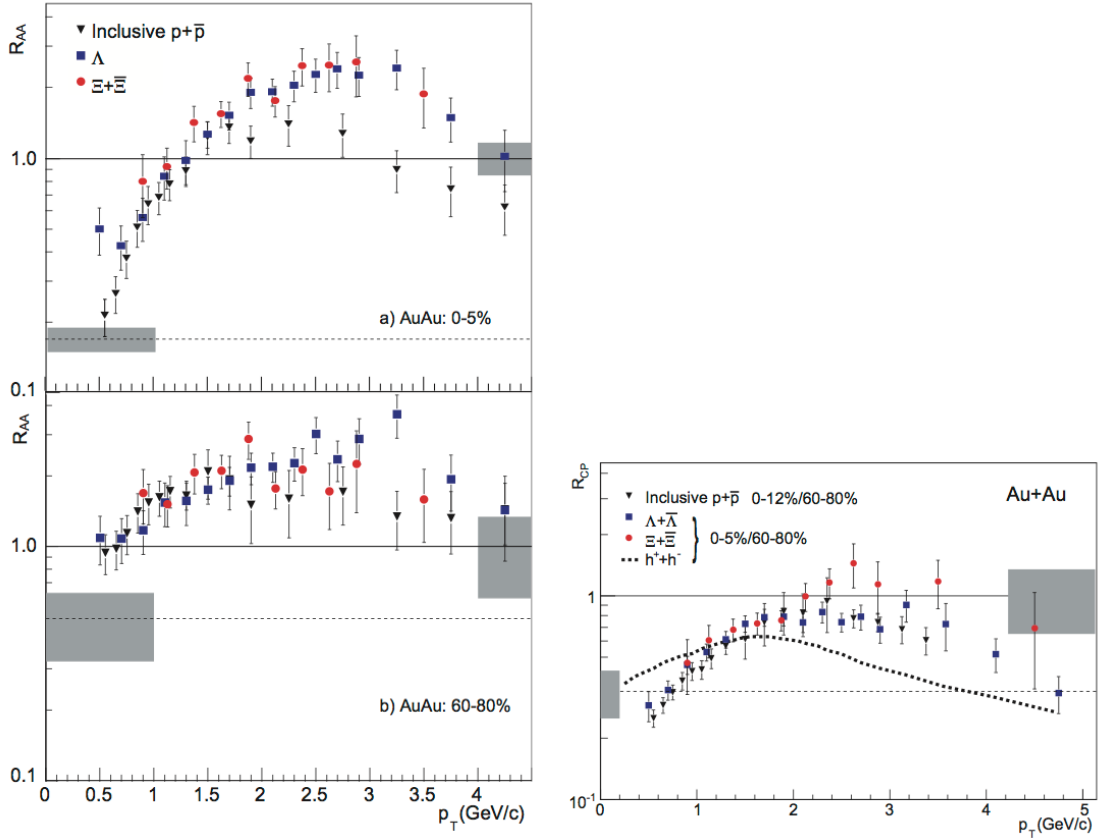


Figure 25: (Left) R_{AA} as a function of transverse momentum for p , Λ and Ξ , in the most central (a) and most peripheral (b) classes. (Right) R_{CP} as a function of p_T for p , Λ and Ξ and unidentified charged particles h (dotted line). Measured by the STAR Collaboration in Au–Au collisions at $\sqrt{s_{NN}} = 200$ GeV. [38]

created in peripheral Au–Au collisions. Note that, as measured by the STAR Collaboration in collisions at $\sqrt{s_{NN}} = 200$ GeV, the charged-particle pseudo-rapidity density ($dN_{ch}/d\eta$) in $|\eta| < 0.5$ is: 691 ± 49 in the $0 - 5\%$ most central Au–Au collisions, 33.5 ± 2.5 in the $60 - 80\%$ most peripheral Au–Au collisions and 2.98 ± 0.34 in minimum bias pp collisions [88].

3

THE ALICE EXPERIMENT

3.1 THE LHC PROJECT

The Large Hadron Collider (LHC) [89] at CERN is, today, the biggest particle accelerator world-wide. The first discussions that led to the project started in 1984. The LHC project was approved in 1994 and construction works in the existing underground tunnel started in 2001 after the dismantling of the LEP collider¹, which had previously been built in the tunnel which is located under the Swiss-French border area close to Geneva at a depth of 50 to 175 m. The LHC has a circumference of 27 km. By design, its maximum achievable energies are 7 TeV for beam of protons and 2.76 TeV per nucleon for beam of lead ions, thus providing collisions at $\sqrt{s} = 14$ TeV and $\sqrt{s_{NN}} = 5.5$ TeV, respectively. These would be the largest energies ever achieved in particle collision experiments.

The LHC is a synchrotron that accelerates two counter-rotating beams in separate parallel beam pipes. In each of them bunches of particles travel many times around the accelerator ring before the collision energy is reached. The accelerator has to bend the beams around the ring, keep the bunches focused and accelerate them to their collision energy. Finally, the spatial dimension of the bunches has to be minimized in order to attain high luminosity, which ensure a high number of collisions per time interval at the collision points, i.e. a high luminosity². A combination of magnetic and electric field components performs

¹ The Large Electron-Positron (LEP) Collider operated in the years 1989 to 2000 with a maximum centre-of-mass energy of 209 GeV.

² For a particle accelerator experiment, the luminosity is defined by: $\mathcal{L} = fnN^2/A$ with n number of bunches in both beams, N number of particles per bunch, cross-sectional area A of the beams that overlap completely, and revolution frequency f . The frequency of interactions (or in general of a given process) can be calculated from the corresponding cross-section σ and the luminosity: $dN/dt = \mathcal{L}\sigma$.

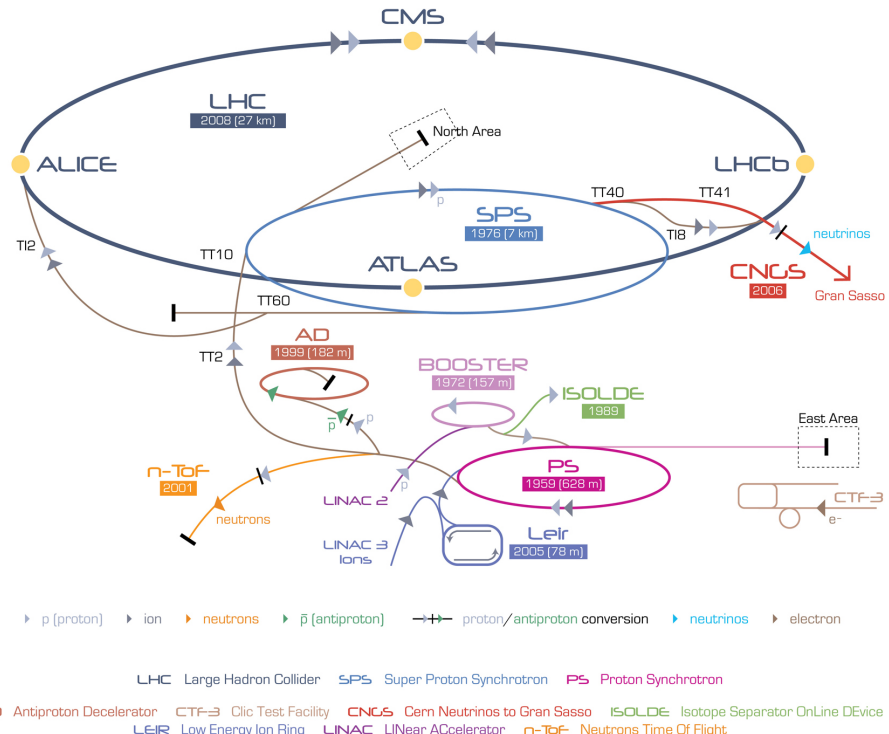


Figure 26: The CERN accelerator complex. [91]

the mentioned tasks. Despite the high luminosity reached, only a very small fraction of the particles of two bunches collides in a single bunch crossing. The others leave the interaction region essentially uninfluenced, are defocused, and continue to circulate in the accelerator.

Injection of bunches into the LHC (Figure 26) is preceded by acceleration in the LINAC₂, PS booster, PS, and SPS accelerators. The acceleration sequence is slightly different for heavy-ions, in which case bunches pass the LINAC₃, LEIR, PS, and SPS accelerators (more information can be found in [90]). Several injections to the LHC are needed until all bunches of both beams are filled.

The first pp collisions at 900 GeV centre-of-mass energy were delivered by the LHC on September 10th 2008. Nine days later, the operations were interrupted due to a failure in an electrical connection between two magnets. The machine operators spent over a year repairing and consolidating the accelerator. On November 20th 2009 low energy proton beams circulated again, and a few days later, by achieving the energy of 1.18 TeV per proton beam, LHC became the most powerful accelerator in the world. The first pp collisions at centre-of-mass energy of 7 TeV were delivered in March 2010, and the first Pb–Pb collisions at centre-of-mass energy of 2.76 TeV per nucleon pair in November

2010. In 2010 the integrated luminosity delivered by the LHC was $\sim 48 \text{ pb}^{-1}$ for pp collisions at $\sqrt{s} = 7 \text{ TeV}$ ($\sim 0.5 \text{ pb}^{-1}$ in ALICE³) and $\sim 10 \mu\text{b}^{-1}$ for Pb–Pb at $\sqrt{s_{\text{NN}}} = 2.76 \text{ TeV}$ ($\sim 10 \mu\text{b}^{-1}$ in ALICE). In 2011 the beam energy was the same as in 2010 both for pp and Pb–Pb. The performance of the LHC improved in terms of luminosity with $\sim 5.61 \text{ fb}^{-1}$ for pp ($\sim 2 \text{ pb}^{-1}$ in ALICE) and $\sim 166 \mu\text{b}^{-1}$ for Pb–Pb collisions ($\sim 143.62 \mu\text{b}^{-1}$ in ALICE). In 2012, the centre-of-mass energy for pp collisions was brought to 8 TeV and the integrated luminosity (up to December 2012, end of the pp programme) was $\sim 23.3 \text{ fb}^{-1}$ ($\sim 10 \text{ pb}^{-1}$ in ALICE). A pilot p–Pb run operated at $\sqrt{s_{\text{NN}}} = 5.02 \text{ TeV}$ on September 2012, followed by a long p–Pb run on February 2013 with a delivered luminosity of 31.2 nb^{-1} . A very short pp run at $\sqrt{s} = 2.76 \text{ TeV}$ ended the Run1 of the LHC programme, marking the start of the first long shutdown (LS1) until the end of 2014. Despite its excellent performance, the LHC has not yet achieved the nominal parameters (\sqrt{s}, \mathcal{L}), that is the main goal for the next ignition of the machine in 2015.

The LHC produces collisions in four so called Interaction Points (IPs) in correspondence of which are located six detectors of different dimensions and with different goals, all able to study the products of the interactions. These are:

ALICE (A Large Ion Collider Experiment - IP2) [93] is a dedicated heavy-ion experiment designed to study strongly-interacting matter at very high energy density. It explores the phase transition to the QGP, its phase diagram, and its properties. Furthermore, ALICE will also study collisions of protons, on one hand as a baseline for heavy-ion measurements and on the other hand it contributes to measurements of identified particles by making use of its excellent particle identification capability and its acceptance at very low transverse momenta.

ATLAS (A Toroidal LHC ApparatuS - IP1) and CMS (Compact Muon Solenoid - IP5) [94] [95] are general-purpose detectors for pp collisions that are built to cover the widest possible range of physics at the LHC. Specific topics are the search for the Higgs boson and physics beyond the Standard Model, e.g. new heavy particles postulated by supersymmetric extensions (SUSY) of the Standard Model and evidence of extra dimensions.

LHCb (The Large Hadron Collider beauty experiment - IP8) [96] is a dedicated experiment for the study of heavy flavour physics at the LHC. In particular, the experiment focuses on the study of CP violation and rare decays of

³ The pp runs have been taken by ALICE in parallel with the other experiments but at reduced luminosity. This is due to the dead time of the slowest detectors, in order to keep the pile-up (multi event in a single colliding bunch) at an acceptable level. In Pb–Pb collisions the limit to the luminosity is imposed by the machine characteristics [92]. Further informations are given in Section 3.2.1.

beauty and charm particles, to test the Standard Model and to search for evidence of New Physics. The LHCb physics programme is complementary to the flavour physics studies conducted at the B-factories and to the direct searches for new particles performed at ATLAS and CMS.

LHCf (Large Hadron Collider forward experiment - IP1) [97] measures forward particles created during LHC collisions to provide further understanding of high energy cosmic rays. The detector is placed close to the ATLAS experiment.

TOTEM (TOTAL Elastic and diffractive cross-section Measurement - IP5) [98] measures the total cross-section, elastic scattering, and diffractive processes. The detector is located close to the CMS experiment.

3.2 THE ALICE PROJECT

The ALICE experiment at the LHC [99] has as main goal the study of nuclear matter under extreme conditions of temperature and energy density such as those reached in ultra-relativistic heavy-ion collisions. The aim is to verify the QCD prediction of the existence of a phase transition from the common hadronic matter to the Quark-Gluon Plasma. Since ALICE is the only LHC experiment specifically designed for Pb–Pb collisions, it has to be able to cope with the large multiplicities associated with these collision systems and at the same time has to cover as many QGP-related observables as possible. ALICE is also interested in the study of pp interactions, as these are crucial for a comparison with Pb–Pb collisions, to tune Monte Carlo models and per se, like the other LHC experiments. With respect to these experiments, ALICE is endowed with an excellent Particle IDentification (PID) performance, obtained combining different PID techniques from different detectors that are optimized in different momentum (p) regions.

3.2.1 The ALICE detector

ALICE is a complex of 14 detector subsystems that can be classified in three groups:

BARREL DETECTORS are housed in a solenoid magnet, previously used in the L3 experiment at LEP, which provides the experiment with a 0.5 T magnetic field and covers the pseudo-rapidity interval $-0.9 < \eta < 0.9$ (corresponding to a polar acceptance $\pi/4 < \theta < 3\pi/4$). The azimuthal ϕ acceptance is 2π . They are mainly dedicated to vertex reconstruction, tracking, particle

identification and momentum measurement. Starting from the interaction region and going outward, we find the following detectors:

- Inner Tracking System (ITS);
- Time Projection Chamber (TPC);
- Transition Radiation Detector (TRD);
- Time of Flight (TOF).

In the mid-rapidity region there are also three detectors with limited azimuthal acceptance:

- High Momentum Particle Identification Detector (HMPID);
- PHOton Spectrometer (PHOS);
- ElectroMagnetic CALorimeter (EMCAL).

MUON SPECTROMETER: this detector, placed in the forward pseudo-rapidity region ($-4.0 < \eta < -2.5$), consists of a dipole magnet and tracking and trigger chambers. It is optimized to reconstruct heavy quark resonances (such as J/Ψ through their $\mu^+\mu^-$ decay channel) and single muons;

FORWARD DETECTORS: placed in the high pseudo-rapidity region (small angles with respect to the beam pipe) they are small and specialized detector systems used for triggering or to measure global event characteristics. They are:

- Time Zero (T0) to measure the event time with precision of the order of tens of picoseconds, as needed by TOF;
- VZERO to reject the beam-gas background and to trigger minimum bias events;
- Forward Multiplicity Detector (FMD) to provide multiplicity information over a large fraction of the solid angle ($-3.4 < \eta < -1.7$ and $1.7 < \eta < 5$);
- Photon Multiplicity Detector (PMD) to measure the multiplicity and the spatial distribution of photons on an event-by-event basis in the $2.3 < \eta < 3.7$ region;
- Zero Degree Calorimeter (ZDC) to measure and trigger on the impact parameter. The ZDC consists of two calorimeters, one for neutrons (ZDC:ZN) and one for protons (ZDC:ZP), and includes also an electromagnetic calorimeter (ZEM).

ACORDE is an array of scintillators installed on top of the L3 magnet to trigger on cosmic rays.

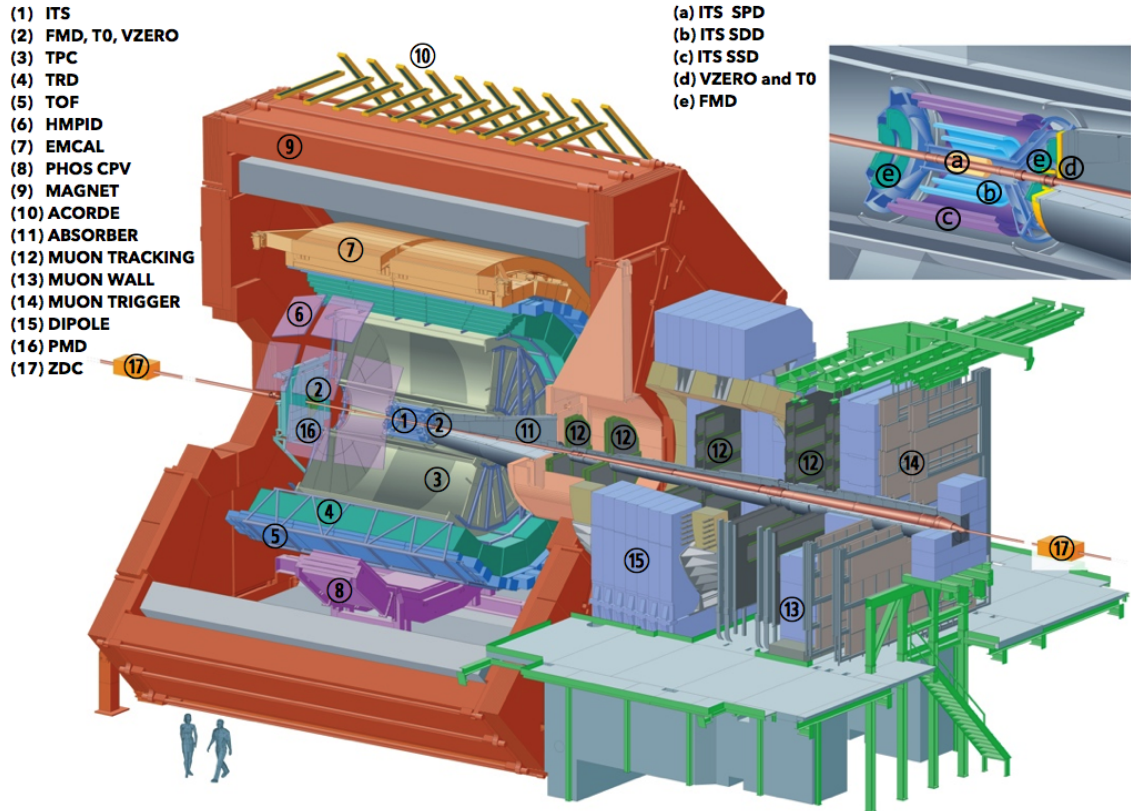


Figure 27: The ALICE detector. [99]

A schematic view of the ALICE experiment is shown in Figure 27 and detectors characteristics are summarized in Table 4.

The ALICE global coordinate system [100] is a right-handed orthogonal Cartesian system with the origin $X, Y, Z = 0$ at the centre of the detector. The three Cartesian axes are defined as follows: the X axis pointing towards the centre of the LHC, the Y axis pointing upward and the Z axis parallel to the local mean beam line pointing in the direction opposite to the muon spectrometer. The azimuthal angle increases counter-clockwise from the positive X axis ($\phi = 0$) to the positive Y axis ($\phi = \pi/2$) with the observer standing at positive Z and looking at negative Z ; the polar angle increases from the positive Z axis ($\theta = 0$) to the X - Y plane ($\theta = \pi/2$) and to the negative Z axis ($\theta = \pi$).

In the following Sections more specific descriptions of the detectors used in the identification of the multi-strange baryons and in the determination of the characteristics of typical collisions will be given.

Table 4: Summary of the ALICE detector sub-systems. The acceptance in η is calculated from the nominal interaction point. The position is the approximate distance from the interaction point to the face of the detector, corresponding to the radius for the barrel detectors or to the position along the beam for the others. The dimension corresponds to the total area covered by the active detector elements. Channels refers to the total number of independent electronic readout channels. In case a detector is divided into sub-detectors, the numbers refer to the individual components. [99]

Detector	Acceptance (η, ϕ)	Position (m)	Dimension (m ²)	Channels
ITS layer 1 / 2 (SPD)	$\pm 2, \pm 1.4$	0.039 / 0.076	0.21	$9.8 \cdot 10^6$
ITS layer 3 / 4 (SDD)	$\pm 0.9, \pm 0.9$	0.150 / 0.239	1.31	133000
ITS layer 5 / 6 (SSD)	$\pm 0.97, \pm 0.97$	0.380 / 0.430	5.0	$2.6 \cdot 10^6$
TPC	± 0.9 at $r = 2.8$ m ± 1.5 at $r = 1.4$ m	0.848 / 2.466	endcup 39.5 Vol. 90 m ³	557568
TRD	± 0.84	2.90 / 3.68	716	$1.2 \cdot 10^6$
TOF	± 0.9	3.78	141	157248
HMPID	± 0.6 $1.2^\circ < \phi < 8.8^\circ$	5.0	11	161280
PHOS	± 0.12 $220^\circ < \phi < 320^\circ$	4.6	8.6	17920
EMCal	± 0.7 $80^\circ < \phi < 187^\circ$	4.36	44	12672
ACORDE	± 1.3 $-60^\circ < \phi < 60^\circ$	8.5	43	120
Muon Spectrometer				
Tracking station 1	$-2.5 < \eta < -4.0$	-5.36	4.7	$1.08 \cdot 10^6$
Tracking station 2		-6.86	7.9	
Tracking station 3		-9.83	14.4	
Tracking station 4		-12.92	26.5	
Tracking station 5		-14.22	41.8	
Trigger station 1	$-2.5 < \eta < -4.0$	-16.12	64.6	21000
Trigger station 2		-17.12	73.1	
ZDC:ZN	$ \eta < 8.8$	± 116	2×0.0049	10
ZDC:ZP	$6.5 < \eta < 7.5$ $-9.7^\circ < \phi < 9.7^\circ$	± 116	2×0.027	10
ZDC:ZEM	$4.8 < \eta < 5.7$ $-16^\circ < \phi < 16^\circ$ $164^\circ < \phi < 196^\circ$	7.25	2×0.0049	2
PMD	$2.3 < \eta < 3.7$	3.64	2.59	$2.2 \cdot 10^6$
FMD disc1	$3.62 < \eta < 5.03$	inner: 3.2		
FMD disc2	$1.7 < \eta < 3.68$	inner: 0.834 outer: 0.752	0.266	51200
FMD disc3	$-3.4 < \eta < -1.7$	inner: -0.628 outer: -0.752		
VZERO-A	$2.8 < \eta < 5.1$	3.4	0.548	32
VZERO-C	$-1.7 < \eta < -3.7$	-0.897	0.315	32
T0A	$4.61 < \eta < 4.92$	3.75	0.0038	12
T0C	$-3.28 < \eta < -2.97$	-0.97	0.0038	12

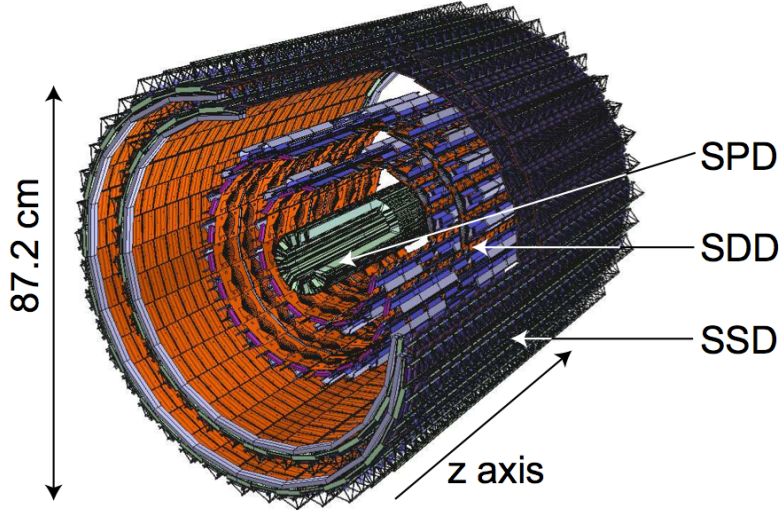


Figure 28: Schematic view of the ITS. [99]

ITS

The ITS [99] (Figure 28) is the barrel detector closest to the beam pipe. Its main goals are:

- to contribute with the TPC to the global tracking of ALICE by improving the angle and momentum resolution;
- to reconstruct the position of the primary interaction vertex;
- to reconstruct secondary vertices from decays of heavy-flavour and strange particle decays;
- to track and identify particles with momentum below 100 MeV/c;
- to improve the momentum, impact parameter and angle resolution for the measurement of high p_T particles performed with the TPC;
- to reconstruct particles traversing dead regions of the TPC.

The ITS surrounds the beam pipe (which is a 800 μm thick cylinder with an outer diameter of 2.9 cm) and consists of six cylindrical layers of silicon detectors located at radii between 4 cm and 43 cm. Due to the high track density, the two innermost layers are Silicon Pixel Detectors (SPD) which guarantee a high granularity. They are followed by two layers of Silicon Drift Detectors (SDD), while the two outmost layers are double-sided Silicon micro-Strip Detectors (SSD). The four outer layers have analogue readout and therefore can be

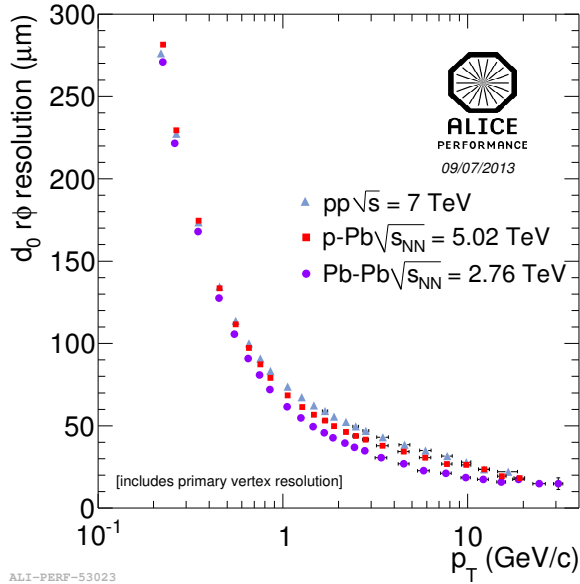


Figure 29: Track impact parameter to primary vertex resolution in the transverse plane ($r\phi$) as a function of p_T for unidentified charged particles, for pp at $\sqrt{s} = 7$ TeV, Pb–Pb at $\sqrt{s_{NN}} = 2.76$ TeV and p–Pb at $\sqrt{s_{NN}} = 5.02$ TeV. The resolution includes the contribution from the primary vertex resolution, which improves from pp to p–Pb and Pb–Pb (with charged multiplicity).

used for particle identification via dE/dx measurement in the non-relativistic region ($dE/dx \sim 1/\beta^2$).

Since the momentum and impact parameter resolutions for low momentum particles are dominated by multiple scattering effects, the amount of material in the active volume has been minimized as much as possible. The granularity of the detector was optimized to keep the occupancy low in all the layers. With the technology chosen, the ITS detectors reach a spatial resolution of the order of a few tens of μm ⁴ resulting in a resolution on the impact-parameter⁵ better than 70 μm in the $r\phi$ plane for $p_T > 1$ GeV/c and thus well suited for the reconstruction of heavy-flavour decays (see Figure 29).

The resolution of X and Z coordinate of the primary vertex reconstruction are shown in the Figure 30. These are obtained dividing the tracks of the event in two random samples and reconstructing two vertices for the two samples;

⁴ $r\phi$ spatial precision: SPD = 12 μm , SDD = 35 μm , SSD = 20 μm ; Z spatial precision: SPD = 100 μm , SDD = 25 μm , SSD = 830 μm .

⁵ The transverse impact parameter in the bending plane $d_0(r\phi)$ is the reference variable to look for secondary tracks from strange, charm and beauty decay vertices and good resolution is needed to separate these from primary tracks (that come from the primary vertex).

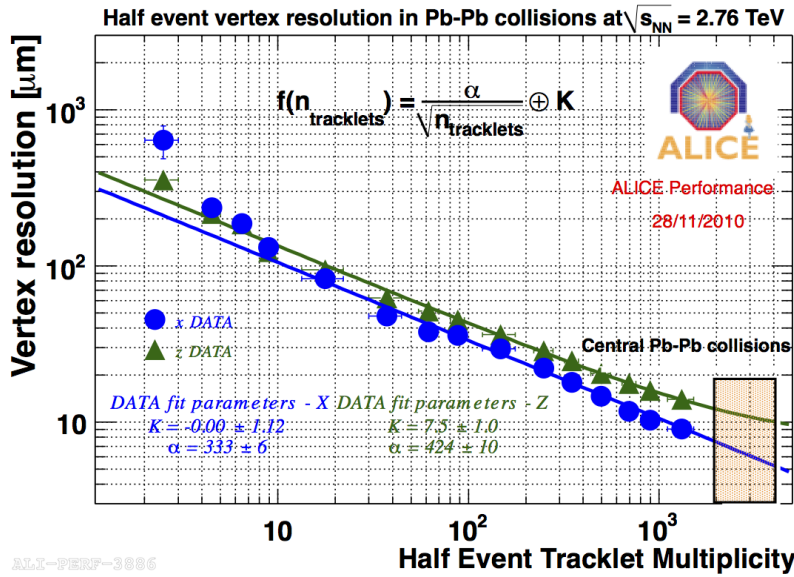


Figure 30: The X (blue points) and Z (green points) coordinate vertex resolutions in Pb–Pb collisions at $\sqrt{s_{\text{NN}}} = 2.76$ TeV as a function of half of the tracklet multiplicity of the event. In the formula the dependency of the resolution on the multiplicity is convoluted with a constant parameter K.

the difference between these two vertices is the measure of the resolution as a function of the half tracklet⁶ multiplicity. The fit allows to extrapolate the value of the resolution for the most central (0 – 5%) Pb–Pb collisions.

TPC

The TPC [101] (Figure 31) is the main tracking detector of the central barrel, optimized to provide, together with the other central barrel detectors, charged-particle momentum measurements with good two-track separation, particle identification and vertex determination. The TPC was designed for an excellent tracking performance in the high multiplicity environment of PbPb collisions. For this reason, it was chosen to be a drift chamber, cylindrical in shape, 5 m long, with the inner radius ($r_{\text{in}} \sim 85$ cm) determined by the maximum acceptable track density, and the external one ($r_{\text{ext}} \sim 250$ cm) by the minimum track length for which dE/dx resolution is < 10%. The TPC volume is filled with 90 m³ of Ne/CO₂/N₂ (90/10/5). The readout planes are divided in 18 sectors in which multiwire proportional chambers (with cathode pad readout) are housed. Because of its good dE/dx resolution, the TPC can identify particles with $p_T < 1$ GeV/c on a

⁶ An SPD tracklet is defined by a pair of hits aligned with the reconstructed vertex.

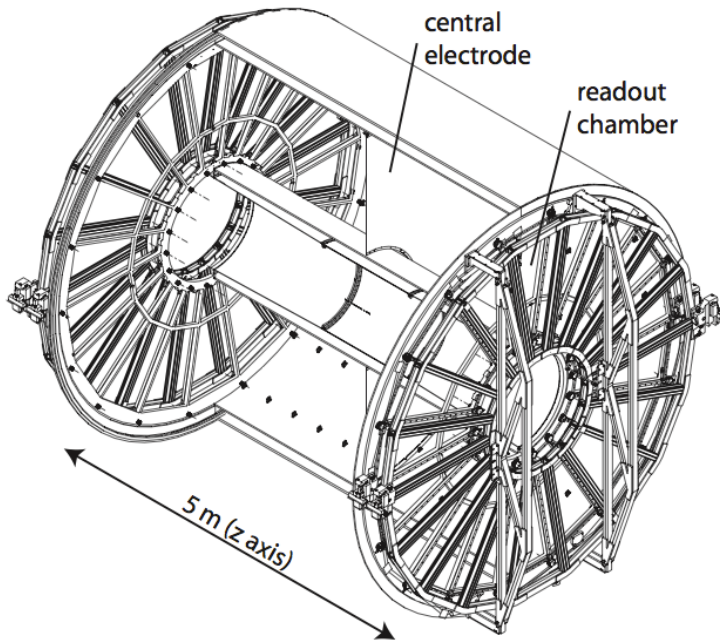


Figure 31: Schematic view of the TPC. [99]

track-by-track basis (more details in Section 3.2.6). The TPC tracking efficiency is $> 90\%$ for $p_T > 100 \text{ MeV}/c$ where the limiting factor are the interactions in the ITS material. Measuring the deflection in the magnetic field, the ITS and the TPC are able to determine the momentum of the charged particles with a resolution better than 1% at low p_T and better than 20% for $p_T \sim 100 \text{ GeV}/c$ (see Figure 32).

The upper limit in the luminosity, which the ALICE central detector can handle, is not a threshold, but rather a progressive deterioration of performance. The large drift time in the TPC ($\sim 100 \mu\text{s}$) is the first limitation and for luminosities higher than $2 \times 10^{29} \text{ cm}^{-2} \text{ s}^{-1}$ events would start overlapping. Even with 20 superimposed events, the growing number of tracks is not a problem because this is still an order lower than in Pb–Pb events, and also the vertex reconstruction is easily feasible. On the other hand, the size of the event will growth linearly with luminosity increasing the load on the data storage and computing without providing any benefit to the physics. At a luminosity of $3 \times 10^{30} \text{ cm}^{-2} \text{ s}^{-1}$ events would start to pile-up also in the SDD which have a drift time of $5 \mu\text{s}$: in this case the tracks from the off-time events would not be reconstructable. At even higher luminosities, pile-up will become progressively more difficult to manage, involving other detectors [102].

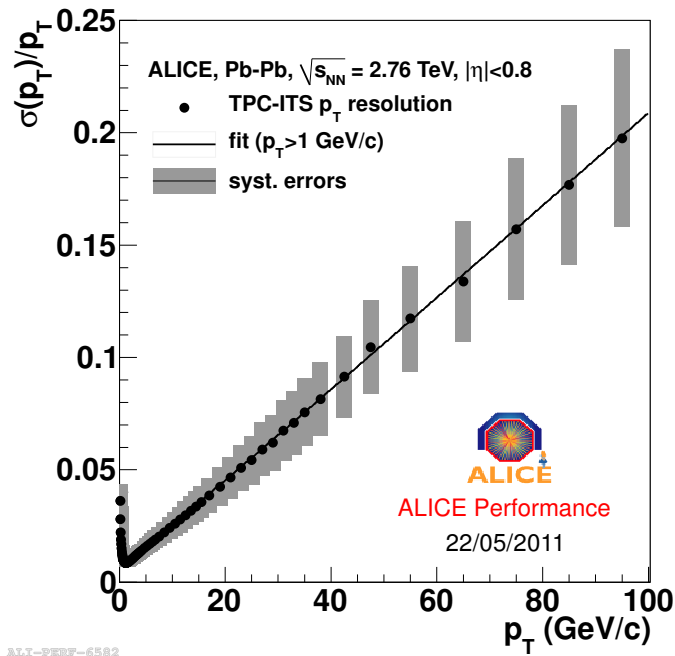


Figure 32: Momentum resolution in Pb–Pb interactions at $\sqrt{s_{\text{NN}}} = 2.76$ TeV.

VZERO

The VZERO detector [103] consists of two segmented arrays of plastic scintillator counters, called VZERO-A and VZERO-C, placed around the beam-pipe on either side of the IP: one at $Z = 340$ cm, covering the pseudo-rapidity range $[2.8; 5.1]$, and the other at $Z = -90$ cm (in front of the absorber), covering the pseudo-rapidity range $[-3.7; -1.7]$. They consist of 32 counters distributed in four rings, each divided in eight 45° sectors. Each counter is made of scintillator material embedded with WaveLength Shifting fibres. Clear fibres collect and transport the signal to photomultipliers 3 – 5 m far from the detector, inside the L3 magnet. The counters have a time resolution better than 1 ns. Their response is recorded in a time window of 25 ns around the nominal beam crossing time.

The VZERO is a trigger detector that will provide a minimum-bias trigger for all colliding systems to the central barrel detectors and three centrality triggers in Pb–Pb collisions (multiplicity, central and semi-central). It has an important role in rejecting background from beam-gas collisions exploiting the relative time-of-flight measurement between the two arrays: when the beam-gas collision takes place outside the region between the two arrays, particles arrive 6 ns before or after the time of a beam-beam collision. If the beam-gas collision takes place in between the two arrays it is not possible to reject it and an offline trigger has

to be employed. It will also participate in the measurement of luminosity in pp collisions with a fairly good precision (about 10%).

3.2.2 Data Acquisition (DAQ) and Trigger systems

The tasks of the ALICE DAQ system are the assembly of event informations from individual detectors into complete events (event building) as well as buffering and export of assembled events to permanent storage. The DAQ is designed to process a data rate up to 1.25 GB/s in heavy-ion runs. Event building is done in two steps. Data from the detectors is received by Detector Data Links (DDLs) on Local Data Concentrators (LDCs). The LDCs assemble the data into sub-events that are then shipped to Global Data Collectors (GDCs). A GDC receives all sub-events from a given event and assembles them into a complete event. These events are subsequently stored on a system called Transient Data Storage (TDS). The export of the data and further processing are described in Section 3.2.3.

ALICE can simultaneously take data in several partitions, where a set of detectors can store their outputs. Since a partition is a group of commonly controlled detectors, a given detector can only be active in one partition at a time. The active detectors in a given partition may be assigned to data taking groups called clusters, for which triggers can be defined. Therefore, upon a trigger only a subset of the whole partition may be read out. Furthermore, a triggering detector does not have to be necessarily part of the partition.

ALICE has a two-layer trigger architecture [104]. The low-level trigger is a hardware trigger called Central Trigger Processor (CTP). The High-Level Trigger (HLT) is implemented as a pure software trigger. The CTP combines inputs from different trigger sources, namely the various detectors. These inputs are single signals, like a hit in the detector, or, can be the result of fast calculation performed directly in the detectors. The HLT allows the implementation of sophisticated logic for the triggering. In contrast to the CTP which governs the readout of the detectors, the HLT receives a copy of the data read out from the detectors and processes them.

The hardware trigger combines the trigger signals of the various detectors to decide if an event is accepted, that means it is read out and written to disk. Several trigger levels reduce the event rate depending on the input signals. The first level, called L0, is delivered after 1.2 μ s, while the second, called L1, after 6.5 μ s. The final trigger, L2, is delivered after 100 μ s, upon completion of the drift time in the TPC. Only after an L2 trigger the event is finally stored. The rates of different trigger classes are very different. By definition minimum-bias triggers have the highest rate; other triggers that look for rare signals are characterized

by much lower rates. In order to cope with different scenarios, downscaling factors can be applied to the trigger classes individually, i.e. only every nth event fulfilling the trigger condition is read out. The total recording rate is limited by the maximum bandwidth of data that can be recorded to disk and tape.

The ALICE software trigger, called HLT, is a farm of multiprocessor computers. The aim is to have about 1000 PCs processing the data in parallel allowing an online analysis of the events. A trigger decision comes from the analysis of a more comprehensive set of information than what happens for the hardware trigger, giving the possibility to apply more sophisticated triggers. Examples include triggers on high energy jets or on muon pairs. Furthermore, the HLT can significantly reduce the event size by selecting regions of interest (partial readout of detectors) and by further compression of the data. The HLT receives a copy of the raw data and performs per detector reconstruction, partly aided by hardware coprocessors. Subsequently, the trigger decision is based on the global reconstructed event. In the same step a region of interest can be selected. In the last optional step, if the trigger decision is positive, the data are compressed. The trigger decision, partial readout information, compressed data, and the reconstruction output is sent to LDCs and subsequently processed by the DAQ. In terms of the overall DAQ architecture, data sent by HLT is treated like stemming from a detector.

3.2.3 Data flow: from the Online to the Offline

The raw data taken by the detectors has to be processed before it is available in the form of reconstructed events for further analysis. This happens in several stages and is illustrated in Figure 33.

Data originating from the detectors (denoted by 1 in Figure 33) is processed by LDCs and global events are built by GDCs (2), as already mentioned in Section 3.2.2. The so-called publish agent registers the assembled events into the AliEn system (3) and ships them to the CERN computing centre where they are stored first on disks (4) and then permanently on tapes (5) by the CASTOR system [105].

During data-taking the detectors also produce conditions data that are relevant for the calibration of individual detector signals. Conditions data provide information about the detector status and environmental variables during data-taking. Examples are inactive and noisy channel maps, distributions that describe the response of a channel, temperatures and pressure in a detector, and detector configuration. Many of the conditions data could in principle be calculated from the raw data and extracted offline after data-taking. However, such an approach would require an additional pass over the raw data before the recon-

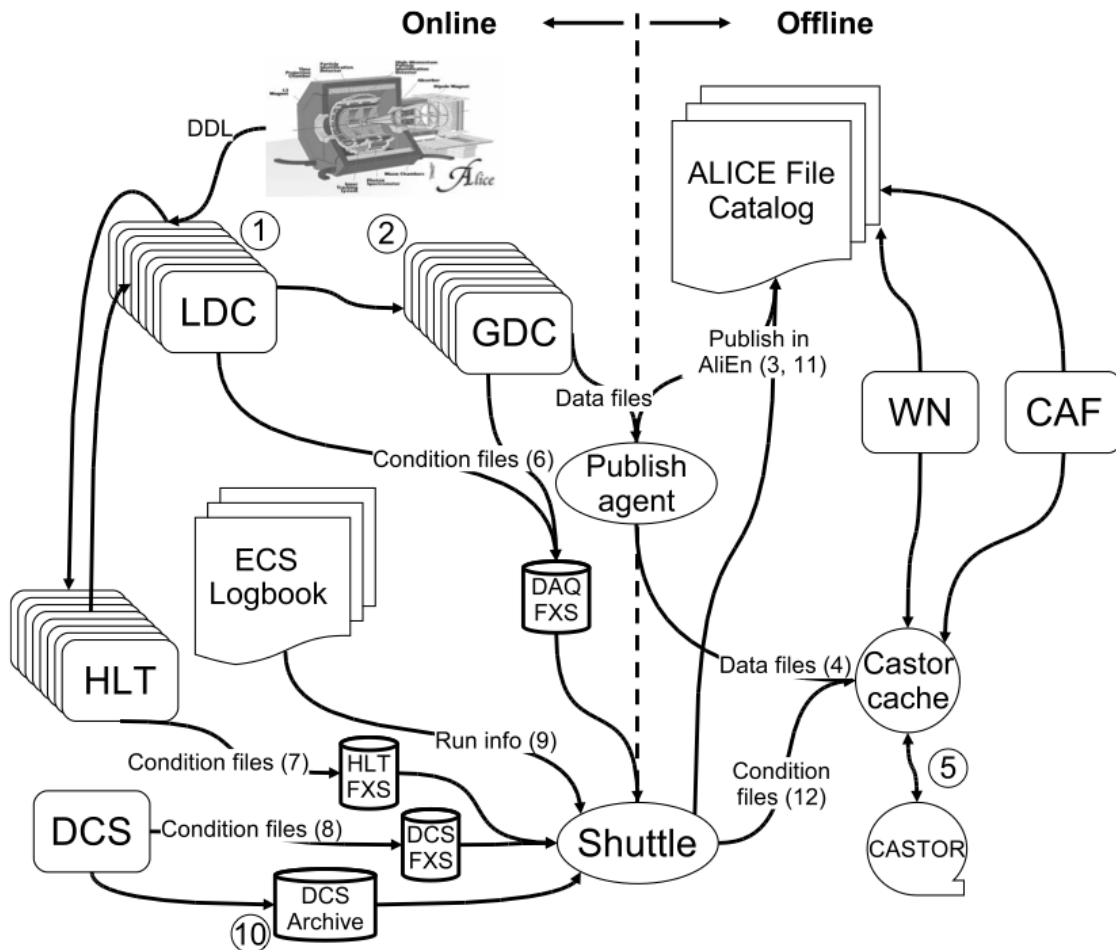


Figure 33: Global view of ALICE’s data flow. [99]

struction which is not feasible due to the limited computing resources. Therefore, conditions data are already extracted during data-taking and stored in the Offline Condition Data Base (OCDB). A dedicated program called Shuttle collects these outputs and makes them available to the reconstruction. Furthermore, it retrieves information about the run from the ECS⁷ logbook (9) and collects continuously monitored values that are written by DCS into the DCS Archive (10).

⁷ The Experiment Control System (ECS) is the top level control of the ALICE experiment. Running an experiment implies performing a set of activities on the online systems that control the operation of the detectors. These online systems are: the Trigger (TRG), the Detector Control Systems (DCS), the Data-Acquisition System (DAQ) and the High-Level Trigger (HLT). The ECS provides a framework in which the operator can have a unified view of all the online systems and perform operations on the experiment seen as a set of detectors. [106]

After processing the data, the Shuttle registers the produced condition files in AliEn (11) and stores the data in CASTOR (12).

With the registration of the raw and conditions data the transition from the online to the offline world has taken place. “Online” denotes all actions and programs that have to run in real time. “Offline” processing is the subsequent step, like for instance the event reconstruction, which is executed on worker nodes (WN) of Grid sites located around the Globe.

3.2.4 ALICE Offline software framework

The required computing resources for the reconstruction and analysis of the raw data as well as the production of simulated events needed for the understanding of the data exceed the computing power of single institutes and even centres like CERN. Therefore, institutes that are part of the Collaboration also provide storage and computing resources. Distribution of the data for reconstruction and analysis cannot be performed manually and this led to the need for an automated system. The concept of a decentralized computing model called Grid [107] was identified as a solution.

The AliEn Framework

The Grid paradigm implies the unification of resources of distributed computing centres, in particular computing power and storage, to provide them to users all over the World. It allows computing centres to offer their resources to a wider community and the local resources to be shared by an entire collaboration.

Software that implements the Grid concept is called Grid middleware. ALICE has developed a Grid middleware called AliEn [108] since 2001. An ALICE user employs AliEn to connect to the ALICE Grid which is composed of a combination of general services that are provided by many Grid middleware solutions and ALICE-specific services provided by AliEn. Parts of the ALICE Grid are: i) a global file catalog that is a directory of files in storage elements distributed over the Globe, ii) the automatic matching of jobs for execution to a suitable location in one of the connected sites, iii) a shell-like user interface and iv) API⁹ services for the ROOT framework [109].

Currently the ALICE Grid consists of about 80 sites located in 21 countries. Figure 34 shows a map of the ALICE Grid sites.

The AliRoot Framework

AliRoot [99, 111] is the offline framework for simulation, alignment, calibration, reconstruction, visualization, quality assurance, and analysis of experimen-



Figure 34: ALICE Grid sites. While most of them are located in Europe, some are in other continents as can be seen in the inset in the bottom right corner. [110]

tal and simulated data. It is based on the ROOT framework. Most of the code is written in C++ with some parts in Fortran that are wrapped inside C++ code. Re-usability and modularity are the basic features of the AliRoot framework. Modularity allows parts of the code to be replaced, with minimum or no impact on the rest (for example changing the event generator, the transport Monte Carlo or the reconstruction algorithms). This is achieved implementing abstract interfaces. In addition codes for each detector subsystem are independent modules with their specific code for simulation and reconstruction and the code can be developed concurrently with minimum interference. Re-usability is meant to maintain a maximum amount of backward compatibility as the system evolves.

The central module of the AliRoot framework is STEER (Figure 35) which provides several common functions such as: steering of program execution for simulation, reconstruction and analysis; general run management, creation and destruction of data structures, initialization and termination of program phases; base classes for simulation, event generation, reconstruction, detectors elements.

For event simulation the framework provides the following functionality:

EVENT GENERATION A lot of MC event generators (e.g. Pythia [112, 75], Photojet [113] for pp events and HIJING [76] for Pb–Pb events) are interfaced

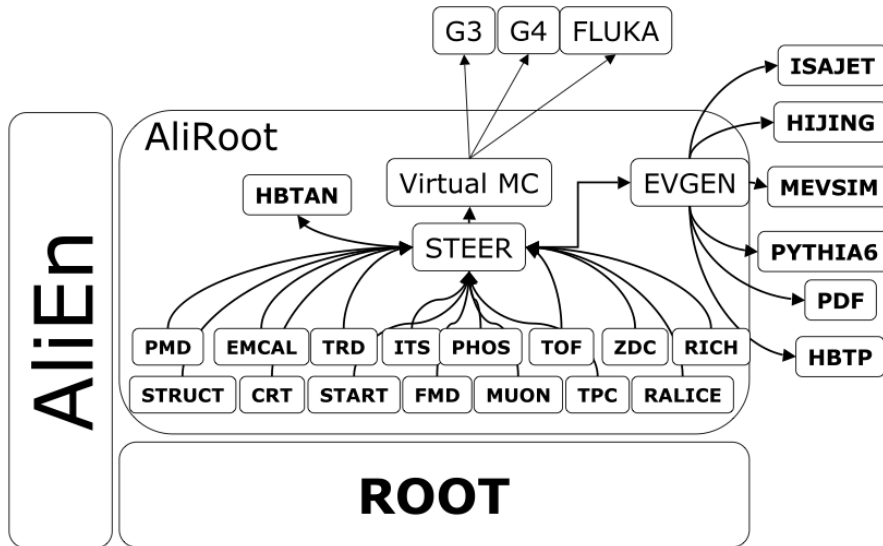


Figure 35: Schema of the AliRoot framework. [99]

with AliRoot. For each generated particle a list of informations (such as type, momentum, charge, production process, originating particle and decay products) is stored in a file (kinematics tree).

TRANSPORT The detector structure, the motion of the particles through it and the possible interactions with the material are simulated using programs such as Geant3 [114], Geant4 [115] and Fluka [116]. During this process for all the interactions of particles with sensitive parts of the detector (hits) informations such as position, time, energy deposition and the tag of track they belong to are recorded.

DIGITIZATION Finally all the hits are translated in the corresponding digital output of the detector, taking into account the detector's response function. All this information are than stored in the specific hardware format of the detector (raw data).

3.2.5 Event reconstruction

At this stage the raw data correspond to the signals that would have been produced by an interaction of the same kind within the detector. The subsequent reconstruction is identical, both for simulated as well as real events. It consists of the following steps:

CLUSTER FINDING Usually, particles that interact with a detector, depending on its spatial segmentation, leave a signal in several adjacent detecting elements. Similarly a signal last in a time interval and can be distributed on more than one time bin. The first needed step in the event reconstruction is the cluster finding, that is the construction of sets of spatial or time close signals, reducing the effect of the random noise in the position or timing measurement.

TRACK RECONSTRUCTION The tracking is a complex and iterative procedure that, starting from clusters, use the Kalman filter technique [117] to follow inward and outward the track fitting. The tracking is a global task as well as an individual procedure per detector. The different steps of the global track reconstruction are schematically reported in Figure 36. The procedure starts from track “seeds” in the outermost part of the TPC, selected under the assumption that the corresponding track originated from the primary vertex. Than the TPC only reconstruction ends with a similar seeding in the innermost part of the TPC, the removal of all the clusters already associated to tracks and the final filtering performed without requiring that the seeds point to the primary vertex. Subsequently, these tracks are complemented with information from the ITS, TRD, and TOF as well as HMPID and PHOS if the track is in their acceptance, which produces so-called global tracks. Tracks can also be formed out of information from the ITS only.

PRIMARY-VERTEX RECONSTRUCTION The position of the primary vertex of the interaction can be found using different method based on the usage of different informations such as tracklets in the SPD, tracks in the TPC and global tracks. The estimated position of the primary vertex in each technique is than used to constrain the tracks during the corresponding reconstruction procedure. Of course this constraint is only used for tracks that actually pass in vicinity of the vertex.

SECONDARY-VERTEX RECONSTRUCTION The other tracks, sufficiently far away from the primary vertex, are combined to find secondary vertices, corresponding to the decays of unstable particles as for the heavy flavor mesons. Such a reconstruction is based on geometrical selection, suggested by the topology of the decay of the considered particles.

The output of the reconstruction is called Event-Summary Data (ESD). This file contains only high-level information such as the position of the event vertex, parameters of reconstructed charged particles together with their PID information, positions of secondary-vertex candidates, parameters of particles reconstructed

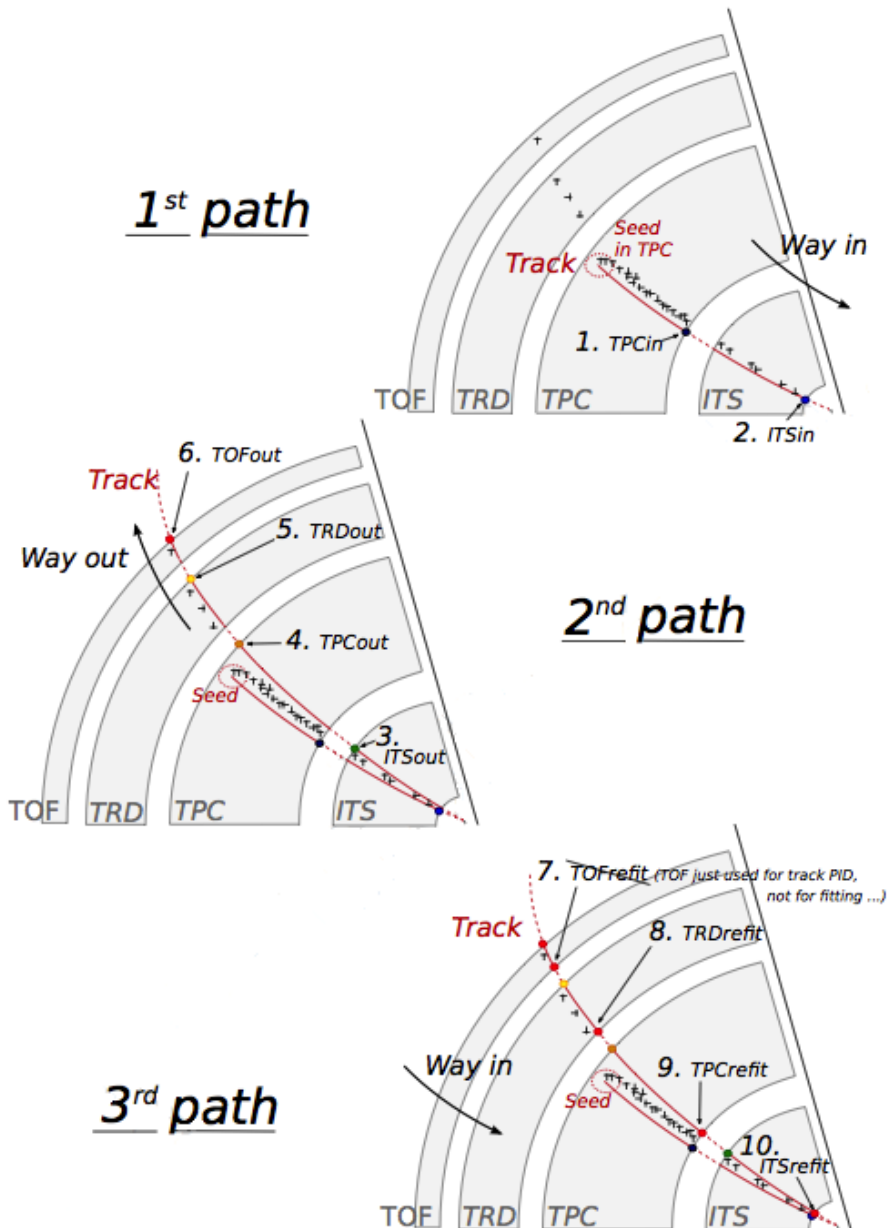


Figure 36: Principle of track reconstruction in an ALICE event: all the three steps of the iterative procedure are shown. The numbers on the plots marks the bits that are activated in each step during the Kalman filter procedure, in case of success. [118]

in the calorimeters and integrated signals of some detectors. This data is further reduced to Analysis-Object Data (AOD) format. These smaller-sized objects contain only information needed for the analysis. Therefore, the transformation procedure may already contain a part of the analysis algorithm, for example track selection. Several AODs, focusing on different physics studies, can be created for a given event.

3.2.6 Particle identification with the TPC

One of the main characteristics of the ALICE detector, as well as the very low transverse momentum threshold of detection, consists in PID capabilities. The identification can be performed in two different ways: by direct identification and by the reconstruction of the topology of the disintegration process of a particle.

In the direct identification, usually five mass hypotheses are considered, that correspond to the particles that live long enough to be identified at track level: $e^\pm, \mu^\pm, \pi^\pm, K^\pm, p^\pm$. Seven of the detectors that compose ALICE (SDD, SSD, TPC, TRD, TOF, HMPID and the EM calorimeter) can provide PID, based on different techniques: specific energy loss (dE/dx), time of flight and photon radiation characteristics. This information can be used individually or combined. A full description of the individual and combined PID can be found in [119].

A second way to identify particles is via invariant mass computation for its daughter particles, as in the case, for instance, for a strong decay of a resonance and also for a weakly decayed particle. In this latter case, reconstruction can be done via topological reconstruction, since the tracks originate from a decay point that is not the primary interaction vertex. In this second case the direct identification of the daughter particles ($e^\pm, \mu^\pm, \pi^\pm, K^\pm, p^\pm$, that are the main products of these decays) has an important role in the background reduction.

The multi-strange baryons are within this second group. During the analysis described in this thesis, the PID information from the TPC has been used, both in pp and Pb–Pb analysis. The ITS can provide PID for tracks not traversing the TPC and with a worst resolution ($\sigma_{dE/dx}^{\text{ITS}} \sim 15\%$ compared to $\sigma_{dE/dx}^{\text{TPC}} \sim 5\%$). Consequently in this Section the procedure for the PID in the TPC is described.

Charged particles travelling through the TPC ionize the detector's gas; the measurement of this loss of energy is what we need to identify a particle. The physics observable in this case is the energy loss per unit length, within the matter crossed by the charged particle, which we call specific energy loss, also denoted by dE/dx . This is described by the Bethe–Bloch equation, 3.1, that highlights the key of the identification technique: this observable depends only on the charge and on velocity (β) of the particle, which, in turn, depends only

on the momentum and the mass of the ionizing particle. Since momentum is already known due to track curvature and charge is unitary for most measured tracks, measuring the dE/dx allows us to indirectly determine mass and thus determine the particle species.

The Bethe-Bloch equation gives the mean specific energy loss:

$$-\langle \frac{dE}{dx} \rangle = k_1 \cdot z^2 \frac{Z}{A} \cdot \frac{1}{\beta^2} \left[\frac{1}{2} \ln(k_2 \cdot m_e c^2 \cdot \beta^2 \gamma^2) - \beta^2 + k_3 \right] \quad (3.1)$$

where $\beta\gamma = p/Mc$ and:

- Z , atomic number of the ionized gas (in this case Ne/CO₂/N₂);
- A , mass number of the ionized gas (g/mol);
- m_e , electron mass;
- z , electric charge of the ionizing particle in unit of electron charge e ;
- M , ionizing particle mass;
- p , ionizing particle momentum;
- β , ionizing particle velocity normalized to the light velocity c ;
- $\gamma = 1/\sqrt{1 - \beta^2}$, Lorentz factor;
- k_1, k_2, k_3 constants depending on the ionized medium.

For a given ionizing particle mass hypothesis, a given momentum and a given length of the trajectory in the ionizing medium, the total charge deposited along the trajectory is subject to statistical fluctuations. This random variable follows a Landau distribution, that give us the opportunity to measure the mean value $\langle dE/dx \rangle$. The long tail of the Landau distribution is usually truncated at 50%-70% of the collected signal.

The specific energy loss in the TPC as a function of momentum is shown in Figure 37. The different bands characteristic for $e^\pm, \mu^\pm, \pi^\pm, K^\pm, p^\pm$ are clearly visible. These are the evidence of the statistical distribution of the measured energy loss around the expected mean value. The expected value correspond to the prediction by a Bethe-Bloch experimental parametrization (superimposed as black lines in the Figure).

For a track within the TPC the relevant quantity to be considered for PID is the difference between the measured specific energy loss and the corresponding predicted value, by the Bethe-Bloch parametrization for a given measured momentum. If normalized to the resolution of the dE/dx measurement in the TPC,

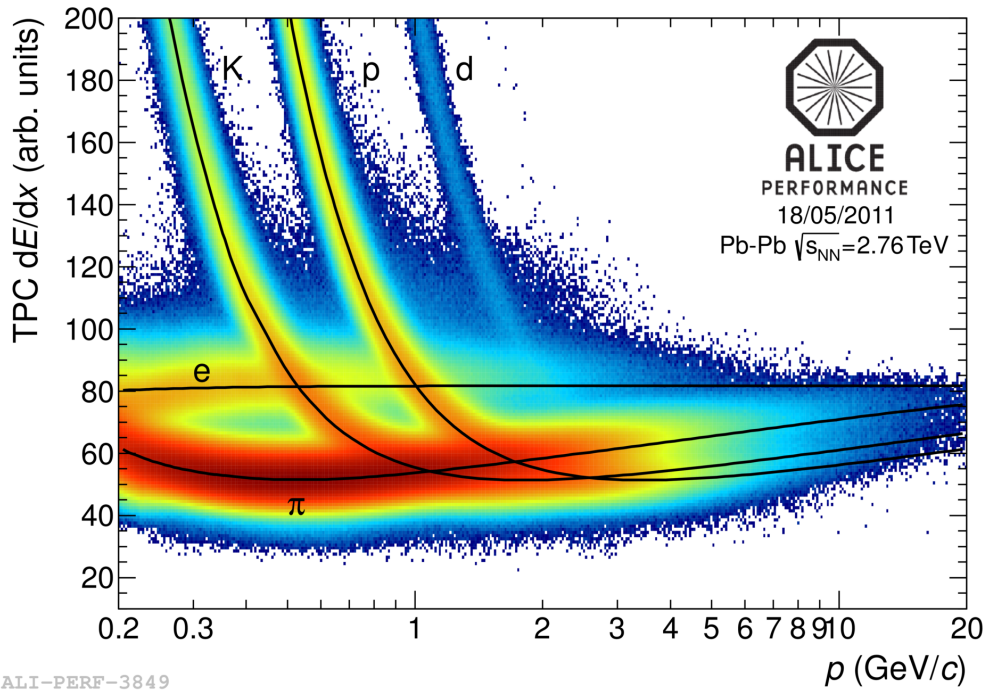


Figure 37: Specific energy loss in the TPC as a function of momentum for Pb–Pb collisions at $\sqrt{s_{\text{NN}}} = 2.76 \text{ TeV}$. The Bethe–Bloch curves for various particle species are superimposed for comparison.

this difference could be expressed in number of σ (see Equation 3.2). In this way it is possible to estimate more quantitatively the goodness of a mass hypothesis. This also gives us the possibility to choose the strictness we want to adopt in the identification of a particle (n_σ , $n = 2, 3, 4$):

$$n_\sigma = \frac{[(dE/dx)_{\text{measured}} - (dE/dx)_{\text{BB}}]}{\sigma_{\text{TPC}}} \quad (3.2)$$

The resolution on the dE/dx measurement for the TPC has been evaluated to be 5% for tracks having 159 clusters [101], better than the value estimated during the detector project phase [119]. The mean resolution on the full reconstructed tracks sample is around 6.5%.

3.2.7 Centrality definition and determination

The first parameter to be determined in A–A collisions is the centrality. This is defined according to the value of the impact parameter (b , introduced in Section 1.3) and provides a geometrical scale of the overlapping region between

the colliding nuclei: a collision will be defined from central to peripheral, as the impact parameter increases. The centrality of a collision is not directly available and must be deduced from a combination of experimentally measured quantities and Monte Carlo simulations.

There are a number of observables that can be measured and used as centrality estimators. The charged-particle multiplicity N_{ch} and the transverse energy E_T measured around mid-rapidity are measurable quantities related to the energy deposited in the interaction region (these are therefore related to N_{part}). These variables increase significantly increasing the centrality of the collisions. Another measurable quantity to estimate the centrality is the zero-degree energy E_{ZDC} , namely the energy carried by spectator nucleons $N_{spec} = 2A - N_{part} = E_{ZDC}/E_A$, where E_A is the beam energy per nucleon.

Typically a measured distribution of one of the previous observables is mapped to the corresponding distribution obtained from phenomenological Glauber calculations. The Glauber model [28, 29] uses a semi-classical approach: the A–A collision is assumed to be an incoherent superposition of N elementary nucleon-nucleon collisions. The main parameters of the model are the inelastic nucleon-nucleon collision cross-section σ_n and the nuclear density distribution $\rho(r)$. In practice, the simulated distribution well reproduce the measured distribution or the latter is fitted with an analytical function. The experimental distribution can then be divided in classes with sharp cuts on the measured observable (E_{ZDC} , E_T or N_{ch}); these “centrality” classes will correspond to well defined percentage of the integral of the distribution. A given centrality class in the measured distribution, corresponds to the same class in the simulated distribution, where the main geometrical variables (N_{part} , N_{coll} and T_{AA}) can be determined. The number of classes that can be defined depends on the resolution achievable on the selection variable.

In the analysis described in this thesis the centrality estimation is based on the measurement of the multiplicities from the VZERO scintillators [120]. This is the method that achieve the best centrality resolution: it ranges from 0.5% in central to 2% in peripheral collisions. Other methods, as the ones based on the E_{ZDC} measurement or based on the estimate of the number of tracks in the SPD or TPC, are used to asses a systematic uncertainty on the centrality determination.

The distribution of the VZERO amplitudes is shown in Figure 38 for minimum bias events, where the centrality percentiles are also indicated. Such percentile is determined for any value of VZERO amplitude by integrating the measured VZERO amplitude distribution normalized to the 90% of the hadronic cross section. The VZERO distribution is simulated by the Glauber Monte Carlo plus a

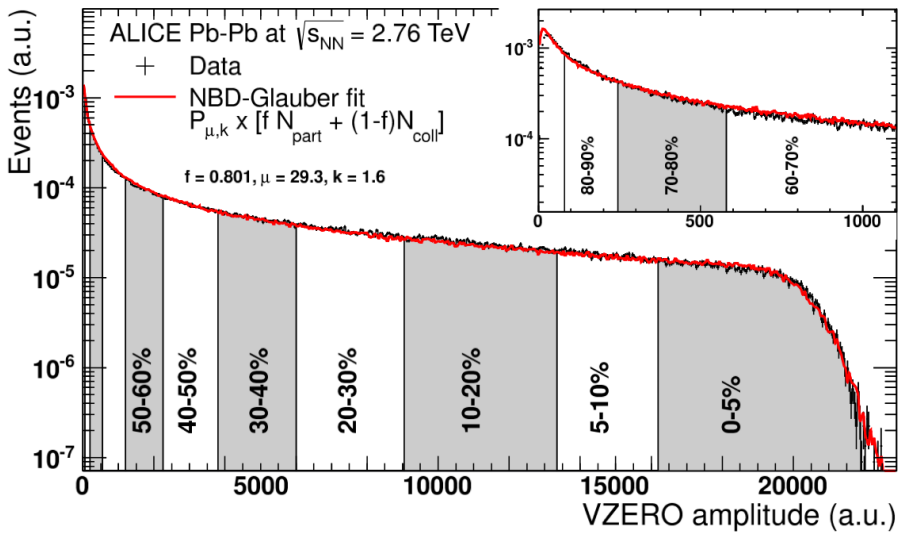


Figure 38: Distribution of the summed amplitudes in the VZERO scintillator tiles (histogram); inset shows the low amplitude part of the distribution. The curve shows the result of the Glauber model fit to the measurement. The vertical lines separate the centrality classes used in the analysis, which in total correspond to the most central 80% of hadronic collisions. [120]

convolution of a model for particle production⁸ and than compared to the measured distribution. A minimization procedure is applied to find the parameters which result in the smallest χ^2 ; such a values are reported in Figure 38.

This creates the connection between the experimental observable and the geometrical model of nuclear collisions used in the Glauber Monte Carlo. The impact parameter (b) distribution and the number of participant nucleons (N_{part}) distribution obtained from the Glauber Monte Carlo simulation are reported in Figure 39. Here the centrality classes are defined using the obtained relation between the experimental observable distribution and the geometrical model distribution. Then finally the mean values for $\langle N_{\text{part}} \rangle$, $\langle N_{\text{coll}} \rangle$ and $\langle T_{\text{AA}} \rangle$ can be estimated in each centrality class. In [120] has been shown that such mean values, obtained using the centrality classes defined as percentile of the measured hadron cross section differ from those calculated from geometrical classes by less than 1% for the most central classes and by less than 2% for the most peripheral

⁸ Such a convolution, based on a negative binomial distribution (NBD), is inspired by the two-component models [121], in which the nucleus-nucleus collisions are decomposed in “soft” interactions (with particle production proportional to N_{part}) and “hard” interactions (with particle production proportional to N_{coll}). The number of independently emitting sources of particles (N_{source}) are than parametrized by $N_{\text{source}} = f \times N_{\text{part}} + (1 - f) N_{\text{coll}}$, where f quantifies the relative contributions of “soft” and “hard” components.

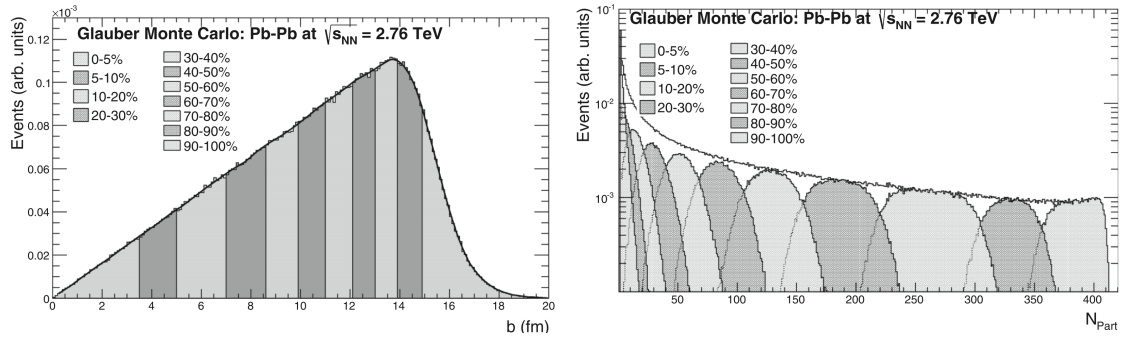


Figure 39: Geometric properties of Pb–Pb collisions at $\sqrt{s_{NN}} = 2.76 \text{ TeV}$ obtained from a Glauber Monte Carlo calculation: Impact parameter distribution (left), sliced for percentiles of the hadronic cross section, and distributions of the number of participants (right) for the corresponding centrality classes. [120]

classes. This means that multiplicity fluctuations and detector resolution only play a minor role in the centrality determination.

4

CASCADE IDENTIFICATION USING TOPOLOGICAL RECONSTRUCTION

4.1 INTRODUCTION TO MULTI-STRANGE BARYONS

As anticipated in Section 2.1, we are especially interested in the baryons containing two or three strange quarks; these are known as *multi-strange baryons* or *cascades*. The elements of this family are: two double strange hadrons $\Xi^0(\text{uss})$ and $\Xi^-(\text{dss})$, the purely strange hadron $\Omega^-(\text{sss})$, and the corresponding antiparticles $\Xi^0(\overline{\text{uss}})$, $\Xi^+(\overline{\text{dss}})$ and $\Omega^+(\overline{\text{sss}})$. To this sextet one could, in principle, add the corresponding resonances, that are five for the Ξ and one for the Ω ¹.

As described in Chapter 3, only charged particles can be tracked and identified using the ALICE detector. As a consequence the Ξ^0 (whose most probable decay channel is $\Xi^0 \rightarrow \Lambda + \pi^0$), and the corresponding antiparticle, cannot be identified in ALICE. The main characteristics of the four charged hyperons (not considering the resonances) and the Λ are reported in Table 5. To better understand the name usually adopted to call these particles, *cascade*, one has to look at the decay channels of these particles, also reported in this Table. A pictorial representation of the decay topology is shown in Figure 40.

Let's try to follow one of these cascades, e.g. the Ξ^- , along all its life. This hyperon, once created, travels in free space for a few centimeters before disintegrating via a weak decay, where the strange quantum number is not conserved. The traveled distance of a given particle depends on its momentum and on the mean lifetime, expressed usually as the product $c\tau$ (decay length²); in the case

¹ $\Xi(1530)$, $\Xi(1690)$, $\Xi(1820)$, $\Xi(1950)$, $\Xi(2030)$ and $\Omega(2250)$. [4]

² If a particle of mass m has mean decay lifetime τ ($= 1/\Gamma$, decay rate, proportional to the hamiltonian of the interaction) and has momentum (E, \vec{p}) , then the probability that it travels a distance

Table 5: Properties of the Λ baryons and the Ξ and Ω multi-strange baryons. The valence quark content, the mass, the main decay channel, together with their branching ratio (B.R.) and $c\tau$ are listed. [4]

Particle	Mass (MeV/c ²)	Decay channel	B.R. (%)	$c\tau$ (cm)
$\Lambda(\text{uds})$	1115.68	$\Lambda \rightarrow p + \pi^-$	63.9	7.89
$\bar{\Lambda}(\overline{\text{uds}})$	1115.68	$\bar{\Lambda} \rightarrow \bar{p} + \pi^+$	63.9	7.89
$\Xi^-(\text{dss})$	1321.71	$\Xi^- \rightarrow \Lambda + \pi^-$	99.887	4.91
$\Xi^+(\overline{\text{dss}})$	1321.71	$\Xi^+ \rightarrow \bar{\Lambda} + \pi^+$	99.887	4.91
$\Omega^-(\text{sss})$	1672.45	$\Omega^- \rightarrow \Lambda + K^-$	67.8	2.46
$\bar{\Omega}^+(\overline{\text{sss}})$	1672.45	$\bar{\Omega}^+ \rightarrow \bar{\Lambda} + K^+$	67.8	2.46

of the Ξ^- this is equal to 4.91 cm (for a momentum equal to m_{Ξ}). The most probable (B.R. = 99.887%) decay channel for the Ξ^- is into a Λ (that contains only one strange quark) and a charged pion π^- (to conserve the electric charge). This latter particle is usually called *bachelor*. The Λ in turn undergoes a weak decay, with a $c\tau$ of 7.89 cm (for a momentum equal to m_{Λ}). In 63.9% of the cases the Λ decays into a pair of particles with opposed electric charge, a proton and a second π^- . This pair is usually referred to as a V^0 for the characteristic topology of the two opposite charge daughter tracks.

The other three charged hyperons follow the same topology during their decay. The only changes are the presence of the antiparticles and the fact that the bachelor in the case of the Ω is a K and not a π .

As anticipated in Section 3.2.1 the main tracking detectors of the ALICE apparatus are the ITS and the TPC. Figure 41 shows the decay topology of such particles with respect to these detectors. The upper panel shows three different views of a Pb–Pb collision measured during the 2010 run, obtained using the ALICE Event Display software. A Ξ^- candidate has been highlighted, removing the background tracks in the cascade angular region. Similar views are shown for a pp collision in the lower panel.

These images tell us that the cascades cannot be directly detected, because of their short decay length (Table 6) compared to the position of the tracking

x_0 or greater is: $P(x_0) = \exp(-mcx_0/c\tau|\vec{p}|)$. The decay length is then defined as the distance, $c\tau$, travelled by a particle with velocity c in the mean decay lifetime. In the laboratory frame it is equal to $(c\tau)_{\text{lab}} = (|\vec{p}|/mc) \cdot c\tau$. In the following the $c\tau$ is meant to be expressed in the laboratory frame. In Sections 5.3.6 and 6.3.6 the measurement of $c\tau$ has been used as a consistency check for the analysis.

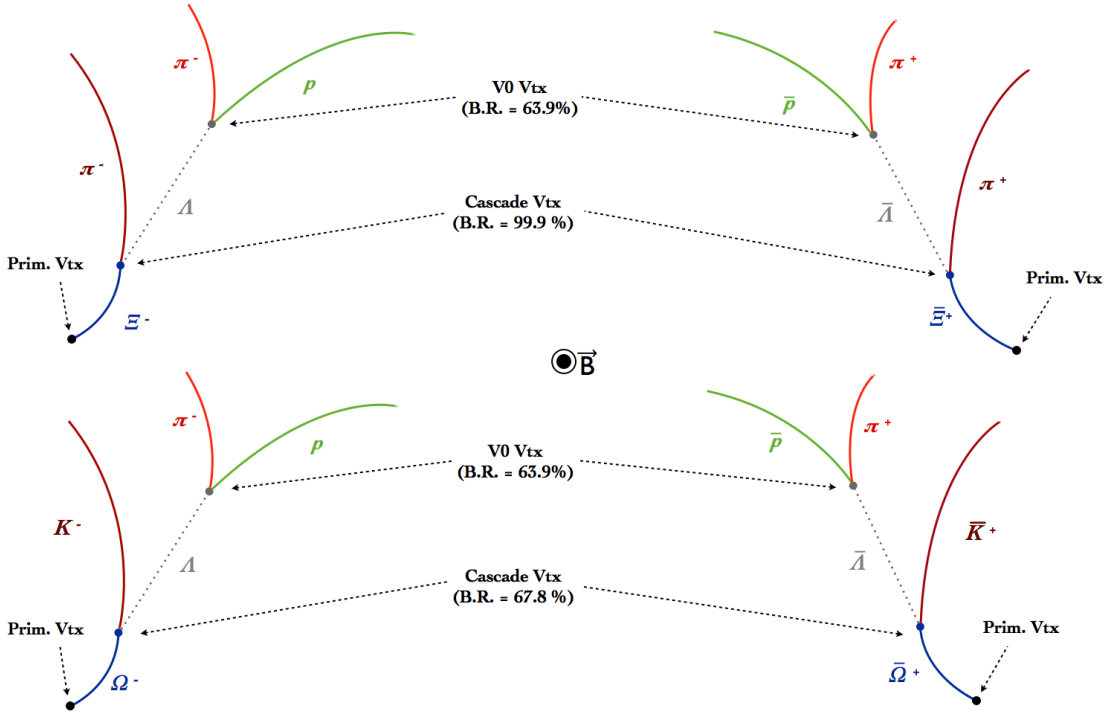


Figure 40: The characteristic *cascade* decay for the charged multi-strange baryons in a magnetic field. The upper part of the plot depicts the Ξ^- and the Ξ^+ decays, while the lower part shows the Ω^- and the Ω^+ decays.

Table 6: Decay length in the laboratory frame for three different values of the total momentum for Ξ and Ω .

	$ \vec{p} = 1 \text{ GeV}/c$	$ \vec{p} = mc$	$ \vec{p} = 3 \text{ GeV}/c$
decay length for Ξ (cm)	3.71	4.91	11.15
decay length for Ω (cm)	1.47	2.46	4.41

detectors³ (3.9 and 7.6 cm, respectively for the two layers of the SPD). The Λ is a neutral particle, and as such cannot be tracked. Practically only the final charged products of the decays need to be reconstructed and identified: the bachelor track and the track pair from the V^0 .

³ Note that, while it is possible that the cascades leaves a hit in the innermost SPD layer, this would not be enough to do tracking and thus this possibility was not explored in this work.

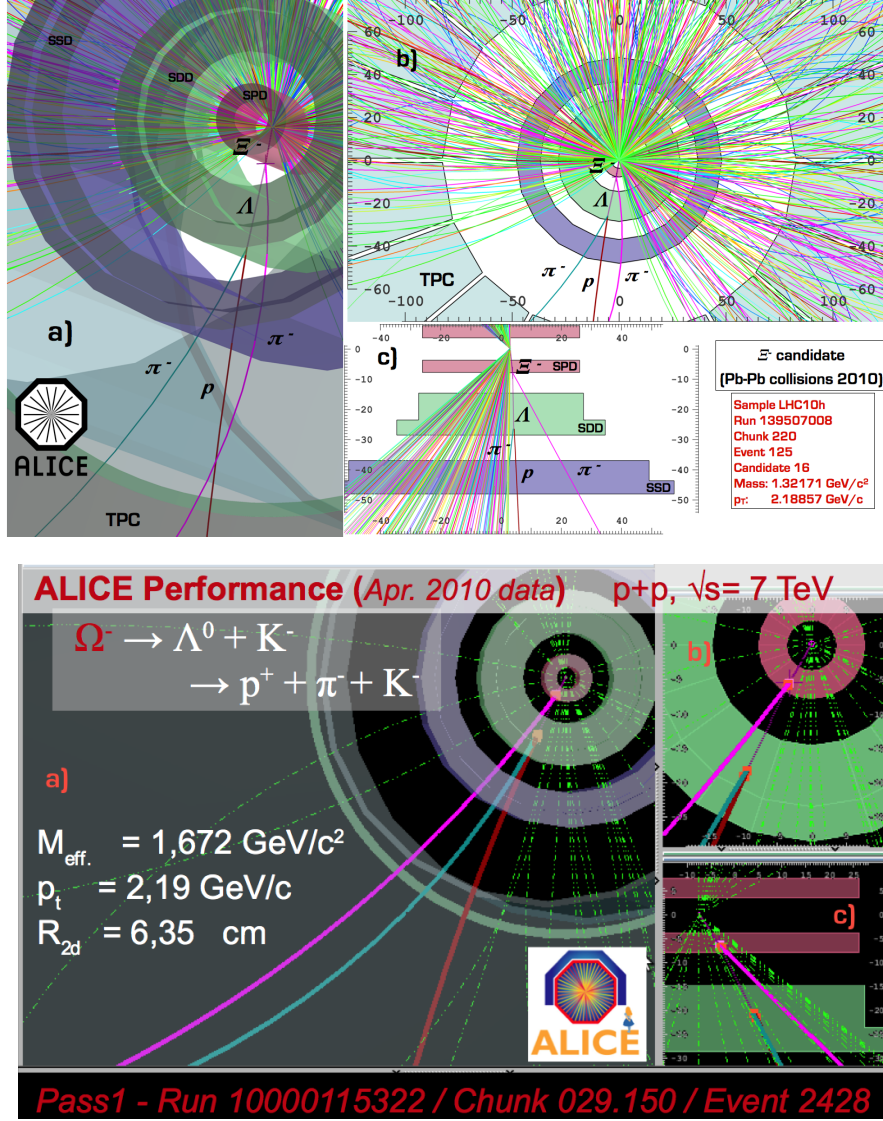


Figure 41: (Upper panel) ALICE Event Display of a Pb–Pb collision, registered during the 2010 run, where a selected Ξ^- candidate is highlighted removing the high number of tracks, typical of the high multiplicity Pb–Pb event. (Lower panel) ALICE Event Display of a pp collision, registered during the 2010 run, where a selected Ω^- candidate is highlighted. In both cases, three different prospects of the event are given a) 3D view, b) XY plane, perpendicular to the beam line, c) ZY plane, along the beam line.

4.2 TOPOLOGICAL RECONSTRUCTION

The reconstruction technique adopted in ALICE for the cascades starts from the assumption that all (or most of) the charged secondary particles⁴ can be tracked. Starting from the reconstruction of Λ (from the V^0 candidates), this is associated to a bachelor track, obtaining the cascade candidate. This technique is known as *topological reconstruction* because the particle association to get the Λ or the cascade is based on geometrical and kinematical criteria. The daughter tracks have to fulfill a set of geometrical and kinematical conditions (selection criteria).

In this Chapter the meaning of the topological cuts and details of the reconstruction technique are given. The chosen values for these variables and the corresponding motivations will be given in the next two Chapters 5 and 6 for analysis in Pb–Pb and pp collisions respectively. The adopted set of variable are depicted in Figure 42. Let's see how and when the selection cuts are applied, following the two steps of the topological reconstruction.

The V^0 finding proceeds combining each secondary track with all the other secondary tracks having an opposite charge. Two distinct cuts are applied on the minimum value of the impact parameters to the primary vertex for the two opposite charged tracks (panel [a] in Figure 42), to ensure that these are secondary particles. Such pair of tracks is also rejected if the distance of closest approach (DCA, again panel [a]) in space between the two tracks is larger than a given value⁵. Once the V^0 vertex position is defined, only the vertices inside a given fiducial volume are kept (panel [b] in Figure 42); the inner boundary of this fiducial area is limited in order to keep track density and number of miscombinations low. Finally, the V^0 finding procedure checks whether the momentum vector of the V^0 ⁶ candidate does not point back to the cascade vertex. This is performed applying a cut on the cosine of the angle between the V^0 momentum vector and a vector connecting the cascade vertex to the V^0 vertex position (pointing angle, panel [c] in Figure 42); this ensures that the selected V^0 comes from the cascade vertex.

⁴ These are all the particles that do not come from the primary vertex (that is the interaction vertex), and are selected looking at the impact parameter (the perpendicular distance between the prolongation of the path of the particle and a selected point) with respect to the primary vertex.

⁵ The resolution on the DCA is strongly dependent on the resolution of the tracking: the variable by construction is a normalized distance obtained weighting the transverse longitudinal components by the corresponding resolutions.

⁶ The momentum vector of the V^0 is evaluated extrapolating the two tracks of this candidate to the points of the DCA and summing the track momenta vectors taken at those points.

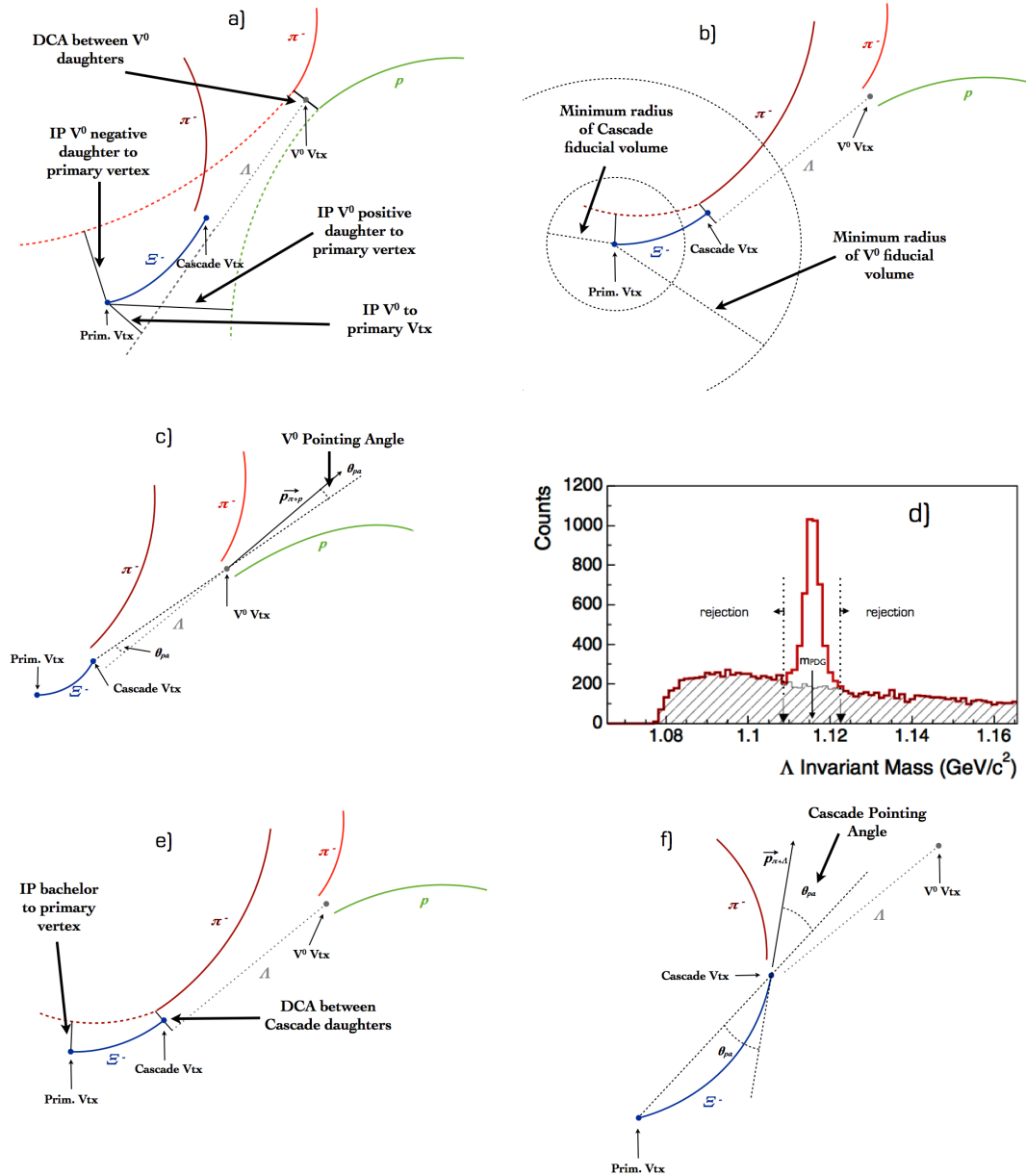


Figure 42: Definition of V^0 and cascade cut variables. In these representations of the cascade decay, the tracks in the vertices are artificially displaced to represent the uncertainty in the track reconstruction.

Then the invariant mass of the V^0 is calculated, under the hypothesis of a Λ or an $\bar{\Lambda}$. The squared mass value for each single candidate, in the case of a true Λ particle, from the kinematic equation, is given by:

$$M_{\text{theor}}^2(\Lambda) = (E_{\pi^-} + E_p)^2 - (\vec{p}_{\pi^-} + \vec{p}_p)^2. \quad (4.1)$$

A similar expression gives the squared mass in the hypothesis of the $\bar{\Lambda}$, where the tracks are a π^+ and an \bar{p} . Experimentally one has to measure the invariant mass starting from the measurement of the two daughter tracks. This can be done using the following quantity:

$$M_{\text{experimental}}^2(\Lambda) = \left(\sqrt{m_{\pi^-}^2 + \vec{p}_{\text{neg}}^2} + \sqrt{m_p^2 + \vec{p}_{\text{pos}}^2} \right)^2 - (\vec{p}_{\text{neg}} + \vec{p}_{\text{pos}})^2, \quad (4.2)$$

where an hypothesis on the nature of the V^0 has been done (Λ in this case), namely an hypothesis on the mass of the two charged daughters (π^- and p in this case). The measured momenta for the V^0 decay tracks have been used (\vec{p}_{neg} and \vec{p}_{pos}). A similar expression for the squared mass in the hypothesis of the $\bar{\Lambda}$ can be obtained, changing the hypothesis on the mass of two charged daughters (π^+ and \bar{p}). Due to limited measurement accuracy, the reconstructed invariant masses for true Λ will be distributed in a peak structure for which the width is determined by detector resolution.

At the end, a last selection is performed applying a window in the invariant mass distribution for the V^0 candidates, around the nominal mass value of the Λ , $m_0 = 1115.68 \text{ MeV}/c^2$ (panel [d] in Figure 42). The resolution of the V^0 daughters transverse momentum constrains this window to be as large as about $10 \text{ MeV}/c^2$.

A similar procedure is adopted to identify the cascades. The V^0 candidates found within the Λ mass window are combined with all possible secondary tracks (bachelor candidates). The impact parameter (panel [e] in Figure 42) of the bachelor must be large enough to have a good rejection of primary particles. A V^0 -bachelor association is accepted if the distance of closest approach (DCA, panel [e] in Figure 42) between the bachelor track and the V^0 mother trajectory (straight line) is small enough.

Finally, a selection on the pointing angle of the cascade candidate (panel [f] in Figure 42) is applied to check whether this candidate points back to the primary vertex. Also the cascade finding is limited to a fiducial region (pane [b] in Figure 42) as done for V^0 reconstruction, and the final request is that the V^0 vertex is further away than the cascade vertex from the primary vertex, simply for causality reason.

At this level, the three tracks that pass all the previous selections could be the decay products of a real cascade or a combination of tracks that simulates the

topology of a cascade decay without being correlated, and compose the combinatorial background. With the final goal to separate the signal from the background one can perform a new invariant mass computation for these candidates.

One can separate the candidates into two groups, depending on the electric charge of the bachelor, corresponding to a $\Xi^-(\Omega^-)$ in case of a negative sign and to a $\Xi^+(\bar{\Omega}^+)$ in case of a positive sign. In the first case, the squared masses for the Ξ^- and Ω^- candidates are given by the following formulas:

$$M_{\text{experimental}}^2(\Xi^-) = \left(\sqrt{m_\Lambda^2 + \vec{p}_{V^0}^2} + \sqrt{m_{\pi^-}^2 + \vec{p}_{\text{bach}}^2} \right)^2 - (\vec{p}_{V^0} + \vec{p}_{\text{bach}})^2, \quad (4.3)$$

$$M_{\text{experimental}}^2(\Omega^-) = \left(\sqrt{m_\Lambda^2 + \vec{p}_{V^0}^2} + \sqrt{m_{K^-}^2 + \vec{p}_{\text{bach}}^2} \right)^2 - (\vec{p}_{V^0} + \vec{p}_{\text{bach}})^2, \quad (4.4)$$

with $\vec{p}_{V^0} = \vec{p}_{\text{neg}} + \vec{p}_{\text{pos}}$, where \vec{p}_{bach} , \vec{p}_{neg} and \vec{p}_{pos} are the measured momenta of the three considered tracks. Similarly, in the second case, the squared mass for a Ξ^+ candidate and for an $\bar{\Omega}^+$ candidate can be obtained using the Λ mass hypothesis for the V^0 candidates and the π^+ (for Ξ^+ decays) and K^+ (for $\bar{\Omega}^+$ decays) mass hypothesis for the bachelor. Let us underline that the value of the Λ mass used in this calculation is not the measured one, but the nominal PDG mass (Table 5). In this way the effect of the experimental resolution on the invariant mass determination for the Ξ and Ω is limited.

4.3 RECONSTRUCTION IN PP AND PB–PB ENVIRONMENTS

As anticipated, in the next two Chapters, 5 and 6, the analysis on the multi-strange baryons in Pb–Pb and pp collisions, respectively, will be described, starting from invariant mass distributions.

Looking at the two panels in Figure 41, one can clearly see the differences in the environments between the two kinds of collisions. The Pb–Pb collisions are characterized by a large amount of reconstructed tracks, corresponding to the large amount of particles produced during the collision. On the other side the pp collision is clearer, with only a few produced particles. The charged particle density ($dN_{\text{ch}}/d\eta$) at mid-rapidity ($|\eta| < 0.5$) has been measured by the Collaboration and is of almost 1600 tracks for a central Pb–Pb collision at $\sqrt{s_{\text{NN}}} = 2.76$ TeV [122]. For comparison, the charged particle density is of only 3 to 6 tracks in pp collisions in the energy range from 0.9 to 7 TeV (in $|\eta| < 1$) [123].

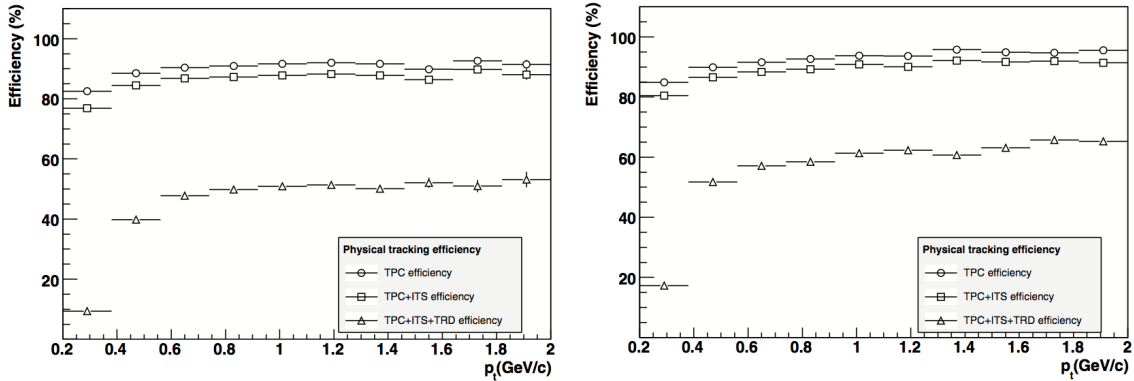


Figure 43: Physical track-finding efficiency (defined as the efficiency that includes also all other factors such as dead zones in the detectors, inefficiency of the electronics, decays, etc.) for different combinations of the tracking detectors. (Left) For central Pb–Pb collisions. (Right) For pp collisions. [119]

ALICE has been built to be highly performant in a high track density environment. The TPC-only tracking efficiency is weakly dependent on the multiplicity of tracks (variations within 5%). The tracking efficiency in simulated Pb–Pb (left Panel) and pp (right Panel) collisions are shown in Figure 43.

The main limitations to the multi-strange analysis come from the environment. The higher number of tracks in Pb–Pb collisions with respect to pp collisions leads to a higher background level which comes from fortuitous construction of cascade candidates that do not correspond to physical particles. These are due to random coincidence in the space between the available tracks. On the other hand the worse primary vertex determination in pp collisions (resolution in the transverse plane $\approx 150 \mu\text{m}$ for pp collisions and $\approx 50 \mu\text{m}$ for Pb–Pb collisions), could introduce biases in the determination of the DCA and the cosine of pointing angle.

The values of the topological selections introduced to identify the cascades, should then be adapted for the two environments. In this analysis, as will be described in the next Chapters, the criteria adopted to determine the values of the topological selections correspond to a compromise between the best signal over background ratio and the minimization of the signal loss.

5

MULTI-STRANGE BARYON ANALYSIS IN Pb–Pb COLLISIONS

5.1 DATA SAMPLE AND EVENT SELECTION

The data used for this analysis were collected during the December 2010 Pb–Pb run (LHC10h period, pass 2 reconstruction¹). The full sample consists of 171 runs with a total of about $83 \cdot 10^6$ events. Out of these, only 93 runs have been used, which have been marked by the Collaboration as “good runs” for the central barrel: by definition, they are characterized by good performance of the detectors and good running conditions (e.g. low level of beam induced background). In particular, all these “good runs” have both the TPC and all the ITS sub-detectors turned on².

The purpose of the event selection is to select hadronic interactions with the highest possible efficiency, while rejecting the machine-induced and physical backgrounds. The ALICE on-line minimum bias (MB) trigger for this Pb–Pb run was configured to require at least two out of the following three conditions:

- (I) at least two pixel chips hit in the outer layer of the SPD,
- (II) a signal above the threshold in VZERO-A,
- (III) a signal above the threshold in VZERO-C.

¹ A few reconstruction processes are needed to obtain data usable for physics analysis. Usually the first two reconstruction passes (pass 0 and pass 1) are needed for quality assurance check and calibration of the main detectors. The pass 2 is the first usable reconstruction for analysis purpose. Further passes are needed to implement signals from detectors requiring special calibrations.

² Out of the remaining 78 runs flagged as “bad” by the Collaboration, 62 runs are actually not really bad for this analysis; the performances of the detectors involved in the specific measurement are indeed not changed. See also Note 5 in this Chapter.

The threshold in the VZERO detector corresponds approximately to the energy deposition of a minimum ionizing particle. In addition to the previous conditions, a further coincidence with two beam bunch crossing in the ALICE interaction point is requested³.

Two different sources of machine-induced background (MIB) can be identified. As a first case, MIB can be caused by beam ions interacting with the residual gas in the beam pipe (beam-gas) or by ions in the halo of the beam interacting with mechanical structures in the machine; these events can be eliminated from the triggered event sample using the VZERO timing information (coincidence of the VZERO-A and VZERO-C signals). The second source of background is due to parasitic collisions from debunched ions. The radio-frequency (RF) structure of the LHC is such that there are 10 RF “buckets” within a 25 ns bunch, spaced by 2.5 ns. Only one of them should be populated by ions. However, sometimes it happens that the ions “jump” into one of the neighboring buckets. This causes a displacement in the vertex position of $(2.5 \text{ ns}/2) \cdot c = 37.5 \text{ cm}$. Those events have to be considered as background and are rejected using the correlation between the sum and the difference of times measured in the ZDC.

The strong electro-magnetic fields generated by the heavy-ions moving at relativistic velocity lead to huge cross-sections for QED processes. This is the main physical background, and needs to be rejected to isolate hadronic interactions. The corresponding events can be classified into several processes: QED pairs, nuclear dissociation and photo-production. All these processes are characterized by soft particles production and low multiplicity at mid-rapidity. A minimal energy deposit (of about 500 GeV) in the ZDCs is also required to further suppress these electromagnetic interactions.

Further off-line selections, based on the status of the primary vertex, have been applied. Only those events for which the primary vertex has been determined using at least two out of the three different techniques (SPD tracklets, TPC-only tracks and global tracks) are selected. In addition, only events with a primary vertex position within 10 cm from the centre of the detector along the beam line were selected. This ensures good rapidity coverage and uniformity for the particle reconstruction efficiency in the ITS and TPC tracking volume.

³ ALICE has been equipped with two Beam Pickup for Timing of eXperiments (BPTX) to monitor the timing of the LHC machine. The BPTX stations are composed of four electrostatic button pick-up detectors, sensitive to the passage of charge distributions and arranged symmetrically in the transverse plane around the LHC beam pipe. The phase of the LHC clock is measured with respect to BPTX signal using Beam Phase and Intensity Monitor (BPIM) boards and adjusted (to compensate the seasonal drift of the LHC clock) at the beginning of each fill using the Clocks & ORbits DElay (CORDE) board with a precision of 10 ps. This is necessary for time of flight measurements which aim for final precision better than 50 ps. [124]

In order to study the centrality dependence of multi-strange baryon production, these events were divided into five centrality classes according to the fraction of the total inelastic collision cross-section: 0 – 10%, 10 – 20%, 20 – 40%, 40 – 60% and 60 – 80%. The definition of the event centrality is based on the sum of the amplitudes measured in the VZERO detectors, as described in Section 3.2.7. The final sample in the 0 – 80% centrality range corresponds to approximately $15.5 \cdot 10^6$ Pb–Pb collisions at $\sqrt{s_{\text{NN}}} = 2.76$ TeV.

Monte Carlo productions have been used to correct the real data for acceptance and efficiency and to check the efficiency calculation. A first MC sample has been generated using HIJING with each event being enriched by one hyperon of each species, generated with flat θ ⁴ and p_T distributions. The “enriched” events were then processed with the same reconstruction chain used for the real data events.

An additional enriched HIJING sample has been produced with events only in the centrality range 0 – 20%, in order to get results in 10% wide centrality bins for the most central events.

Finally, a pure HIJING sample was also produced in order to compare the efficiency with that computed on the enriched sample and make sure that the injection of particles does not affect the efficiency significantly.

These productions are anchored to 155 runs⁵ from LHC10h real data. The whole statistics was used, since a comparison of the efficiencies in good runs (the 93 runs used in the experimental data) and that in bad runs showed no significant difference (Section 5.3.2).

The statistics after event selection (the same adopted for the experimental data) for the three samples correspond to about $2.7 \cdot 10^6$ enriched HIJING with events in 0 – 90% centrality, $0.72 \cdot 10^6$ enriched HIJING with events in 0 – 20% centrality and $0.495 \cdot 10^6$ pure HIJING events.

5.2 TOPOLOGICAL CUTS AND INVARIANT MASS DISTRIBUTION

The analysis was performed using two tasks, written in C++ and compatible with the Aliroot framework:

⁴ θ is the polar angle (for further info, the definition of the ALICE global coordinate system is given in Section 3.2.1).

⁵ “To anchor” a MC production to an experimental sample means adopt, run by run, the same detector conditions, e.g. the calibrations. The usage of 155 runs in these MC productions is consistent because, as already observed (Note 2, this Chapter), the large part of the events in the “bad” flagged runs have indeed similar detector performance to the “good” runs.

AliAnalysisTaskCheckCascadePbPb: this task handles the experimental data for raw yield extraction and for the optimization of topological selections;

AliAnalysisTaskCheckPerformanceCascadePbPb: this task handles MC data for a performance study of cascade identification and for acceptance-efficiency correction calculations.

The main object produced by these two analysis tasks is the `AliCFContainer`. This is a container structured as a grid of arrays with n steps and m variables, that has an easy way to handle cuts on variables. In this analysis such object has been used to hold information characterizing the reconstructed cascade candidates such as the topological variables needed for the study of the selection cuts and the particle properties (invariant mass, p_T , rapidity y , centrality) needed to produce the spectra and apply all the corrections.

As described in Section 4.2, candidates are found by combining charged tracks reconstructed in the ITS and TPC volume and imposing topological and kinematic restrictions, first to select the V^0 and then to match it with one of the remaining secondary tracks (“bachelor” candidate). All the cuts are fine-tuned in the final analysis in order to find the best compromise between the combinatorial background minimization and the significance of the signals. In Table 7 the values in the last column are the cut values optimized at the analysis level. These values have been chosen and validated via a quality assurance study which will be described in detail in the following.

In addition, all candidates falling within a $\pm 8 \text{ MeV}/c^2$ region around the Ξ PDG mass are rejected to avoid Ξ contamination in the Ω analysis. The two-dimensional distribution (shown in Figure 44) has been obtained measuring the invariant mass in the Ξ mass hypothesis (assuming a π as a bachelor) for the three charged tracks, correlated to the invariant mass measured in the Ω mass hypothesis. These candidates are compatible with the Ξ mass hypothesis and then are rejected from the Omega candidate sample.

The PID information from the TPC ($n_\sigma = 4$, Section 3.2.6) is also applied to the daughter tracks to reduce the background; in addition candidates are rejected if at least one daughter track does not satisfy the following quality conditions:

1. the track has the TPC refit flag active, which means that its parameters have been successfully determined also in the third stage of the tracking reconstruction (Figure 36);
2. the track has at least 70 clusters in the TPC (out of a maximum of 159 clusters), intended to guarantee a good p_T resolution and a quite stable PID using the dE/dx in the TPC.

Table 7: Summary of the selection cuts utilized for cascade candidate selection. The values tightened at the analysis level are highlighted in grey. A clarification on the dimension of the DCA between V^0 daughters variable has been given in the Note 5 in Chapter 4.

Cuts on Cascades	Value for Pb–Pb reconstruction	Optimized value for Pb–Pb analysis
Min Allowed V^0 ip (cm)	0.05	0.1
Window around the Λ mass (GeV/c^2)	± 0.008	± 0.005
Min allowed bachelor ip (cm)	0.03	0.03
Max allowed DCA Ξ daugh (cm)	0.3	0.3
Min allowed cos of cascade PA	0.999	0.9992
Min radius of the fid. vol. (cm)	0.9	1.5 (Ξ) 1.0 (Ω)
Max radius of the fid. vol. (cm)	100.	100.
Cuts on V^0 s		
Min allowed ip for 1° daught (cm)	0.1	0.1
Min allowed ip for 2° daught (cm)	0.1	0.1
Max allowed DCA between daught. tracks (cm)	1.0	0.8
Min allowed cosine of V^0 's PA	0.998	0.998
Min radius of fiducial volume (cm)	0.9	3.0
Max radius of fiducial volume (cm)	100.	100.
Added cuts		
Window around the Ξ mass value for Ω (GeV/c^2)	-	± 0.008
Maximum decay length (cm)	-	15 (Ξ) 8 (Ω)

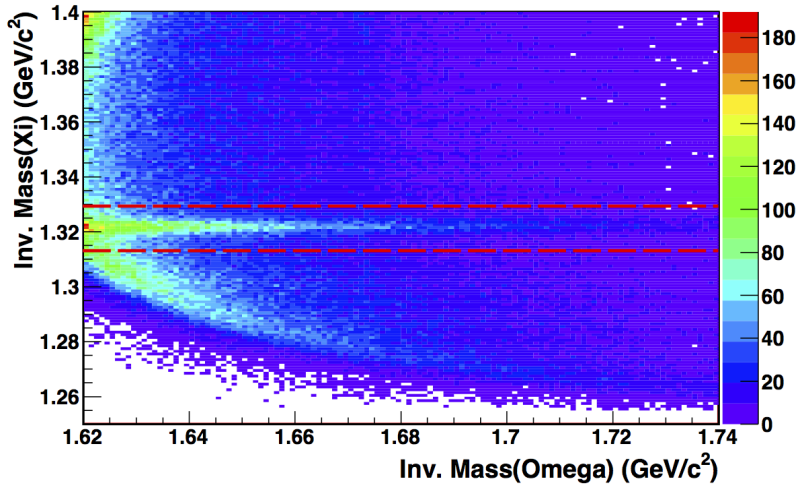


Figure 44: Invariant mass values for Ω^- candidates plotted against the invariant mass values obtained in the Ξ mass hypothesis in the Ω^- reconstruction.

Table 8: Values of signal (S) and background (B) reduction after the $c\tau$ cut (ΔS and ΔB), and corresponding variations of the signal-to-background and significance ratios. These values have been obtained from the real data invariant mass distributions, extracting the signal and the background in the peak region as described in the text.

Ξ	$\Delta S/S$ (%)	$\Delta B/B$ (%)	S/B (w/o cut)	S/B (w cut)	$S/\sqrt{S+B}$ (w/o cut)	$S/\sqrt{S+B}$ (w cut)
$p_T < 2 \text{ GeV}/c$	-3.1	-12.3	4.1	4.5	144.3	144.4
$p_T > 2 \text{ GeV}/c$	-0.7	-5.1	3.4	3.5	141.6	141.9
Ω	$\Delta S/S$ (%)	$\Delta B/B$ (%)	S/B (w/o cut)	S/B (w cut)	$S/\sqrt{S+B}$ (w/o cut)	$S/\sqrt{S+B}$ (w cut)
$p_T < 2 \text{ GeV}/c$	-7.3	-31.1	0.75	1.0	23.8	24.8
$p_T > 2 \text{ GeV}/c$	-6.2	-12.7	0.72	0.77	35.4	35.0

These cuts based on TPC track informations effectively exclude the possibility of reconstructing cascades at very low p_T ($p_{T\text{casc}} \leq 0.6 \text{ GeV}/c$). Below that p_T limit, most of the cascades would decay into low momentum tracks, reconstructed in the ITS only. However, the long life-time, especially for the Ξ and the Λ , allows this particles to cross many layers of the ITS, reducing the possibility that the daughters can be tracked with the ITS alone.

A cut on the decay length of each cascade was studied in order to remove candidates with a too long life time, hence not corresponding to real particles. The maximum acceptable values correspond to 3 times the $c\tau$ value (PDG value) for the two cascades. The effectiveness of this cut in two different ranges of momentum ($p_T > 2$ and $p_T < 2 \text{ GeV}/c$) can be inferred from Figure 45, for the two cascades, where the invariant mass distributions from the real data with and without the application of this cut are compared: even though the S/B ratio and the significance do not increase much (Table 8), this cut reduces the background (particularly for the Ω) without affecting the signal too much, and then improves the stability of the signal extraction procedure. The gain is more relevant at low p_T , as expected. The values shown in Table 8 have been obtained by fitting the invariant mass distribution as described in Section 5.3.1. All the other analysis cuts are applied in both cases. The cut has been also studied with a quality assurance (QA) analysis, as described in the following.

Quality Assurance (QA) analysis for the selection cuts

The distribution of all the variables used for the selection cuts are studied in detail in three steps. The following distributions are compared:

STEP A signal and background in MC;

STEP B background in experimental data and in MC;

STEP C signal in experimental data and in MC.

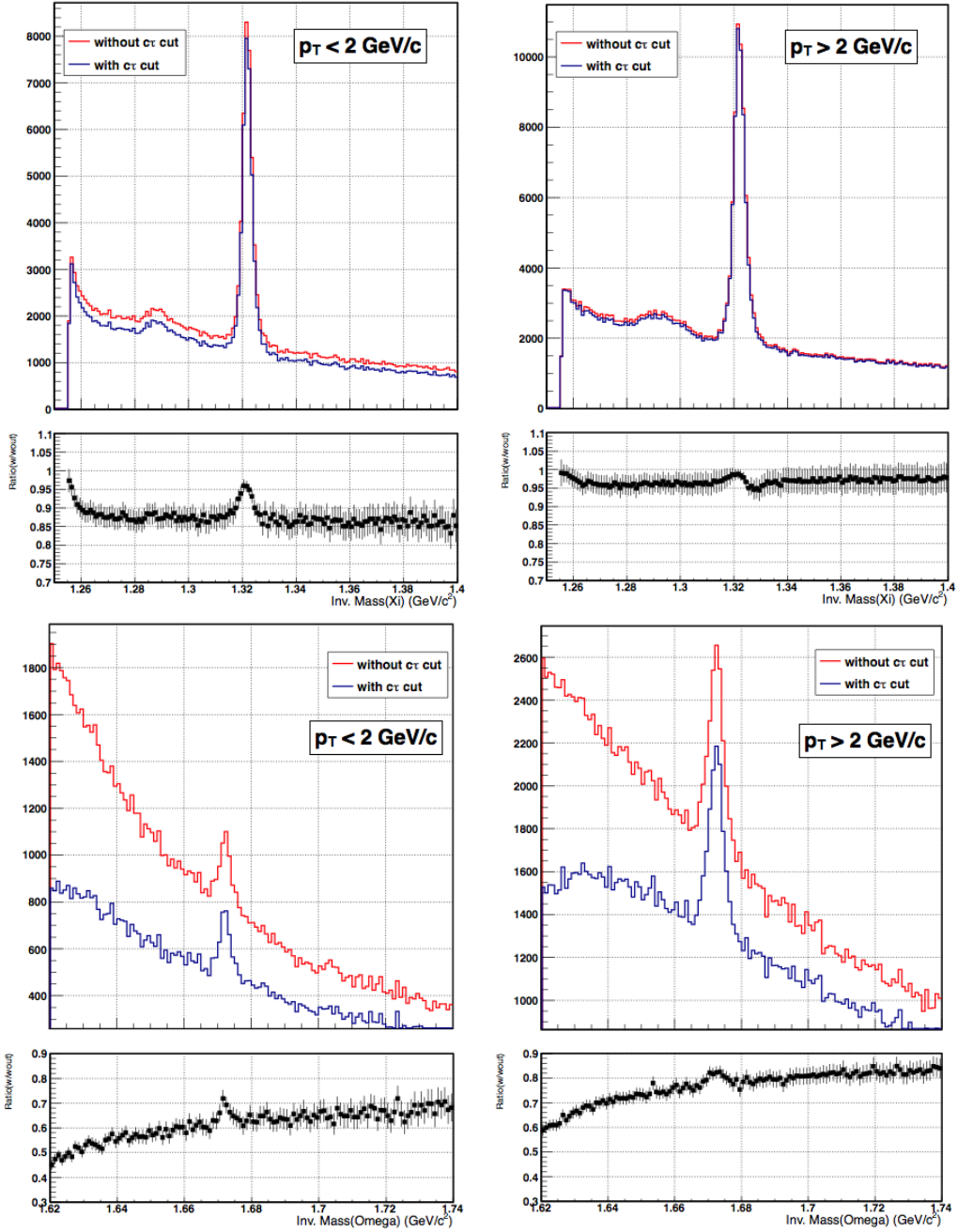


Figure 45: Comparisons of the invariant mass spectra for Ξ (top panels) and Ω (bottom panels) before and after the $c\tau$ cuts, with all the other cuts applied, for two different p_T ranges: low ($< 2 \text{ GeV}/c$, on the left) and high ($> 2 \text{ GeV}/c$, on the right). The bottom panels show the ratios between the invariant mass distributions with and without the cut on the decay length applied.

STEP A is performed to determine the effectiveness of each cut, in order to remove the largest fraction of the background while keeping as much signal as possible. STEP B and C are used to verify that the MC reasonably reproduces the experimental data distribution for the variables on which the cuts are applied. In particular, it has been carefully checked that compatible fractions of signal are removed both in experimental data and in the MC for each of the cuts applied in the final analysis, to avoid a bias in the results when applying the correction.

In STEP A, the distributions of each cut variable for the signal and the background are normalized to the corresponding number of entries and compared. In addition, the integral of the distributions as a function of the cut value is plotted to check the fraction of signal and background removed for any given value of the cut. The signal in this case consists of candidates which have been associated to a true cascade decay in the MC record. The background is obtained using the multi-dimensional container from which each variable can be projected applying cuts on other variables, with the following procedure (Figure 46):

1. define the peak region, by fitting the invariant mass distribution using a polynomial function plus a gaussian function (details on the fit procedure are reported in Section 5.3.1);
2. cut on the invariant mass coordinate in the container in the region defined above;
3. plot the distribution of a given variable, to get the peak (i.e. signal) distribution;
4. cut again on the invariant mass coordinate in the container, in a 10σ -wide region around the PDG mass of the cascade;
5. plot again the distribution of the variable, to get the distribution in a wider region around the peak;
6. subtract this distribution from the full one (for the same variable) to obtain what is assumed to be the background distribution.

In STEP B the two background distributions are obtained as described in STEP A. In STEP C the main assumption to extract the cut variable distributions for the signal is, as in STEP A, that the shape of background in the peak region is the same of the background outside. To obtain the signal distribution the following steps are needed:

- extract the background distribution in the region far from the peak, as described before, and normalize it to the number of entries;

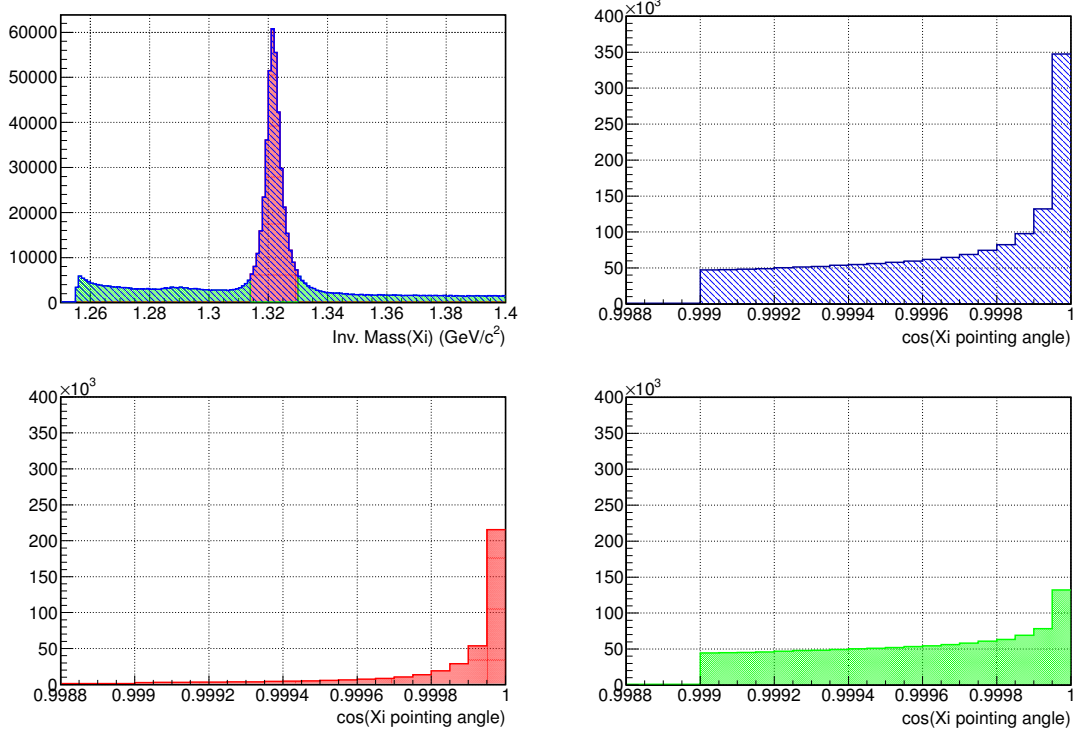


Figure 46: Example of invariant mass distribution with the signal (red) and background regions (green) (top left panel). The other pads show the distributions of the cosine of cascade pointing angle in the full region (blue), in the signal region (red) and in the background region (green).

- assuming this shape for the background in the peak region, the signal distribution is obtained by subtracting the normalized background in peak region distribution from the peak region distribution (that contains both signal and background).

The normalization factor for the background in the peak region is given by the measured background in the peak region of the invariant mass distribution, which is obtained from the real data with the procedure described in the signal extraction Section 5.3.1.

The cuts are studied first with their reconstruction values. Afterwards, when studying how to tighten the cut on one of the variables, all the other cuts (tuned or not) are applied. The analysis is performed in different p_T ranges: in this way the effect of a cut at low, medium and high transverse momentum can be compared.

In Figures 47-50 examples of STEP A of the QA procedure for four of the topological variables are shown. These variables are the cosine of pointing angle

of the Ξ candidates, the radius of fiducial volume of the Ξ candidates, the DCA of the V^0 daughters in a Ξ candidates and the decay length of the Ξ candidates respectively. As anticipated, the distributions of the variable for the signal (red) and for the background (blue) in the MC are reported in the left pads. The right pads show the corresponding integrated distributions. The dashed vertical lines indicate the value of the cut chosen for the analysis. In addition, in Figures 51-54 examples of STEP C of the QA procedure for the same four topological variables are shown. In the left pads the distributions of the variable for the signal in the real data (blue) and in the MC (red) are reported. In the right pads the corresponding integrated distributions are reported. The dashed vertical lines indicate the value of the cut chosen for the analysis. Examples of plots for STEP B of the QA procedure are not reported. Indeed in the present analysis the background is estimated directly on the real data and the comparison with the MC distribution, while being an additional consistency check, is much less crucial than for the signal (STEP C).

In some cases, as for the cosine of pointing angle (Figure 47), a cut behaves differently in different p_T regions. These dependencies have not been considered in the final set of values, since considering these dependencies would have produced limited improvements in the significance of the extracted signal. In Figures 51 and 54 it can be seen that the MC distributions, in the STEP C, agrees quite well the real data distributions. Even if there is a discrepancy between data and MC in the high p_T range (likely due to the different p_T distributions in the two samples), the cut is safe enough to avoid biases in the corresponding correction.

The cut values obtained as result of this study are reported in Table 7 both for Ξ and Ω . From the STEPs B and C, no anomalies have been observed in the behaviour of real and MC data for the chosen values.

To conclude, the effect of the cut optimization is shown in the invariant mass distributions in Figure 55, where the black line corresponds to the set of reconstruction cut values and the coloured line to the analysis ones (TPC PID is applied in both cases): the background is reduced by more than 50% and 60% for the Ξ and the Ω respectively, while the signal decreases by 15% and 20% respectively.

In Figure 56, the invariant mass distributions for Ξ^- and Ω^- are shown in six centrality bins (0 – 5%, 5 – 10%, 10 – 20%, 20 – 30%, 30 – 50% and 50 – 90%). As expected, the background decreases when going from central to peripheral collisions.

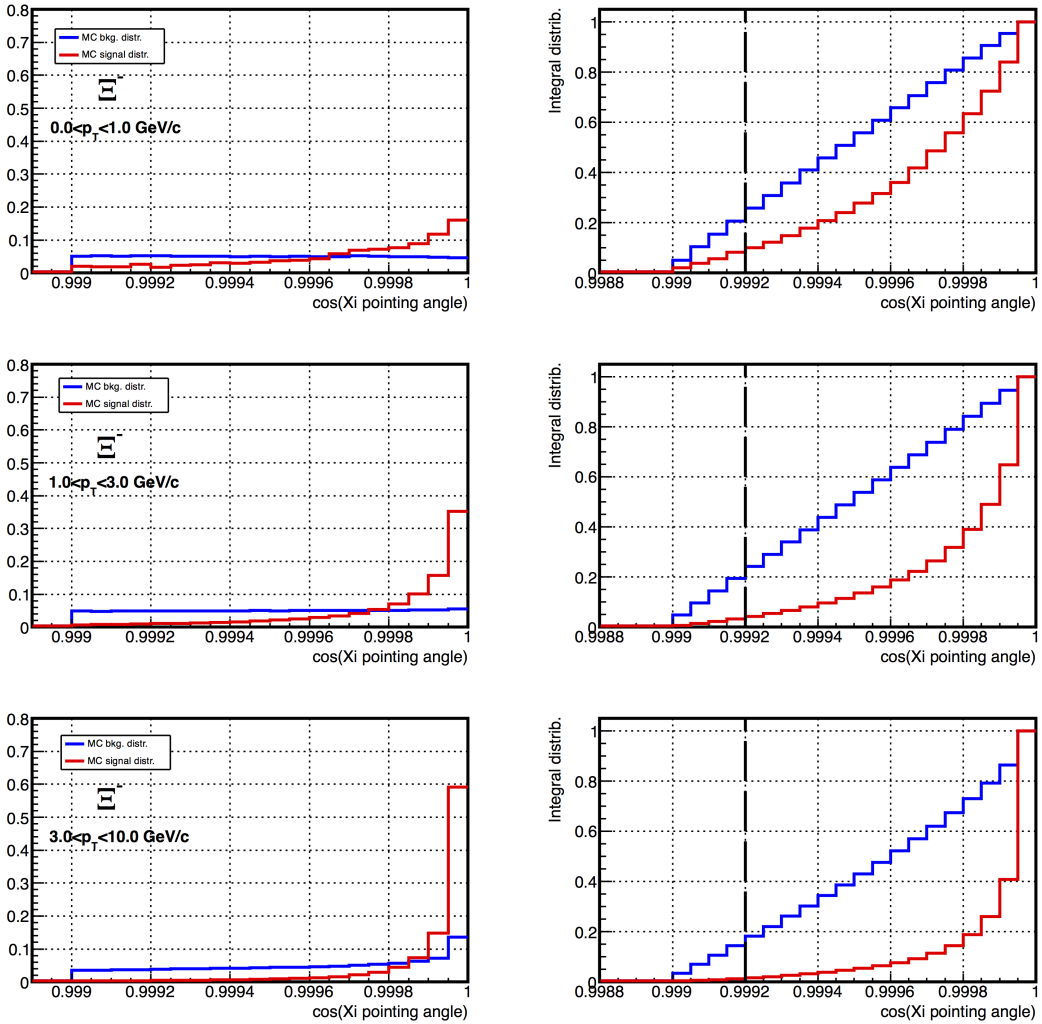


Figure 47: QA plots, STEP A, for the cosine of pointing angle for the Ξ^- , shown in 3 p_T intervals. On the left pad the background distribution (in blue) and the signal distribution (in red) from the MC are compared. On the right pad the corresponding integrated distributions are shown. The dashed lines indicate the value of the cut chosen for the analysis.

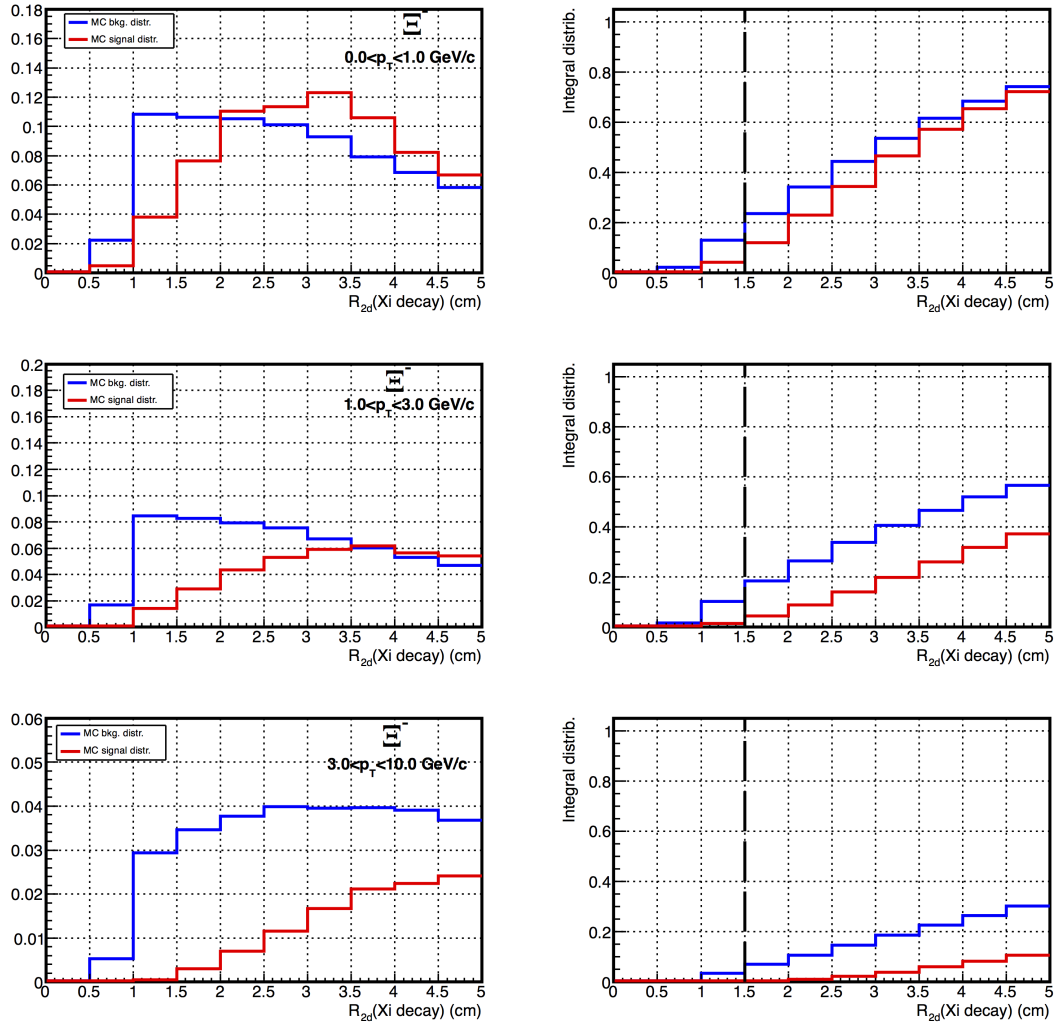


Figure 48: QA plots, STEP A, for the fiducial radius in the transverse plane for Ξ , shown in 3 p_T intervals. On the left pad the background distribution (in blue) and the signal distribution (in red) from the MC are compared. On the right pad the corresponding integrated distributions are shown. The dashed lines indicate the value of the cut chosen for the analysis.

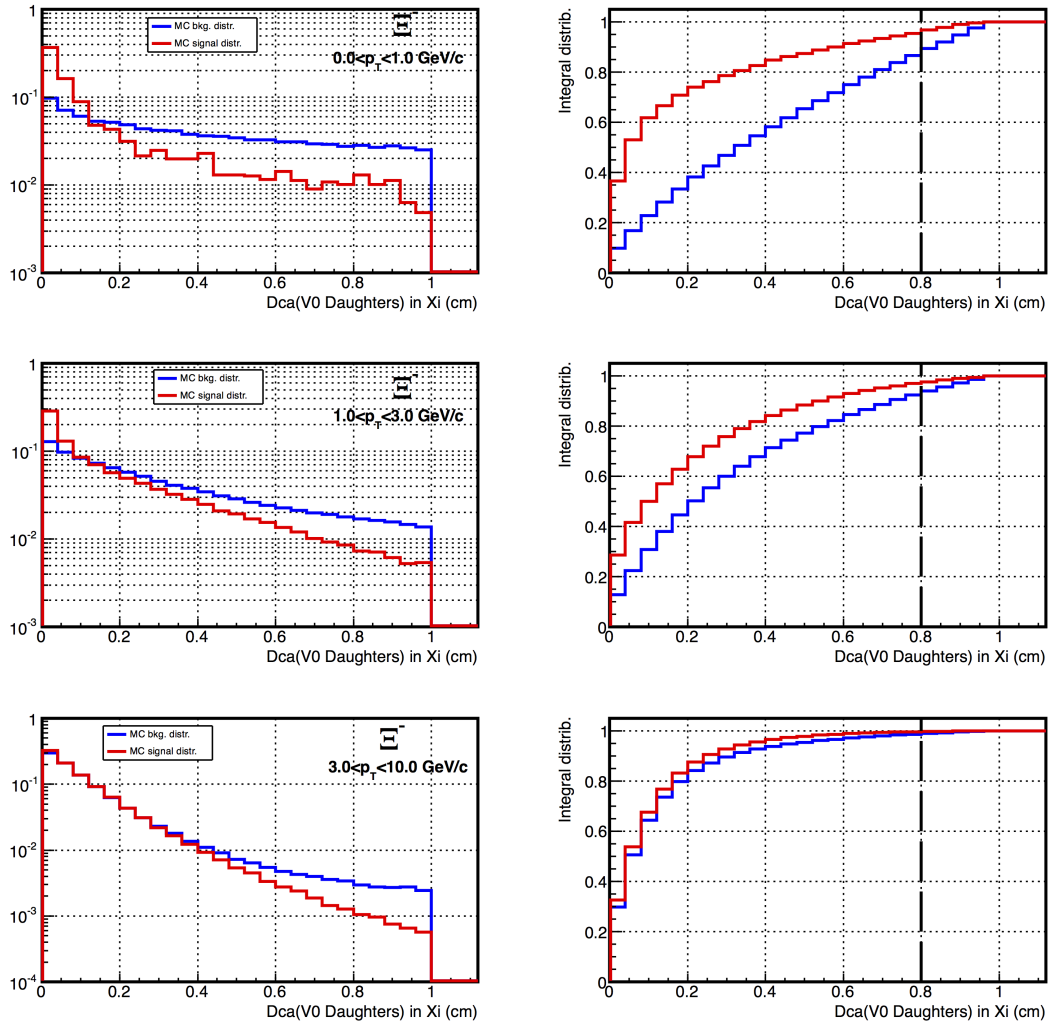


Figure 49: QA plots, STEP A, for the DCA between the V⁰ daughters, shown in 3 p_T intervals. On the left pad the background distribution (in blue) and the signal distribution (in red) from the MC are compared. On the right pad the corresponding integrated distributions are shown. The dashed lines indicate the value of the cut chosen for the analysis. A clarification on the dimension of such a variable has been given in the Note 5 in Chapter 4.

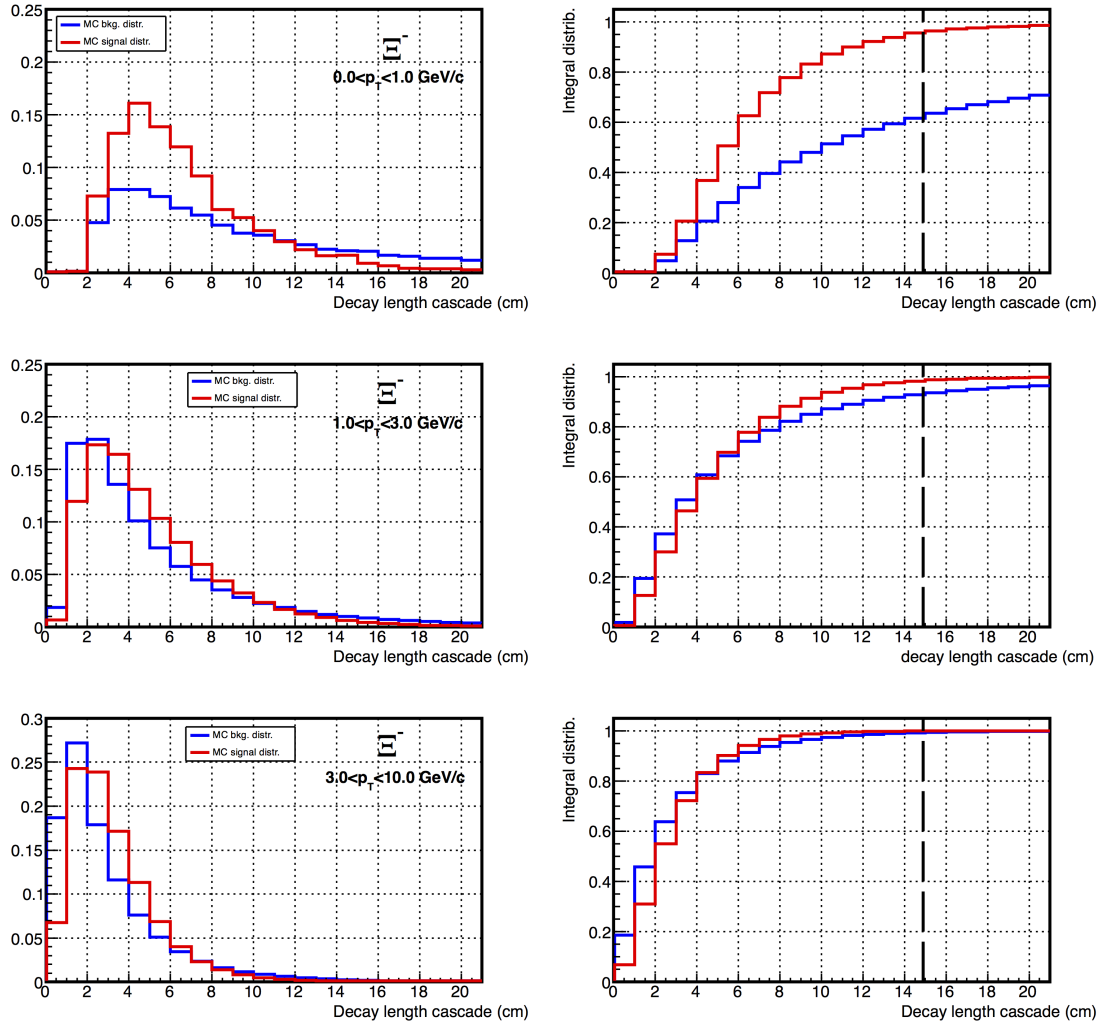


Figure 50: QA plots, STEP A, for the decay length distribution of the Ξ^- in 3 different p_T intervals. On the left pad the background distribution (in blue) and the signal distribution (in red) from the MC are compared. On the right pad the corresponding integrated distributions are shown. The dashed lines indicate the value of the cut chosen for the analysis.

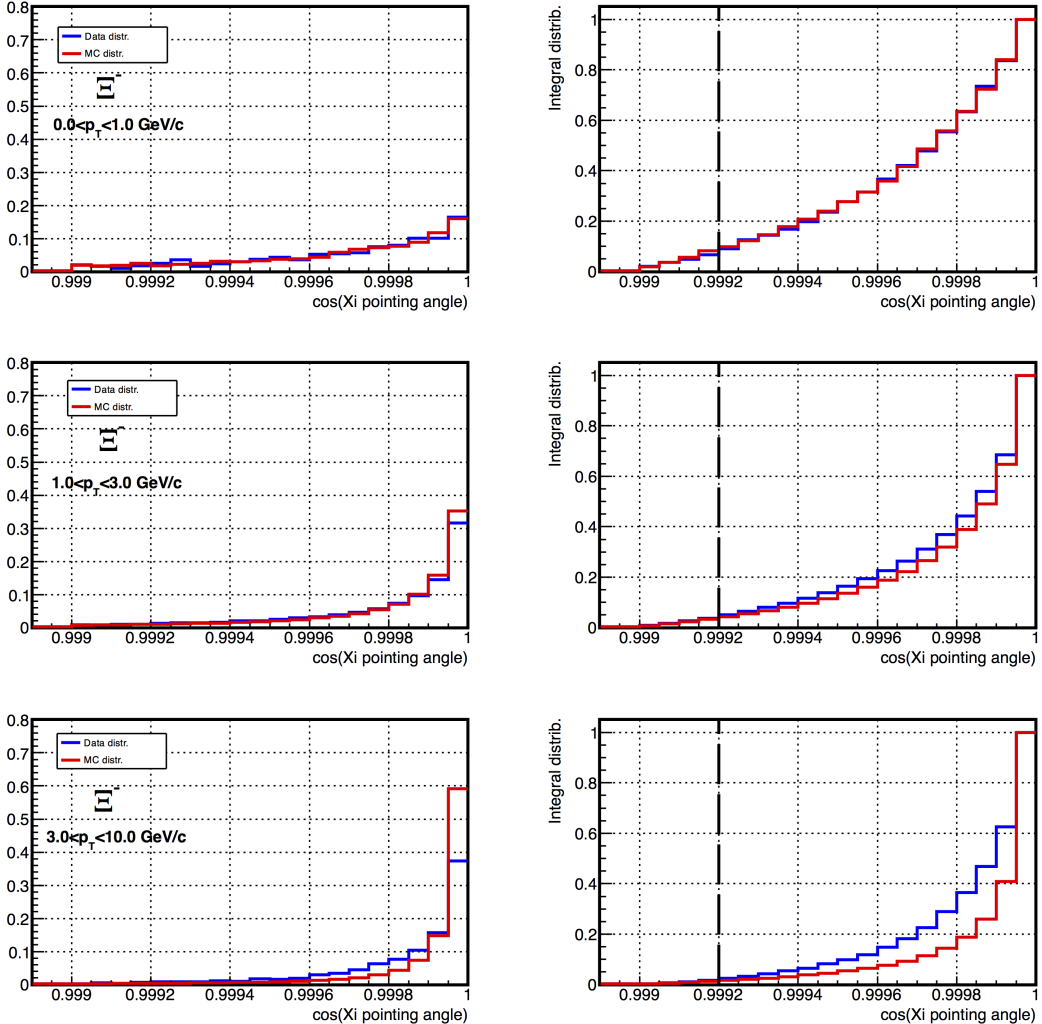


Figure 51: QA plots, STEP C, for the cosine of pointing angle for the Ξ^- , shown in 3 p_T intervals. On the left pad the signal distribution from the real data (in blue) and the signal distribution from the MC (in red) are compared. On the right pad the corresponding integrated distributions are shown. The dashed lines indicate the value of the cut chosen for the analysis.

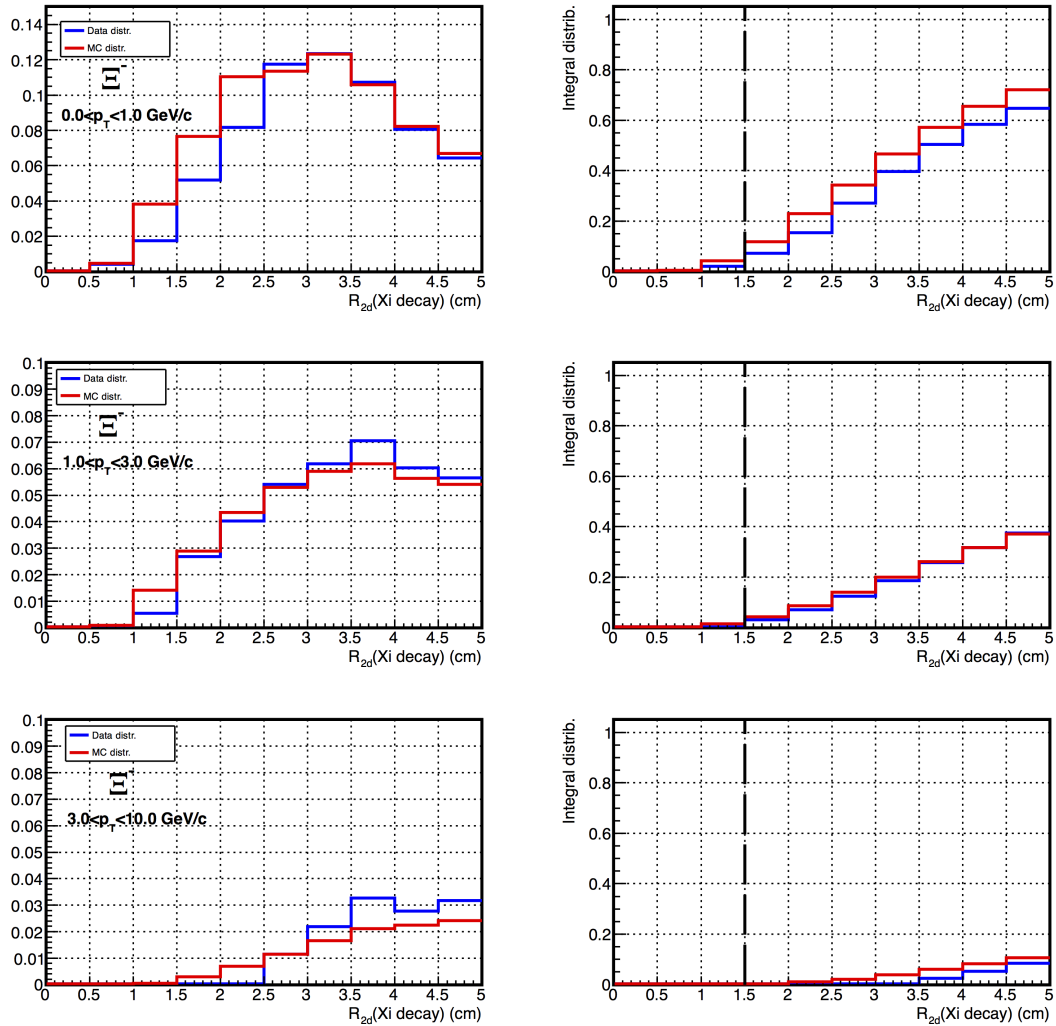


Figure 52: QA plots, STEP C, for the fiducial radius in the transverse plane for Ξ , shown in 3 p_T intervals. On the left pad the signal distribution from the real data (in blue) and the signal distribution from the MC (in red) are compared. On the right pad the corresponding integrated distributions are shown. The dashed lines indicate the value of the cut chosen for the analysis.

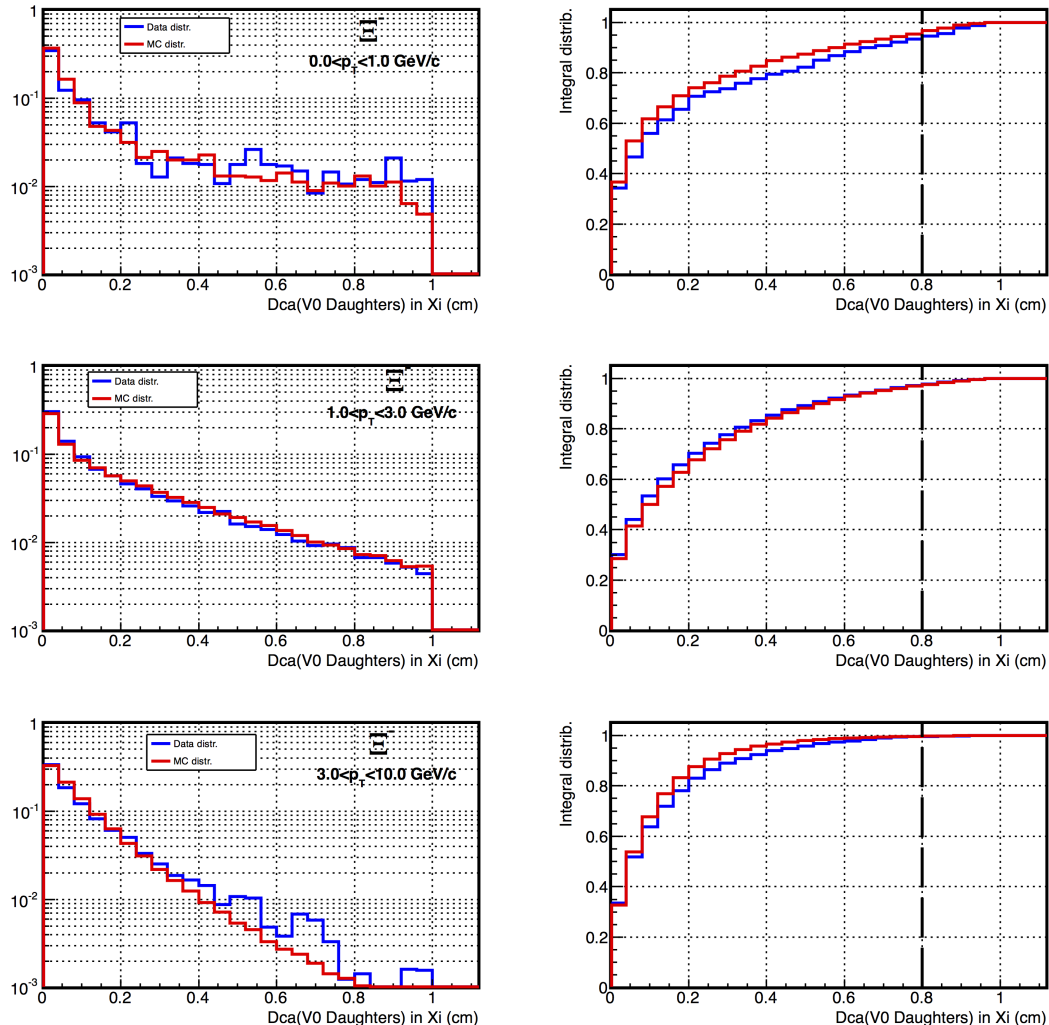


Figure 53: QA plots, STEP C, for the DCA between the V^0 daughters, shown in 3 p_T intervals. On the left pad the signal distribution from the real data (in blue) and the signal distribution from the MC (in red) are compared. On the right pad the corresponding integrated distributions are shown. The dashed lines indicate the value of the cut chosen for the analysis. A clarification on the dimension of such a variable has been given in the Note 5 in Chapter 4.

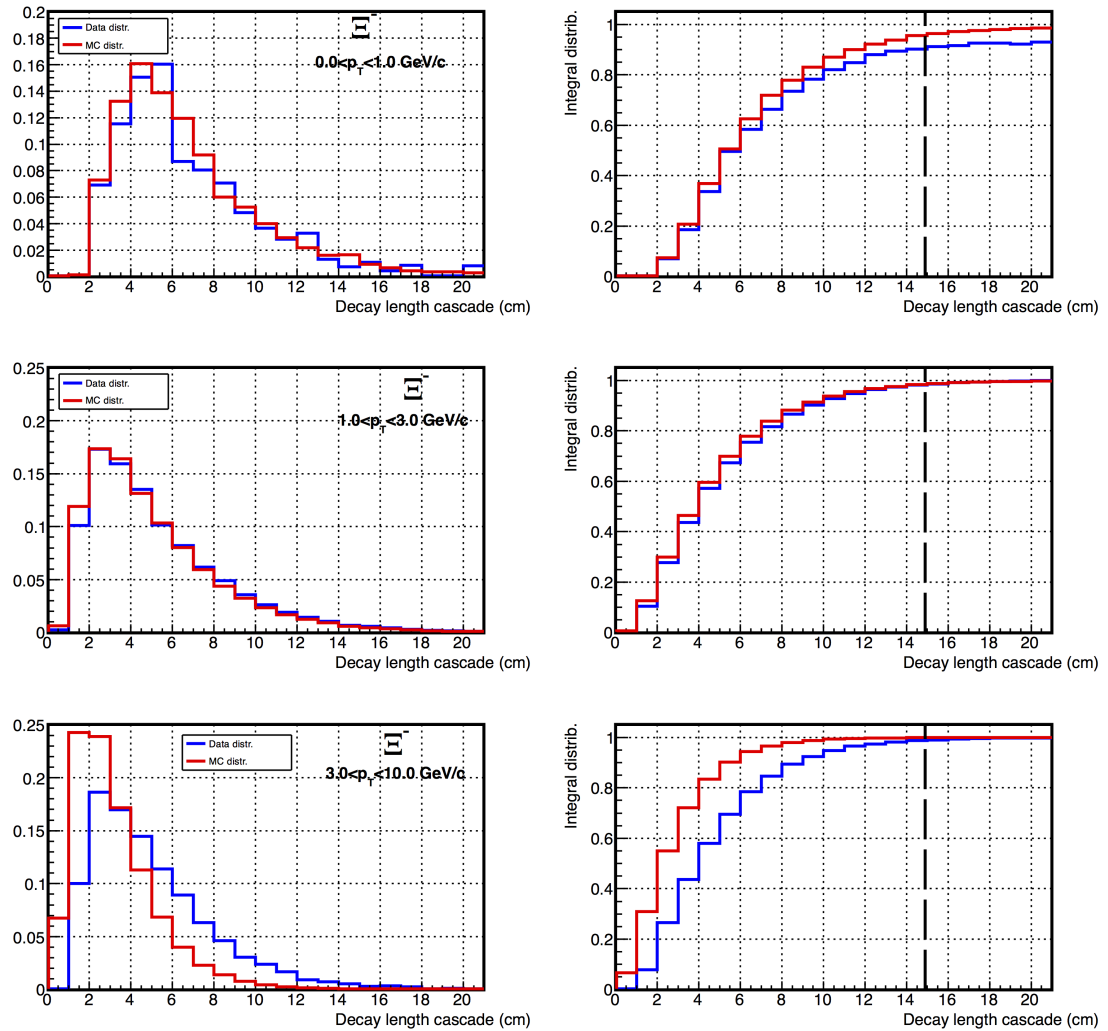


Figure 54: QA plots, STEP C, for the decay length distribution of the Ξ^- signal in 3 different p_T intervals. On the left pad the signal distribution from the real data (in blue) and the signal distribution from the MC (in red) are compared. On the right pad the corresponding integrated distributions are shown. The dashed lines indicate the value of the cut chosen for the analysis.

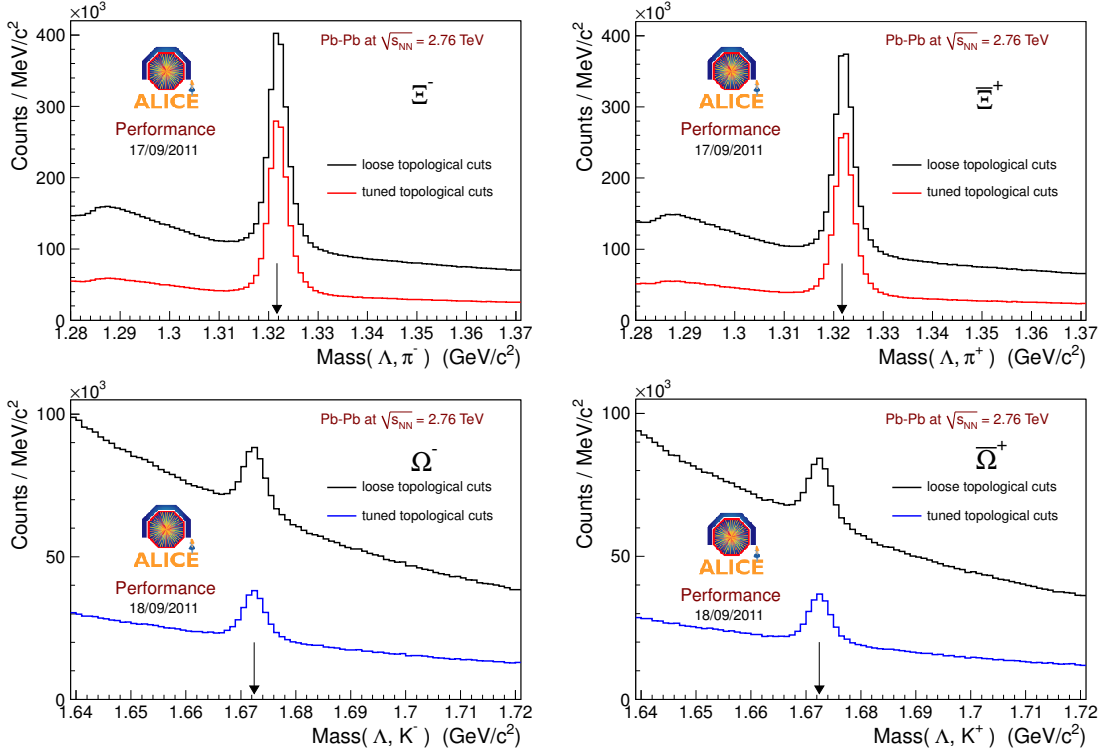


Figure 55: Invariant mass distributions for the Ξ (top panels) and the Ω candidates (bottom panels) integrated in p_T and centrality, with two different sets of cuts: loose cuts for candidate reconstruction (black histograms) and tuned cuts for the final analysis (coloured histograms). The TPC PID condition is required for each of the three daughters in both cases.

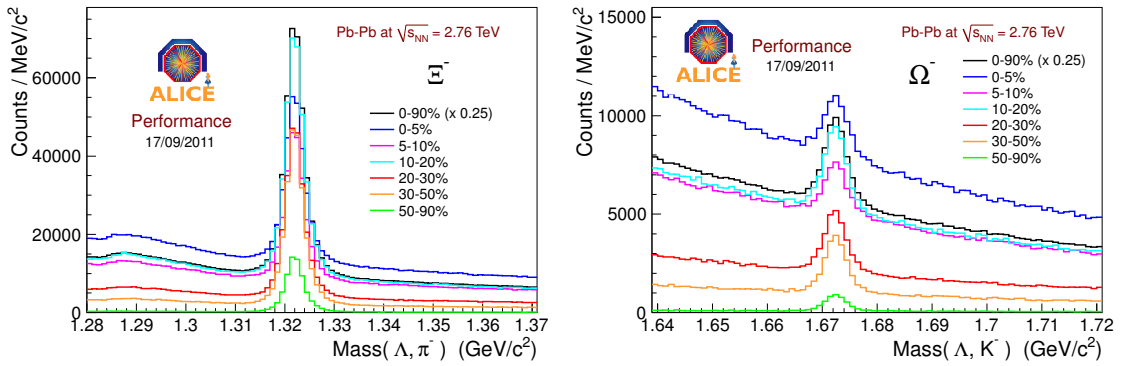


Figure 56: Invariant mass distributions for the Ξ^- (left panel) and the Ω^- candidates (right panel) integrated in p_T for different centrality bins. The TPC PID is requested for the three daughters in both cases.

5.3 TRANSVERSE MOMENTUM SPECTRA

The objective of the analysis is to measure the production rates of multi-strange baryons in Pb–Pb collisions as a function of the transverse momentum and integrated in p_T in the central rapidity region. To achieve this goal many steps need to be performed.

1. The signal should be extracted from the invariant mass distribution for each momentum interval. This p_T dependent study has its precision limited by the available statistics and the performance of the detector. The results is the so-called “raw” spectrum.
2. This spectrum is subject to all the inefficiencies and the acceptance limitation of the detector, and must therefore be corrected for these effects.
3. The corrected spectrum must be normalized to the number of events.
4. Finally, any source of systematics must be studied and corresponding uncertainties have to be estimated.

The corrected spectra can be expressed in the following way:

$$\frac{1}{N_{\text{events}}} \frac{d^2N_{\text{cascade}}}{dy dp_T}(p_T) = \frac{\epsilon_{\text{PhysSel}}}{N_{\text{evt, PhysSel}}} \frac{1}{\Delta y} \left(\frac{S_{\text{raw count}}}{\epsilon(p_T)} \frac{1}{\Delta p_T} \right)_{\text{i } p_T \text{ bin}}, \quad (5.1)$$

where $d^2N/dp_T dy$ is the differential yield in transverse momentum and rapidity, $N_{\text{evt, PhysSel}}$ is the number of events used in the analysis, N_{events} is the corresponding number of Pb–Pb interactions, $\epsilon_{\text{PhysSel}}$ is the event selection efficiency, $S_{\text{raw count}}$ is the raw signal of cascade extracted in a given p_T bin, $\epsilon(p_T)$ is the detector acceptance-efficiency correction in the same p_T bin, Δp_T is the width of the given p_T bin and Δy is the chosen rapidity interval.

The previous experimental quantities are affected by uncertainties: these have to be propagated in the previous formula to obtain the global uncertainty on the yield.

5.3.1 Signal extraction

Data are partitioned into the five centrality bins mentioned above and, for each centrality, into different p_T intervals (chosen for each particle species in order to have enough statistics for the signal extraction). To extract the raw yields (Figure 57), a symmetric region around the peak ($\pm 3\sigma$) is defined by fitting the

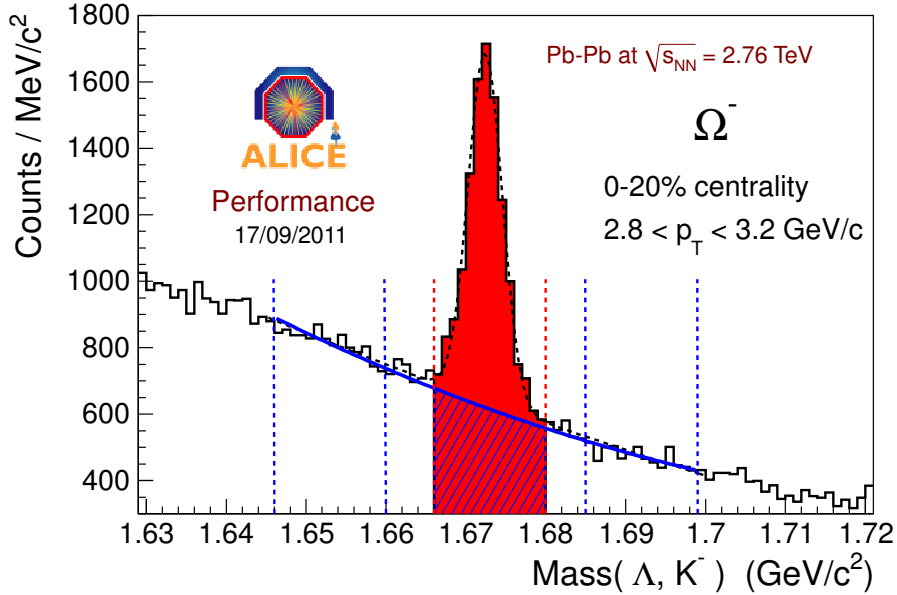


Figure 57: Ω^- invariant mass distribution (0 – 20% centrality, $2.8 < p_T < 3.2$ GeV/c) that illustrates the signal extraction procedure. The signal region is marked off by the red dashed lines, whereas the background regions by the blue dashed lines. The black dashed curve represents the fit of the whole distribution with the sum of a Gaussian plus a polynomial function, whereas the blue curve represents the fit of the background sampled on both sides of the peak.

distribution with the sum of a Gaussian and a polynomial. The background is determined by sampling the regions on both sides of the peak; in these regions, whose width and distance from the peak vary with centrality, p_T and particle species, the invariant mass distribution is fitted with a second order polynomial for low p_T and a first order for high p_T bins. The raw yield in each p_T and centrality bin is then obtained by subtracting the integral of the background fit function (B_{fit}) in the peak region from the total yield in the peak region obtained from bin counting ($(S + B)_{\text{BC}}$):

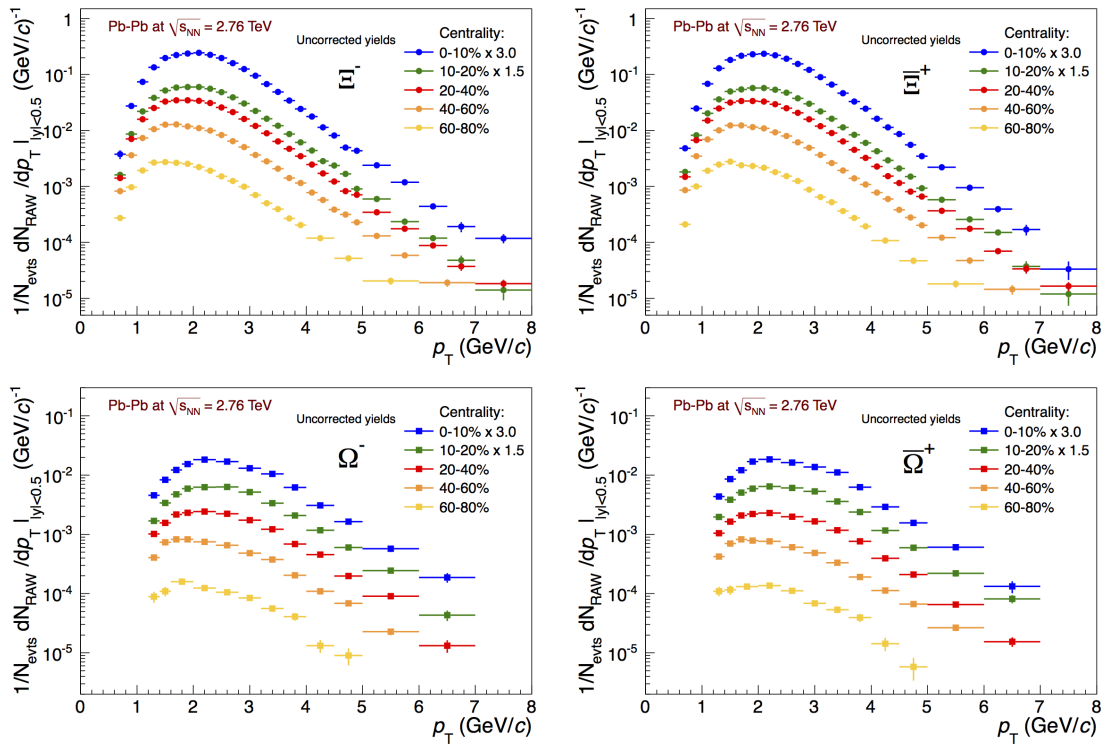
$$S_{\text{raw}} = (S + B)_{\text{BC}} - B_{\text{fit}}. \quad (5.2)$$

The statistical error on the raw counts is then calculated as the sum in quadrature of the two terms in Equation 5.2, namely:

$$\begin{aligned} (\sigma_{S_{\text{raw}}})^2 &= (\sigma_{(S+B)_{\text{BC}}})^2 + (\sigma_{B_{\text{fit}}})^2 \\ &= (S + B)_{\text{BC}} + B_{\text{fit}}. \end{aligned} \quad (5.3)$$

Table 9: Transverse momentum binning chosen for the cascade spectra.

Particle	Centrality	Number of bins	Bin limits (GeV/c)
Ξ	0 – 10%	27	{0.6,0.8,1.0,1.2,1.4,1.6,1.8,2.0,2.2,2.4,2.6,2.8,3.0,3.2,3.4,3.6,3.8,4.0,4.2,4.4,4.6,4.8,5.0,5.5,6.0,6.5,7.0,8.0}
	10 – 20%	27	{0.6,0.8,1.0,1.2,1.4,1.6,1.8,2.0,2.2,2.4,2.6,2.8,3.0,3.2,3.4,3.6,3.8,4.0,4.2,4.4,4.6,4.8,5.0,5.5,6.0,6.5,7.0,8.0}
	20 – 40%	27	{0.6,0.8,1.0,1.2,1.4,1.6,1.8,2.0,2.2,2.4,2.6,2.8,3.0,3.2,3.4,3.6,3.8,4.0,4.2,4.4,4.6,4.8,5.0,5.5,6.0,6.5,7.0,8.0}
	40 – 60%	25	{0.6,0.8,1.0,1.2,1.4,1.6,1.8,2.0,2.2,2.4,2.6,2.8,3.0,3.2,3.4,3.6,3.8,4.0,4.2,4.4,4.6,4.8,5.0,5.5,6.0,6.5,7.0,8.0}
	60 – 80%	20	{0.6,0.8,1.0,1.2,1.4,1.6,1.8,2.0,2.2,2.4,2.6,2.8,3.0,3.2,3.4,3.6,3.8,4.0,4.5,5.0,6.0}
Ω	0 – 10%	13	{1.2,1.4,1.6,1.8,2.0,2.4,2.8,3.2,3.6,4.0,4.5,5.0,6.0,7.0}
	10 – 20%	13	{1.2,1.4,1.6,1.8,2.0,2.4,2.8,3.2,3.6,4.0,4.5,5.0,6.0,7.0}
	20 – 40%	13	{1.2,1.4,1.6,1.8,2.0,2.4,2.8,3.2,3.6,4.0,4.5,5.0,6.0,7.0}
	40 – 60%	12	{1.2,1.4,1.6,1.8,2.0,2.4,2.8,3.2,3.6,4.0,4.5,5.0,6.0}
	60 – 80%	10	{1.2,1.4,1.6,2.0,2.4,2.8,3.2,3.6,4.0,4.5,5.0}

**Figure 58:** Uncorrected p_T spectra for Ξ^- , Ξ^+ , Ω^- and Ω^+ in $|y| < 0.5$, in five centrality bins (0 – 10%, 10 – 20%, 20 – 40%, 40 – 60%, 60 – 80%). [125]

The p_T bins chosen to extract the signal and obtain the raw counts are summarized in Table 9, for the different centrality classes and for the two particle species separately.

In Figure 58 the uncorrected p_T spectra are shown in five centrality bins and for $|y| < 0.5$. The cut on rapidity is made to assure that the efficiency is flat in the selected rapidity range and is far from the edges of the acceptance as explained in the following. Particle and antiparticle spectra look quite similar, as expected.

5.3.2 Acceptance-efficiency correction

To obtain the corrected spectra from the raw counts, the acceptance and efficiency corrections have been computed as a function of p_T . The acceptance-efficiency is defined as the following ratio:

$$\epsilon(p_T) = \frac{N_{\Xi,\Omega}(p_T, MC)(\text{associated})|_{|y|<0.5}}{N_{\Xi,\Omega}(p_T, MC)(\text{generated})|_{|y|<0.5}}. \quad (5.4)$$

The denominator is the number of all the generated cascades, regardless of the decay channel through which they decayed (this way the branching ratio contribution to the efficiency is included automatically). The numerator is the number of Ξ or Ω candidates reconstructed using the same algorithm applied in the experimental data, with the additional requirement that the cascade candidate corresponds to a true cascade decay in the Monte Carlo record. This ensures that the numerator corresponds to the number of successfully reconstructed true cascades, while the denominator corresponds to the number of all generated cascades. Therefore, the efficiency will correspond to the fraction of successfully detected cascades, which is the number needed for correcting the raw spectra measurements. As done for the experimental data, for each p_T bin a 3σ cut in the peak region is applied to the invariant mass, where the σ of the signal is determined from a Gaussian fit. The p_T interval is the same for both the numerator and the denominator.

The efficiency in different p_T bins is calculated in each of the five centrality classes and for each particle.

In principle the acceptance-efficiency can also depend on rapidity but a two-dimensional correction requires high statistics. The rapidity range is chosen such that the efficiency is flat over the full measured range in p_T , and far from the edge of the acceptance, where the efficiency in rapidity starts decreasing. This range corresponds to $|y| < 0.5$ for all particles at $p_T > 1.8$ GeV/c; for lower transverse momenta, a narrower rapidity range ($|y| < 0.3$) has been chosen both for raw yield extraction and for the correction calculation. The rapidity distributions for the different p_T bins are shown in Figure 59 for the Ξ^- and in Figure 60 for the Ω^- in the most central class (0 – 10%). At $p_T < 0.6$ GeV/c for Ξ and $p_T < 1.2$ GeV/c for Ω the available statistics in the experimental data is rather poor and does not allow a robust signal extraction.

Some improvements and the most relevant cross-checks for the acceptance-efficiency correction factors are described in the following.

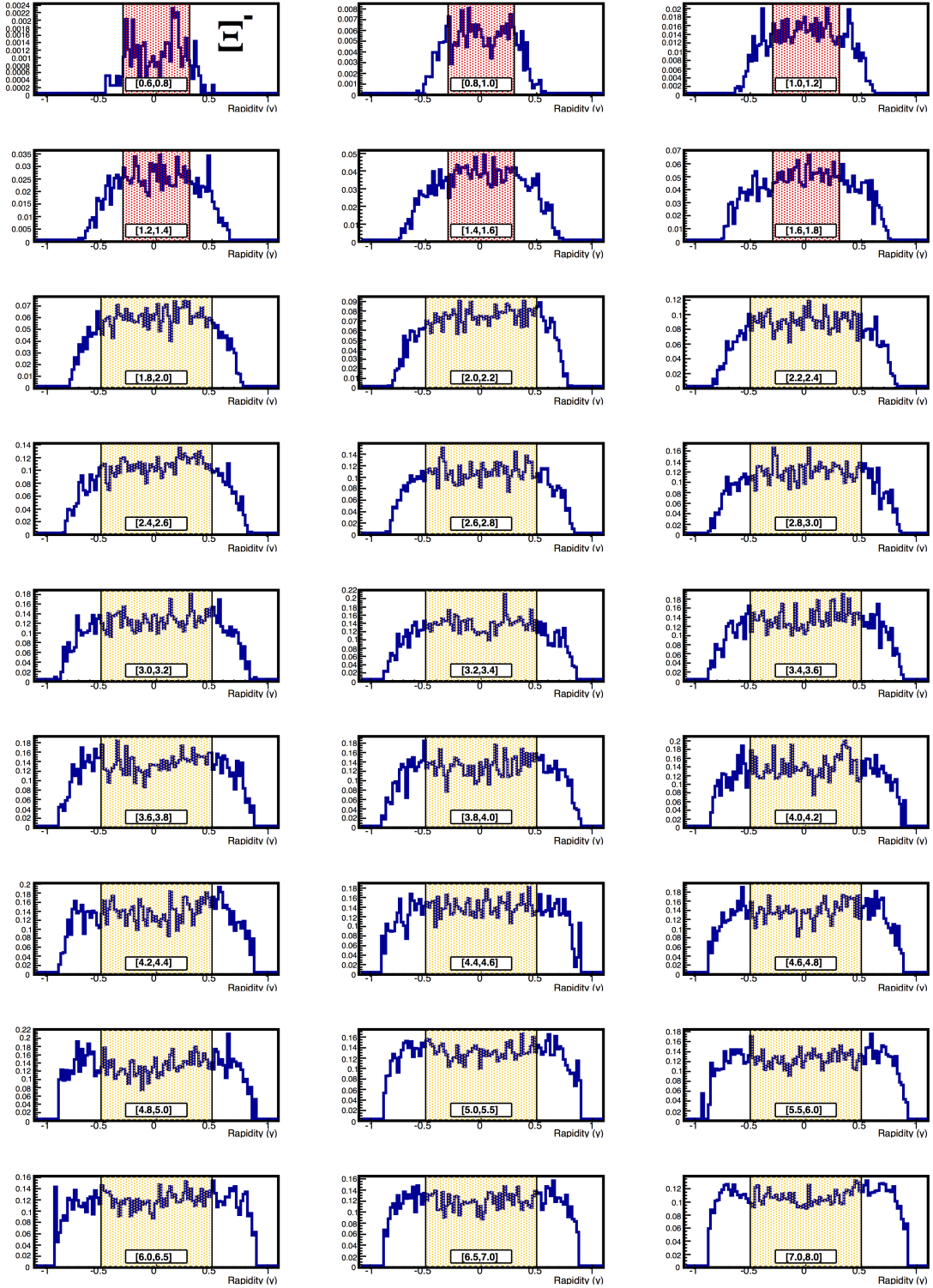


Figure 59: Distribution in rapidity of the Ξ^- acceptance-efficiency for different transverse momentum bins in the most central class 0 – 10%. The regions in y , where the distributions can be assumed to be almost flat, are highlighted with a coloured transparent box.

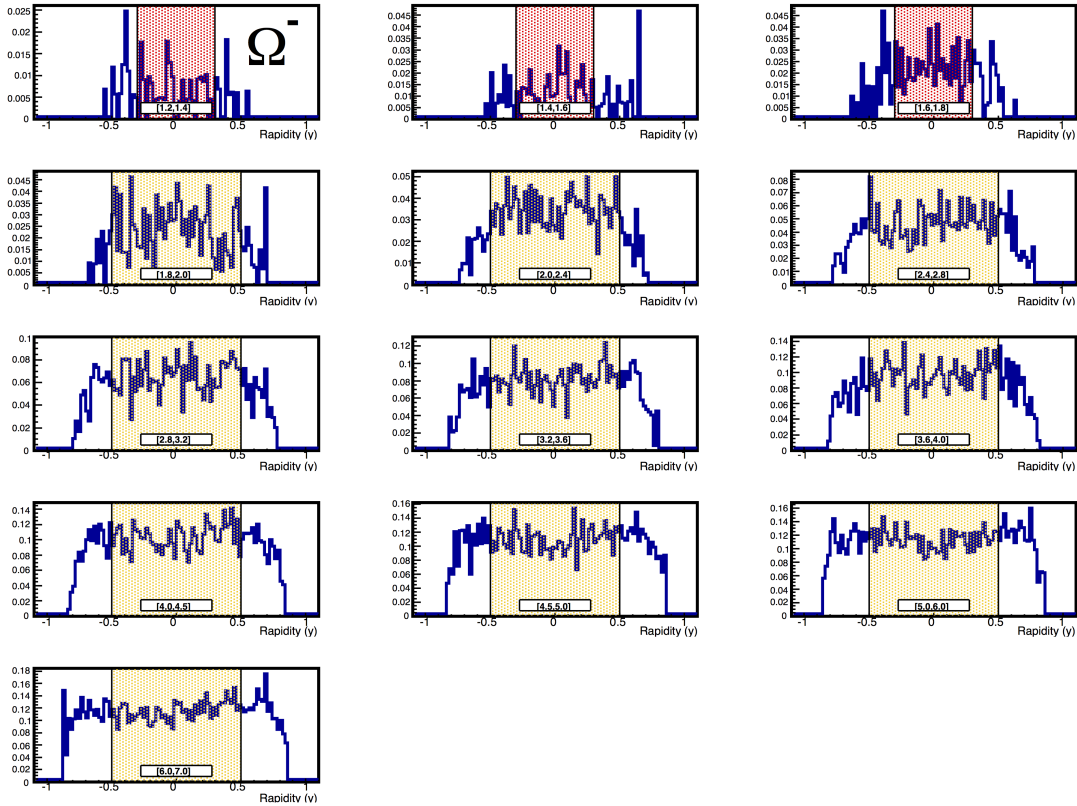


Figure 60: Distribution in rapidity of the Ω^- acceptance-efficiency for different transverse momentum bins in the most central class $0 - 10\%$. The regions in y , where the distributions can be assumed to be almost flat, are highlighted with a coloured transparent box.

Check good and bad runs

As explained in Section 5.1, the used MC productions are anchored on 155 runs, including not only the “good” runs for the experimental data (see Note 2, this Chapter). To increase the available statistics, crucial to improve the efficiency calculation, one could try to use the full list of runs. To do this one has to check if the efficiencies measured using the events in the two subsamples are compatible. In Figure 61 examples of the ratios of the efficiency calculated including the good anchor runs only for the three MC samples and the efficiency from the bad ones are shown in some centrality classes for the Ξ^- and the Ω^- . It can be concluded that within the errors the efficiencies obtained from the two parts of the samples (the one anchored to the “good” and the one anchored to the “bad” runs) are compatible. Thus, the full statistics has been used for the final correction calculation.

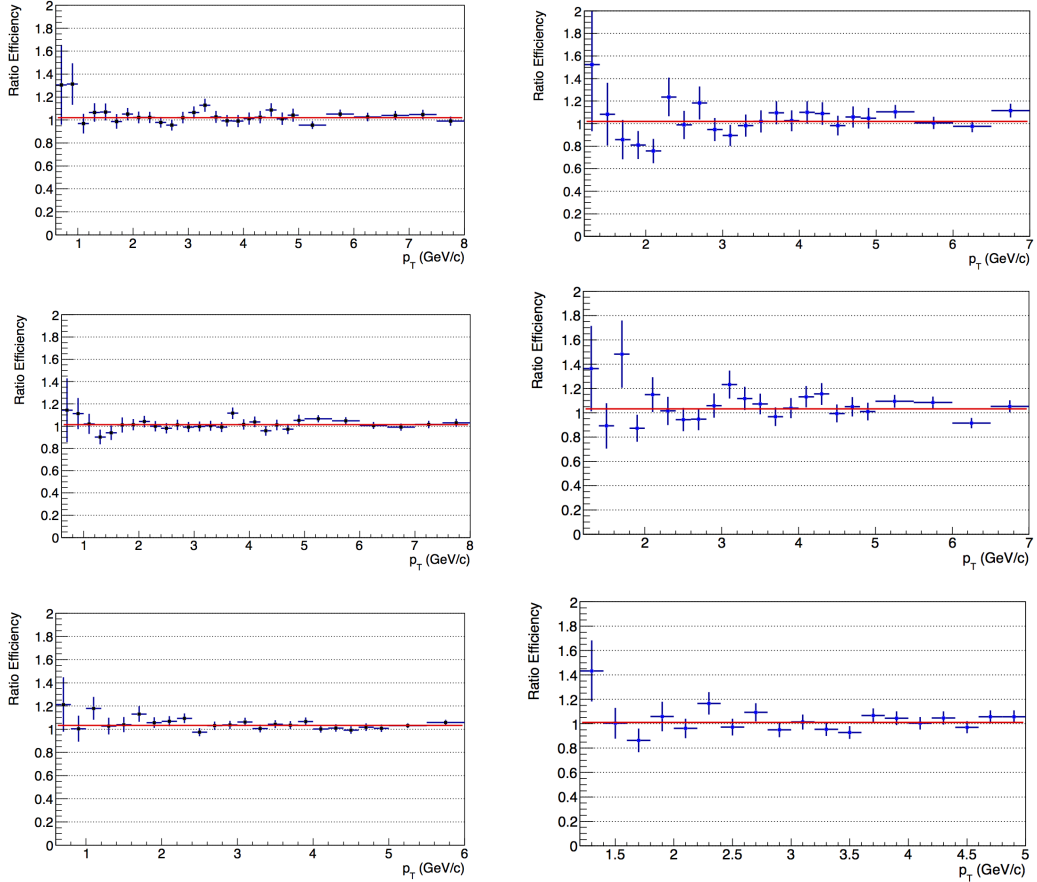


Figure 61: Ratios of efficiencies computed with the simulation anchored to good real data runs and the simulation anchored to bad real data runs in the 0 – 10% (top panels), 20 – 40% (mid panels) and 60 – 90% (bottom panels) centrality for the Ξ^- (left panels) and the Ω^- (right panels).

Check of the injected MC sample with the standard HIJING

As already mentioned, two of the MC sample used are enriched with injected cascades to improve the statistics. It is necessary to check that this particle injection does not introduce a bias in the events which may also affect the efficiency estimate. As a check, a MC sample without injected signals is used to compute the efficiency, which can then be compared to the one computed with enriched MC samples. The ratios of the two efficiencies show no significant differences within the statistical errors. The ratios are shown in Figure 62 for the 0 – 20% centrality class.

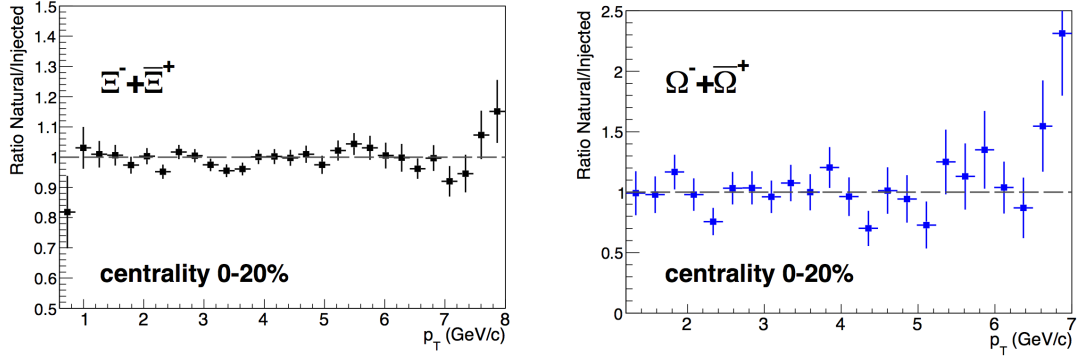


Figure 62: Ratios of efficiency in the 0 – 20% centrality class for the Ξ and Ω (added particle and antiparticle): efficiency calculated with the standard HIJING sample and efficiency calculated with the injected sample in $|y| < 0.5$ over the full p_T range.

dy/dθ correction

The first correction needed is connected to the injection of cascades in the MC samples. Since these particles were not injected with a flat distribution in rapidity, but with a flat distribution in θ , their distribution has been weighted as a function of rapidity (y) and p_T to obtain a flat distribution in rapidity. This procedure has been applied both to the generated and to the associated particles, starting from their bi-dimensional (y, p_T) distribution. In the acceptance-efficiency distributions as a function of rapidity in different slices of p_T , shown in Figures 59 and 60, such weighting correction has been already applied. It can be shown that the weight, w_{y,p_T} , that must be applied in each (y, p_T) cell is equal to:

$$w_{y,p_T} = \frac{dy}{d\theta} = \left(\frac{dy}{d\eta} \right) \cdot \left(\frac{d\eta}{d\theta} \right) = -0.5 \cdot \frac{p_T}{E} \cdot (e^\eta + e^{-\eta}) \cdot \frac{1}{\sin\theta}. \quad (5.5)$$

Here, all the ingredients depend only on the rapidity, the transverse momentum and the mass of the particle (m_0), as shown in the following relations:

$$E = \sqrt{m_0^2 + p_T^2 \cosh y}, \quad (5.6)$$

$$\theta = \arccos(p_L/p), \quad (5.7)$$

$$\eta = -\ln(\tan(\theta/2)), \quad (5.8)$$

where E is the total energy, $p_L = \sqrt{m_0^2 + p_T^2 \sinh y}$ is the longitudinal momentum, $p = \sqrt{p_L^2 + p_T^2}$ is the total momentum, θ is the polar angle and η is the pseudo-rapidity.

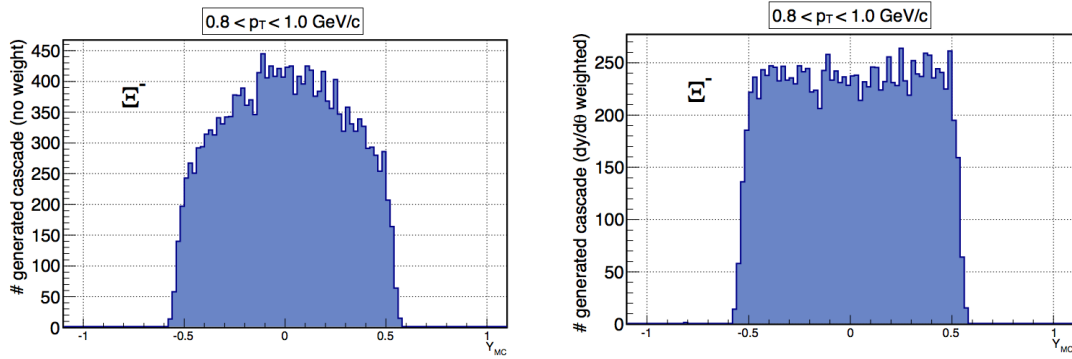


Figure 63: Rapidity distributions for MC generated particle injected in the HIJING standard event before (left) and after (right) the $dy/d\theta$ weighting.

As an example, the effect of this weighting process on the injected HIJING generated particles rapidity distribution is shown in Figure 63 for a given p_T bin.

The error on this weighted efficiency can be computed to be:

$$\delta \text{Eff}_{p_T} = \frac{\sqrt{\sum_y N_{\text{ass},y,p_T} \cdot w_{y,p_T}^2}}{\sum_y N_{\text{gen},y,p_T} \cdot w_{y,p_T}}. \quad (5.9)$$

After the weighting of the injected particles and the associated reconstructed cascades (N_{ass}), their bi-dimensional distributions are integrated in rapidity and added to the natural HIJING (N'_{ass}) to obtain the numerator and the denominator transverse momentum distributions for the efficiency calculation:

$$\text{Eff}_{\text{final},p_T} = \frac{\sum_y N_{\text{ass},y,p_T} \cdot w_{y,p_T} + N'_{\text{ass},p_T}}{\sum_y N_{\text{gen},y,p_T} \cdot w_{y,p_T} + N'_{\text{gen},p_T}}. \quad (5.10)$$

The error on the final efficiency is then given by the following formula:

$$\begin{aligned} \delta \text{Eff}_{\text{final},p_T} &= \frac{\delta(\sum_y N_{\text{ass},y,p_T} \cdot w_{y,p_T} + N'_{\text{ass},p_T})}{\sum_y N_{\text{gen},y,p_T} \cdot w_{y,p_T} + N'_{\text{gen},p_T}} = \\ &= \frac{\sqrt{\delta(\sum_y N_{\text{ass},y,p_T} \cdot w_{y,p_T})^2 + \delta N'_{\text{ass},p_T}^2}}{\sum_y N_{\text{gen},y,p_T} \cdot w_{y,p_T} + N'_{\text{gen},p_T}} = \\ &= \frac{\sqrt{\sum_y N_{\text{ass},y,p_T} \cdot w_{y,p_T}^2 + N'_{\text{ass},p_T}^2}}{\sum_y N_{\text{gen},p_T} \cdot w_{y,p_T} + N'_{\text{gen},p_T}}. \end{aligned} \quad (5.11)$$

The effect of the weighting on the efficiency was evaluated to be of the order of a few per mill for $p_T > 2$ GeV/c and up to 4% going down in p_T for all particles and all centralities. The effect has been evaluated comparing the efficiencies calculated with and without weighting the particles (examples in Figure 64).

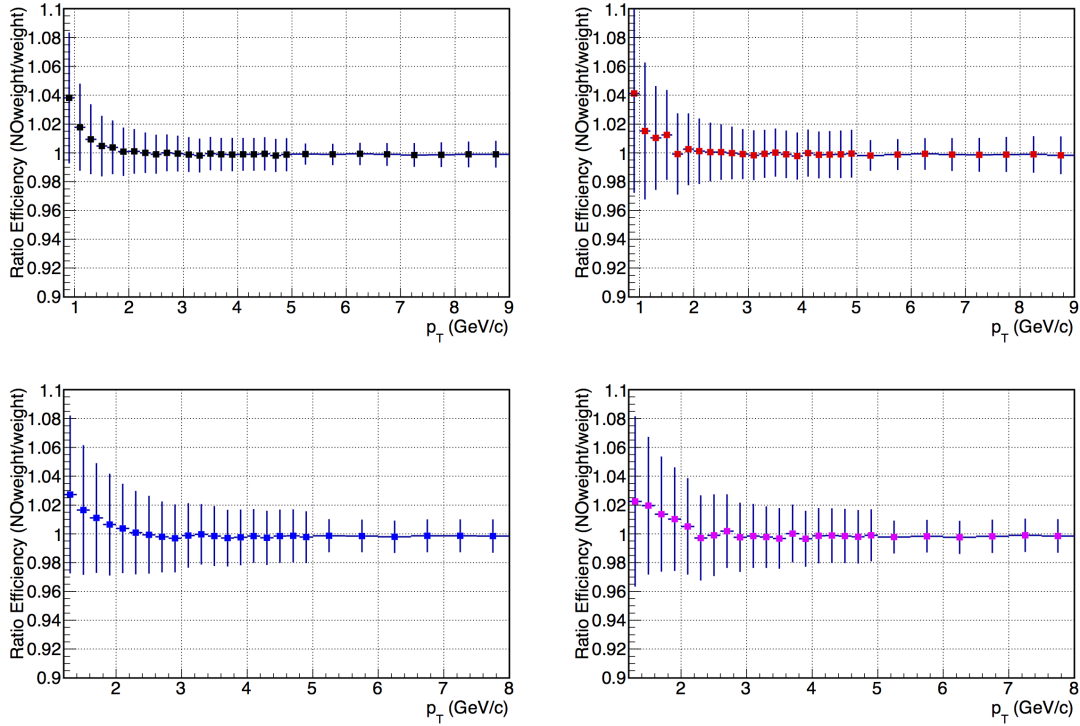


Figure 64: Ratios of efficiency in the $0 - 90\%$ centrality for the Ξ (top panels) and the Ω (bottom panels) for the injected sample with and without the weights applied.

GEANT3/FLUKA correction

During the preparation of the article on the ratio \bar{p}/p in pp collisions [126] by the ALICE Collaboration, the pion, kaon and proton effective interaction cross sections with the material have been studied. The effective cross sections for the π and K are well reproduced by the GEANT3 transport code. This is not the case for protons and antiprotons. For those particle species, the GEANT3 absorption cross-sections are overestimated, particularly at low p_T , giving an acceptance-efficiency correction that is overestimated for the cascades.

A correction to this effect has been obtained by means of a comparison between GEANT3 and another transport code, FLUKA [127], which gives a better description of the proton and antiproton absorption cross-sections. Since existing simulations use GEANT3 and it would be computationally prohibitive to re-execute, one has to produce an a-posteriori correction to the estimated acceptance-efficiency correction factors for the cascades, based on the corre-

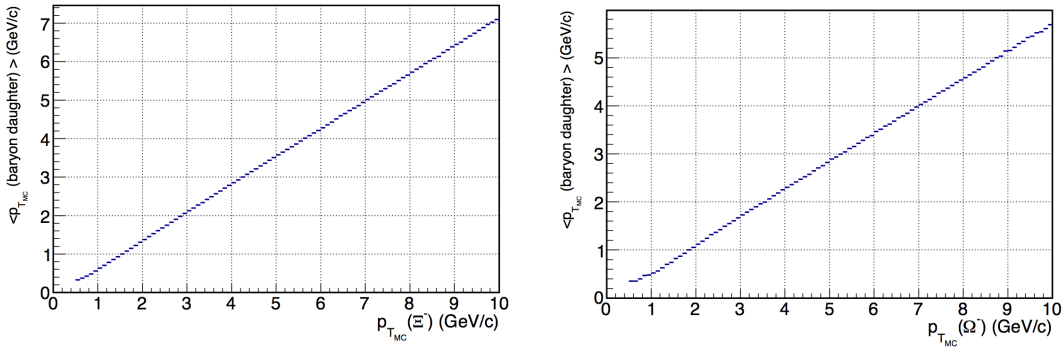


Figure 65: Correlation between the mean transverse momentum of the baryon daughter of a cascade and the transverse momentum of the parental cascade, on left for Ξ^- and on the right for the Ω^- .

tion of the acceptance-efficiency correction factors measured using GEANT3 and FLUKA for the primary proton and antiproton.

The fundamental step is to connect the baryon daughter transverse momentum to the parent cascade transverse momentum. The correlation between these two variables can be computed using MC information and is shown in Figure 65 for the Ξ^- and Ω^- , and seems to be almost linear. Similar plots have been obtained for the corresponding antiparticles.

Once such a relation is obtained, one can use the ratio of the acceptance-efficiency correction factors by GEANT3 and FLUKA for the (anti)proton as a function of the (anti)proton transverse momentum, $\epsilon_{\text{GEANT3}}/\epsilon_{\text{FLUKA}}(p_T)$, shown in Figure 66, to obtain the corresponding correction factor for the cascades acceptance-efficiency factors. The basic assumption is that the correction, calculated for primary (anti)protons, is the same for all secondaries.

Once the GEANT3/FLUKA correction has been applied, a small difference between particle and antiparticle is still present at low momenta: this is expected since the antiprotons from the Λ decays have higher probability of interaction with the material and therefore less chance of being reconstructed.

The corrected efficiency is then fitted with the following function:

$$f_{\text{fit}} = [a] \cdot e^{-\frac{(x-[b])^2}{[c]^2}} + [d] \cdot \log(x^{\frac{1}{2}} - [f]) \cdot (1 - e^{([g]-x)}), \quad (5.12)$$

which is then used to correct the raw counts. As an example, the calculated efficiency as a function of p_T is shown in Figure 67 for Ξ^- and Ω^- in the 40–60% centrality interval; the fitted curves are superimposed.

The efficiency is found to increase going from most central to more peripheral events, as expected as a consequence of the increased tracking efficiency

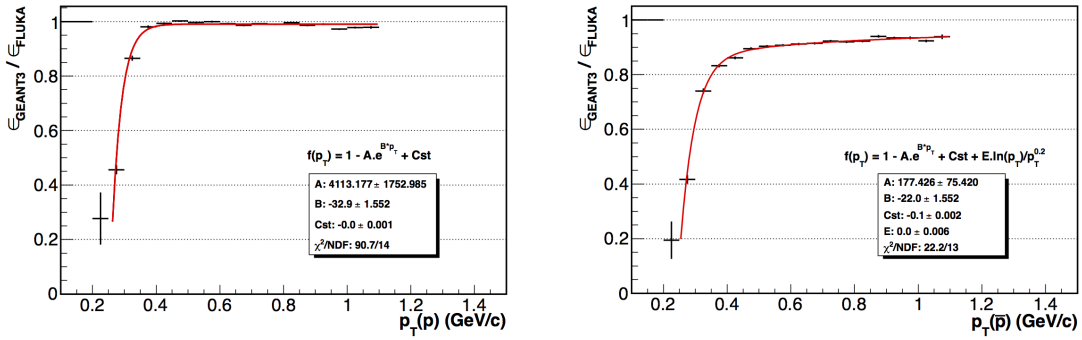


Figure 66: GEANT3/FLUKA correction factors for the primary proton (left panel) and antiproton (right panel) within the ALICE geometry. The fit function and the measured parameters are also reported.

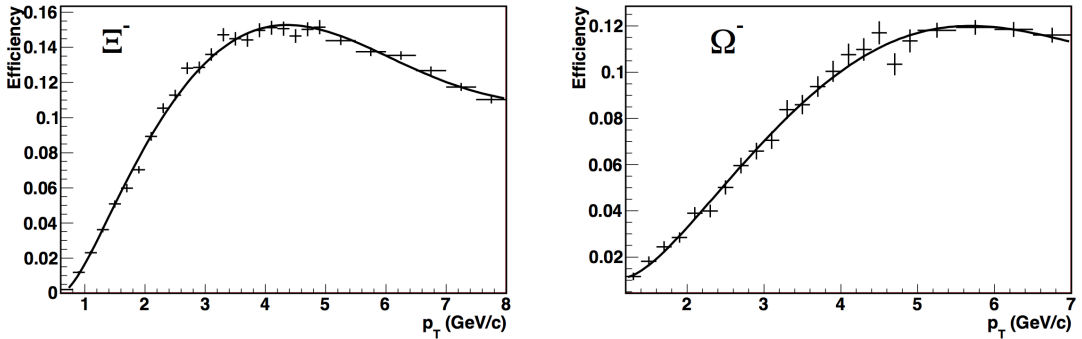


Figure 67: Efficiency factors (including acceptance and branching ratios) as a function of p_T in the rapidity window $|y| < 0.5$ for the Ξ^- (left panel) and for the Ω^- (right panel) in the 40 – 60% centrality interval. The fit function for each case is also shown.

in a poorest tracks environment. This is shown in Figure 68, for Ξ^- and Ω^- , respectively.

5.3.3 Normalization

The normalization factor can be easily computed in the case of Pb–Pb collisions. In this case the event selection is practically 100% efficient, so the $\epsilon_{\text{PhysSel}}$ is equal to one in Formula 5.1, and the factor is exactly equal to the number of events used in the analysis.

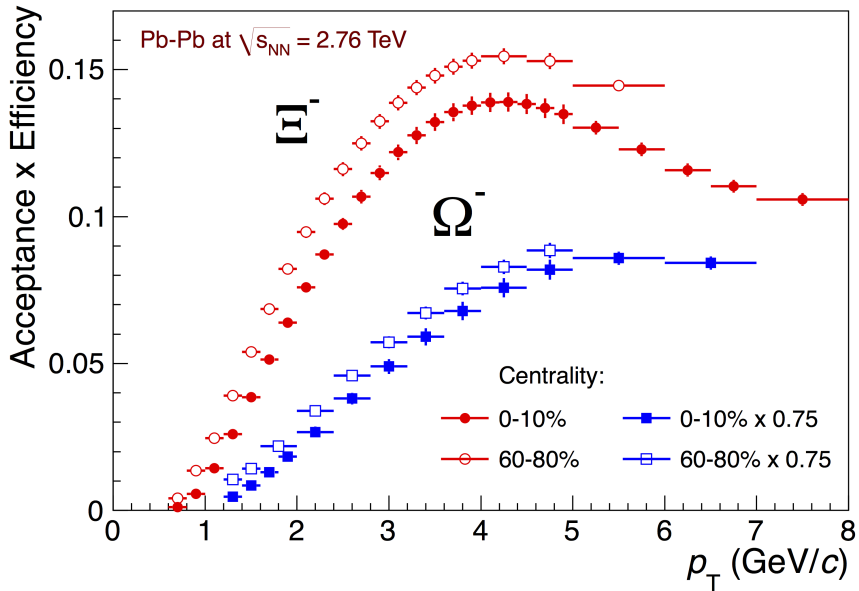


Figure 68: Efficiency as a function of p_T in the most central (0 – 10%) and most peripheral (60 – 80%) events for Ξ^- (red) and Ω^- (blue). [125]

5.3.4 Point-by-point systematic uncertainties

All the main contributions to the systematic uncertainty of particle spectra have been studied. In particular those that come from signal extraction, topological and kinematical selection cuts, track quality selection and the centrality range for the efficiency calculation. The study of the systematics has been performed for the most central class (0 – 10%). The 10 – 20% centrality class has been used only to study the contribution to systematics from the centrality dependence of the efficiency, as explained below.

Each condition applied in the cascade selection has been modified by a certain amount both in experimental data and in MC data; the yield⁶ in the measured p_T region has been recomputed and compared with the corresponding value obtained in the standard analysis. To evaluate the systematic uncertainty in p_T bins, the ratios of the spectra with varied selection criteria and the standard analysis spectra have also been produced.

The meaning of each source of systematic uncertainty studied is described in the following:

⁶ In this case the yield is simply estimated as the sum of the corrected and normalized yields in each measured p_T bin.

TOPOLOGICAL CUTS To evaluate the stability of the chosen set of values for the topological cuts, three different sets, loose, tight and very tight, have been defined in order to vary by +15%, -15% and -30% respectively the amount of candidates in the peak region of the invariant mass distribution.

SIGNAL EXTRACTION TECHNIQUE With the same spirit the signal extraction technique has been tested. In particular the width of the peak region has been changed from the standard 3σ to 4σ and 2.5σ . In each case the bin counting ($S+B$) and the integral of the background (B) are evaluated and subtracted. Also, to test the goodness of the fit of the background in the two side bands, the width of these two regions has been changed.

TRACK QUALITY SELECTION To estimate the systematics due to the track quality selection, the analysis has been redone with a tighter cut at 80 minimum required clusters in the TPC (instead of the default 70).

CENTRALITY DEPENDENCE OF THE EFFICIENCY The correction for acceptance-efficiency adopted in each centrality class can be slightly overestimated because cascade production may depend on centrality in a different way in Monte Carlo and real data. In a given centrality class the centrality distribution of the cascades in the real data decreases when going from central to peripheral collisions. The injected particle in the HIJING simulation, instead, are generated with a flat distribution in centrality: since the efficiency depends on centrality, this introduces a bias in the correction. This bias can be covered by a systematic error: to estimate such systematics the efficiency has been calculated in the class 5 – 20% and used to correct the raw spectra measured in the real data centrality class 10 – 20%.

MATERIAL BUDGET A possible source of uncertainty comes from the description of the material, active (detecting area) or dead (structure and cable), that the particles cross during their travel in the MC with respect to the real material present in the detector. Such description could affect the reconstruction efficiency in different aspects (e.g. multiple scattering, energy loss dE/dx , \bar{p} absorption). Such a study has been performed in the cascade analysis in pp collisions at $\sqrt{s} = 7$ TeV; more details can be found in [118, 128]. The value estimated in this study has been used, also for Pb–Pb, assuming no differences due to the different colliding system.

GEANT3/FLUKA CORRECTION The correction applied on the efficiency due to the wrong description of the (anti)proton cross section has already been discussed. Here the systematics due to the application of this correction has been estimated applying or not the correction.

Table 10: Overview of the variation of the measured yields due to the different sources of systematics studied in the 0 – 10% centrality range and also in the 10 – 20% centrality class for the contribution coming from the efficiency correction. Statistical errors for the standard analysis yields are also reported.

	Measured yield Ξ^-	$\Delta Y/Y (\%)$	Measured yield Ω^-	$\Delta Y/Y (\%)$
Standard analysis 0 – 10%	2.957 ± 0.058	-	0.351 ± 0.016	-
Loose cuts	2.975	+0.6	0.354	+0.8
Tight cuts	2.898	-2.0	0.365	+4.0
Very tight cuts	2.851	-3.6	0.380	+8.4
All cuts but mass Ξ	-	-	0.347	-1.1
4- σ window in signal extraction	2.951	-0.2	0.353	+0.5
2.5- σ window in signal extraction	2.954	-0.1	0.358	+2.0
Reduced window for background in signal extraction	2.951	-0.2	0.350	-0.1
Minimum number of TPC clusters per track	2.922	-1.2	0.362	+3.2
Standard analysis 10 – 20%	2.150 ± 0.037	-	0.244 ± 0.010	-
Correcting with efficiency in 5 – 20%	2.187	+1.7	0.252	+3.2
Correcting with efficiency in 0 – 20%	2.266	+5.4	0.255	+4.7
Correcting with efficiency in 0 – 10%	2.376	+10.5	0.268	+10.0

In Table 10 the variation of the measured yields for each of the sources of systematic uncertainties and cases are summarized for Ξ^- and Ω^- .

As for the systematics on the efficiency, a stronger effect is obtained selecting the 0 – 20% and 0 – 10% centrality intervals for the efficiency to correct the spectrum in the 10 – 20% class, as expected. These are however overestimations and are only shown as a check.

In Figure 69 and in the following Figures (70 and 71) the ratios of the spectra are shown and it can be concluded that no significant p_T dependence is present.

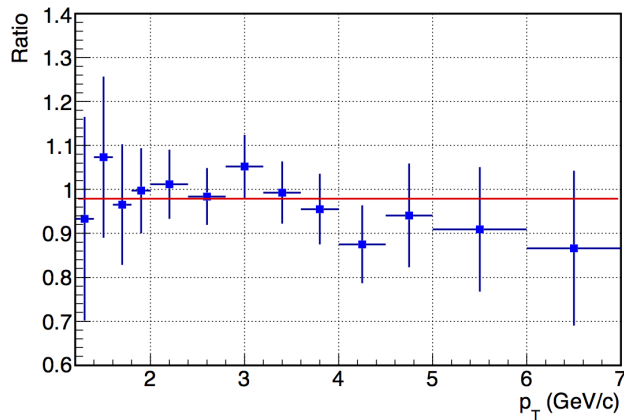


Figure 69: Ratio of corrected transverse momentum spectra obtained applying or not the analysis cut on the Ξ mass hypothesis for Ω . All the other analysis cuts are applied except this one.

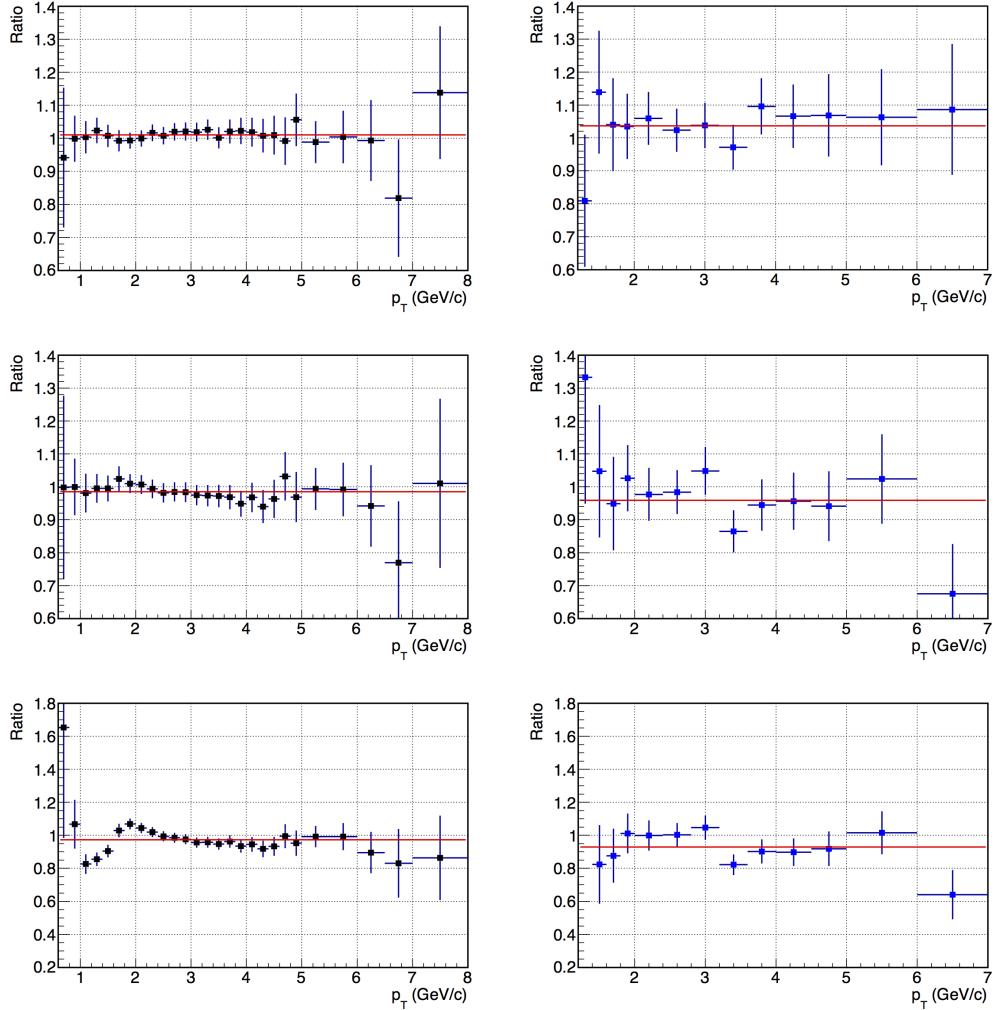


Figure 70: Ratio of corrected transverse momentum spectra obtained using different analysis cuts (Ξ^- on the left panels, Ω^- on the right panels): looser cuts than the standard ones (upper panels), tighter (central panels) and much tighter (lower panels) are applied.

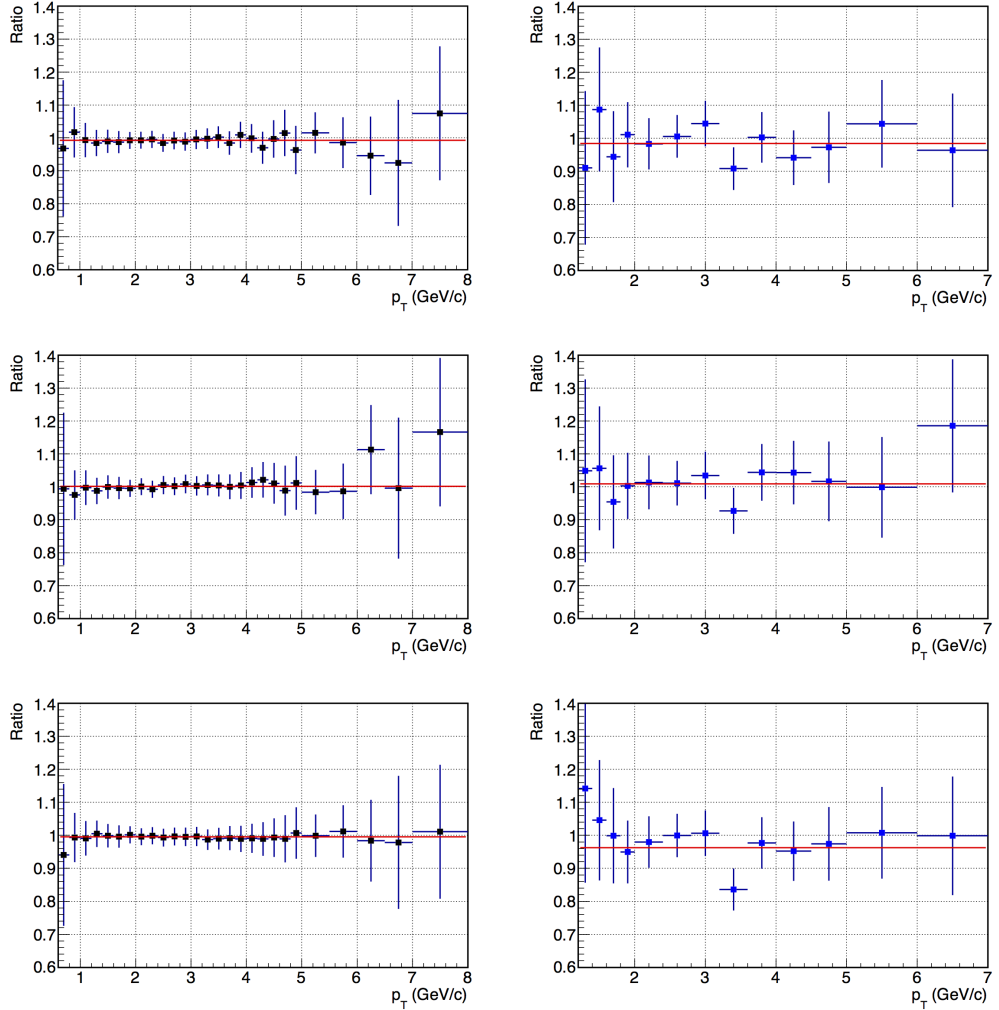


Figure 71: Ratio of corrected transverse momentum spectra obtained using different signal extraction procedures (Ξ^- on the left panels, Ω^- on the right panels): the width of the peak region is 2.5σ in the upper panels and 4σ in the central panels, whereas the windows for background sampling are reduced in the lower panels.

In summary the following sources of systematic uncertainty on the final yields have been estimated:

- material budget in the simulation (4%),
- track selection in the TPC, through the restriction on the number of TPC pad plane clusters used in the particle reconstruction (1% for Ξ and 3% for Ω),
- topological and kinematic selection cuts (1% for Ξ and 3% for Ω),
- for the Ω , removal of candidates satisfying the Ξ mass hypothesis (1%),
- signal extraction procedure (1%),
- use of FLUKA to correct the antiproton absorption cross section in GEANT3 (1%),
- centrality dependence of the correction (3%).

Assuming each of these sources to be independent from the others, the total systematic uncertainty has been then obtained adding in quadrature the single contributions and are of 5% for Ξ and 7% for Ω , independent of p_T and centrality. It will be added to the statistical error for each spectra point before fitting the distribution and extracting the yields, as described later. Additional comments on the systematics affecting directly the yield will be given in Section 5.4.

5.3.5 Corrected spectra

The corrected spectra are shown in Figure 72 in five centrality bins for the four cascades in $|y| < 0.5$. Spectra for particles and antiparticles are compatible within the errors, as expected at the LHC energy.

As already mentioned in Section 5.2, the requirement on the quality of the tracks in the TPC and the limited possibility of tracking the daughter particles using only the ITS detector system determine the lowest value of p_T for which the cascade spectra are measurable. This minimum is equal to 0.6 GeV/c for the Ξ and 1.2 GeV/c for the Ω . On the other hand, the maximum value in the p_T range is restricted only by the available statistics.

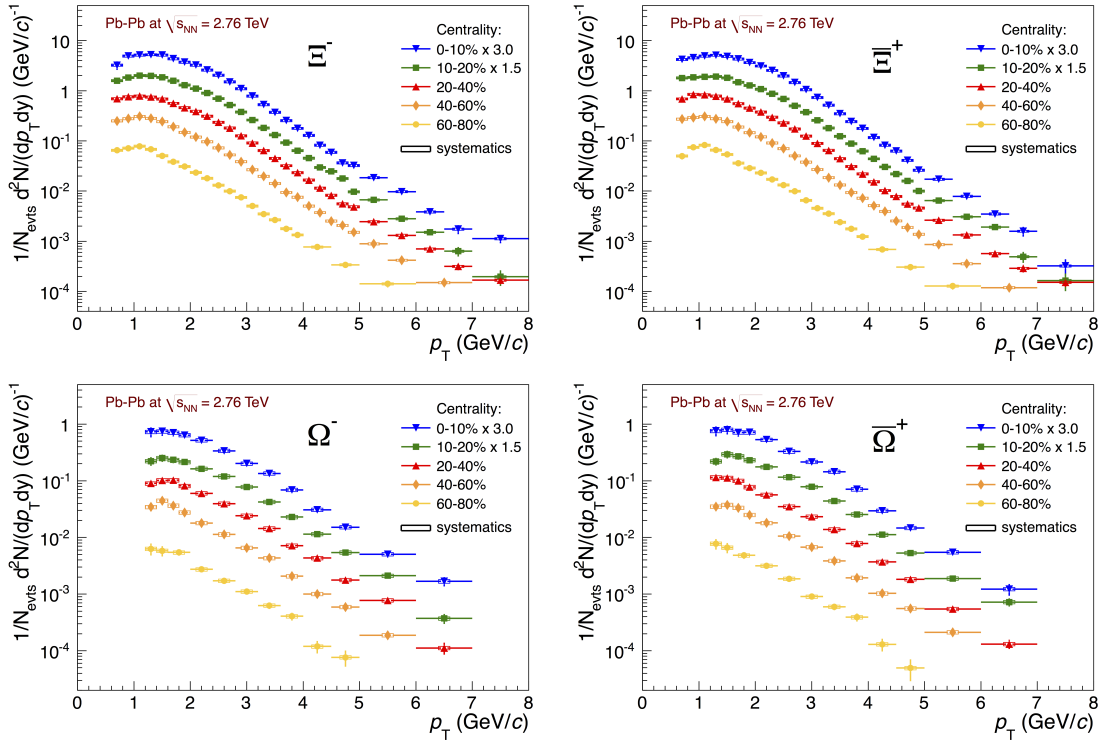


Figure 72: Corrected p_T spectra in the five centrality classes for each particle. The statistical error bars are smaller than the symbols for most data points, while the systematic uncertainties are represented by the open boxes. [125]

5.3.6 Analysis check: $c\tau$

An important cross-check for the analysis consists in studying the corrected distributions of the decay length and comparing their inverse slopes ($c\tau$), obtained by fitting them with an exponential, to the corresponding PDG value:

$$\frac{dN}{d(mcL/p)} = e^{\frac{1}{c\tau}(\frac{mcL}{p})}. \quad (5.13)$$

For this test, the efficiency corrections have been computed as a function of mcL/p , where m is the mass of the cascade in GeV/c^2 , L is the distance of the decay vertex from the primary vertex (in three dimensions) in centimetres and p is the total momentum in GeV/c . These efficiencies are applied to the raw distributions extracted for different intervals of the same variable. L is a first order approximation since the Ξ and Ω are charged particles and therefore have curved trajectories at low momenta.

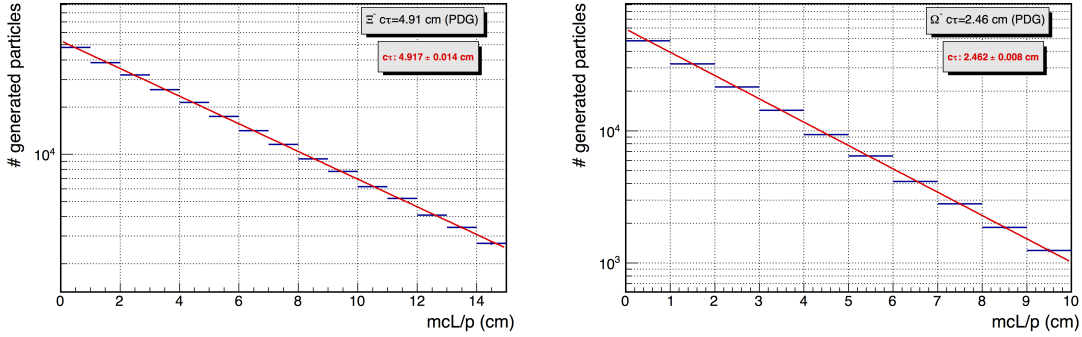


Figure 73: Distributions of mcL/p for generated (injected) particles with the exponential fit and the average value of the decay length. The distributions are integrated in $0.8 < p_T < 1.6 \text{ GeV}/c$ for Ξ and $1.2 < p_T < 2.0 \text{ GeV}/c$ for Ω , in the 0 – 90% centrality range. The measured values for the $c\tau$ are $4.917 \pm 0.014 \text{ cm}$ (Ξ^-) and $2.462 \pm 0.008 \text{ cm}$ (Ω^-).

Since the efficiency correction depends on p_T , a one-dimensional correction is not suitable for the following reasons: i) the Monte Carlo p_T distributions are not reliable; ii) injected particles with flat p_T distributions are used to compute the efficiency. Two-dimensional efficiencies should be calculated in $c\tau$ and p_T for each centrality class, as the efficiency also depends on centrality. In addition, a narrow rapidity interval should be used because the injected particles do not have a flat distribution in rapidity as they should. All the above mentioned constraints would make the statistics required for the correction calculation rather large.

As a compromise, the rapidity interval has been restricted to $|y| < 0.5$ and to a single bin at low p_T where the p_T distributions in the real data are flat within 10% ($0.8 < p_T < 1.6 \text{ GeV}/c$ for Ξ and $1.2 < p_T < 2.0 \text{ GeV}/c$ for Ω). The GEANT₃/FLUKA correction has not been applied.

The PDG values for the $c\tau$ are indicated in Table 5: these are 4.91 cm for $\Xi^- (\bar{\Xi}^+)$ and 2.46 cm for $\Omega^- (\bar{\Omega}^+)$. These values have been checked by fitting the distributions of generated injected particles (Figure 73): the average decay length values have been found consistent with the PDG values (Ξ^- : $4.917 \pm 0.014 \text{ cm}$ and Ω^- : $2.462 \pm 0.008 \text{ cm}$).

In order to have enough statistics, instead of the 0 – 10% centrality class used in the analysis, the 0 – 20% centrality class has been used to extract the raw spectra and calculate the efficiency as a function of mcL/p . In Figure 74 the corrected distributions are shown with the fit and the average decay length values. The p_T independent systematics of 5% and 7%, for Ξ and Ω respectively, have been added to the corrected spectra before fitting. The values obtained from the

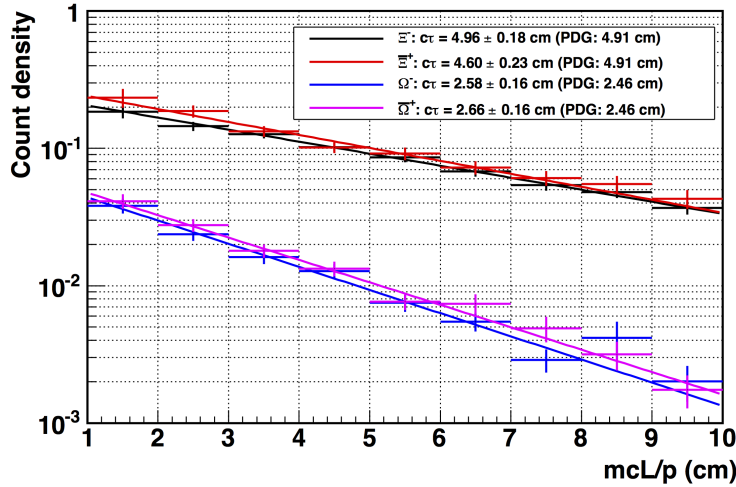


Figure 74: Corrected mcL/p distributions in the $0 - 20\%$ centrality class for the four cascades are shown. The average values from the fits are also shown and compared to the PDG $c\tau$ values in parenthesis. The errors on the corrected spectra are the sum in quadrature of the statistical and systematic uncertainties.

fits are consistent with the PDG values within 1σ for the particles and 1.5σ for the antiparticles (Ξ^- : 4.96 ± 0.18 cm, Ξ^+ : 4.60 ± 0.23 cm, Ω^- : 2.58 ± 0.16 cm and Ω^+ : 2.66 ± 0.16 cm).

5.4 YIELD EXTRACTION

In order to extract particle yields integrated over the full p_T range, the spectra are fitted using the blast-wave model parametrization [129]. This is a hydrodynamics inspired model, which assumes a transversely expanding emission source in local thermal equilibrium at a given temperature and with statistical distribution approximated by the Boltzmann distribution. The parameters of this model are the kinetic freeze-out temperature T and the transverse flow velocity β_t . Assuming a linear radial velocity profile, the spectrum can be computed from:

$$\frac{1}{m_T} \frac{dN}{dm_T} \propto \int_0^R r dr I_0\left(\frac{p_T \sinh \rho}{T}\right) K_1\left(\frac{m_T \cosh \rho}{T}\right), \quad (5.14)$$

where $\rho = \tanh^{-1}(\beta_t)$. This model is used because it best fits the experimental data.

Yields are then calculated by adding to the integral of the real data in the measured p_T region, the integral of the fit function outside that region. The extrapolation to low p_T is a much larger fraction of the yield than that for high p_T : it contributes between 10 – 20% of the final total yields for the Ξ , and 35 – 50% for Ω , depending on centrality.

Other functions of the transverse momentum have been used for comparison with the blast-wave shape:

$$\frac{d^2N}{dp_T dy} = A p_T \exp\left(-\frac{p_T}{T_e}\right), \quad (5.15)$$

$$\frac{d^2N}{dm_T dy} = A m_T \exp\left(-\frac{m_T}{T_e}\right), \quad (5.16)$$

$$\frac{d^2N}{dp_T dy} = A p_T \frac{1}{\exp\left(\frac{\sqrt{p_T^2 + m_0^2}}{T}\right) - 1}, \quad (5.17)$$

$$\frac{d^2N}{dp_T dy} = A p_T \frac{1}{\exp\left(\frac{\sqrt{p_T^2 + m_0^2}}{T}\right) + 1}, \quad (5.18)$$

$$\frac{d^2N}{dp_T dy} = \frac{dN}{dy} p_T \frac{m_T}{T_b[(m_0 + T_b)^2 + T_b^2]} \exp\left(-\frac{m_T - m_0}{T_b}\right), \quad (5.19)$$

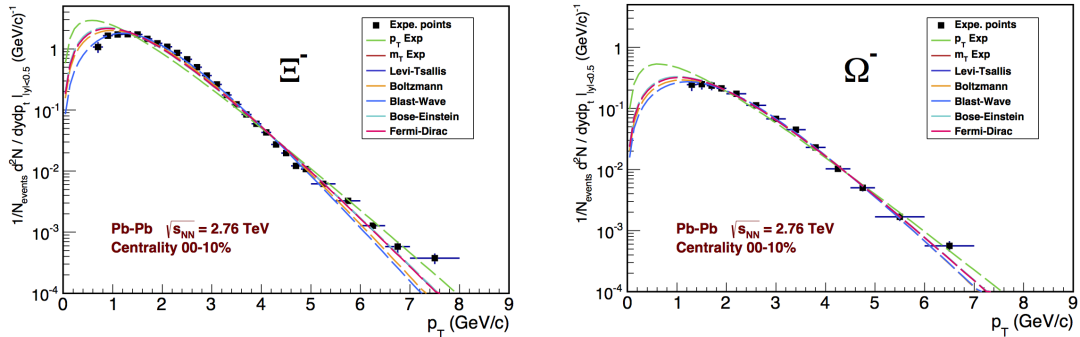
$$\frac{d^2N}{dp_T dy} = \frac{dN}{dy} p_T \frac{(n-1)(n-2)}{nT[nT + m(n-2)]} \left(1 + \frac{m_T - m}{nT}\right)^{-n}, \quad (5.20)$$

where $m_T = \sqrt{p_T^2 + m_0^2}$. They correspond to p_T exponential (Equation 5.15), m_T exponential (Equation 5.16), Bose-Einstein distribution (Equation 5.17), Fermi-Dirac distribution (Equation 5.18), Maxwell-Boltzmann distribution (Equation 5.19), Lévi-Tsallis model [130] (Equation 5.20). The average difference in the total integrated yield, obtained using these fit functions and the blast-wave parametrization, has been taken as an estimate of the systematic uncertainty due to the extrapolation. In Table 11 the values of the yields and the corresponding systematics are reported for each of the previous functions.

In Figure 75 the fit functions have been overlapped with the spectra points for Ξ^- and Ω^- in the most central collision class (0 – 10%).

Table 11: Yields from the fitting of corrected spectra using different functions.

Particle	Fit function	Yield	$\Delta Y/Y (\%)$	$\chi^2/n.d.f.$	Extr. frac. yield at low p_T
Ξ^-	Blast-wave	3.34	-	84.56/23	0.106
	p_T exponential	4.28	-28.1	461.04/25	0.302
	m_T exponential	3.66	-8.7	184.39/25	0.184
	Bose-Einstein	3.69	-10.5	198.27/25	0.190
	Fermi-Dirac	3.64	-9.0	172.31/25	0.179
	Boltzmann	3.55	-6.3	128.78/25	0.159
	Lévi-Tsallis	3.66	-9.6	184.50/24	0.184
Ω^-	Blast-wave	0.58	-	8.44/9	0.361
	p_T exponential	0.88	-34.1	26.33/11	0.585
	m_T exponential	0.64	-10.3	10.86/11	0.429
	Bose-Einstein	0.65	-12.1	11.24/11	0.434
	Fermi-Dirac	0.64	-10.3	10.51/11	0.423
	Boltzmann	0.60	-3.4	9.62/11	0.394
	Lévi-Tsallis	0.64	-10.3	10.86/10	0.429

**Figure 75:** Corrected spectra for Ξ^- (left) and Ω^- fitted with the functions listed in Table 11 in most central (0 – 10%) Pb–Pb collisions.

This contribution to the systematic uncertainty on the yields is centrality dependent: it increases going from central to peripheral collisions since the extrapolated fraction of the spectra also increases for peripheral collisions. An additional systematic error of 7% (15%) has been added to the final Ξ (Ω) yield to take into account the uncertainty due to the extrapolation at low p_T , resulting to be the maximum value obtained from the centrality dependence study.

The total integrated yields for Ξ^- , Ξ^+ , $\Xi^- + \Xi^+$, Ω^- , Ω^+ and $\Omega^- + \Omega^+$ have been determined in each centrality class, and are presented in Table 12. Statistical and systematic uncertainties are quoted. The systematic errors include both the contribution due to the correction factors and that associated to the extrapolation to the unmeasured p_T region. Particle and antiparticle yields are found to be compatible within the errors. The yield for particle and antiparticle combined

Table 12: Total integrated mid-rapidity yields, dN/dy , for multi-strange baryons in Pb–Pb collisions at $\sqrt{s_{NN}} = 2.76$ TeV for different centrality intervals. Both statistical (first) and systematic (second) errors are shown.

Centrality	0 – 10%	10 – 20%	20 – 40%	40 – 60%	60 – 80%
Ξ^-	$3.34 \pm 0.06 \pm 0.24$	$2.53 \pm 0.04 \pm 0.18$	$1.49 \pm 0.02 \pm 0.11$	$0.53 \pm 0.01 \pm 0.04$	$0.124 \pm 0.003 \pm 0.009$
Ξ^+	$3.28 \pm 0.06 \pm 0.23$	$2.51 \pm 0.05 \pm 0.18$	$1.53 \pm 0.02 \pm 0.11$	$0.54 \pm 0.01 \pm 0.04$	$0.120 \pm 0.003 \pm 0.008$
$\Xi^- + \Xi^+$	$6.66 \pm 0.08 \pm 0.47$	$5.14 \pm 0.06 \pm 0.36$	$3.03 \pm 0.03 \pm 0.22$	$1.07 \pm 0.01 \pm 0.08$	$0.240 \pm 0.006 \pm 0.019$
Ω^-	$0.58 \pm 0.04 \pm 0.09$	$0.37 \pm 0.03 \pm 0.06$	$0.23 \pm 0.01 \pm 0.03$	$0.087 \pm 0.005 \pm 0.014$	$0.015 \pm 0.002 \pm 0.003$
Ω^+	$0.60 \pm 0.05 \pm 0.09$	$0.40 \pm 0.03 \pm 0.06$	$0.25 \pm 0.01 \pm 0.03$	$0.082 \pm 0.005 \pm 0.013$	$0.017 \pm 0.002 \pm 0.003$
$\Omega^- + \Omega^+$	$1.19 \pm 0.06 \pm 0.19$	$0.78 \pm 0.04 \pm 0.15$	$0.48 \pm 0.02 \pm 0.08$	$0.170 \pm 0.007 \pm 0.029$	$0.032 \pm 0.003 \pm 0.005$

have been determined by fitting the spectra resulting from adding particle and antiparticle yields in each p_T interval separately, as opposed to adding integrated yields.

6

MULTI-STRANGE BARYON ANALYSIS IN PP COLLISIONS

6.1 DATA SAMPLE AND EVENT SELECTION

The data used for this analysis were collected during the March 2011 pp run at the centre-of-mass energy of 2.76 TeV (LHC11a period, pass 2 reconstruction): this is then the reference sample to be used as a baseline for studying the Pb–Pb collisions. It consists of 24 runs with a total of about $94 \cdot 10^6$ events. Among these, 16 runs have been identified by the Collaboration as good runs for the central barrel detectors: they correspond to about $80 \cdot 10^6$ events. All these data have been taken with good data tracking conditions for both the TPC and the ITS.

The whole data sample was collected and processed in a somewhat unusual way: in order to increase the total statistics, some events were recorded without the slowest detector (SDD) in the readout. Data were then processed, providing two different productions:

wo-SDD: all events are reconstructed without using the SDD information, giving the largest possible homogenous set of events;

w-SDD: all events are reconstructed using the SDD information where available; for the events where the SDD information is not available the reconstruction provides the same results as in the **wo-SDD** production. This sample contains almost one half of the statistics compared to the previous one.

The events are selected based on the minimum-bias trigger MB_{OR} requiring at least one hit in the SPD or VZERO detectors, in coincidence with two beam bunches crossing the ALICE interaction region.

In addition other offline selections have been applied to reject beam induced background. The VZERO counters are used to remove beam-gas or beam-halo

events. As in the case of the Pb–Pb collisions the following other quality selection have been applied:

- (a) events with good vertex reconstruction (rejection of events with TPC-only vertex);
- (b) events without pile-up¹;
- (c) events with vertex position satisfying $|Z_{PV}| < 10$ cm.

The meaning of the conditions (a) and (c) is the same as for Pb–Pb analysis. In the pp case a further check is applied on the possibility that a pile-up event happens: this is done exploiting the information from the SPD [123].

When using the sample **w-SDD** one has to select only events for which the information from the SDD is available and then used during the reconstruction, in order to deal with a homogenous sample.

The effect of each selection on the number of the events for the two reprocessings of the sample is reported in the upper part of Table 13; as anticipated, the selection based on the SDD status, when applied to the **w-SDD** sample, reduces the statistics to about one half.

To correct the data for acceptance and efficiency two Monte Carlo productions have been used. These are two Pythia (Perugia 0 tune) productions anchored to the 16 good runs selected for the real data. To reduce the total processing time only generated events containing at least one Ξ (Ω) are propagated through the detector and reconstructed. In this sense these two productions are triggered: one for the presence of a Ξ^- or $\bar{\Xi}^+$ and the other for the presence of a Ω^- or $\bar{\Omega}^+$, randomly choosing between particle and antiparticle for each small batch of generated events and thus statistically generating a sample that is 50%/50% enriched. The two samples are both re-processed using or not using the information from the SDD, in order to have the same situation as for the real data.

The statistics for both samples and the effect of each selection on the number of events are reported in the lower part of Table 13. The SDD-based selection is not applied on the MC, since the re-productions are already fully homogenous.

All the following results have been obtained using the **withSDD** sample. This choice is justified, since the detectors used in this analysis will then match those used in Pb–Pb. Furthermore, the information from the SDD can improve the reconstruction of cascades especially at low p_T . The improvements to this preliminary analysis that could be applied in a final analysis will be discussed in Section 7.3.

¹ In high luminosity colliders, there is a non-negligible probability that one single bunch crossing may produce several separate collisions in the single event, so-called event with pile-up.

Table 13: Effect of each selection on the number of events for the two reprocessings of the data-sample and the two MC samples. “Physics selected” means that the background events are removed from the sample as explained in the text.

Event Selection (10^6 events)	without SDD	with SDD
On MonAlisa	80.4	80.4
Analyzed	79.5	78.7
SDD	79.5	35.7
Physics selected	65.5	32.1
Well established vertex	57.6	28.7
No Pileup	57.2	28.5
Z_{PV} position Cut	51.1	25.5

Event Selection (10^6 events)	Ξ trig. MC with (without) SDD	Ω trig. MC with (without) SDD
On MonAlisa	4.8 (4.8)	5.2 (5.2)
Analyzed	4.7 (4.7)	5.1 (5.2)
Physics selected	4.7 (4.7)	5.1 (5.2)
Well established vertex	4.6 (4.7)	5.1 (5.1)
No Pileup	4.6 (4.7)	5.1 (5.1)
Z_{PV} position Cut	4.3 (4.4)	4.8 (4.8)

6.2 TOPOLOGICAL CUTS AND INVARIANT MASS DISTRIBUTION

As anticipated in Section 4.3, the analysis technique to identify the cascades and study their production as a function of the transverse momentum in pp collisions is substantially the same used in the analysis of the Pb–Pb collisions, with the obvious differences coming from the large difference in multiplicity between the two collision systems.

The code has been derived from the one used for the analysis of the Pb–Pb collisions. In particular the main object produced is still a container with steps and variables. Most of the variables are exactly the same, but their number is reduced; e.g. the centrality definition is no longer necessary in pp collisions. Again there are two tasks: one for the real data, devoted to optimize the topological selections and produce the invariant mass distributions for the raw spectra extraction; while the other task for the MC data, devoted to performance studies and production of the acceptance-efficiency correction factors.

As for the analysis of the Pb–Pb data the TPC PID ($n_\sigma = 4$) on the three daughters of the cascade candidate is used and the same cuts on the track quality are applied: the presence of an active TPC refit flag and a minimum number of TPC clusters equal to 70 are required.

Table 14: Summary of the cut values used for the cascade candidate selection in pp collisions. The values tuned at the analysis level are highlighted in grey. For completeness, the values of the same cuts used for the initial reconstruction of the events are shown in the first column.

Cuts on Cascades	pp reconstruction	Optimized analysis value for Ξ	Optimized analysis value for Ω
Max allowed DCA cascade daughter (cm)	2.0	1.5	0.5
Min allowed bachelor ip (cm)	0.01	0.03	0.01
Min allowed cos of cascade PA	0.98	0.985	0.990
Min radius of the fiducial volume (cm)	0.2	0.4	0.4
<hr/>			
Cuts on V^0 's			
Window around the Λ mass (GeV/c^2)	± 0.008	± 0.006	± 0.008
Max allowed DCA between daughter tracks (cm)	1.5	1.5	1.5
Min allowed cosine of V^0 's PA	0.9	0.9	0.9
Min radius of fiducial volume (cm)	0.2	0.2	0.2
Min Allowed V^0 ip (cm)	0.01	0.05	0.01
Min allowed ip for 1° daughter (cm)	0.05	0.05	0.05
Min allowed ip for 2° daughter (cm)	0.05	0.05	0.05
<hr/>			
Added cuts			
Window around the Ξ mass value for Ω (GeV/c^2)	-	-	± 0.008

In Table 14 the values in the second and third columns are the optimized cuts set at the analysis level for Ξ and Ω . These values have been chosen and validated via the same quality assurance study performed in Pb–Pb analysis and described in detail in Section 5.2. The list of topological variables is exactly the same as for the Pb–Pb data analysis, as reported in the Table. The cut on the decay length of the cascades has also been studied. It seems to have a negligible effect and therefore has not been applied. For the Ω candidates, the cut on the invariant mass in the Ξ hypothesis is applied (a $\pm 8 \text{ MeV}/c^2$ region around Ξ PDG mass is rejected).

Compared to the values set for the Pb–Pb analysis, the topological cuts used in pp are looser: this was expected due to the much lower multiplicity.

The effect of the cut optimization in the invariant mass distributions is shown in Figure 76, where the gray line corresponds to the set of reconstruction cut values and the coloured line to the analysis ones (TPC-PID on daughter tracks is applied in both cases): the background is reduced by about 60% (40%), and the signal decreases by 10% (less than 10%) for the Ξ (Ω). The adopted cut values are also looser than the ones used in the multi-strange analysis in pp collisions at 7 TeV: this was done due to the lower available signal in pp collisions at 2.76 TeV and considering that the (almost flat) background can be fitted quite easily.

Due to the low available event statistics combined with the low Ω yield, as seen in Figure 76, the analysis was performed on the sum of particle and antiparticle.

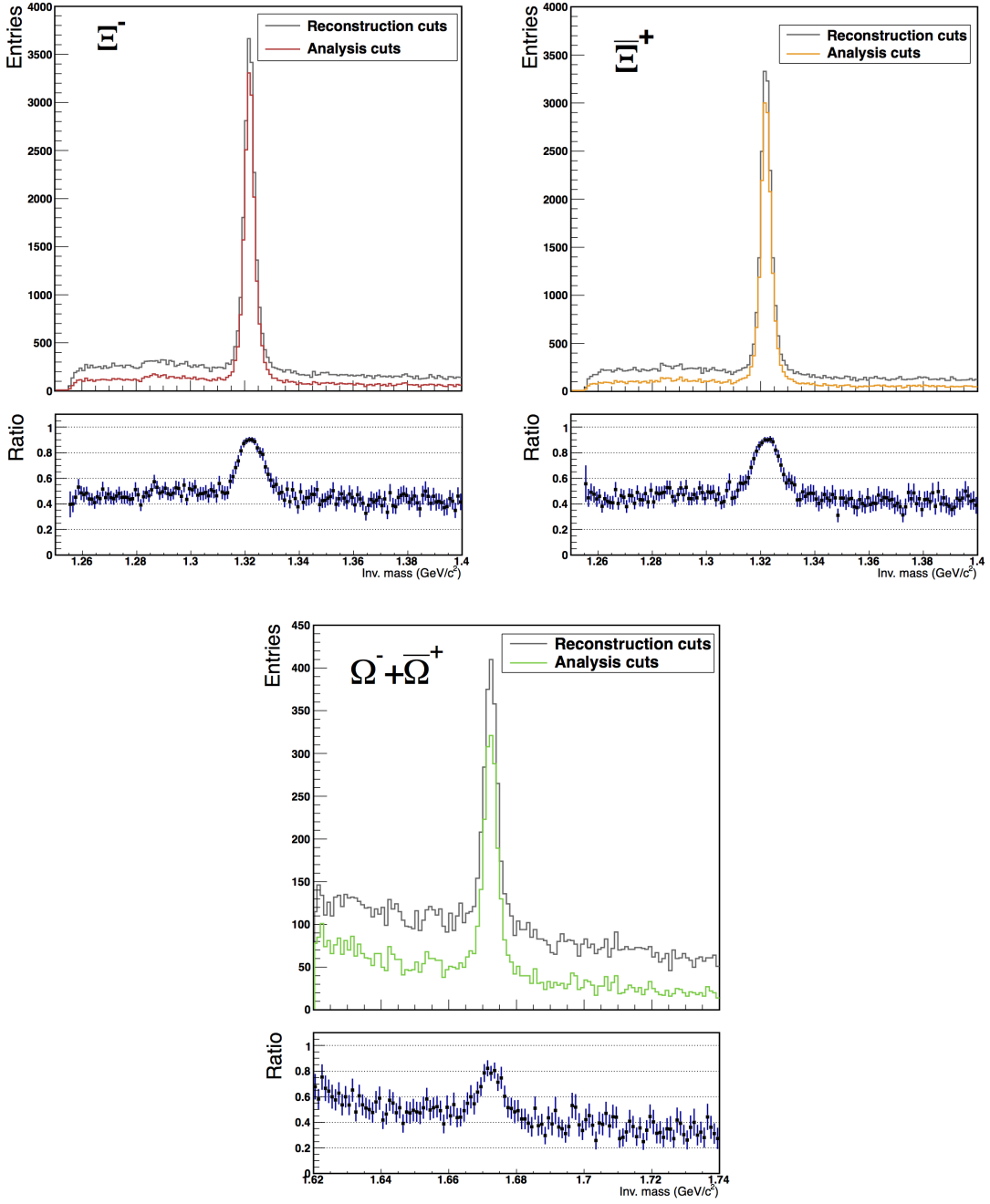


Figure 76: Invariant mass distributions for Ξ^- , Ξ^+ and $\Omega^- + \Omega^+$ candidates (top panels) integrated over p_T with two different sets of cuts: looser reconstruction cuts (black histograms) and final cuts (coloured histograms). A TPC-PID 4σ -cut is requested for each of the three daughters in all the cases. The ratios between the two distributions are also reported (bottom panel).

6.3 TRANSVERSE MOMENTUM SPECTRA

As in the case of Pb–Pb analysis, the goal is to measure the cascade yield in pp collisions as a function of the transverse momentum and integrated in p_T . The steps to reach this result are the same described in the previous Chapter, with some specific features and additional details described in the following Sections.

6.3.1 Signal extraction

To extract the signal, a symmetric 3σ wide region around the peak is defined fitting the distribution with the sum of a gaussian and a polynomial: the fit is only used to obtain the σ . The peak region is represented in red in Figure 77 and contains both the signal and the background. In the case of pp collisions the shape of the background, especially for the Ξ , is particularly flat and is easily fitted in the two side band regions with a first degree polynomial function. As done in the analysis of Pb–Pb collisions, the difference between the signal plus background counts in the peak region and the estimated background in the same region provides the pure signal raw counts.

The procedure to extract the signal raw counts is repeated in several p_T bins, whose limits are listed in Table 15. In Figure 78 the uncorrected p_T spectra are shown for the Ξ^- , the $\bar{\Xi}^+$ and the $\Omega^- + \bar{\Omega}^+$, with $|y| < 0.3$ in the first (low p_T) 10 bins for the Ξ and the first 3 bins for the Ω and to $|y| < 0.5$ in the remaining parts of the p_T range. The reduction of the rapidity window at low p_T is made to ensure that the efficiency is flat in rapidity in the selected range and far from the edges of the acceptance as explained in the next Section (6.3.2). In the Figure 78 the raw counts have been normalized to a unitary rapidity window for all the p_T bins.

Table 15: Binning for the cascade transverse momentum spectra.

Particle	Number of bins	Bin limits (GeV/c)
Ξ	14	{0.6, 0.8, 1.0, 1.2, 1.4, 1.6, 1.8, 2.0, 2.2, 2.4, 2.6, 3.0, 3.6, 4.8, 6.0}
Ω	7	{1.0, 1.2, 1.6, 2.0, 2.4, 3.2, 4.0, 5.0}

6.3.2 Acceptance–efficiency correction

In the efficiency definition (Equation 5.4) for pp collisions, the denominator is filled with all MC primary cascades, no matter which decay channel they have (in this way the branching ratio contribution to the efficiency is included) and before any event selection, ensuring that the correction we use is an inclusive

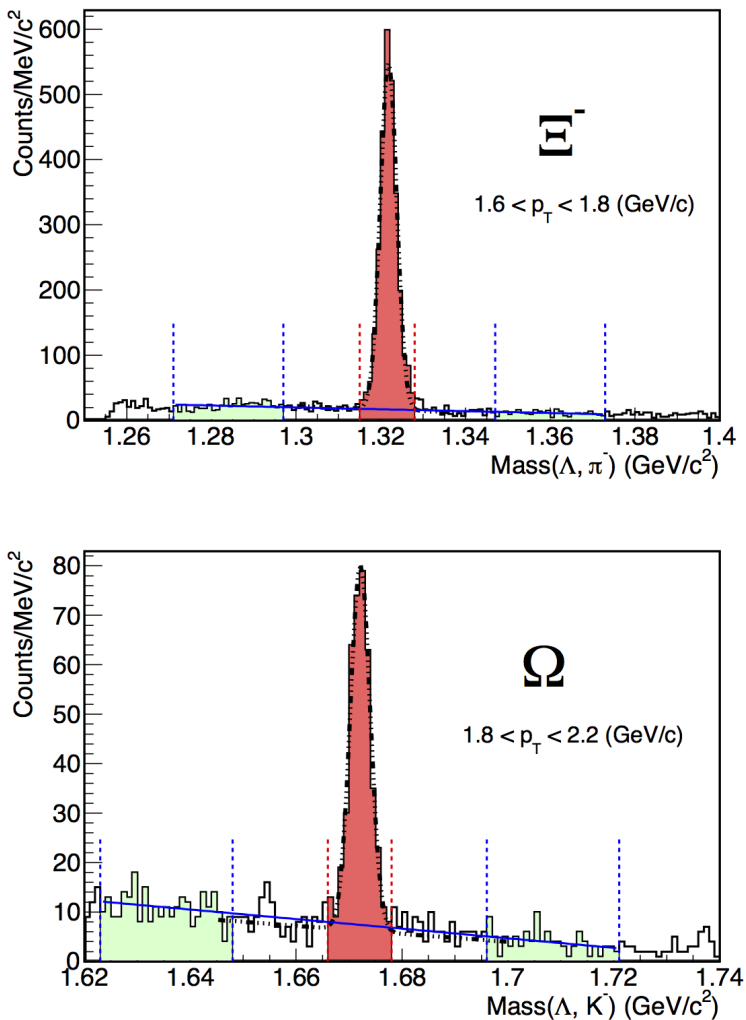


Figure 77: Two invariant mass distributions ($1.6 < p_T < 1.8$ GeV/c for Ξ^- and $1.8 < p_T < 2.2$ GeV/c for $\Omega^- + \bar{\Omega}^+$) illustrating the signal extraction procedure. The signal region is marked off by the red dashed lines and red fill, while the background regions are marked with blue dashed lines and green filled areas. The black dashed curve represents the fit of the whole distribution with the sum of a Gaussian plus a polynomial function, whereas the blue curve represents the fit of the background sampled on both sides of the peak.

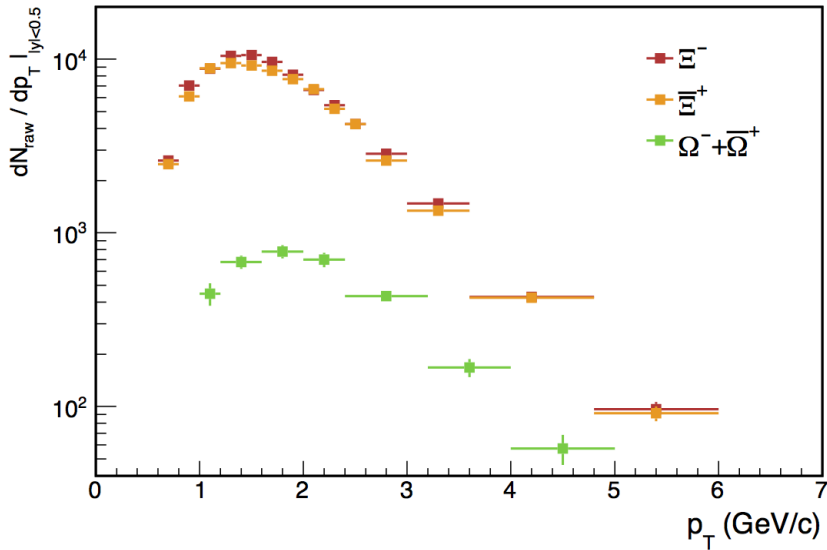


Figure 78: Uncorrected p_T spectra for Ξ^- , Ξ^+ , and $\Omega^- + \bar{\Omega}^+$, in $|y| < 0.5$ ($|y| < 0.3$ at low p_T , as mentioned in the text).

correction, i.e. contains vertexing and triggering efficiencies embedded. On the other side, the numerator, as for the Pb–Pb data analysis, is the number of Ξ or Ω reconstructed using the same algorithm as for the real data, after the event selections and requiring the presence of an associated cascade in the MC stack for the same event. As done for the real data, for each p_T bin a 3σ cut in the peak region is applied to the invariant mass, where the σ of the signal region is determined from a Gaussian fit. In addition the generated p_T is used both for the numerator and the denominator.

As anticipated in the description of raw spectra extraction, in the low p_T bins a narrow range in rapidity is applied. Similarly to the Pb–Pb analysis, this rapidity range is the one in which the efficiency is almost flat (within $\sim 10\%$) over the full measured range in p_T . This can be seen in the projection of the two dimensional efficiency on the rapidity axis shown in Figure 79. This range corresponds to $|y| < 0.5$ for $\Xi(\Omega)$ $p_T > 2.6(2.4)$ GeV/c; for lower transverse momenta, the narrower rapidity range ($|y| < 0.3$) has been adopted.

At $p_T < 0.6$ GeV/c for Ξ and $p_T < 1.0$ GeV/c for Ω the statistics in the data is rather poor and a robust signal extraction cannot be performed.

In the following, a few improvements to the first estimation of the correction factors are discussed.

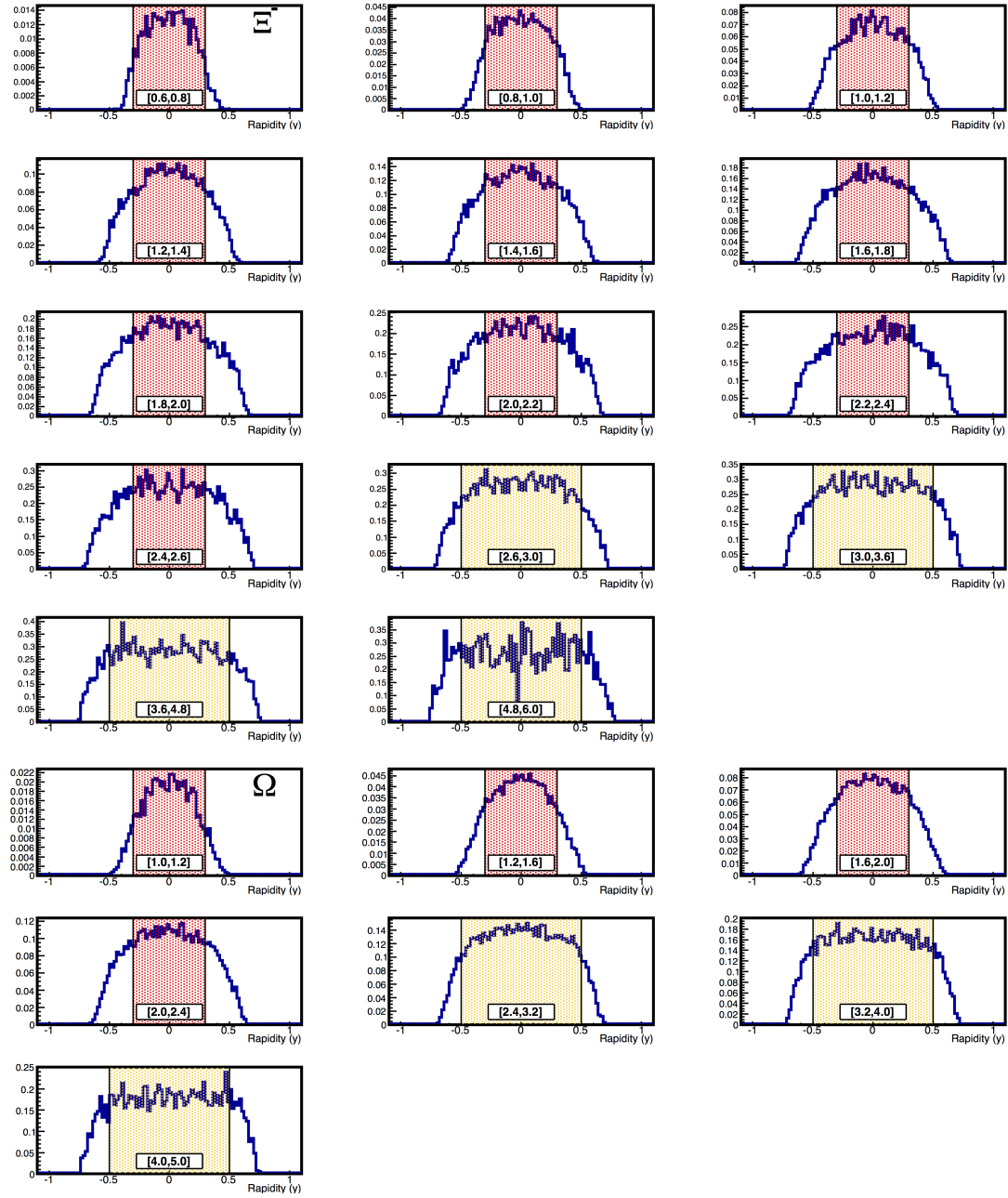


Figure 79: Distribution in rapidity of the Ξ^- (upper pads) and $\Omega^- + \bar{\Omega}^+$ (lower pads) acceptance-efficiency for different transverse momentum bins. The regions in y , where the distributions can be assumed to be almost flat, are highlighted with a coloured transparent box.

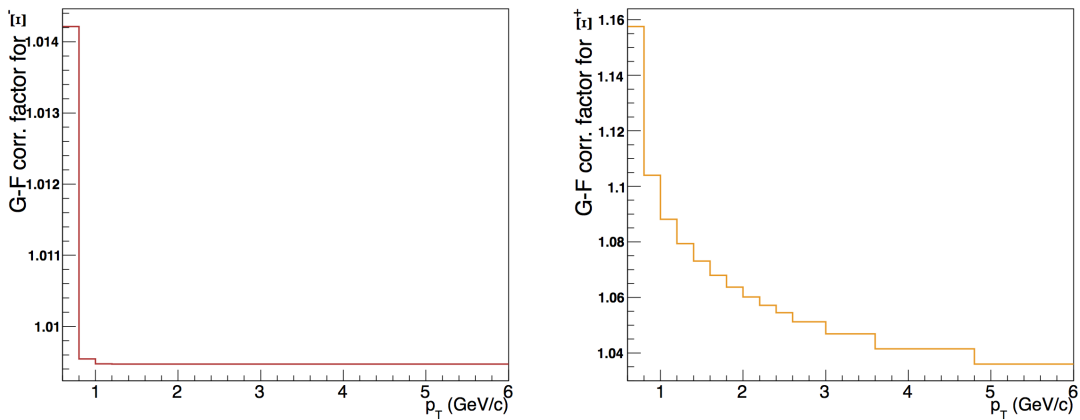


Figure 80: Correction factors for the efficiency due to the inappropriate GEANT3 description of the $p(\bar{p})$ cross sections.

GEANT3/FLUKA correction

The GEANT3/FLUKA correction (described in Section 5.3.2 for the analysis of the Pb–Pb collisions) has been applied also in the pp data analysis. The $\epsilon_{\text{GEANT3}}/\epsilon_{\text{FLUKA}}$ ratio is the same but the correlation between the baryon daughter transverse momentum and the parent cascade transverse momentum (MC dependent) has been recalculated, also considering that different selections were used.

In Figure 80, as an example, the correction factors to be applied to the efficiency are shown for Ξ^- and Ξ^+ .

As can be seen this correction is larger for the antiparticle than for the particle and becomes smaller for p_T higher than 3 GeV/c. Here again, after the GEANT3/FLUKA correction, a slight difference between particle and antiparticle is still present at low momenta. As an example, in Figure 81 the calculated efficiencies as a function of p_T are shown for Ξ^- , Ξ^+ and $\Omega^- + \bar{\Omega}^+$. The efficiency for the Ω with particle and antiparticle added has been obtained averaging the efficiency calculated separately for the Ω^- and for the $\bar{\Omega}^+$.

Dependence of the efficiency on the Z position of the primary vertex

When considering the definition of the efficiency for this analysis, where the denominator is measured before any event selections, it is necessary to check that all the applied event selections have the same effect for real and MC data. Thus we look for some systematic contributions coming from one of these selection, focusing here on the cut $|Z_{\text{PV}}| < 10$ cm. In Figure 82 the Z coordinate distribu-

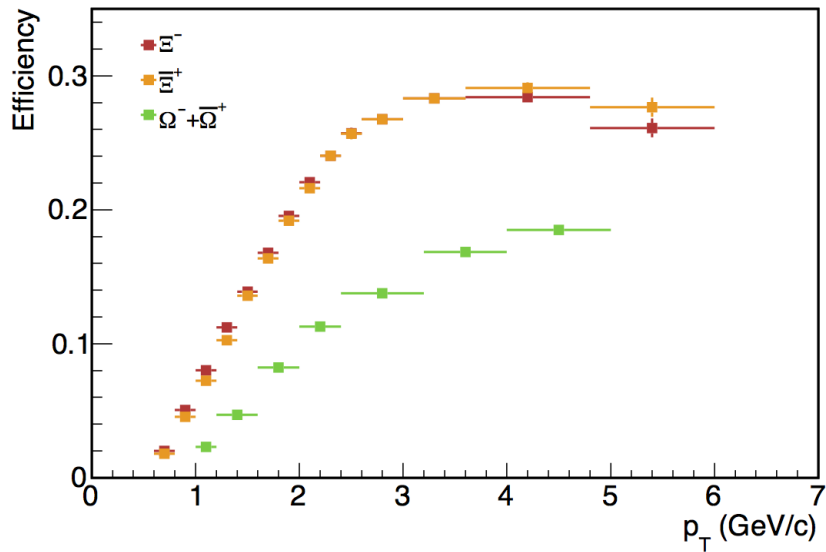


Figure 81: Efficiency factors (including acceptance and branching ratios) as a function of p_T in the rapidity window $|y| < 0.5$ (< 0.3 at low p_T) for Ξ^- , Ξ^+ and $\Omega^- + \Omega^+$.

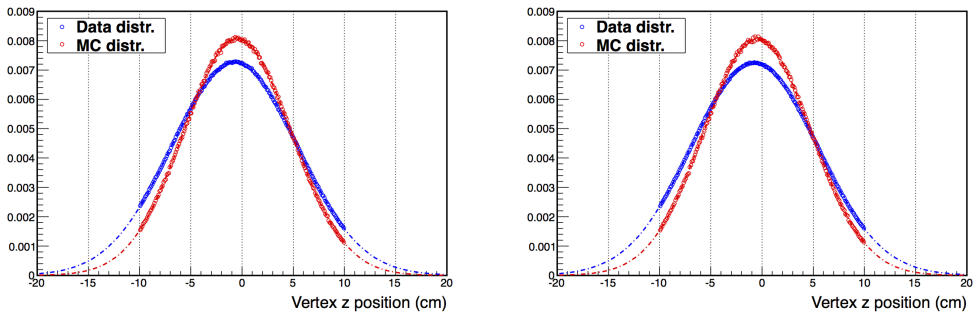


Figure 82: Distribution of the Z coordinate of Primary Vertex, in Data and MC, for all the available samples: (left) with SDD, (right) without SDD.

tion of the primary vertex is compared for all the events in the two available samples with SDD and without SDD. In each case the distribution is compared with the same distribution for the corresponding MC samples. These plots are obtained, at the analysis level, after the application of all the event selections, and in particular after the cut on Z_{PV} . A Gaussian fit on both the distributions (real and MC data) is performed to measure the fraction of events cut away by the selection on Z_{PV} .

The fraction of such events has been evaluated taking the integral of the Gaussian function for $|Z_{PV}| > 10$ cm, both for real and MC data. For the two samples it is found that:

WITH SDD SAMPLE

Data Integral Residual - MC Integral Residual = 10.6% - 5.7% = 4.9%;

WO-SDD SAMPLE

Data Integral Residual - MC Integral Residual = 10.7% - 5.7% = 5.0%.

As a first approach, this percentage was directly applied to correct the normalization factor, scaling the chosen data set by the corresponding fraction. Then, we tried to improve the description of the dependence of the efficiency on the Z_{PV} of each events. The best way would be to perform a multi-dimensional study (transverse moment, rapidity, Z vertex position) of the efficiency, but because of the poor available statistics, we decided to produce the efficiency versus p_T in two different Z_{PV} regions: $0 < |Z_{PV}| < 5$ cm and $5 < |Z_{PV}| < 10$ cm.

In Figure 83, the efficiencies measured using events coming from these two regions only are compared with those measured using all the events within $|Z_{PV}| < 10$. The efficiency shown in these plots is the “physics efficiency”²; to emphasize only the differences due to the cut on the Z vertex position. It can be appreciated that there is a small difference at low p_T both for Ξ and Ω .

In order to improve the efficiency measurement, taking into account the difference in the Z vertex distribution between real and MC data, a new efficiency is computed using the efficiencies measured in the two Z vertex regions ($0 < |Z_{PV}| < 5$ cm and $5 < |Z_{PV}| < 10$ cm), weighted using the fraction of events for each of these regions in the Z_{PV} distribution of the real data. This corresponds to the following formula:

$$\begin{aligned} eff' &= J \times eff_{0-5} + K \times eff_{5-10} \\ &= \left(\frac{A+B+C}{A'+B'+C'} \right) \left\{ \left(\frac{A'}{A} \right) eff_{0-5} + \left(\frac{B'}{B} \right) eff_{5-10} \right\}, \end{aligned} \quad (6.1)$$

where the two weights J and K are defined as the fraction of events for each Z vertex regions in the real data normalized to the same quantities in the MC. So A, B and C correspond respectively to the number of the events in the regions $0 < |Z_{PV}| < 5$ cm, $5 < |Z_{PV}| < 10$ cm and $|Z_{PV}| > 10$ cm for MC, and A', B' and C' are the same quantities for the real data.

² This “physics efficiency” can be defined as an efficiency where the denominator is taken after all the event selections, as done in the Pb–Pb analysis.

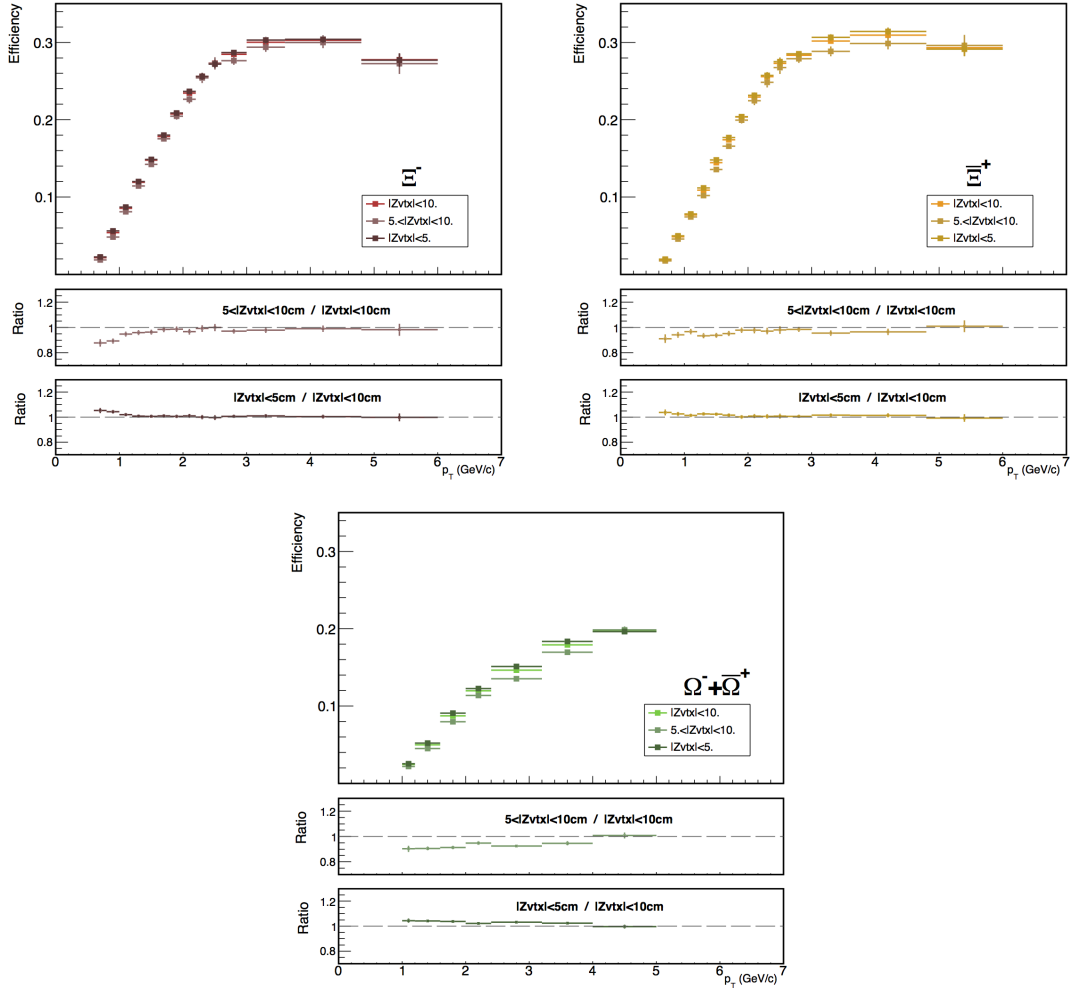


Figure 83: Dependence of the efficiency on the Z vertex selection, in the conditions described in the text (top panel). In the bottom part of each plot one can see the ratio of the efficiency measured using events with $0 < |Z_{PV}| < 5$ cm and $5 < |Z_{PV}| < 10$ cm on the efficiency measured using events with $|Z_{PV}| < 10$ cm and the superposition of the efficiencies measured applying the three different Z_{PV} cuts.

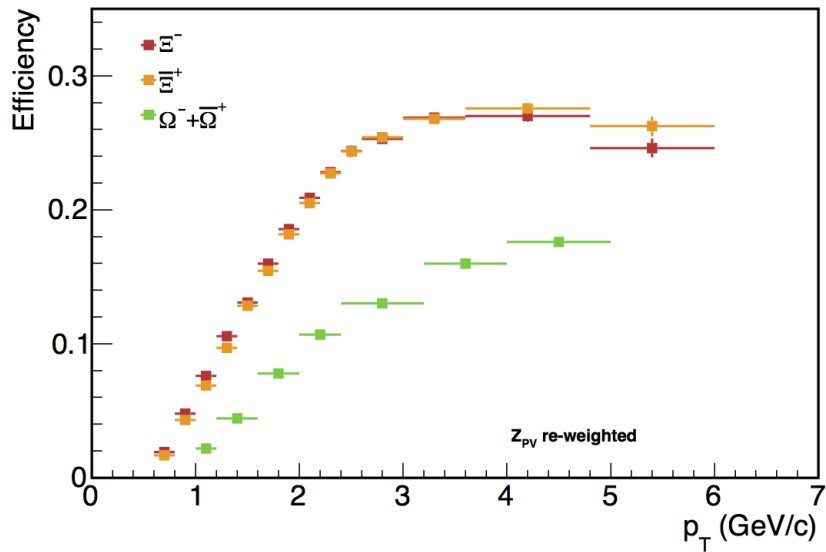


Figure 84: Efficiency factors (including acceptance and branching ratios) as a function of p_T in the rapidity window $|y| < 0.5$ (< 0.3 at low p_T) for the Ξ^- , Ξ^+ and for the $\Omega^- + \Omega^+$ added, re-weighted with the respect to the experimental data Z_{PV} distribution as described in the text.

The new re-weighted efficiencies are shown in Figure 84. In Figure 85 the ratios of the efficiencies with and without this re-weighting are shown: as can be seen, there is approximately a 5% difference between the weighted and the unweighted efficiencies. Of course, the new efficiency takes into account the different widths of the vertex Z distribution in the real data and in the MC, and are thus used for the correction.

6.3.3 Normalization to the inelastic collisions

The normalization to the number of events can be performed with respect to different classes of interactions. In particular pp interactions can be classified as elastic or inelastic (INEL, where new particles are produced). The inelastic pp collision can be diffractive or not. A diffractive event is characterized by the colliding particle(s) being exited and consequently de-exited (fragmentation). Based on this, the following classes can be distinguished within the inelastic collisions: single-diffractive events (SD) where only one of the colliding particles becomes a diffractive system, double-diffractive events (DD) where both of particles become diffractive systems and non-diffractive events (ND) where no

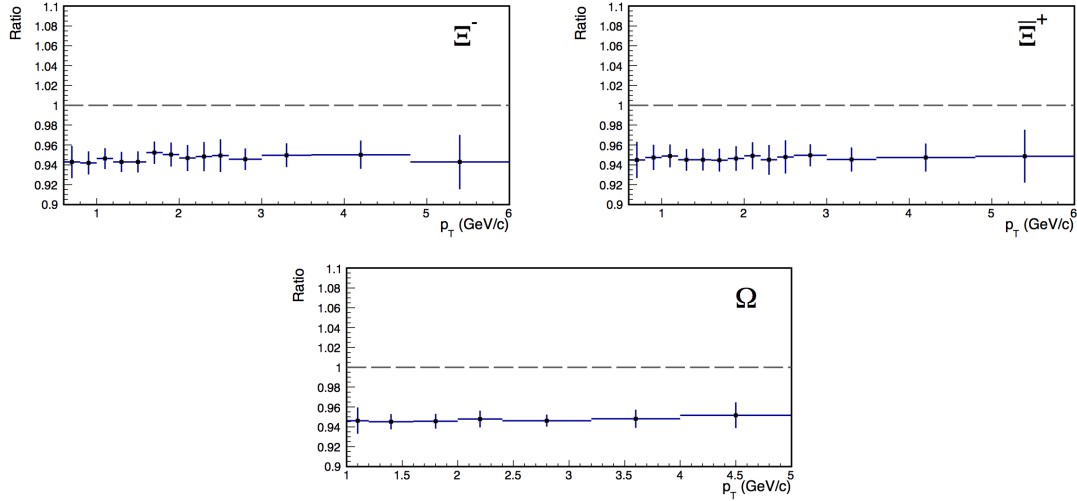


Figure 85: Comparison of the standard and re-weighted efficiency as a function of p_T for the Ξ^- , Ξ^+ and for the $\Omega^- + \bar{\Omega}^+$ added: ratio re-weighted over standard.

diffractive systems are created. In diffractive events particles are mainly created at rapidity close to the one of the parent particle. As a consequence, the multi-strange particles at mid-rapidity come from ND events. Historically, experiments have measured Non Single Diffraction events (NSD, i.e. excluding the SD events). This is experimentally possible by discriminating the SD events due to their rapidity asymmetry. The DD events however are difficult to separate from the ND events and are sensibly fewer than the ND events, why the NSD event class is often used as a good approximation of the ND event class.

In this analysis has been decided to normalize to the number of inelastic collisions, regardless if diffractive or not, for a seek of simplicity.

From Equation 5.1 and the definition of acceptance-efficiency used in this analysis, with the denominator taken before any event selection, if one normalizes to the triggered events (that means after the so-called physics selection) needs one last ingredient to obtain the corrected normalization to the inelastic events: the correction factor given from the ratio of triggered events to inelastic events ($N_{\text{trig}}/\text{INEL}$), i.e. the trigger efficiency.

This factor has been measured by the ALICE Collaboration to be equal to $0.883^{+0.058}_{-0.035}$ [131] and is applied to the raw counts, in addition to the acceptance-efficiency correction.

Table 16: Overview of the variation of the measured yields due to the different sources of systematics studied. Also reported are the differences of the modified measurement and the standard one as a fraction of the standard yield.

Ξ^-	Measured yield	$\Delta\sigma/Y$ (%)	$\Delta Y/Y$ (%)
Standard analysis	0.0044511 ± 0.0000713	-	-
Very loose cuts	0.0044748 ± 0.0000742	+0.46	+0.53
Loose cuts	0.0044809 ± 0.0000731	+0.36	+0.67
Tight cuts	0.0044593 ± 0.0000719	+0.21	+0.18
Very tight cuts	0.0044593 ± 0.0000719	+0.21	+0.18
All cuts but mass Ξ	-	-	-
4σ window in signal extraction	0.0044308 ± 0.0000727	+0.32	-0.46
2.5σ window in signal extraction	0.0044507 ± 0.0000711	+0.12	-0.01
Bin-counting method in background measurement	0.0044508 ± 0.0000713	+0.00	-0.01
y cut at low p_T	0.0044071 ± 0.0000654	+0.64	-0.99
Minimum number of TPC clusters per track	0.0044492 ± 0.0000791	+0.77	-0.04
Ω	Measured yield	$\Delta\sigma/Y$ (%)	$\Delta Y/Y$ (%)
Standard analysis	0.0005691 ± 0.0000263	-	-
Very loose cuts	0.0005671 ± 0.0000277	+1.53	-0.35
Loose cuts	0.0005732 ± 0.0000269	+0.99	+0.72
Tight cuts	0.0005407 ± 0.0000253	+1.26	-4.99
Very tight cuts	0.0005325 ± 0.0000250	+1.43	-6.43
All cuts but mass Ξ	0.0005614 ± 0.0000261	+0.57	-1.36
4σ window in signal extraction	0.0005670 ± 0.0000269	+0.99	-0.37
2.5σ window in signal extraction	0.0005587 ± 0.0000257	+0.98	-1.82
Bin-counting method in background measurement	0.0005698 ± 0.0000262	+0.40	+0.12
y cut at low p_T	0.0006000 ± 0.0000247	+1.59	+5.44
Minimum number of TPC clusters per track	0.0005670 ± 0.0000276	+1.47	-0.37

6.3.4 Point-by-point systematic uncertainties

The main contributions to the systematic uncertainty on the particle spectra have been studied. The starting point has been the list of systematic uncertainties considered in Pb–Pb analysis. In particular for the study of topological cuts, four sets of values have been defined (very loose, loose, tight and very tight cuts) varying by -15%, -10%, + 10% and +15%, respectively, the amount of candidates in the peak region of the invariant mass distribution. As done for the Pb–Pb analysis, to estimate the systematics due to the track quality selection, the analysis has been redone with a tighter cut requiring 80 minimum clusters in the TPC (instead of 70, used as default). The contribution related to the description of the material budget in the MC has again been assumed to be the same estimated in the pp analysis at 7 TeV. In Table 16 the variation of the measured yields for each of the sources of systematic uncertainties and cases are summarized, both for Ξ^- and $\Omega^- + \bar{\Omega}^+$.

Due to the low available statistics, one has to put attention to the meaning of these variations. To check the statistical significance of the estimated systematic

uncertainties the so-called Barlow's criterion has been applied [132]. Taken two measurements of a physical quantity a_1 and a_2 , with statistical uncertainties σ_1 and σ_2 , obtained changing some cuts in the analysis, Barlow suggested to compare the difference $\Delta = a_2 - a_1$ with the difference $\Delta\sigma = \sqrt{|\sigma_2^2 - \sigma_1^2|}$: if the ratio $\Delta/\Delta\sigma$ is larger than 3 the corresponding difference Δ should be accounted as a systematic uncertainty. In Table 16 the values of the difference $\Delta\sigma$, normalized to the yield, for each estimated sources of uncertainties are also reported. They have to be compared with the corresponding $\Delta Y/Y$. This check is important especially for the Ω , for which the statistics is rather low. As can be seen in the Table, only the contribution coming from the variation of the minimum number of cluster in the TPC for the Ω seems to come from statistical instability. As a safety choice the full difference $\Delta Y/Y$ has been taken as estimate of the uncertainty.

The systematic uncertainties have been also studied as a function of p_T . In Figures 86-90 the ratios of the spectra computed in different conditions to the default spectra are shown. No significant p_T dependence is present in all cases.

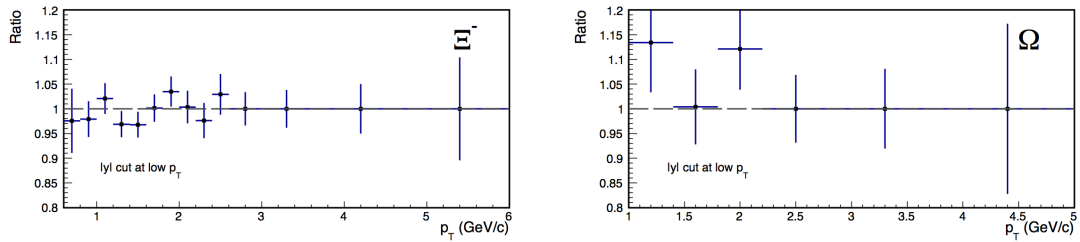


Figure 86: Ratio of corrected spectra when using the y cut in the first 10(3) bins for $\Xi^-(\Omega^- + \bar{\Omega}^+)$ at low p_T for p_T dependence of systematic errors. All the other analysis cuts are applied but this one.

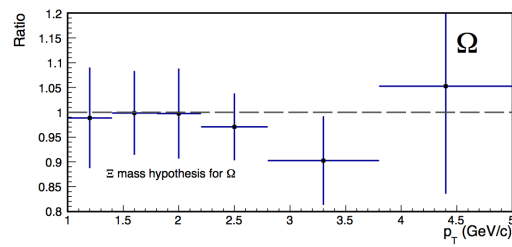


Figure 87: Ratio of corrected spectra using different analysis cuts on the Ξ mass hypothesis for Ω for p_T dependence of systematic errors. All the other analysis cuts are applied but this one.

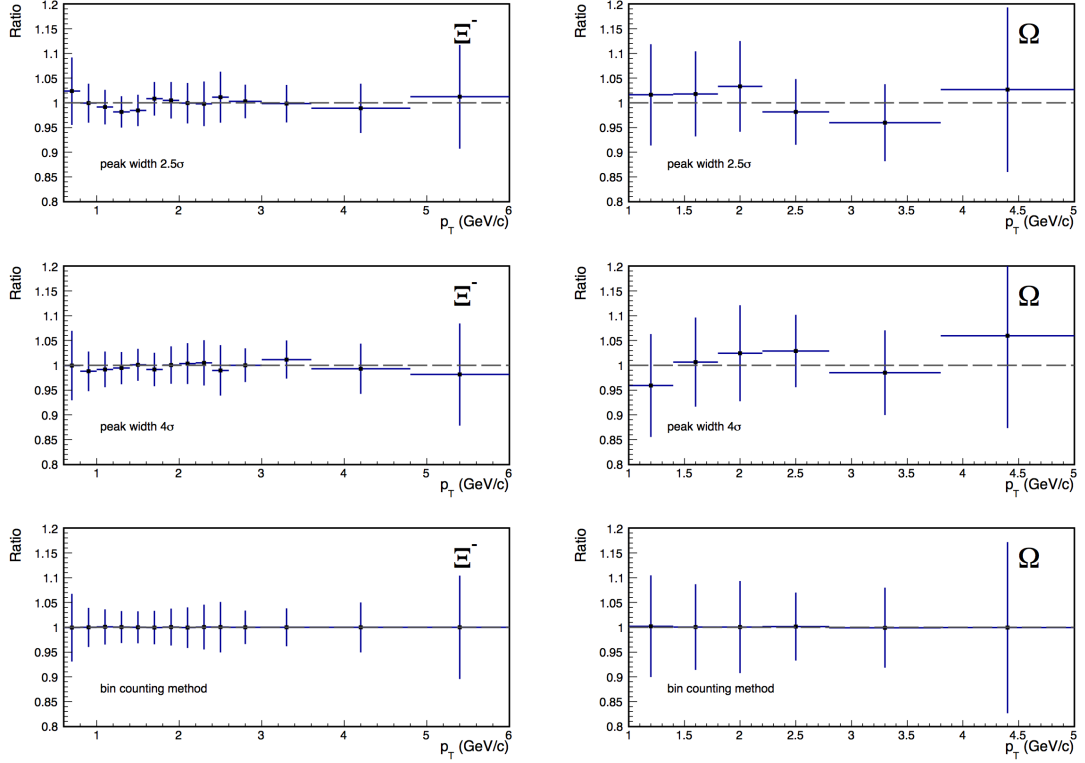


Figure 88: Ratio of corrected spectra using a different signal extraction procedure for p_T dependence of systematic errors (Ξ^- on the left panels, $\Omega^- + \bar{\Omega}^+$ on the right panels): the width of the peak region is 2.5σ in the upper panels and 4σ in the central panels, whereas the windows for background sampling are reduced in the lower panels.

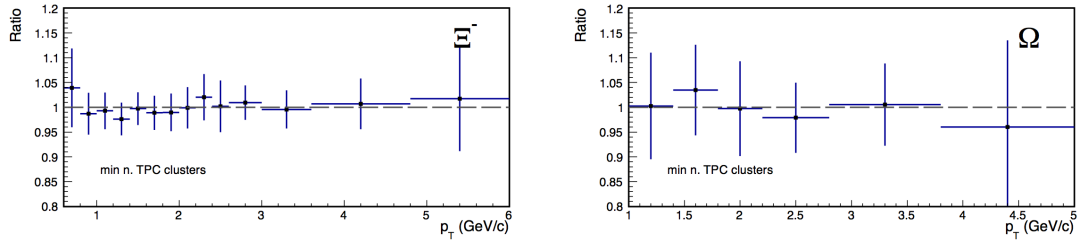


Figure 89: Ratio of corrected spectra using different minimum number of clusters in the TPC used for track quality selection for p_T dependence of systematic errors.

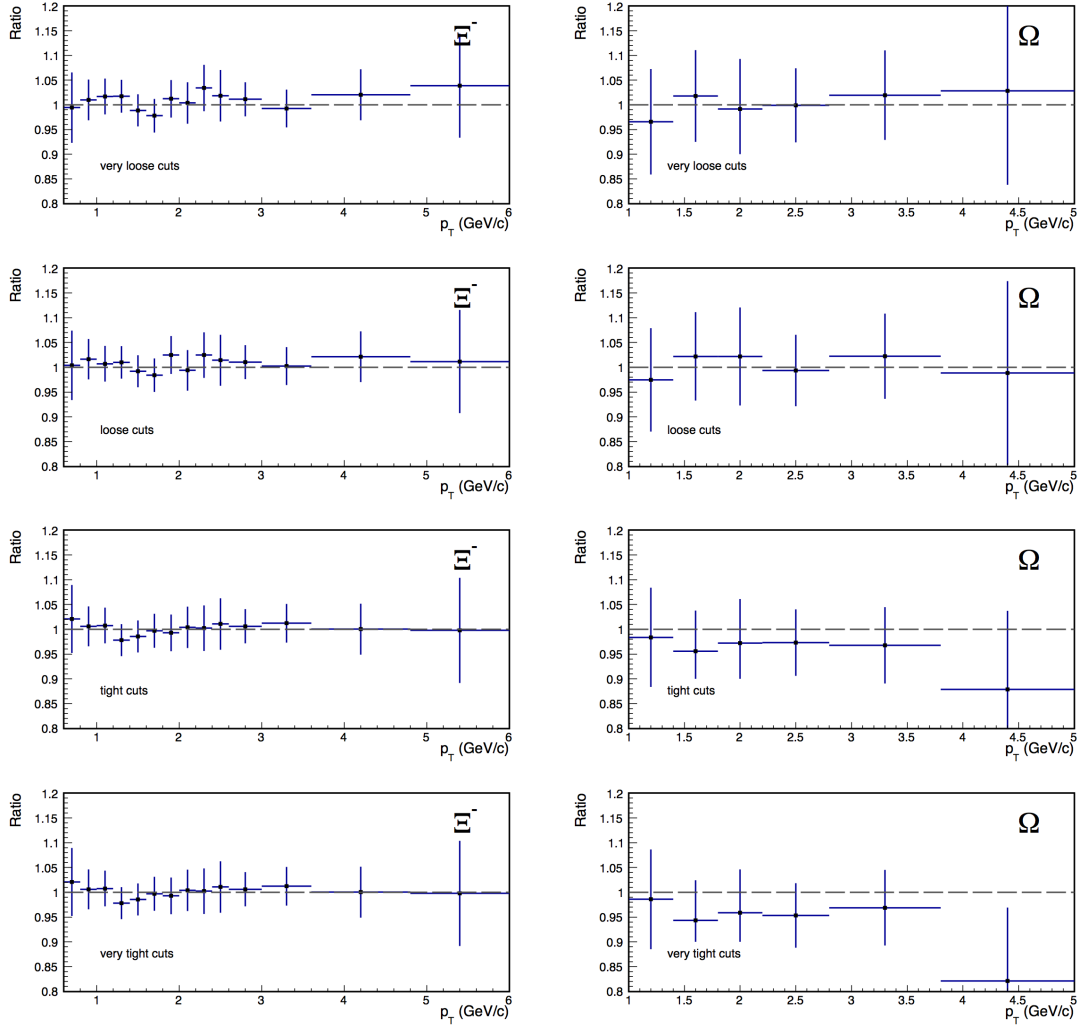


Figure 90: Ratios of corrected spectra computed with different selection cuts to the spectra in the standard analysis (Ξ^- on the left panels, $\Omega^- + \bar{\Omega}^+$ on the right panels): very loose cuts (first panels), loose cuts (second panels), tight cuts (third panels) and very tight cuts (lower panels) are applied.

In summary, the following values are added in quadrature to get the final systematic error:

- material budget in the simulation (4%);
- topological and kinematic selection cuts (1% for Ξ and 6% for Ω);
- for the Ω , removal of candidates within the Ξ mass hypothesis (2%);
- signal extraction procedure (1% for Ξ and 2% for Ω);
- use of FLUKA to correct the antiproton absorption cross section in GEANT3 (1%);
- minimum number of TPC clusters selection (0% for Ξ and 1% for Ω);
- y cut at low p_T (1% for Ξ and 5% for Ω).

Assuming each of the previous sources as independent from the others, the total systematic uncertainty has been obtained by adding in quadrature the single contributions mentioned above and results to be in 5% for Ξ and 9% for Ω , independent of p_T . This systematic uncertainty will be added to the statistical error for each spectra point before fitting the distribution and extracting the yields, as described in the following. A few more considerations on the systematic uncertainty to be added directly on the final p_T integrated yield will be discussed in Section 6.4.

6.3.5 Corrected spectra

The corrected spectra for the cascades in $|y| < 0.5$ are shown in Figure 91. Statistical and systematic errors have been separated and represented with lines and boxes, respectively. Spectra for particles and antiparticles are compatible within the errors, as expected at the LHC energy. This analysis has been approved as preliminary by the Collaboration and presented for the first time at Strangeness in Quark Matter 2013 Conference, 21 – 27 July 2013 in Birmingham.

6.3.6 Analysis check: $c\tau$

Also for the analysis of the pp data the $c\tau$ estimated from the distribution of the decay length ($m c L/p$) has been checked to be consistent with the PDG values.

In Figure 92 the corrected spectra are shown with the fit and the average decay length values. The p_T independent systematic errors of 5% and 9%, for Ξ and Ω

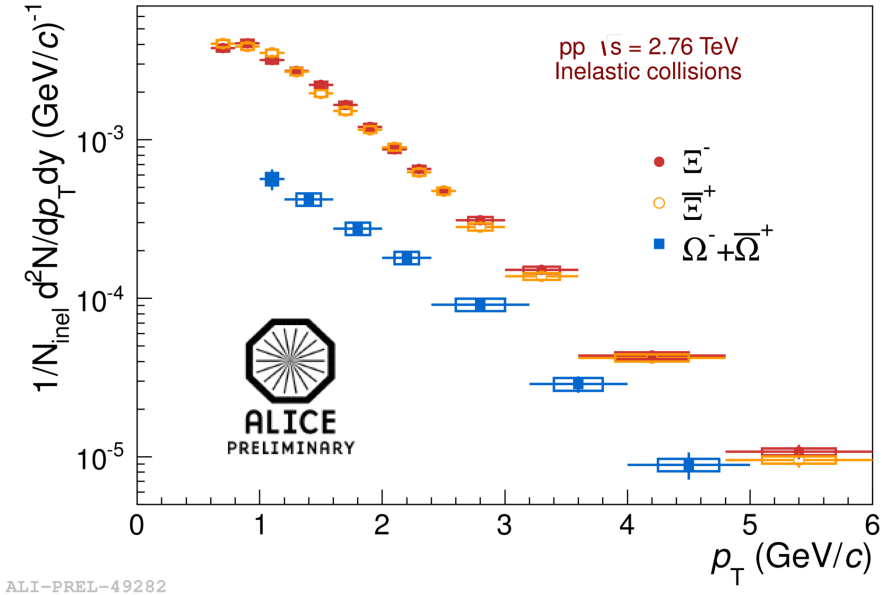


Figure 91: Corrected p_T spectra for the Ξ^- , Ξ^+ and $\Omega^- + \bar{\Omega}^+$ at mid-rapidity. The error bars represent the statistical uncertainties, and the boxes the systematic ones.

respectively, have been added to the corrected spectra before fitting. The values obtained from the fits are consistent with the PDG values well within 1σ , both for Ξ and Ω .

6.4 YIELD EXTRACTION

In order to extract particle yields integrated over the full p_T range, the spectra are fitted using a Lévy-Tsallis function (Equation 5.19), which gives the best fit to the spectra (see χ^2/ndf in Table 18). Examples of fits are shown in Figure 93.

The production yields are then calculated integrating the corrected spectra in the measured p_T range and extrapolating with the fit function outside the measured range: they are presented in Table 17.

In Table 17 the statistical and systematic errors are quoted separately. For the final p_T integrated yields, two additional systematic uncertainty contributions have to be taken into account.

First, an additional systematic error of 10% (15%) has been added to the final Ξ (Ω) yield to safely take into account the uncertainty due to the extrapolation at low and high p_T . As done for the Pb–Pb analysis this has been estimated fitting the distribution with different functions and comparing the standard yield

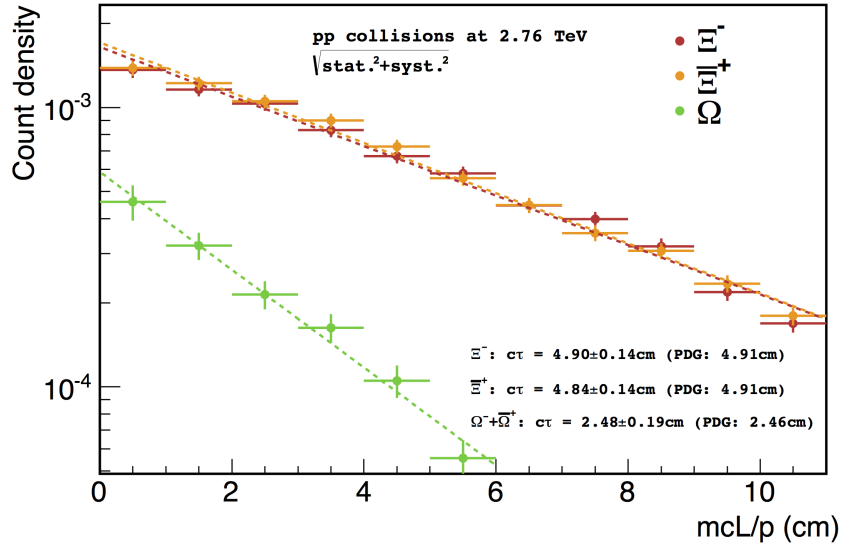


Figure 92: Corrected mcL/p distributions for the cascades with the PDG $c\tau$ values in parenthesis compared to the average values from the fit in the range shown. The errors on the corrected spectra are the sum in quadrature of the statistical and systematic uncertainties.

with the one obtained from each functions (Figure 94). The values of the yields and the corresponding systematics from the different functions are reported in Table 18.

Moreover the uncertainty on the normalization procedure must be considered. This is provided by the Collaboration and is estimated to be asymmetrical ($+6.6\%$, -4.0%), to be applied to all the yield values [131].

SEPARATE PARTICLE AND ANTI PARTICLE FOR Ω

The exercise to perform the same analysis separately for the Ω^- and Ω^+ , has been performed.

The main problem concerns the available statistics, which is rather poor especially at high p_T and makes it difficult to perform reliable signal extraction. Due to the large available statistics in the MC the same problem is not there for the acceptance-efficiency correction calculation.

The corrected spectra, shown in Figure 95, are compatible within the statistical uncertainties. The values of the separate yields for particle and antiparticle,

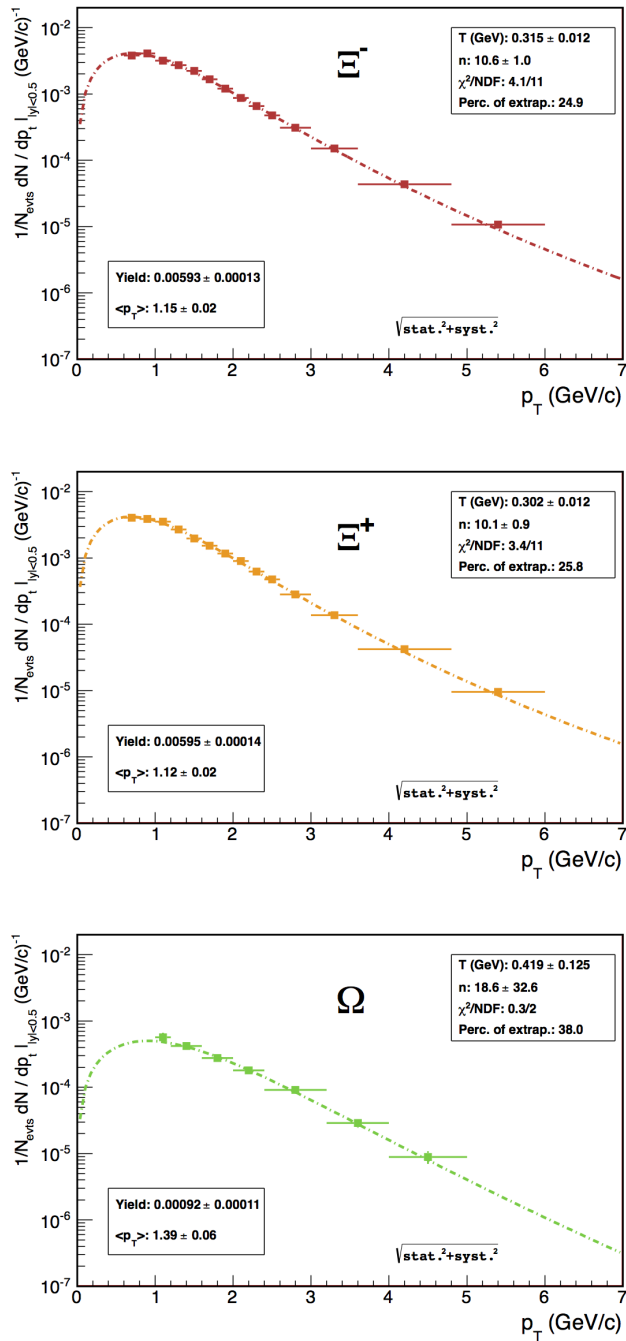


Figure 93: Corrected Ξ^- , Ξ^+ and $\Omega^- + \bar{\Omega}^+$ transverse momentum spectra plotted with Lévy-Tsallis fit curves. In the up right pad the fit parameters T and n , the χ^2/ndf and the total extrapolated yield percentage are shown. In the bottom left pad the yield and the mean transverse momentum are provided. The error on each point includes both statistical and systematical uncertainties.

Table 17: Integrated mid-rapidity ($|y| < 0.5$) yields of multi-strange baryons in pp collisions at $\sqrt{s} = 2.76$ TeV. The yields are compared with the those at lower (900 GeV) and higher (7 TeV) energies, measured by the ALICE Collaboration.

Yield	Ξ^-	Ξ^+
pp at 900 GeV[133]	$(\Xi^- + \Xi^+)$	$0.0101 \pm 0.0020 \pm 0.00009$
pp at 2.76 TeV	$0.0059 \pm 0.0001^{+0.0007}_{-0.0007}$	$0.0060 \pm 0.0001^{+0.0007}_{-0.0007}$
pp at 7 TeV[128]	$0.0080 \pm 0.0001^{+0.0007}_{-0.0005}$	$0.0078 \pm 0.0001^{+0.0007}_{-0.0005}$
Yield	Ω^-	Ω^+
pp at 900 GeV[133]	-	-
pp at 2.76 TeV	$(\Omega^- + \Omega^+)$	$0.00092 \pm 0.00007^{+0.00017}_{-0.00017}$
pp at 7 TeV[128]	$0.00067 \pm 0.00003^{+0.00008}_{-0.00007}$	$0.00068 \pm 0.00003^{+0.00008}_{-0.00007}$

Table 18: Yields from the fitting of corrected spectra using different functions.

Particle	Fit function	Yield	$\Delta Y/Y (\%)$	$\chi^2/n.d.f.$	Extr. frac. yield at low p_T
Ξ^-	Lévi-Tsallis	0.0059	-	4.10/11	0.249
	p_T exponential	0.0064	-8.5	29.48/12	0.308
	m_T exponential	0.0055	6.8	92.60/12	0.186
	Bose-Einstein	0.0055	5.8	88.13/12	0.189
	Fermi-Dirac	0.0054	8.5	96.88/12	0.183
	Boltzmann	0.0054	8.5	134.31/12	0.170
	Blast-wave	0.0057	3.4	44.43/10	0.231
Ω	Lévi-Tsallis	0.0010	-	0.73/4	0.402
	p_T exponential	0.0011	-17.5	0.33/5	0.492
	m_T exponential	0.0009	8.8	3.14/5	0.347
	Bose-Einstein	0.0009	8.4	2.98/5	0.350
	Fermi-Dirac	0.0009	9.2	3.31/5	0.344
	Boltzmann	0.0009	11.6	4.94/5	0.327

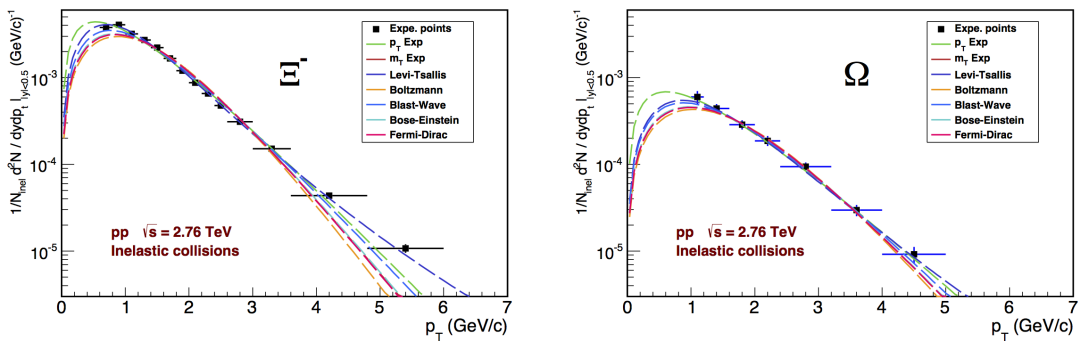


Figure 94: Corrected spectra for Ξ^- (left) and $\Omega^- + \Omega^+$ (right) in pp collisions fitted with the functions listed in Table 18.

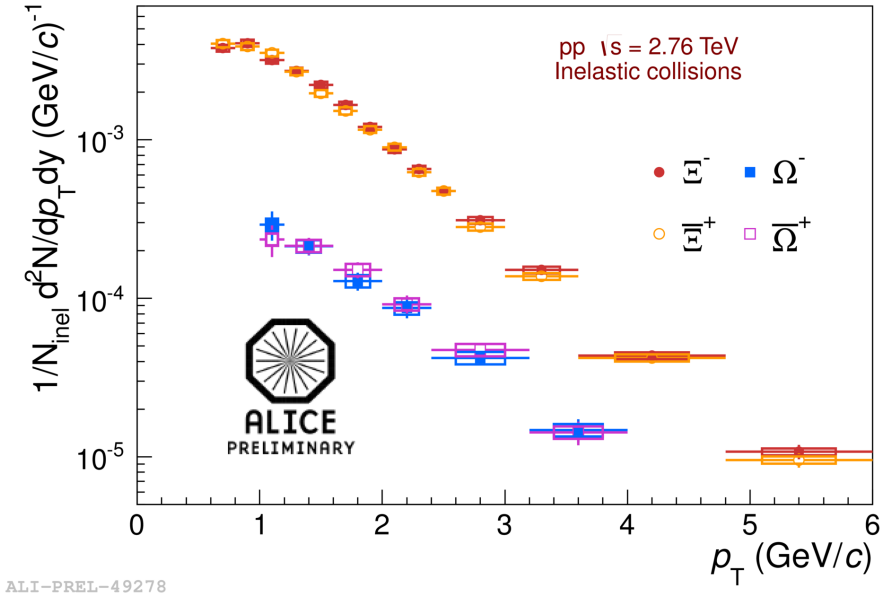


Figure 95: Corrected p_T spectra, for Ξ^- , Ξ^+ , Ω^- and Ω^+ . The error bars represent the statistical uncertainties, and the boxes the systematic ones.

reported in Table 19, confirm such observation. The transverse momentum bin between 4 and 5 GeV/c has been taken out due to the very poor statistics. This is clear looking at Figure 96, where the signal extraction procedure in that bin is shown both for Ω^- and Ω^+ .

Table 19: Integrated mid-rapidity ($|y| < 0.5$) yields for Ω^- and Ω^+ separated. The errors contain both statistical and systematic uncertainties added in quadrature.

Particle	Yield
Ω^-	0.00048 ± 0.00009
Ω^+	0.00046 ± 0.00006

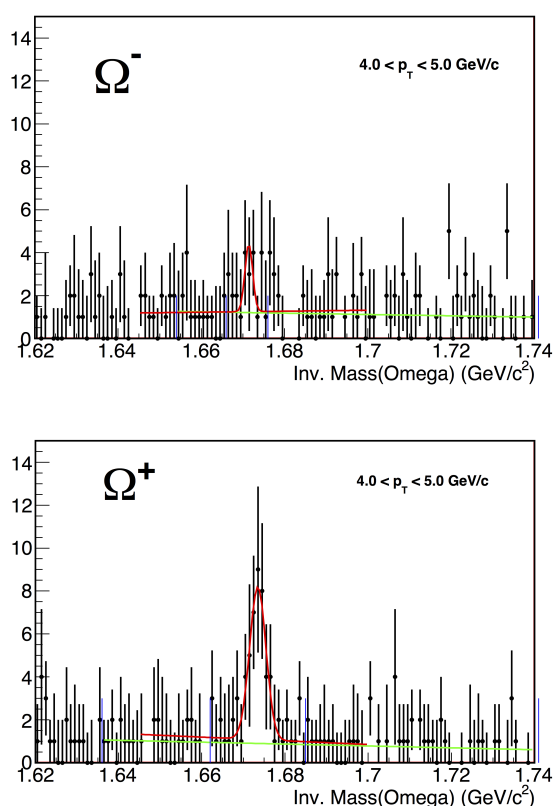


Figure 96: Signal extraction in the higher p_T bins in the binning adopted for the Ω added analysis and excluded in this analysis, for Ω^- and $\bar{\Omega}^+$.

FURTHER RESULTS AND DISCUSSION

Transverse momentum spectra and yields at mid-rapidity for Ξ and Ω baryons in Pb–Pb and pp collisions at $\sqrt{s_{\text{NN}}} = 2.76$ TeV have been already presented in Chapters 5 and 6. In the present Chapter these results are discussed in connection with the following three topics:

- comparison of spectra and yields with model predictions;
- study of strangeness enhancement;
- study of nuclear modification factors for the cascades compared to those for lighter particles.

Most of the theoretical aspects related to these topics and, in particular, the description of the models have already been addressed in Chapter 2.

7.1 SPECTRA COMPARISON WITH MODEL PREDICTIONS

The Ξ and Ω transverse momentum spectra in Pb–Pb collisions are compared to hydrodynamic model calculations. The purpose of this comparison is to test the ability of the models to reproduce yields, spectral shape and centrality dependence. Four models are considered: VISH2+1 [45], HKM [52, 53], Krakòw [46] and EPOS [54, 55, 56].

The results are shown in Figure 97 for the Ξ and Ω hyperons in the five centrality intervals of the present analysis. Predictions in each centrality are available for all the models, except for HKM, which provides spectra only for the 10–20% and 20–40% most central collisions. Moreover, for EPOS the curves correspond to the average of particle and antiparticle as for the data points, while for the

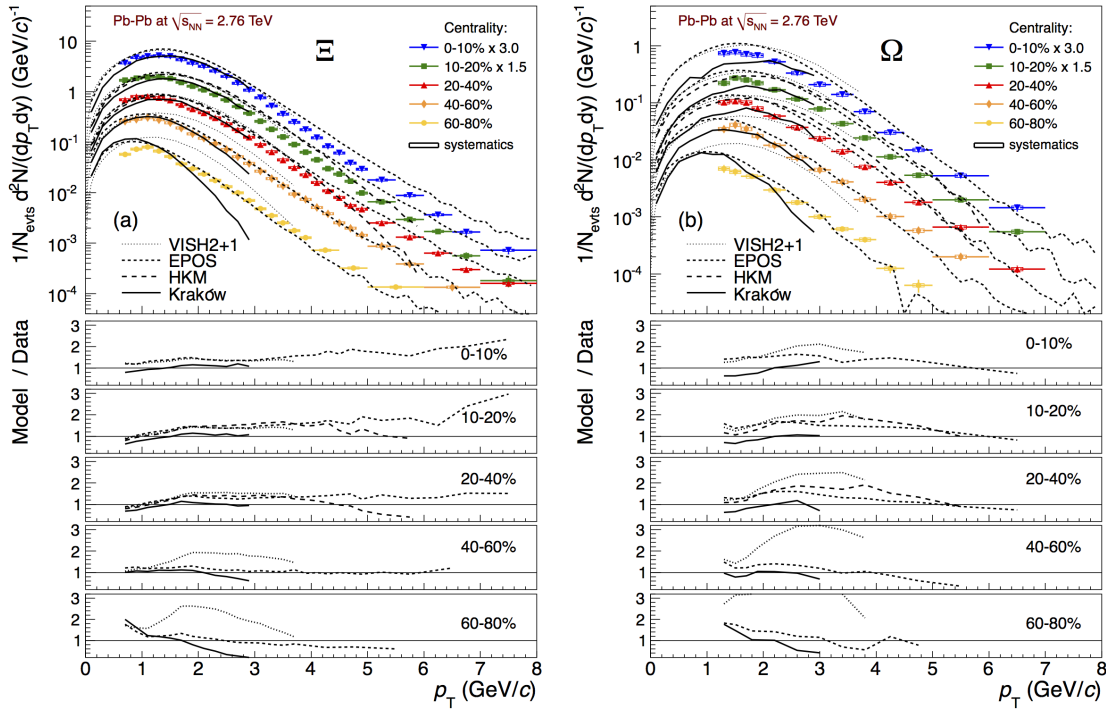


Figure 97: Transverse momentum spectra for Ξ (a) and Ω (b) hyperons (average of particle and antiparticle) in five different centrality classes, compared to hydrodynamic models. Ratios of models to data are also shown. [125]

other models only the predictions for the Ξ^- and Ω^- are available at the time of writing.

Starting from the Ξ (left pad in Figure 97), note that in the most central events ($0 - 10\%$) all the available models succeed in describing the shape of the transverse momentum spectrum up to $3 \text{ GeV}/c$, even though only the Kraków model correctly reproduces the yield. Moving to the less central events, the quality of the agreement remains similar. The Kraków model describes both the yield and the shape to within about 30% over the centrality range $0 - 60\%$, while it fails to describe the spectrum in the most peripheral class. EPOS describes the shape correctly for all centralities and also reproduces the yield in the most peripheral class, while the other two models provide a worse description. The agreement is less successful for the Ω (right pad in Figure 97). In the most central events VISH2+1 and EPOS both overestimate the yield, though EPOS reproduces the shape; Kraków underestimates the yield and does not reproduce the slope. Moving to the most peripheral events the agreement deteriorates. The EPOS and Kraków models again provide the most successful description, reproducing the shape rather well (i.e. up to $\sim 30\%$ disagreement) in all the cen-

trality classes, although EPOS consistently overestimates the yields. As in the case of the Ξ , VISH2+1 and HKM provide a less accurate description of the data, though HKM works better than VISH2+1. Such general agreement corroborates the hydrodynamic interpretation of the transverse momentum spectra in central collisions at the LHC. In addition, comparing these models gives an insight into the mechanism at work in hyperon production. VISH2+1, which results in the least successful description, does not include the hadronic cascade mechanism. The Kraków model indeed provides a good description for both the yields and shapes in the p_T range up to 3 GeV/c. EPOS, on the other hand, includes all these processes and gives the most successful description overall in a wider p_T range. Good agreement has already been observed between EPOS and ALICE data for pion, kaon and proton spectra in central and semi-central collisions [65]; in this study the agreement is confirmed for the Ξ and Ω hyperons, and extended to peripheral events.

For pp collision at $\sqrt{s} = 2.76$ TeV, the corrected transverse momentum spectra, both for Ξ and Ω , have been compared with predictions by PYTHIA [75]. This simulator is available in different tunes, for example those listed in [134], each reflecting a distinct aspect of particle production inferred from experimental data. For the comparisons discussed in the following, the central PYTHIA Perugia 2011 (P2011, “350” tune), a PYTHIA 6.4.25 tune, has been used. Perugia 2011 is tuned to the charged particle multiplicity and p_T distributions measured in the 2010 LHC data. It utilizes the CTEQ5L parton distribution function, and differs from other PYTHIA tunes by a significant increase in multi-strange baryon yields. This feature is achieved mainly by removing the baryon suppression inherently present in the built-in “pop corn” meson creation mechanism, but also by tuning the s quark production rate relative to u and d, and adjusting the suppression of the diquark–antidiquark hadron production scale [134].

In the upper panel of Figure 98 the spectra for Ξ^- , $\bar{\Xi}^+$ and $\Omega^- + \bar{\Omega}^+$ are shown, with the predictions by PYTHIA superimposed. The ratio between the data points and the corresponding predictions are illustrated in the bottom panel of the same Figure. Although PYTHIA Perugia 2011 provides an improved description of data with respect to earlier tunes (Perugia 0), it still underestimates the measured spectra by up to a factor ~ 3 for charged Ξ and ~ 5 for the Ω .

Similar results have been obtained in the multi-strange baryon analysis in pp collisions at $\sqrt{s} = 7$ TeV [128], as shown in Figure 99. Rather similar disagreement is observed also for more recent versions of PYTHIA, such as the Perugia 2012 tune [135] (P2012, “370” tune) as shown in Figure 100.

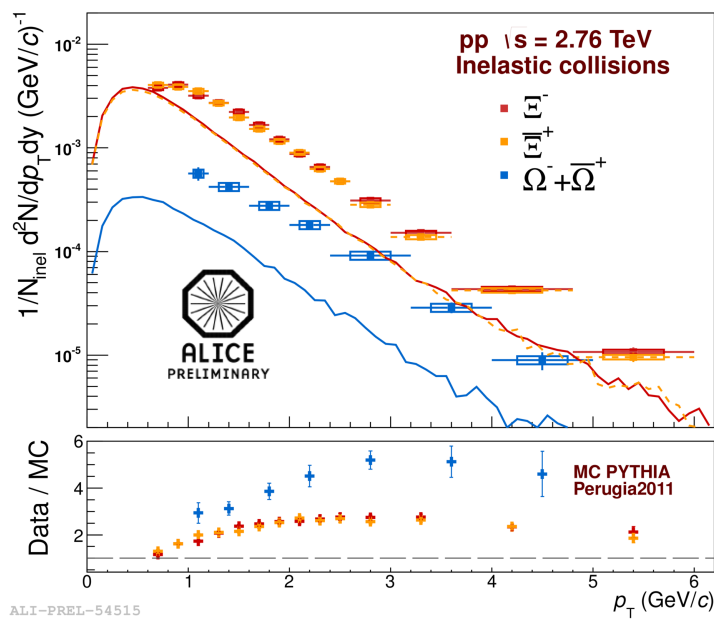


Figure 98: Comparison between the corrected spectra and the predictions from PYTHIA Perugia 2011 Monte Carlo, both for Ξ and Ω , in pp collisions at $\sqrt{s} = 2.76$ TeV.

7.2 STRANGENESS ENHANCEMENTS

As defined in Section 2.2 (Equation 2.5), the enhancements have been calculated as the ratio between the yields in Pb–Pb collisions and those in pp interactions at the same energy, both normalized to the number of participant nucleons.

At the time when this analysis was carried out, the yields for multi-strange baryons in pp collisions at the reference energy were not available. They had been obtained interpolating available measurements at higher and lower energies. In particular, the results used are:

- for the Ξ , ALICE measurements at two energies ($\sqrt{s_{NN}} = 0.9$ and 7 TeV);
- for the Ω , STAR measurements at 200 GeV (not enough statistics to extract Ω yields at 0.9 TeV with ALICE) and ALICE results at 7 TeV.

A power law describes the energy dependence seen both in real data and MC rather well. A larger exponent of 0.13 has been shown to work better for multi-strange baryons (Figure 101) than $s^{0.11}$ as measured for the charged-particle pseudo-rapidity density by the ALICE Collaboration [122]. The systematic errors on the interpolated values of the yields have been estimated moving

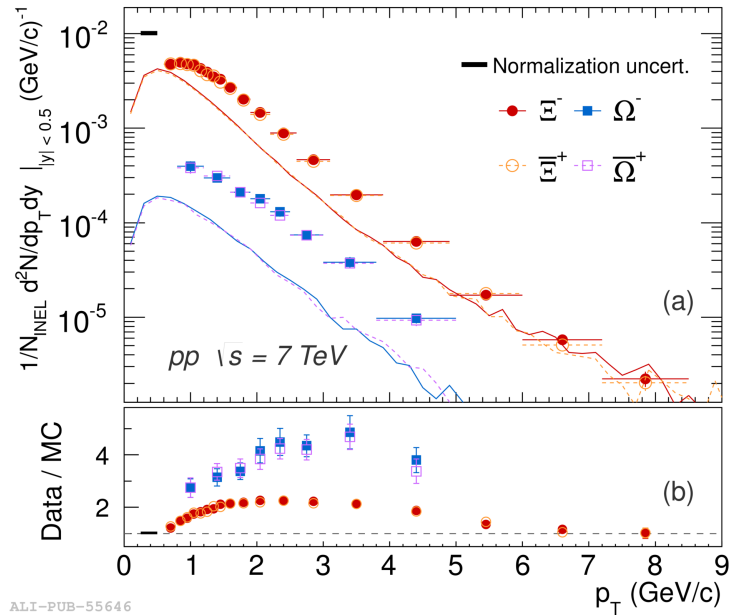


Figure 99: Comparison between the corrected spectra and the predictions from PYTHIA Perugia 2011 Monte Carlo, both for Ξ and Ω , in pp collisions at $\sqrt{s} = 7 \text{ TeV}$. [128]

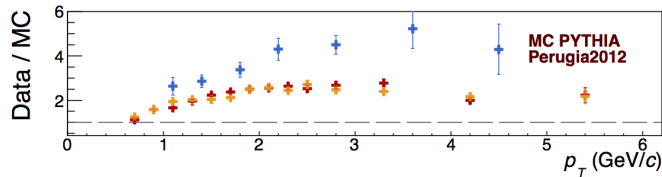


Figure 100: Comparison between the corrected spectra and the predictions from PYTHIA Perugia 2012 Monte Carlo, both for Ξ and Ω , in pp collisions at $\sqrt{s} = 2.76 \text{ TeV}$.

the extreme points to the edge of their error bars and fitting again with the same energy dependence.

The interpolated values have been checked with the measured values, now available. As can be seen in Table 20, the interpolated values are fully compatible with the measured ones.

Having the measured yields in Pb–Pb collisions in different centrality classes (Table 12) and the interpolated values for the yields in pp collisions at the same energy (Table 20), the remaining ingredients to compute the enhancements are the mean number of participant nucleons, $\langle N_{\text{part}} \rangle$, for the different centrality classes. These values are reported in Table 21.

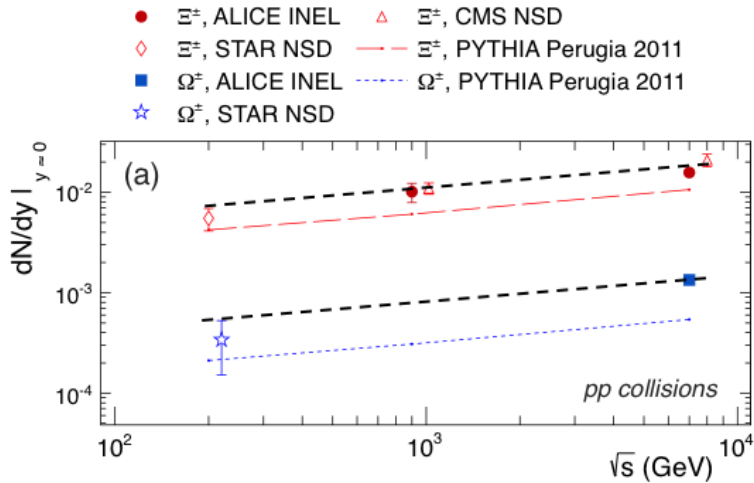


Figure 101: dN/dy as a function of collision energy. Data from ALICE and CMS at the LHC energies and from STAR at the RHIC energy are reported. The STAR and CMS data are normalized to NSD events, while the ALICE data are normalized to inelastic collisions. Multi-strange baryons produced using PYTHIA Perugia 2011 simulation are shown as coloured dashed lines, red for Ξ and blue for Ω . The black dashed lines are the PYTHIA energy dependence function shifted to fit with the data. [128].

Table 20: Integrated mid-rapidity ($|y| < 0.5$) yields of multi-strange baryons in pp collisions at $\sqrt{s} = 2.76$ TeV, compared with the yields interpolated using the PYTHIA energy dependence and the measurements at higher and lower energies by the ALICE and STAR Collaborations.

Yield	Ξ^-	$\bar{\Xi}^+$	$\Omega^- + \bar{\Omega}^-$
Interpolated	0.0068 ± 0.0023	0.0066 ± 0.0022	0.00107 ± 0.00050
Measured	$0.0059 \pm 0.0001^{+0.0007}_{-0.0007}$	$0.0060 \pm 0.0001^{+0.0007}_{-0.0007}$	$0.00092 \pm 0.00007^{+0.00017}_{-0.00017}$

Figure 102 (a and b) shows the enhancements for Ξ^- , $\bar{\Xi}^+$ and $\Omega^- + \bar{\Omega}^-$ in Pb–Pb collisions at $\sqrt{s_{NN}} = 2.76$ TeV (full symbols), as a function of the mean number of participants. For the Ω , particle and antiparticle have been added for the sake of comparison with the corresponding results at lower energies. A few first considerations on these measurements are that the enhancements:

- 1) are larger than unity for all the particles;
- 2) increase with the strangeness content of the particle, showing the hierarchy already observed at lower energies and also consistent with the picture of enhanced s – quark production in a hot and dense partonic medium;

Table 21: Geometric properties ($\langle N_{\text{part}} \rangle$, $\langle N_{\text{coll}} \rangle$ and $\langle T_{\text{AA}} \rangle$) of Pb–Pb collisions for centrality classes defined by sharp cuts on the impact parameter. The mean values and the systematic uncertainties are obtained with a Glauber Monte Carlo calculation. The values for the classes signed with a * have been obtained here as the average of the values from the corresponding finer classes (given by the Collaboration [120]).

Centrality class (%)	$\langle N_{\text{part}} \rangle$	(syst.)	$\langle N_{\text{coll}} \rangle$	(syst.)	$\langle T_{\text{AA}} \rangle$	(syst.)
00 – 05	382.7	3.0	1685	190	26	0.85
05 – 10	329.4	4.3	1316	110	21	0.67
00 – 10*	356.1	3.65	1500.5	165	23.5	0.76
10 – 20	260.1	3.8	921.2	96	14	0.45
00 – 20*	324.1	3.7	1307.4	142	18.75	0.605
20 – 40	157.2	3.1	438.4	42	6.8	0.23
40 – 60	68.56	2.0	127.7	11	2.0	0.097
60 – 80	22.52	0.77	26.71	2.0	0.42	0.026
60 – 90*	17.51	0.59	17.89	1.4	0.3754	0.02424

- 3) show the same shape and scale for baryons and antibaryons (see Ξ^- and $\bar{\Xi}^+$ in the Figure), as expected because of the vanishing net-baryon number at the LHC energy;
- 4) show a centrality dependence for which the multi-strange particle yields grow faster than linearly with $\langle N_{\text{part}} \rangle$, at least up to the three most central classes ($\langle N_{\text{part}} \rangle \sim 100 – 150$), where there are indications of a possible saturation.

Measurements of the enhancements from the experiments NA57 at the SPS (Pb–Pb collisions at $\sqrt{s_{\text{NN}}} = 17.2$ GeV) and STAR at RHIC (Au–Au collisions at $\sqrt{s_{\text{NN}}} = 200$ GeV), already shown in Figure 15, are reported on the same Figure (open symbols). From the comparison with ALICE measurements it can be observed that the enhancements are found to decrease with increasing centre-of-mass energy, continuing the trend established at lower energies, and already commented in Section 2.2.

A different way to investigate at the enhancement of the strangeness production is the hyperon-to-pion ratios, defined as:

$$\begin{aligned}\Xi/\pi &\equiv (\Xi^- + \bar{\Xi}^+)/(\pi^- + \pi^+), \\ \Omega/\pi &\equiv (\Omega^- + \bar{\Omega}^+)/(\pi^- + \pi^+),\end{aligned}$$

for A–A and pp collisions. These ratios are shown in Figure 103 as a function of $\langle N_{\text{part}} \rangle$ for LHC [128, 65, 133, 136] and RHIC [137, 88, 138] energies. Such a

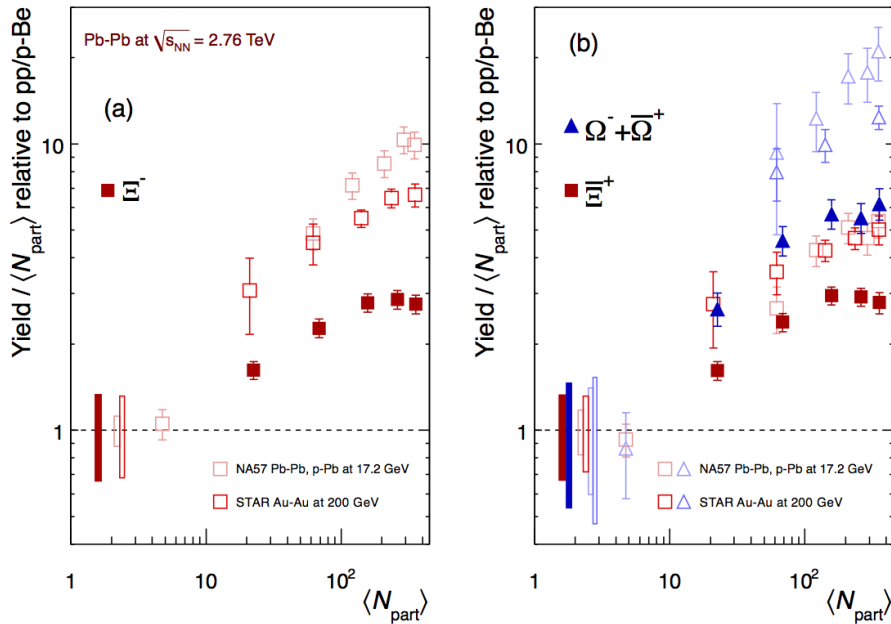


Figure 102: (a,b) Enhancements in the rapidity range $|y| < 0.5$ as a function of the mean number of participants $\langle N_{\text{part}} \rangle$, showing LHC (ALICE, full symbols), RHIC and SPS (hollow symbols) data. Boxes on the dashed line at unity indicate statistical and systematic uncertainties on the pp reference. Error bars on the data points represent those for p-Pb at the SPS and all the heavy-ion measurements. [125]

ratio could remove any dependence on the particle multiplicity at the different collision energies. These ratios indeed indicate that more than one mechanism contribute to the evolution of the enhancements with centrality as defined in the classical way.

Firstly one has to observe that the relative production of strangeness in pp collisions at the LHC energies is larger than at lower energies. This is consistent with a reduction of the canonical suppression at higher energies.

A clear increase in the strangeness production (relative to π production) is visible moving from pp to A-A. This increase in the hyperon-to-pion ratios is of the order of ~ 1.6 and 3.3 for Ξ and Ω respectively, and is of about half that of the standard enhancement ratio as defined by the participant-scaled yields. This enhancement rises with centrality up to about $\langle N_{\text{part}} \rangle \sim 150$, and apparently saturates thereafter. A small drop is observed in the Ξ/π ratio for the most central collisions, which is however of limited significance given the size of the systematic errors.

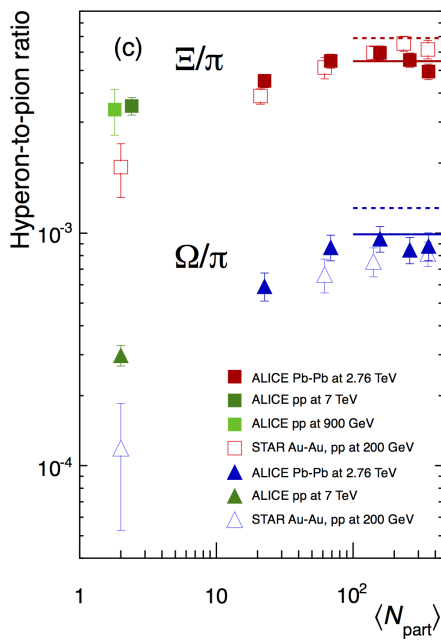


Figure 103: Hyperon-to-pion ratios as a function of $\langle N_{\text{part}} \rangle$, for A–A and pp collisions at LHC and RHIC energies. [125]

As described in Section 2.3.3 the statistical models are able to predict the yields of the particles. Figure 103 also shows the predictions for the hyperon-to-pion ratios at the LHC from the thermal models, based on a Grand-Canonical approach, described in [62] (full line, with a chemical freeze-out temperature parameter $T = 164$ MeV) and [139] (dashed line, with $T = 170$ MeV). The predictions for $T = 164$ MeV agree reasonably with the present data.

As anticipated in Section 2.3.3 the proton-to-pion ratio, for this temperature, is overpredicted by about 50% [65]. It is now an interesting question whether a Grand-Canonical thermal model can give a good description of the complete set of hadron yields in Pb–Pb collisions at LHC energy with a somewhat lower T value.

Alternatively, the low p/π ratio has been addressed in three different approaches:

- a) suppression governed by light quark fugacity in a non-equilibrium model [67, 68];
- b) baryon-antibaryon annihilation in the hadronic phase, which would have a stronger effect on protons than on multi-strange particles [140, 141, 142, 143];

- c) effects due to pre-hadronic flavour-dependent bound states above the QCD transition temperature [144, 145].

I've been personally involved, as a member of the editorial committee, in the preparation of a paper on multi-strange baryon spectra at mid-rapidity and strangeness enhancement at LHC energies by the ALICE Collaboration. The paper has been recently published on Physic Letters B [125].

7.3 NUCLEAR MODIFICATION FACTORS

As defined in Equation 2.7 the ingredients required to compute the nuclear modification factor are:

- the transverse momentum spectrum in Pb–Pb collisions;
- the transverse momentum cross-section in pp inelastic collision at the same centre-of-mass energy per nucleon pair;
- a normalization factor that attempts to describe the Pb–Pb collision as a superposition of nucleon-nucleon collisions (the number of binary collisions, N_{coll}).

To perform the ratio between the two spectra in Pb–Pb and pp, the corresponding binning should be compatible. This is the case for the Ω but not for the Ξ , where the two binnings are different for $p_T > 2.6 \text{ GeV}/c$. After the re-binning of the pp spectrum this results in more bins in the same p_T range, still with reasonable statistical errors.

Moreover, to improve the p_T coverage for the R_{AA} , one could try to find a way to extend the pp spectra to the maximum p_T of the Pb–Pb spectra. Looking at the different centrality classes in Pb–Pb collisions, one could retrieve at most the following numbers of bins in each centrality class:

CLASS 00-10% 2 bins: for Ξ [6.0,7.0] and [7.0,8.0] GeV/c and for Ω [5.0,6.0] and [6.0,7.0] GeV/c ;

CLASS 10-20% 2 bins: for Ξ [6.0,7.0] and [7.0,8.0] GeV/c and for Ω [5.0,6.0] and [6.0,7.0] GeV/c ;

CLASS 20-40% 2 bins: for Ξ [6.0,7.0] and [7.0,8.0] GeV/c and for Ω [5.0,6.0] and [6.0,7.0] GeV/c ;

CLASS 40-60% 1 bins: for Ξ [6.0,7.0] GeV/c and for Ω [5.0,6.0] GeV/c ;

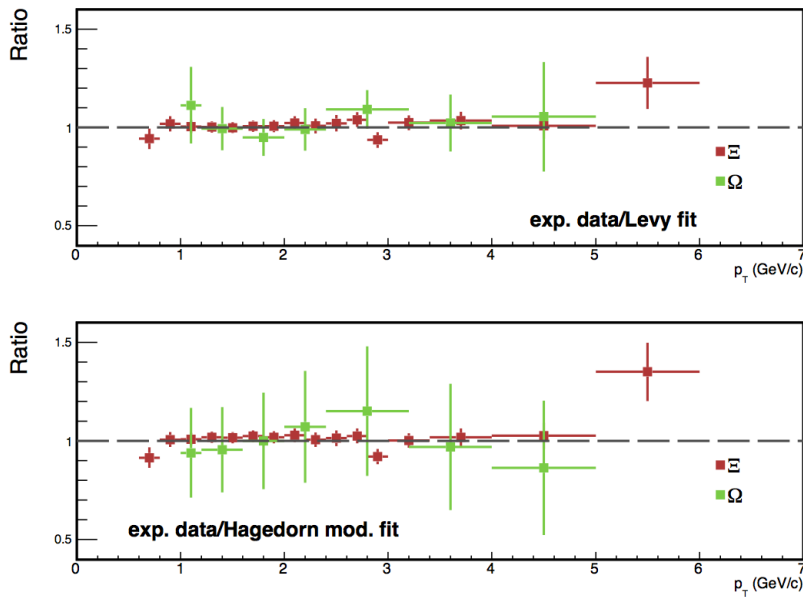


Figure 104: Ratio of the experimental spectra and the ones obtained from the Lévy-Tsallis fit function in the corresponding bins (top plot). Ratio of the experimental spectra to those obtained from the modified Hagedorn fit function (Equation 7.1, see text) in the corresponding bins (bottom plot).

CLASS 60-80% 0 bins both for Ξ and Ω .

A possible way to extend the p_T range of the pp spectra is to use a fit. The most natural choice is the Lévy-Tsallis function (Equation 5.20), already used to extrapolate the spectrum at low p_T to measure the yield over the full p_T range.

The ratio of the pp spectra experimental points over the corresponding points obtained from the Lévy-Tsallis fit function are shown in Figure 104, both for Ξ and Ω . This plot gives an idea of the discrepancy of the fit with respect to the experimental data. The ratios for Ξ and Ω are both practically flat in the full range.

One can extrapolate the fit function outside the measured region to estimate the value of the new points at high p_T . The corrected spectra with the two extrapolated points at high p_T (coloured ones: red for Ξ and green for Ω) are shown in Figure 105.

The statistical error on the extrapolated points have been estimated taking into account the uncertainties on the function parameters from the fit¹. The values and the uncertainties of the Lévy-Tsallis fits for Ξ and Ω are reported in Table 22.

¹ This has been done using the IntegralError method in Root [146].

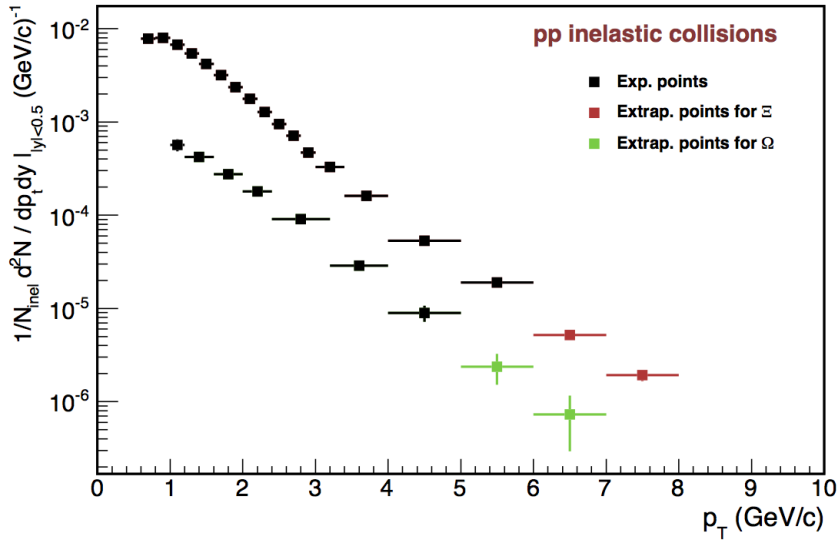


Figure 105: Corrected spectra for Ξ and Ω in pp collisions with the extrapolated points at high p_T , obtained from the Lévy-Tsallis fit function.

The fits have been performed on the spectra with their statistical and systematic errors added in quadrature. Table 23 shows the values of the statistical errors for the last three bins of the spectra, and illustrates the trend of the errors moving from the experimental points to the extrapolated ones. The errors on the Ω become particularly large because of the uncertainty on the fit, as can be seen also in Table 22.

The contribution to the systematic uncertainty in the extrapolated points coming from the extrapolation procedure should be considered. To estimate this contribution one can study the differences between different extrapolation procedures. The following different fits to extrapolate the spectra at high p_T have been tested:

- Lévy-Tsallis function with a reduced fit range, excluding a few points at low p_T ;
- transverse momentum exponential function;
- modified Hagedorn function.

The so-called modified Hagedorn parametrization is defined as follows [147]:

$$\frac{1}{2\pi p_T} \frac{d^2\sigma_{\text{part.}}^{\text{pp}}}{dy dp_T} = A \frac{p_T}{m_T} \left(1 + \frac{P_T}{p_{T,0}}\right)^{-n}, \quad (7.1)$$

Table 22: Values of the three fit parameters for the Lévy-Tsallis function, both for Ξ and Ω . The parameter α is proportional to the yield, dN/dy .

Particle	Parameter	Value	Error	Relative error
Ξ	T	0.01194	0.00025	2%
	n	0.30709	0.00827	3%
	α	10.3326	0.63008	6%
Ω	T	0.00094	0.00008	9%
	n	0.39368	0.05376	14%
	α	14.2683	7.67511	54%

Table 23: Statistical errors for the last experimental point and the two extrapolated points in the pp spectra for Ξ and Ω .

Particle	Bin 14 (exp. point)		
	Bin 15 (extr. point)	Bin 16 (extr. point)	
Ξ	8.3%	10.2%	13.6%
Ω	12.0%	36.4%	59.6%

where m_T denotes the transverse mass $m_T = \sqrt{m_0^2 + p_T^2}$, and m_0 is the rest mass of the particle. For small p_T values the term $(1 + p_T/p_{T,0})^{-n}$ behaves like an exponential function with an inverse slope parameter of $p_{T,0}/n$, while for large p_T ones the Hagedorn function behaves like a power-law function.

Comparisons between these fits and the one with the Lévy-Tsallis function on the full p_T range are reported in Figure 106: here all the used functions are overlapped with the experimental points, both for Ξ and Ω . The best description of the measured spectra has been obtained by a fit using the modified Hagedorn function. In Figure 107 the ratio between the spectra obtained fitting the experimental points using the Lévy-Tsallis function and the modified Hagedorn function are reported for Ξ and Ω .

As an estimate of the systematic uncertainty coming from the extrapolation, the difference in the prediction of the two points at high p_T between the Lévy-Tsallis fit function (considered the standard measurement) and the Hagedorn fit function has been taken. The value of the systematic uncertainties coming from the extrapolation procedure for the two extrapolated points are reported in Table 24.

Looking at the definition of the R_{AA} , this can be obtained dividing the ratio of the yields as a function of the transverse momentum by the mean nuclear overlap function $\langle T_{AA} \rangle$ (Note 7 in Chapter 2). The T_{AA} is connected to the number of binary collision by the following relation: $\langle T_{AA} \rangle = \langle N_{\text{coll}} \rangle / \sigma_{\text{inel}}^{\text{NN}}$. The inelastic nucleon-nucleon cross section is equal to $\sigma_{\text{INEL}}^{\text{NN}} = 62.8 \pm 2.4$ mbar for pp

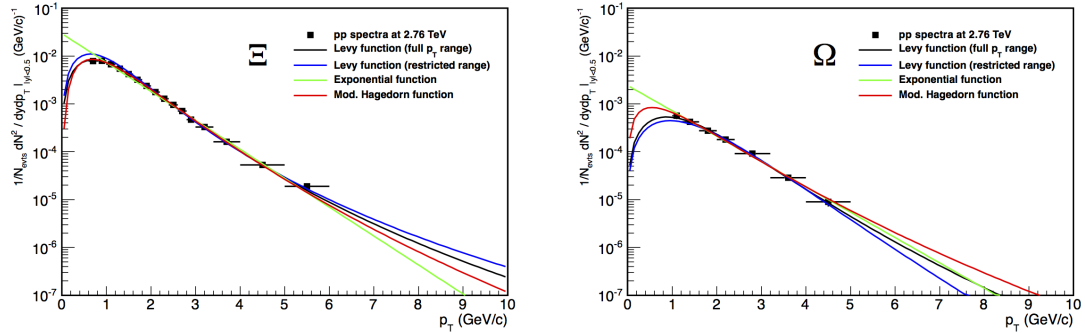


Figure 106: Comparison of the functions used to fit the cascade spectra in pp collisions at 2.76 TeV: (Black) Lévy-Tsallis fit function over the full p_T range, (Blue) Lévy-Tsallis fit function on a reduced p_T range, (Green) p_T exponential function and (Red) Modified Hagedorn function.

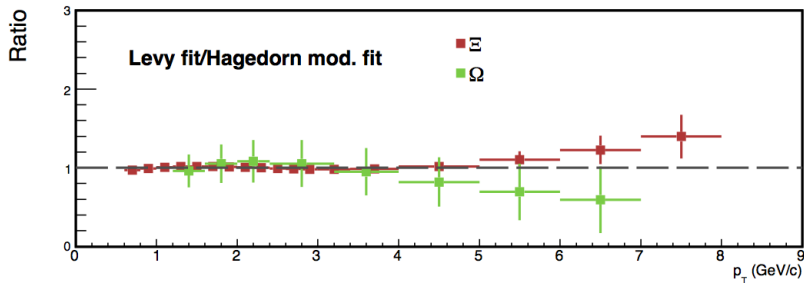


Figure 107: Ratio between the spectra obtained fitting the pp spectra at $\sqrt{s} = 2.76$ TeV with the Lévy-Tsallis function and the modified Hagedorn function.

collisions at $\sqrt{s} = 2.76$ TeV as measured by the ALICE Collaboration [131]. The values of the mean nuclear overlap function $\langle T_{AA} \rangle$ for each centrality class are reported in Table 21 together with the corresponding systematic uncertainties in each centrality class.

The R_{AA} as a function of the transverse momentum in the five centrality classes ($0 - 10\%$, $10 - 20\%$, $20 - 40\%$, $40 - 60\%$ and $60 - 80\%$), for the Ξ and Ω , are shown in Figure 108. They are also compared with the corresponding measurements for lighter particles: charged π , charged K , p and ϕ . The measurements obtained in the most central class for the π , K and p , and compared with the measurements for the cascade in the $0 - 10\%$ centrality class, are performed in the $0 - 5\%$ centrality class. For the ϕ the following five centrality classes are used: $0 - 10\%$, $10 - 20\%$, $20 - 30\%$, $40 - 50\%$ and $60 - 80\%$. On the left part of each plot at $R_{AA} = 1$ the systematic errors coming from the normalization factor $\langle T_{AA} \rangle$ are

Table 24: Values of the systematic uncertainty on the extrapolated points for Ξ and Ω .

Particle	Exp. points	Second to the last Bin	Last Bin
Ξ	7.1%	23.8%	40.2%
Ω	11.4%	33.0%	42.6%

reported. For all the particles, statistical and systematic uncertainties have been separated and are represented by lines and boxes respectively. For the cascades, the measurement obtained with the extrapolated points in the pp spectra are marked with a shaded systematic error box.

The differences in shape of the R_{AA} shown in Figure 108 between baryons and mesons are a consequence of the interplay between the shapes of the p_T distributions and the collective flow (both depending on the particle mass), jet quenching phenomena (sensitive to the parton species) and eventually new hadronization mechanisms such as parton recombination. In particular, the following observations can be made:

- 1) the R_{AA} for Ξ shows similar values as for the protons at high p_T ($> 5 \text{ GeV}/c$), where the suppression is expected not to depend on the particle mass; this may indicate that progenitor partons of these baryons show similar energy loss;
- 2) at intermediate p_T there are indications of mass-ordering among the baryons and among the mesons, with the R_{AA} for the mesons lower than the one for the baryons;
- 3) the R_{AA} for the Ω is greater than unity and becomes closer to one when going from the most central to the most peripheral event class; such behaviour might be interpreted as an effect of the strangeness enhancement, which is larger for the Ω compared with the Ξ and thus has a larger effect on the R_{AA} value.

Measurements of the R_{AA} for p , Λ and Ξ by the STAR Collaboration have been presented in Chapter 2 (Figure 25). These results have been obtained in two centrality classes (0 – 5% and 60 – 80%) for the Au–Au collisions at $\sqrt{s_{NN}} = 200 \text{ GeV}$. The R_{AA} for the Ξ at the LHC energy is smaller than at the RHIC energy; in particular the maximum of the distribution for the Ξ at LHC is compatible with the unity, while at RHIC it is well over unity. The maxima are reached at similar values of transverse momentum ($\sim 3 \text{ GeV}/c$). Similar behaviour moving from the lower to the higher energy can be observed in the most peripheral class. The lowering of the R_{AA} for the Ξ in the common p_T region might be connected with the lowering of the strangeness enhancement from the RHIC to the LHC

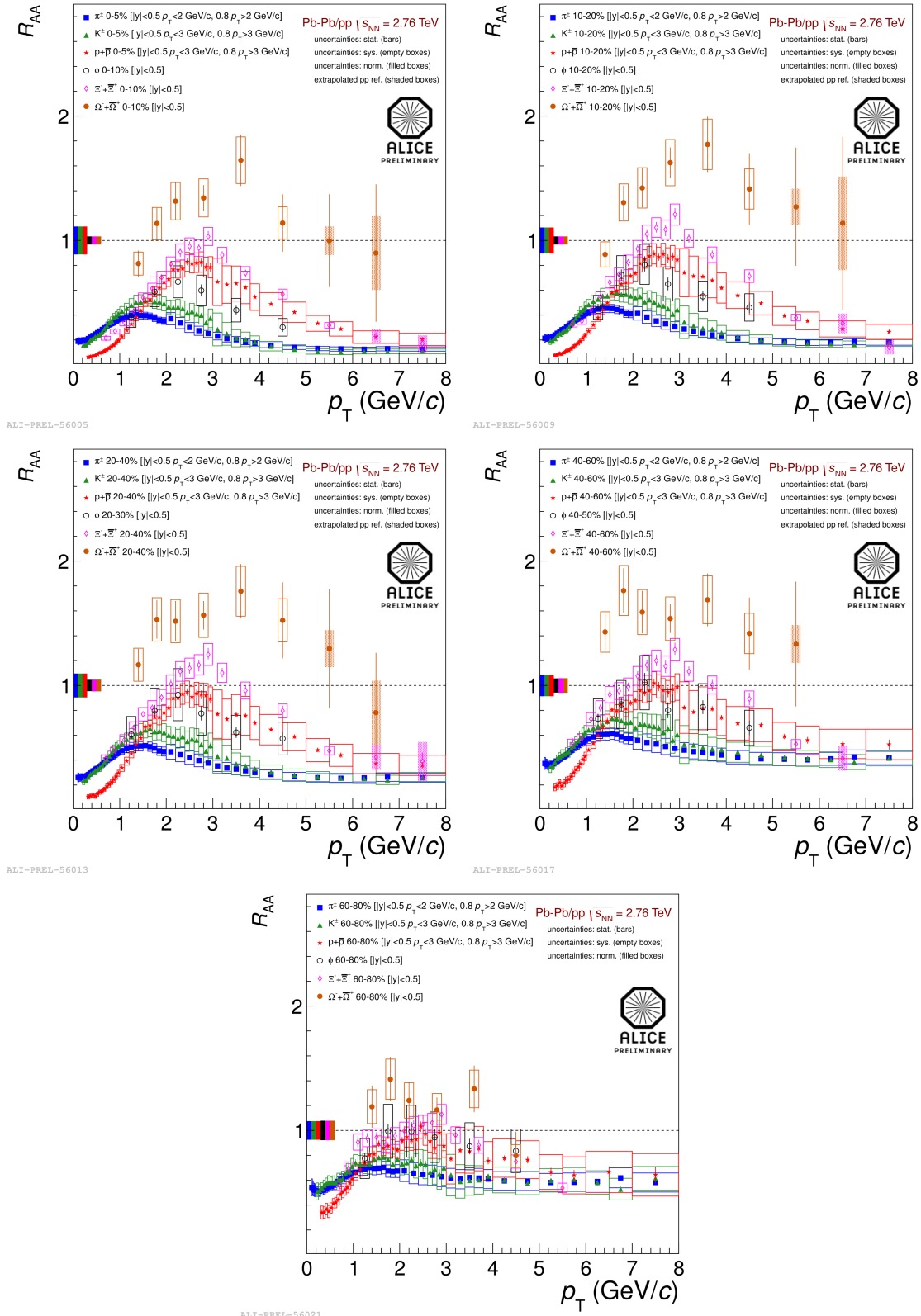


Figure 108: R_{AA} as a function of p_T in five centrality classes for Ξ and Ω with the addition of the extrapolated points obtained from the Lévy-Tsallis fit in the pp spectra.

energy. The covered transverse momentum range in the measurement by STAR does not allow a comparison with the higher p_T behaviour observed by ALICE. No measurement of the R_{AA} for the Ω by the STAR Collaboration has been published. Further comparisons could come with the measurement of the R_{CP} for the cascades by the ALICE Collaboration.

The results presented on the R_{AA} for the cascades by the ALICE Collaboration are preliminary. In view of the final analysis few improvements could be achieved. As explained in Chapter 6 the measurement of the transverse momentum spectra for the cascades in pp collisions at $\sqrt{s} = 2.76$ TeV has been performed using the reduced sample that takes into account the information from the SDD. The available homogeneous production that does not use the information from the SDD has almost twice the statistics of the sample used for the preliminary results. Using this last sample might enable a reduction in the number of extrapolated bins in the measured multi-strange spectra in pp collisions, leading to an improvement of the R_{AA} precision in the high p_T region. In addition, finer binning could be obtained for the spectra in pp collisions (especially in the higher statistics region, between 2 and 3 GeV/c) providing an overall better description of the R_{AA} as a function of p_T .

The final results will be the subject of a dedicated ALICE publication on the R_{AA} , which should include both cascades and single-strange hadrons (Λ and K_S^0). The corresponding editorial committee, which I've been proposed to join, is going to be appointed in January 2014.

CONCLUSIONS

In this thesis the measurement of the multi-strange baryon production in Pb–Pb and pp collisions at the centre-of-mass energy of 2.76 TeV using the ALICE apparatus have been presented. The cascade identification technique, based on the topological reconstruction of weak decays into charged particles, has been described. Such a technique is very effective thanks to the excellent particle identification and tracking capability of the ALICE central barrel detectors.

The measurements of the strangeness enhancement for the Ξ and Ω at the LHC energy have been presented and compared with the lower energies measurements obtained by the NA57 and STAR Collaborations. The enhancements are larger than unity for all the particles. They increase with the strangeness content of the particle, showing the hierarchy already observed at lower energies and is also consistent with the picture of enhanced $s\bar{s}$ pair production in a hot and dense partonic (deconfined) medium. The centrality dependence shows that the multi-strange particle yields grow faster than linearly with $\langle N_{\text{part}} \rangle$, at least up to the three most central classes ($N_{\text{part}} > 100 - 150$), where there are indications of a possible saturation of the enhancements. Compared to measurements at lower energies, the enhancements are found to decrease as the centre-of-mass energy of the collision increases, continuing the trend established at SPS and between SPS and RHIC. The historical role of the strangeness enhancement measurement within the context of the QGP study has been emphasized, focusing on a possible explanation of the energy dependence of this observable as being due to the gradual reduction of the canonical suppression mechanism in the proton-proton system.

The hyperon-to-pion ratios as a function of $\langle N_{\text{part}} \rangle$, both in A–A and pp collisions, from the ALICE and STAR measurements, have been proposed as an

alternative way to look at the strangeness enhancement. They indicate that different factors contribute to the evolution of the enhancements with centrality. Indeed the relative production of strangeness in pp collisions is larger than at lower energies. In addition, the enhancements are seen to be in part the result of a general relative increase of multiplicity at mid-rapidity, not entirely related to strangeness. The increase in the hyperon-to-pion ratios in A–A relative to pp is indeed about half that of the usual enhancement ratio as defined by the participant-scaled yields.

The transverse momentum spectra for the Ξ^- , $\bar{\Xi}^+$, Ω^- and $\bar{\Omega}^+$ in Pb–Pb collisions have been compared with hydrodynamic model predictions finding that the best agreement is obtained with the Kraków and EPOS models, with the latter covering a wider p_T range. In addition, the p_T spectra in pp collisions for Ξ^- , $\bar{\Xi}^+$ and $\Omega^- + \bar{\Omega}^+$ have been compared with predictions by recent PYTHIA tunes; both the Perugia 2011 and Perugia 2012 tunes underestimate the yields for the cascades.

The nuclear modification factors for the Ξ and Ω have been calculated in five centrality classes and compared with the corresponding factors for π^\pm , K^\pm , p and ϕ also measured by the ALICE Collaboration. The Ξ seems to follow the same behaviour of the protons at high p_T to indicate that progenitor partons of the two baryons show similar energy loss, while the Ω seems to be strongly affected by the strangeness enhancement, showing an R_{AA} larger than unity. At mid- p_T , indications of mass-ordering between the different baryons (and mesons) are present. The higher p_T reach for all the particles compared to the spectra at RHIC and the nuclear modification factor for the Ω , not even measured at lower energies, make these preliminary results uniquely interesting: the observed features provide crucial constraints for the various energy loss models. The analysis is expected to be finalized in the next months and will bring the corresponding results to publication.

BIBLIOGRAPHY

- [1] F. Halzen and A.D. Martin.
Quarks and Leptons: an introductory course in modern particle physics.
By John Wiley and Sons (1984).
ISBN: 0471887412.
(Cited on page 5.)
- [2] P.A.M. Dirac.
The quantum theory of the electron.
In Proceedings of The Royal Society A **117**, p. 610-624 (1928).
DOI: 10.1098/rspa.1928.0023.
(Cited on page 7.)
- [3] P.M.S. Blackett and G.P.S. Occhialini.
Some photographs of the tracks of penetrating radiation.
In Proceedings of The Royal Society A **139**, p. 699-727 (1933).
DOI: 10.1098/rspa.1933.0048.
(Cited on page 7.)
- [4] K. Nakamura et al.
Particle physics booklet.
LINK: <http://pdg.lbl.gov/>.
(Cited on pages 8, 71, and 72.)
- [5] S. Bethke.
The 2009 world average of α_S .
In European Physical Journal C **64**, p. 689-703 (2009).
DOI: 10.1140/epjc/s10052-009-1173-1.
(Cited on page 11.)

- [6] V. Koch.
Introduction to chiral symmetry.
 In LBL-38000 (1995).
 (Cited on page 12.)
- [7] B. Moussallam.
Symmetrie chirale en QCD et theorie effective de basse energie.
 In La QCD a l'oeuvre: des hadrons au plasma by Institut national de Physique Nucleaire et de Physique des Particules du CNRS (2005).
<http://ipnweb.in2p3.fr/PhT-IPN/enseignements/cours-pdf/>.
 (Cited on page 12.)
- [8] L. Chang and C.D. Roberts.
Hadron Physics: the essence of matter.
 In AIP Conference Proceedings 1361, p. 91-114 (2011).
 DOI: 10.1063/1.3622689.
 (Cited on page 12.)
- [9] N. Cabibbo and G. Parisi.
Exponential hadronic spectrum and quark liberation.
 In Physics Letters B 59, p. 67-69 (1975).
 DOI: 10.1016/0370-2693(75)90158-6.
 (Cited on page 12.)
- [10] J.C. Collins and M.J. Perry.
Superdense matter: neutrons or asymptotically free quarks?
 In Physical Review Letters 34, p. 1353-1356 (1975).
 DOI: 10.1103/PhysRevLett.34.1353.
 (Cited on page 12.)
- [11] A. Chodos, R.L. Jaffe, K. Johnson, C.B. Thorn, and V.F. Weisskopf.
New extended model of hadrons.
 In Physical Review D 9, p. 3471-3495 (1974).
 DOI: 10.1103/PhysRevD.9.3471.
 (Cited on page 12.)
- [12] C. Kuhn.
Plasma de quarks et de gluons et matiere etrangé du SPS au LHC.
 In Matiere hadronique. De la structure du nucléon au déconfinement des quarks by Institut national de Physique Nucleaire et de Physique des Particules du CNRS (1998).
<http://cel.archives-ouvertes.fr/docs/00/65/29/35/PDF/8-Kuhn.pdf>.
 (Cited on page 13.)

- [13] F. Karsch.
Lattice QCD at high temperature and density.
 By Publications at Bielefeld University in Lecture Notes in Physics **583**, p. 209-249 (2002).
 LINK: <http://pub.uni-bielefeld.de/publication/2333905>.
 (Cited on page 14.)
- [14] K. Yagi, T. Hatsuda and Y. Miake.
Quark-Gluon Plasma. From Big Bang to Little Bang.
 By Cambridge University Press (2008).
 ISBN: 9780521089241.
 (Cited on page 14.)
- [15] E. V. Shuryak.
The QCD vacuum, hadrons and superdense matter.
 In World Scientific Lecture Notes in Physics (volume 71) by World Scientific Publishing (2004).
 ISBN: 9789812385741.
 (Cited on page 14.)
- [16] J. S. Lange.
A comparison between an ultra-relativistic Au+Au collision and the primordial universe.
 In Origin of Matter and Evolution of Galaxies by World Scientific Publishing (2004).
 ISBN: 9812388249.
 (Cited on page 15.)
- [17] P. Braun-Munziger.
Chemical equilibration and the Hadron-QGP phase transition.
 In Nuclear Physics A **681**, p. 119-123 (2001).
 DOI: 10.1016/S0375-9474(00)00492-9.
 (Cited on pages 15 and 16.)
- [18] M.G. Alford.
QCD at high density/temperature.
 In Nuclear Physics B - Proceedings Supplements **117**, p. 65-82 (2003).
 DOI: 10.1016/S0920-5632(03)01411-7.
 (Cited on page 15.)
- [19] Accelerator division annual reports, 1 July 1972.
<http://www.osti.gov/scitech/biblio/937059>.
 (Cited on page 16.)

- [20] Yu. A. Lazarev.
New heavy-ion cyclotron.
In Soviet Atomic Energy **4**, p. 329-330 (1979).
DOI: [10.1007/BF01118382](https://doi.org/10.1007/BF01118382).
(Cited on page 16.)
- [21] H. A. Gustafsson et al.
Collective flow observed in relativistic nuclear collisions.
In Physical Review Letters **52**, p. 1590-1593 (1984).
DOI: [10.1103/PhysRevLett.52.1590](https://doi.org/10.1103/PhysRevLett.52.1590).
(Cited on page 16.)
- [22] *History of GSI. A Laboratory for Everyone.*
http://www.gsi.de/en/start/about_us/history.htm.
(Cited on page 16.)
- [23] *CERN press release - February 2000.*
<http://press.web.cern.ch/press-releases/2000/02/new-state-matter-created-cern>.
(Cited on page 17.)
- [24] B. Muller and J.L. Nagle.
Results from the Relativistic Heavy Ion Collider.
In Annual Review of Nuclear and Particle Science **56**, p. 93-135 (2006).
DOI: [10.1146/annurev.nucl.56.080805.140556](https://doi.org/10.1146/annurev.nucl.56.080805.140556).
(Cited on page 18.)
- [25] *RHIC scientists serve up "perfect" liquid.*
<http://www.bnl.gov/rhic/news2/news.asp?a=303&t=pr>.
(Cited on page 18.)
- [26] *Run overview of the Relativistic Heavy Ion Collider.*
<http://www.agsrhichome.bnl.gov/RHIC/Runs/>.
(Cited on page 18.)
- [27] *UrQMD Animations.*
<http://urqmd.org/~weber/CERNmovies/index.html>.
(Cited on page 19.)
- [28] R.J. Glauber.
Lectures in Theoretical Physics Volume I, p. 315.
By Interscience Publishers (1959).
(Cited on pages 19 and 68.)

- [29] K.C. Chung, C.S. Wang, A.J. Santiago and G. Pech.
Transverse and forward energy distributions in ultrarelativistic heavy-ion collisions by an absorption model.
In Physical Review C **57**, p. 847-856 (1998).
DOI: [10.1103/PhysRevC.57.847](https://doi.org/10.1103/PhysRevC.57.847).
(Cited on pages [19](#) and [68](#).)
- [30] J.D. Bjorken.
Highly relativistic nucleus-nucleus collisions: the central rapidity region.
In Physical Review D **27**, p. 140-151 (1983).
DOI: [10.1103/PhysRevD.27.140](https://doi.org/10.1103/PhysRevD.27.140).
(Cited on page [19](#).)
- [31] B. Hippolyte.
Probing the (s)QGP with strangeness.
Contribution to Strangeness in Quark Matter (2013).
LINK: <http://www.ep.ph.bham.ac.uk/SQM2013/Home.html>.
(Cited on page [21](#).)
- [32] BRAHMS Collaboration.
Nuclear stopping in Au+Au collisions at $\sqrt{s_{NN}} = 200 \text{ GeV}$.
In Physical Review Letters **93**, n. 10 (2004).
DOI: [10.1103/PhysRevLett.93.102301](https://doi.org/10.1103/PhysRevLett.93.102301).
(Cited on page [22](#).)
- [33] M. Gell-Mann and Y. Ne'eman.
The Eightfold Way.
By W.A. Benjamin (1964).
OCoLC: 593984056.
(Cited on page [23](#).)
- [34] J. Rafelski and B. Müller.
Strangeness production in the Quark-Gluon Plasma.
In Physical Review Letters **48**, p. 1066-1069 (1982).
DOI: [10.1103/PhysRevLett.48.1066](https://doi.org/10.1103/PhysRevLett.48.1066).
(Cited on pages [25](#) and [27](#).)
- [35] P. Koch, B. Müller and J. Rafelki.
Strangeness in relativistic heavy ion collisions.
In Physics Reports **142**, p. 167-262 (1986).
DOI: [10.1016/0370-1573\(86\)90096-7](https://doi.org/10.1016/0370-1573(86)90096-7).
(Cited on page [27](#).)

- [36] NA57 Collaboration.
Enhancement of hyperon production at central rapidity in 158 A GeV/c Pb–Pb collisions.
In Journal of Physics G: Nuclear and Particle Physics **32**, p. 427-441 (2006).
DOI: [10.1088/0954-3899/32/4/003](https://doi.org/10.1088/0954-3899/32/4/003).
(Cited on page 28.)
- [37] NA57 Collaboration.
Strangeness enhancement at central rapidity in 40 A GeV/c Pb–Pb collisions.
In Journal of Physics G: Nuclear and Particle Physics **37**, n. 045105 (2010).
DOI: [10.1088/0954-3899/37/4/045105](https://doi.org/10.1088/0954-3899/37/4/045105).
(Cited on page 28.)
- [38] STAR Collaboration.
Enhanced strange baryon production in Au+Au collisions compared to p+p at $\sqrt{s_{NN}} = 200$ GeV.
In Physical Review C **77**, n. 044908 (2008).
DOI: [10.1103/PhysRevC.77.044908](https://doi.org/10.1103/PhysRevC.77.044908).
(Cited on pages 28, 29, 42, and 44.)
- [39] L.D. Landau.
On the multiparticle production in high-energy collisions.
In Izvestiya Akademii Nauk Seriya Fizicheskaya **17**, p. 51-64 (1953).
(Cited on page 30.)
- [40] STAR Collaboration.
Centrality dependence of charged hadron and strange hadron elliptic flow from $\sqrt{s_{NN}} = 200$ GeV Au+Au collisions.
In Physical Review C **77**, n. 054901 (2008).
DOI: [10.1103/PhysRevC.77.054901](https://doi.org/10.1103/PhysRevC.77.054901).
(Cited on page 30.)
- [41] ALICE Collaboration.
Elliptic flow of charged particles in Pb–Pb Collisions at $\sqrt{s_{NN}} = 2.76$ TeV.
In Physical Review Letters **105**, n. 252302 (2010).
DOI: [10.1103/PhysRevLett.105.252302](https://doi.org/10.1103/PhysRevLett.105.252302).
(Cited on page 30.)
- [42] G. Policastro, D.T. Don and A.O. Starinets.
Shear viscosity of strongly coupled $N = 4$ supersymmetric Yang-Mills plasma.
In Physical Review Letters **87**, n. 081601 (2001).
DOI: [10.1103/PhysRevLett.87.081601](https://doi.org/10.1103/PhysRevLett.87.081601).
(Cited on page 31.)

- [43] G. Policastro, D.T. Don and A.O. Starinets.
From AdS/CFT correspondence to hydrodynamics, 2: sound waves.
 In *Journal of High Energy Physics* **6**, p. 1175-1190 (2001).
 DOI: [10.1088/1126-6708/2002/12/054](https://doi.org/10.1088/1126-6708/2002/12/054).
 (Cited on page 31.)
- [44] P. Kovtun, D.T. Son and A.O. Starinets.
Holography and hydrodynamics: diffusion on stretched horizons.
 In *Journal of High Energy Physics* **7**, p. 1675-1701 (2003).
 DOI: [10.1088/1126-6708/2003/10/064](https://doi.org/10.1088/1126-6708/2003/10/064).
 (Cited on page 31.)
- [45] C. Shen, U. Heinz, P. Huovinen and H. Song.
Radial and elliptic flow in Pb+Pb collisions at energies available at the CERN Large Hadron Collider from viscous hydrodynamics.
 In *Physical Review C* **84**, n. 044903 (2011).
 DOI: [10.1103/PhysRevC.84.044903](https://doi.org/10.1103/PhysRevC.84.044903).
 (Cited on pages 31 and 151.)
- [46] P. Bożek.
Flow and interferometry in (3+1)-dimensional viscous hydrodynamics.
 In *Physical Review C* **85**, n. 034901 (2012).
 DOI: [10.1103/PhysRevC.85.034901](https://doi.org/10.1103/PhysRevC.85.034901).
 (Cited on pages 31 and 151.)
- [47] F. Cooper and G. Frye.
Single-particle distribution in the hydrodynamic and statistical thermodynamic models of multiparticle production.
 In *Physical Review D* **10**, p. 186-189 (1974).
 DOI: [10.1103/PhysRevD.10.186](https://doi.org/10.1103/PhysRevD.10.186).
 (Cited on page 31.)
- [48] S.A. Bass et al.
Microscopic models for ultrarelativistic heavy ion collisions.
 In *Progress in Particle and Nuclear Physics* **41**, p. 255-369 (1998).
 DOI: [10.1016/S0146-6410\(98\)00058-1](https://doi.org/10.1016/S0146-6410(98)00058-1).
 (Cited on page 32.)
- [49] M. Bleicher et al.
Relativistic hadron-hadron collisions in the ultra-relativistic quantum molecular dynamics model.
 In *Journal of Physics G: Nuclear and Particle Physics* **25**, p. 1959-1896 (1999).

- DOI: [10.1088/0954-3899/25/9/308](https://doi.org/10.1088/0954-3899/25/9/308).
 (Cited on page 32.)
- [50] H. Sorge, H. Stöcker and W. Greiner.
Relativistic quantum molecular dynamics approach to nuclear collisions at ultra-relativistic energies.
 In Nuclear Physics A **498**, p. 567-576 (1989).
 DOI: [10.1016/0375-9474\(89\)90641-6](https://doi.org/10.1016/0375-9474(89)90641-6).
 (Cited on page 32.)
- [51] W. Cassing and E.L. Bratkovskaya.
Hadronic and electromagnetic probes of hot and dense nuclear matter.
 In Physics Reports **308**, p. 65-233 (1999).
 DOI: [10.1016/S0370-1573\(98\)00028-3](https://doi.org/10.1016/S0370-1573(98)00028-3).
 (Cited on page 32.)
- [52] Y. Karpenko and Y. Sinyukov.
Femtoscopic scales in central A+A collisions at RHIC and LHC in a hydrokinetic model.
 In Journal of Physics G: Nuclear and Particle Physics **38**, n. 124059 (2011).
 DOI: [10.1088/0954-3899/38/12/124059](https://doi.org/10.1088/0954-3899/38/12/124059).
 (Cited on pages 32 and 151.)
- [53] Y. Karpenko and Y. Sinyukov.
Uniform description of bulk observables in the hydrokinetic model of A+A collisions at the BNL Relativistic Heavy Ion Collider and the CERN Large Hadron Collider.
 In Physical Review C **87**, n. 024914 (2013).
 DOI: [10.1103/PhysRevC.87.024914](https://doi.org/10.1103/PhysRevC.87.024914).
 (Cited on pages 32 and 151.)
- [54] K. Werner, I. Karpenko, M. Bleicher, T. Pierog, and S. Porteboeuf-Houssais.
Jets, bulk matter, and their interaction in heavy ion collisions at several TeV.
 In Physical Review C **85**, n. 064907 (2012).
 DOI: [10.1103/PhysRevC.85.064907](https://doi.org/10.1103/PhysRevC.85.064907).
 (Cited on pages 32 and 151.)
- [55] K. Werner.
Lambda-to-Kaon ratio enhancement in heavy ion collisions at several TeV.
 In Physical Review Letters **109**, n. 102301 (2012).
 DOI: [10.1103/PhysRevLett.109.102301](https://doi.org/10.1103/PhysRevLett.109.102301).
 (Cited on pages 32 and 151.)

- [56] K. Werner.
 V_2 Scaling in PbPb Collisions at 2.76 TeV.
In arXiv:1205.3379 (2012).
(Cited on pages 32 and 151.)
- [57] ALICE Collaboration.
 K_S^0 and Λ in Pb–Pb collisions at $\sqrt{s_{NN}} = 2.76$ TeV.
In Physical Review Letters **111**, n. 222301 (2013).
DOI: 10.1103/PhysRevLett.111.222301.
(Cited on page 32.)
- [58] F. Beccattini et al.
Features of particle multiplicities and strangeness production in central heavy ion collisions between $1.7A$ and $158A$ GeV/c.
In Physical Review C **64**, n. 024901 (2000).
DOI: 10.1103/PhysRevC.64.024901.
(Cited on page 33.)
- [59] C. Blume and C. Markert.
Strange hadron production in heavy ion collisions from SPS to RHIC.
In Progress in Particle and Nuclear Physics **66**, p. 834-879 (2011).
DOI: 10.1016/j.ppnp.2011.05.001.
(Cited on page 33.)
- [60] P. Braun-Munziger, I. Heppe and J. Stachel.
Chemical equilibration in Pb+Pb collisions at the SPS.
In Physics Letters B **465**, p. 15-20 (1999).
DOI: 10.1016/S0370-2693(99)01076-X.
(Cited on page 33.)
- [61] ALICE Collaboration.
Pion, Kaon and Proton production in central Pb–Pb collisions at $\sqrt{s_{NN}} = 2.76$ TeV.
In Physical Review Letters **109**, n. 252301 (2012).
DOI: 10.1103/PhysRevLett.109.252301.
(Cited on page 33.)
- [62] A. Adronic, P. Braun-Munziger and J. Stachel.
Thermal hadron production in relativistic nuclear collisions: the hadron mass spectrum, the horn, and the QCD phase transition.
In Physics Letters B **673**, p. 142-145 (2009).
DOI: 10.1016/j.physletb.2009.06.021.
(Cited on pages 34 and 159.)

- [63] J. Stachel, A. Adronic, P. Braun-Munziger and K. Redlich.
Confronting LHC data with statistical hadronization model.
 In arXiv:1311.4662v1 (2013).
 (Cited on page 34.)
- [64] A. Adronic, P. Braun-Munziger, K. Redlich and J. Stachel.
The statistical model in Pb-Pb collisions at the LHC.
 In Nuclear Physics A **904-905**, p. 535c-538c (2013).
 DOI: [10.1016/j.nuclphysa.2013.02.070](https://doi.org/10.1016/j.nuclphysa.2013.02.070).
 (Cited on page 34.)
- [65] ALICE Collaboration.
Centrality Dependence of π , K , p production in Pb–Pb collisions at $\sqrt{s_{NN}} = 2.76$ TeV.
 In Physical Review C **88**, n. 044910 (2013).
 DOI: [10.1103/PhysRevC.88.044910](https://doi.org/10.1103/PhysRevC.88.044910).
 (Cited on pages 34, 153, 157, and 159.)
- [66] F. Beccattini, M. Gazdzicki and J. Sollfrank.
On chemical equilibrium in nuclear collisions.
 In European Physical Journal C **5**, p. 143-153 (1998).
 DOI: [10.1007/s100529800831](https://doi.org/10.1007/s100529800831).
 (Cited on page 34.)
- [67] J. Lettessier and J. Rafelski.
Chemical non-equilibrium and deconfinement in 200A GeV sulphur induced reactions.
 In Physical Review C **59**, p. 947-954 (1999).
 DOI: [10.1103/PhysRevC.59.947](https://doi.org/10.1103/PhysRevC.59.947).
 (Cited on pages 35 and 159.)
- [68] J. Lettessier and J. Rafelski.
Hadron production and phase changes in relativistic heavyion collisions.
 In European Physics Journal A **35**, p. 221-242 (2008).
 DOI: [10.1140/epja/i2007-10546-7](https://doi.org/10.1140/epja/i2007-10546-7).
 (Cited on pages 35 and 159.)
- [69] G. Torrieri, S. Jeon, J. Lettessier and J. Rafelski.
SHAREv2: fluctuations and a comprehensive treatment of decay feed-down.
 In Computer Physics Communications **175**, p. 635-649 (2006).
 DOI: [10.1016/j.cpc.2006.07.010](https://doi.org/10.1016/j.cpc.2006.07.010).
 (Cited on page 35.)

- [70] M. Petran, J. Latessier, V. Petracek and J. Rafelski.
Hadron production and QGP hadronization in Pb–Pb collisions at $\sqrt{s_{NN}} = 2.76$ TeV.
In Physical Review C **88**, n. 034907 (2013).
DOI: [10.1103/PhysRevC.88.034907](https://doi.org/10.1103/PhysRevC.88.034907).
(Cited on page 35.)
- [71] S. Hamieh, K. Redlich and A. Tounsi.
Canonical Description of Strangeness Enhancement from p-A to Pb-Pb Collisions.
In Physics Letters B **486**, p. 61-66 (2000).
DOI: [10.1016/S0370-2693\(00\)00762-0](https://doi.org/10.1016/S0370-2693(00)00762-0).
(Cited on page 36.)
- [72] K. Redlich and A. Tounsi.
Strangeness enhancement and Energy dependence in Heavy Ion Collisions.
In European Physics Journal C **24**, p. 589-594 (2002).
DOI: [10.1007/s10052-002-0983-1](https://doi.org/10.1007/s10052-002-0983-1).
(Cited on page 36.)
- [73] F. Beccattini and J. Manninen.
Centrality dependence of strangeness production in heavy-ion collisions as a geometrical effect of core-corona superposition.
In Physics Letters B **673**, p. 19-23 (2009).
DOI: [10.1016/j.physletb.2009.01.066](https://doi.org/10.1016/j.physletb.2009.01.066).
(Cited on page 36.)
- [74] STAR Collaboration.
Strangeness Enhancement in Cu-Cu And Au-Au Collisions at $\sqrt{s_{NN}} = 200$ GeV.
In Physical Review Letters **108**, n. 072301 (2012).
DOI: [10.1103/PhysRevLett.108.072301](https://doi.org/10.1103/PhysRevLett.108.072301).
(Cited on page 36.)
- [75] T. Sjstrand et al.
PYTHIA 6.2 - Physics and Manual.
In arXiv:0108264 (2001).
(Cited on pages 37, 61, and 153.)
- [76] X. Wang and M. Gyulassy.
HJING: a Monte Carlo model for multiple jet production in pp, pA and AA collisions.
In Physical Review D **44**, p. 3501-3516 (1991).
DOI: [10.1103/PhysRevD.44.3501](https://doi.org/10.1103/PhysRevD.44.3501).
(Cited on pages 38 and 61.)

- [77] K.J. Eskola, K.Kajantie and J. Lindfors.
Quark and gluon production in high energy nucleus-nucleus collisions.
 In Nuclear Physics B **323**, p. 37-52 (1989).
 DOI: [10.1016/0550-3213\(89\)90586-5](https://doi.org/10.1016/0550-3213(89)90586-5).
 (Cited on page 38.)
- [78] G. Calucci and D. Treleani.
Minijet: cross section and energy distribution in very-high-energy nuclear collisions.
 In Physical Review D **41**, p. 3367–3380 (1990).
 DOI: [10.1103/PhysRevD.41.3367](https://doi.org/10.1103/PhysRevD.41.3367).
 (Cited on page 38.)
- [79] R.J. Fries, B. Muller and C. Nonaka.
Hadronization in heavy ion collisions: recombination and fragmentation of partons.
 In Physical Review Letters **90**, n. 202303 (2003).
 DOI: [10.1103/0954-3899/30/1/025](https://doi.org/10.1103/0954-3899/30/1/025).
 (Cited on page 39.)
- [80] B. Hippolyte.
Bulk matter physics and its future at the Large Hadron Collider.
 In European Physical Journal C **62**, p. 237-242 (2009).
 DOI: [10.1140/epjc/s10052-009-0910-9](https://doi.org/10.1140/epjc/s10052-009-0910-9).
 (Cited on page 39.)
- [81] R.J. Fries and B. Müller.
Heavy ions at LHC: theoretical issues.
 In European Physical Journal C **34**, p. s279-285 (2004).
 DOI: [10.1140/epjcd/s2004-04-026-6](https://doi.org/10.1140/epjcd/s2004-04-026-6).
 (Cited on page 40.)
- [82] D. d'Enterria.
Jet quenching.
 In arXiv:0902.2011 (2009).
 (Cited on page 40.)
- [83] ALICE Collaboration.
Suppression of charged particle production at large transverse momentum in central Pb-Pb collisions at $\sqrt{s_{NN}} = 2.76$ TeV.
 In Physics Letters B **696**, p. 30-39 (2010).
 DOI: [10.1016/j.physletb.2010.12.020](https://doi.org/10.1016/j.physletb.2010.12.020).
 (Cited on pages 41 and 42.)

- [84] ALICE Collaboration.
Transverse Momentum Distribution and Nuclear Modification Factor of Charged Particles in p–Pb Collisions at $\sqrt{s_{\text{NN}}} = 2.76 \text{ TeV}$.
 In Physical Review Letters **110**, n. 082302 (2013).
 DOI: [10.1103/PhysRevLett.110.082302](https://doi.org/10.1103/PhysRevLett.110.082302).
 (Cited on pages [41](#) and [42](#).)
- [85] K. Tywoniuk, I. Arsenet, L.V. Bravina, A.B. Kaidalov and E.E. Zabrodin.
Nuclear suppression at RHIC and LHC in Glauber-Grobov approach.
 In Journal of Physics G: Nuclear and Particle Physics **35**, n. 044039 (2008).
 DOI: [10.1088/0954-3899/35/4/044039](https://doi.org/10.1088/0954-3899/35/4/044039).
 (Cited on page [41](#).)
- [86] J.W. Cronin et al.
Production of hadron at large transverse momentum at 200, 300, and 400 GeV.
 In Physical Review D **11**, p. 3105-3123 (1975).
 DOI: [10.1103/PhysRevD.11.3105](https://doi.org/10.1103/PhysRevD.11.3105).
 (Cited on page [41](#).)
- [87] D. Colella for the ALICE Collaboration.
Multi-strange baryon production in Pb–Pb and pp collisions at $\sqrt{s_{\text{NN}}} = 2.76 \text{ TeV}$ with the ALICE experiment at the LHC.
 In arXiv:1311.6003 (2013).
 (Cited on page [43](#).)
- [88] STAR Collaboration.
Systematic measurements of identified particle spectra in pp, d+Au, and Au+Au collisions at the STAR detector.
 In Physical Review C **79**, n. 034909 (2009).
 DOI: [10.1103/PhysRevC.79.034909](https://doi.org/10.1103/PhysRevC.79.034909).
 (Cited on pages [44](#) and [157](#).)
- [89] L. Evans and P. Bryant.
LHC Machine.
 In Journal of Instrumentation **3**, n. S08001 (2008).
 DOI: [10.1088/1748-0221/3/08/S08001](https://doi.org/10.1088/1748-0221/3/08/S08001).
 (Cited on page [45](#).)
- [90] CERN Scientific Information Service.
LHC Design Report Volume I+II+III.
 In CERN-2004-003-V1(-V2)(-V3) (2004).
 (Cited on page [46](#).)

- [91] *TE-EPC-LPC LHC units.*
<http://te-epc-lpc.web.cern.ch/te-epc-lpc/machines/lhc/general.stm>.
 (Cited on page 46.)
- [92] ALICE Collaboration.
ALICE: Physics Performance Report, Volume I.
 In Journal of Physics G: Nuclear and Particle Physics **30**, p. 1517-1763 (2004).
 DOI: 10.1088/0954-3899/30/11/001.
 (Cited on page 47.)
- [93] ALICE Collaboration.
ALICE Technical Proposal.
 In CERN-LHCC-95-71 (1995).
 ISBN: 9789290830771.
 (Cited on page 47.)
- [94] ATLAS Collaboration.
ATLAS Technical Proposal.
 In CERN-LHCC-94-43 (1994).
 ISBN: 9789290830672.
 (Cited on page 47.)
- [95] CMS Collaboration.
CMS Technical Proposal.
 In CERN-LHCC-94-38 (1994).
 ISBN: 9789290830689.
 (Cited on page 47.)
- [96] LHCb Collaboration.
LHCb Technical Proposal.
 In CERN-LHCC-98-004 (1998).
 ISBN: 9789290831235.
 (Cited on page 47.)
- [97] LHCf Collaboration.
Technical Proposal for CERN LHCf Experiment.
 In CERN-LHCC-05-032 (2005).
 (Cited on page 48.)
- [98] TOTEM Collaboration.
Total Cross Section, Elastic Scattering and Diffraction Dissociation at the LHC.
 In CERN-LHCC-99-007 (1999).
 (Cited on page 48.)

- [99] ALICE Collaboration.
The ALICE experiment at the CERN LHC.
 In JINST **3**, n. S08002 (2008).
 DOI: [10.1088/1748-0221/3/08/S08002](https://doi.org/10.1088/1748-0221/3/08/S08002).
 (Cited on pages [48](#), [50](#), [51](#), [52](#), [55](#), [59](#), [60](#), and [62](#).)
- [100] L. Betev et al.
Definition of the ALICE coordinate system and basic rules for sub-detector components numbering.
 In Internal Note ALICE-INT-2003-038 (2003).
 (Cited on page [50](#).)
- [101] J. Alme et al.
The ALICE TPC, a large 3-dimensional tracking device with fast readout for ultra-high multiplicity events.
 In Nuclear Instruments and Methods in Physics Research A **622**, p. 316-367 (2010).
 DOI: [10.1016/j.nima.2010.04.042](https://doi.org/10.1016/j.nima.2010.04.042).
 (Cited on pages [54](#) and [67](#).)
- [102] P. Giubellino et al.
Day one Proton-Proton physics with the ALICE central detector.
 In ALICE Internal Note 2000-28 (2000).
 (Cited on page [55](#).)
- [103] ALICE Collaboration.
 Technical Design Report on Forward Detectors: FMD, To and VZERO.
 In CERN-LHCC-2004-025 (2004).
 (Cited on page [56](#).)
- [104] ALICE Collaboration.
ALICE Technical Design Report of the Trigger, Data Acquisition, High-Level Trigger, Control System.
 In CERN-LHCC-2003-062 (2003).
 ISBN: 9789290832171.
 (Cited on page [57](#).)
- [105] O. Bärring, B. Couturier, J.-D. Durand and S. Ponce.
CASTOR: operational issues and new developments.
 In CHEP2004 proceedings (2004).
 (Cited on page [58](#).)

- [106] F. Carena et al.
The ALICE experiment Control System.
 In CHEP2004 proceedings (2004).
 (Cited on page 59.)
- [107] I. Foster and C. Kesselman.
The Grid – Blueprint for a New Computing Infrastructure.
 By Morgan Kaufmann Publishers (1999).
 ISBN: 1-55860-475-8.
 (Cited on page 60.)
- [108] S. Bagnasco et al.
AliEn: ALICE Environment on the GRID.
 In Journal of Physics: Conference Series 119, n.062012 (2008).
 DOI: 10.1088/1742-6596/119/6/062012.
 (Cited on page 60.)
- [109] R. Brun and F. Rademakers.
ROOT - An object oriented data analysis framework.
 In Nuclear Instruments and Methods in Physics Research Section A 389, p. 81-86 (1997).
 DOI: 10.1016/S0168-9002(97)00048-X.
 (Cited on page 60.)
- [110] *MonALISA repository for ALICE.*
<http://alimonitor.cern.ch/map.jsp>.
 (Cited on page 61.)
- [111] *ALICE Offline pages.*
<http://aliweb.cern.ch/Offline/>.
 (Cited on page 60.)
- [112] T. Sjöstrand et al.
High-Energy-Physics Event Generation with PYTHIA 6.1.
 In Computer Physics Communication 135, p. 238-259 (2001).
 DOI: 10.1016/S0010-4655(00)00236-8.
 (Cited on page 61.)
- [113] R. Engel, J. Ranft, and S. Roesler.
Hard diffraction in hadron-hadron interactions and in photoproduction.
 In Physical Review D 52, n. 3 (1995).
 DOI: 10.1103/PhysRevD.52.1459.
 (Cited on page 61.)

- [114] R. Brun, F. Bruyant, M. Maire, A. C. McPherson, and P. Zanarini.
Geant: simulation program for particle physics experiments. User guide and reference manual.
In CERN-DD-78-2-REV (1978).
(Cited on page 62.)
- [115] S. Agostinelli et al.
Geant4 - a simulation toolkit.
In Nuclear Instruments and Methods in Physics Research A **506**, p. 250-303 (2003).
DOI: [10.1016/S0168-9002\(03\)01368-8](https://doi.org/10.1016/S0168-9002(03)01368-8).
(Cited on page 62.)
- [116] A. Fassò et al.
The physics models of FLUKA: status and recent developments.
In arXiv:0306267 (2003).
(Cited on page 62.)
- [117] P. Billoir.
Progressive track recognition with a Kalman-like fitting procedure.
In Computer Physics Communications **57**, p. 390-394 (1989).
DOI: [10.1016/0010-4655\(89\)90249-X](https://doi.org/10.1016/0010-4655(89)90249-X).
(Cited on page 63.)
- [118] A. Maire.
Production des baryons multi-étranges au LHC dans les collisions proton-proton avec l'expérience ALICE.
PhD thesis, Institut Pluridisciplinaire Hubert Curien - IPHC, 2011.
LINK: <http://cds.cern.ch/record/1490315?ln=it>.
(Cited on pages 64 and 113.)
- [119] ALICE Collaboration.
ALICE: Physics Performance Report, Volume II.
In Journal of Physics G: Nuclear and Particle Physics **32**, p. 1295-2040 (2006).
DOI: [10.1088/0954-3899/32/10/E01](https://doi.org/10.1088/0954-3899/32/10/E01).
(Cited on pages 65, 67, and 79.)
- [120] ALICE Collaboration.
Centrality determination of Pb-Pb collisions at $\sqrt{s_{\text{NN}}} = 2.76 \text{ TeV}$ with ALICE.
In Physical Review C **88**, n. 044909 (2013).
DOI: [10.1103/PhysRevC.88.044909](https://doi.org/10.1103/PhysRevC.88.044909).
(Cited on pages 68, 69, 70, and 157.)

- [121] D. Kharzeev, Eugene Levin, and Marzia Nardi.
Color glass condensate at the LHC: hadron multiplicities in pp, pA and AA collisions.
 In Nuclear Physics A **747**, p. 609-629 (2005).
 DOI: [10.1016/j.nuclphysa.2004.10.018](https://doi.org/10.1016/j.nuclphysa.2004.10.018).
 (Cited on page 69.)
- [122] ALICE Collaboration.
Charged-particle multiplicity density at midrapidity in central Pb-Pb collisions at $\sqrt{s_{NN}} = 2.76 \text{ TeV}$.
 In Physical Review Letters **105**, n. 252301 (2010).
 DOI: [10.1103/PhysRevLett.105.252301](https://doi.org/10.1103/PhysRevLett.105.252301).
 (Cited on pages 78 and 154.)
- [123] ALICE Collaboration.
Charged-particle multiplicity measurement in proton-proton collisions at $\sqrt{s_{NN}} = 7 \text{ TeV}$ with ALICE at LHC.
 In European Physical Journal C **68**, p. 345-354 (2010).
 DOI: [10.1140/epjc/s10052-010-1350-2](https://doi.org/10.1140/epjc/s10052-010-1350-2).
 (Cited on pages 78 and 126.)
- [124] M. Krivda et al.
The ALICE trigger system performance for pp and Pb-Pb collisions.
 In JINST **7**, n. C01057 (2012).
 DOI: [10.1088/1748-0221/7/01/C01057](https://doi.org/10.1088/1748-0221/7/01/C01057).
 (Cited on page 82.)
- [125] ALICE Collaboration.
Multi-strange baryon production at mid-rapidity in Pb-Pb collisions at $\sqrt{s_{NN}} = 2.76 \text{ TeV}$.
 In Physics Letters B **728**, p. 216-227 (2014).
 DOI: [10.1016/j.physletb.2013.11.048](https://doi.org/10.1016/j.physletb.2013.11.048).
 (Cited on pages 102, 112, 118, 152, 158, 159, and 160.)
- [126] ALICE Collaboration.
Midrapidity antiproton-to-proton ratio in pp collisions at $\sqrt{s} = 0.9$ and 7 TeV measured by the ALICE experiment.
 In Physical Review Letters **105**, n. 072002 (2010).
 DOI: [10.1103/PhysRevLett.105.072002](https://doi.org/10.1103/PhysRevLett.105.072002).
 (Cited on page 109.)
- [127] A. Fassò et al.
The FLUKA code: present applications and future developments.

- In CHEP03 proceedings (2003).
 (Cited on page 109.)
- [128] ALICE Collaboration.
Multi-strange baryon production in pp collisions at $\sqrt{s} = 7 \text{ TeV}$ with ALICE.
 In Physics Letters B **712**, p. 309-318 (2012).
 DOI: [10.1016/j.physletb.2012.05.011](https://doi.org/10.1016/j.physletb.2012.05.011).
 (Cited on pages 113, 148, 153, 155, 156, and 157.)
- [129] E. Schnedermann, J. Sollfrank and U. Heinz.
Thermal phenomenology of hadrons from 200A GeV S+S collisions.
 In Physical Review C **48**, p. 2462-2475 (1993).
 DOI: [10.1103/PhysRevC.48.2462](https://doi.org/10.1103/PhysRevC.48.2462).
 (Cited on page 120.)
- [130] C. Tsallis.
Possible generalization of Boltzmann-Gibbs statistics.
 In Journal of Statistical Physics **52**, p. 479-487 (1988).
 DOI: [10.1007/BF01016429](https://doi.org/10.1007/BF01016429).
 (Cited on page 121.)
- [131] ALICE Collaboration.
Measurement of inelastic, single- and double-diffraction cross sections in proton-proton collisions at the LHC with ALICE.
 In European Physical Journal C **73**, n. 2456 (2012).
 DOI: [10.1140/epjc/s10052-013-2456-0](https://doi.org/10.1140/epjc/s10052-013-2456-0).
 (Cited on pages 139, 146, and 164.)
- [132] SLUO Lectures on Statistics and Numerical Methods in HEP.
http://www-group.slac.stanford.edu/sluo/lectures/Stat_Lectures.html.
 (Cited on page 141.)
- [133] ALICE Collaboration.
Strange particle production in proton-proton collisions at $\sqrt{s} = 0.9 \text{ TeV}$ with ALICE at the LHC.
 In European Physics Journal C **71**, n. 1594 (2011).
 DOI: [10.1140/epjc/s10052-011-1594-5](https://doi.org/10.1140/epjc/s10052-011-1594-5).
 (Cited on pages 148 and 157.)
- [134] P.Z. Skands.
Tuning Monte Carlo generators: the Perugia tunes.
 In Physical Review D **82**, n. 074018 (2010).

- DOI : [10.1103/PhysRevD.82.074018](https://doi.org/10.1103/PhysRevD.82.074018).
 (Cited on page 153.)
- [135] PYTHIA version 6.4.
http://www.hepforge.org/archive/pythia6/update_notes-6.4.28.txt.
 (Cited on page 153.)
- [136] ALICE Collaboration.
Production of pions, kaons and protons in pp collisions at $\sqrt{s} = 900$ GeV with ALICE at the LHC.
 In European Physics Journal C **71**, n. 1655 (2011).
 DOI: [10.1140/epjc/s10052-011-1655-9](https://doi.org/10.1140/epjc/s10052-011-1655-9).
 (Cited on page 157.)
- [137] STAR Collaboration.
Strange particle production in p+p collisions at $\sqrt{s} = 200$ GeV.
 In Physical Review C **75**, n. 064901 (2007).
 DOI: [10.1103/PhysRevC.75.064901](https://doi.org/10.1103/PhysRevC.75.064901).
 (Cited on page 157.)
- [138] STAR Collaboration.
Scaling properties of hyperon production in Au+Au collisions at $\sqrt{s_{NN}} = 200$ GeV.
 In Physical Review Letters **98**, n. 62301 (2007).
 DOI: [10.1103/PhysRevLett.98.062301](https://doi.org/10.1103/PhysRevLett.98.062301).
 (Cited on page 157.)
- [139] J. Cleymans, I. Kraus, H. Oeschler, K. Redlich and S. Wheaton.
Statistical model predictions for particle ratios at $\sqrt{s_{NN}} = 5.5$ TeV.
 In Physical Review C **74**, n. 034903 (2006).
 DOI: [10.1103/PhysRevC.74.034903](https://doi.org/10.1103/PhysRevC.74.034903).
 (Cited on page 159.)
- [140] F. Becattini et al.
Hadronization and hadronic freeze-out in relativistic nuclear collisions.
 In Physical Review C **85**, n. 044921 (2012).
 DOI: [10.1103/PhysRevC.85.044921](https://doi.org/10.1103/PhysRevC.85.044921).
 (Cited on page 159.)
- [141] Y. Pan.
Baryon annihilation in heavy ion collisions.
 In arXiv:1210.1577 (2012).
 (Cited on page 159.)

- [142] F. Becattini, M. Bleicher, T. Kollegger, M. Mitrovski, and T. Schuster.
Hadron formation in relativistic nuclear collisions and the QCD phase diagram.
 In Physical Review Letters **111**, n. 082302 (2013).
 DOI: [10.1103/PhysRevLett.111.082302](https://doi.org/10.1103/PhysRevLett.111.082302).
 (Cited on page 159.)
- [143] J. Steinheimer, J. Aichelin and M. Bleicher.
Nonthermal p/π Ratio at LHC as a Consequence of Hadronic Final State Interactions.
 In Physical Review Letters **110**, n. 042501 (2013).
 DOI: [10.1103/PhysRevLett.110.042501](https://doi.org/10.1103/PhysRevLett.110.042501).
 (Cited on page 159.)
- [144] C. Ratti, R. Bellwied, M. Cristoforetti and M. Barbaro.
Are there hadronic bound states above the QCD transition temperature?
 In Physical Review D **85**, n. 014004 (2012).
 DOI: [10.1103/PhysRevD.85.014004](https://doi.org/10.1103/PhysRevD.85.014004).
 (Cited on page 160.)
- [145] R. Bellwied.
Hadron formation in the deconfined matter at RHIC and LHC.
 In arXiv:1205.3625 (2012).
 (Cited on page 160.)
- [146] Root: IntegralError.
<http://root.cern.ch/root/html/TF1.html#TF1:IntegralError@1>.
 (Cited on page 161.)
- [147] R. Hagedorn.
Multiplicities, p_T distributions and the expected hadron → Quark-Gluon phase transition.
 In Nuovo Cimento **6**, p. 1-50 (1983).
 DOI: [10.1007/BF02740919](https://doi.org/10.1007/BF02740919).
 (Cited on page 162.)